HIGHLY STRUCTURED NANO-COMPOSITE ANODES FOR SECONDARY LITHIUM ION BATTERIES

A Dissertation
Presented to
The Academic Faculty

by

Kara Evanoff

In Partial Fulfillment
of the Requirements for the Degree
Doctor of Philosophy in the
School of Materials Science and Engineering

Georgia Institute of Technology
May 2014

HIGHLY STRUCTURED NANO-COMPOSITE ANODES FOR SECONDARY LITHIUM ION BATTERIES

Approved by:

Dr. Gleb Yushin, Advisor
School of Materials Science and Engineering
Georgia Institute of Technology

Dr. W. Brent Carter
School of Materials Science and Engineering
Georgia Institute of Technology

Dr. Jud Ready
Electro-Optical Systems Laboratory
Georgia Tech Research Institute

Dr. Rosario Gerhardt
School of Materials Science and Engineering
Georgia Institute of Technology

Dr. Tom Fuller
School of Chemical and Biomolecular Engineering
Georgia Institute of Technology

Date Approved: December 6, 2013

ACKNOWLEDGEMENTS

There are several individuals who I would like to acknowledge for their guidance and support in completing this body of work. First, I would like to extend thanks and appreciation to my advisors Dr. Gleb Yushin, Dr. Jud Ready, and Dr. Tom Fuller. I am extremely appreciative for the support and mentorship, both intellectually and professionally, from all of you. Thank you for allowing me to be a part of your group. I enjoyed the opportunity to learn new topics and approaches. Thank you Dr. Yushin for sharing your knowledge, experience, and drive for excellence, all of which has helped guide me in my own endeavors. You are an excellent advisor and I feel fortunate that I was able to be a part of your group. I would also like to thank Dr. Ready for his care and mentorship of me as a professional and a person. Some of my fondest memories of graduate school are those spent with the group. I would also like to thank Dr. Fuller for his support and insightful guidance. I would also like to thank the members of my thesis committee, Dr. Brent Carter and Dr. Rosario Gerhardt, for offering their expertise and time.

I would like to extend my gratitude to all my friends and coworkers who have been supportive of me during my graduate studies. Throughout my time at Georgia Tech, I have had the pleasure of working with one of the most selfless persons I know, Dr. Alexandre "Sacha" Magasinski. I want to thank Sacha for being very instrumental in my research and for being a joy to be around. I will miss working with you. I would also like to acknowledge Jim Benson for providing great insight and thoroughness into all of the studies we worked on together. I also extend gratitude to Zoran Milicev for not only the TEM analysis but also for having a dedication and interest in research that is admirable. I am very appreciative of Stephan Turano for his willingness to assist me whenever I asked and for always having a great attitude. Finally, many thanks to Dr. Hyea Kim for experimental assistance and good conversation.

In addition, I am thankful for the contributions of my collaborators including Dr. Junbing Yang (Argonne National Laboratory) for synthesis of the graphene particles; Diana Lewis, Dr. Mark Schauer, Dr. David Lashmore and Nanocomp Technologies for the CNT fabric production and insightful discussion; Jung Tae Lee for TGA measurements; Dr. Javed Khan and Prof. Alexander Balandin for conductivity measurements; Justin Nguyen for development of methods to produce vertically aligned CNTs on metal foils; Nox Nitta and Feixiang Wu for EDS measurements; and Dr. Yang Liu for *in situ* TEM studies.

Most importantly, I would like to offer my deepest thanks to my family who have unconditionally encouraged and supported me in every avenue I have pursued. I am extremely fortunate to have been raised in a very loving and supportive environment. I am indebted to my family for instilling a strong foundation of hard work and integrity.

TABLE OF CONTENTS

LIST OF TABLES

LIST OF FIGURES

Page

LIST OF ABBREVIATIONS

CE	coulombic efficiency
CNT	carbon nanotube
CTE	coefficient of thermal expansion
CV	cyclic voltammetry
CVD	chemical vapor deposition
DEC	diethyl carbonate
DMC	dimethyl carbonate
e-beam	electron beam
EC	ethylene carbonate
EDS	energy dispersive X-ray spectroscopy
EELS	electron energy loss spectroscopy
EFTEM	energy filtered TEM
EIS	electrochemical impedance spectroscopy
FLG	few layer graphene
FTIR	Fourier transform infrared spectroscopy
GITT	galvanostatic intermittent titration technique

GNR	graphene nanoribbon
GNS	graphene nanosheet
HF	hydrofluoric acid
Li-ion	Lithium-ion
MCMB	mesocarbon microbeads
MWCNT	multi-walled carbon nanotubes
PAA	polyacrylic acid
PANI	polyaniline
PE	polyethylene
PECVD	plasma-enhanced CVD
PEG	purified exfoliated graphite
PP	polypropylene
PVD	physical vapor deposition
PVDF	polyvinylidene fluoride
SEI	solid electrolyte interface
SEM	scanning electron microscopy
SLG	single layer graphene
SWCNT	single-wall carbon nanotubes

TEM	transmission electron microscopy
TGA	thermogravimetric analysis
TMA	trimethyl aluminum
UTS	ultimate tensile strength
VACNT	vertically aligned carbon nanotube
VC	vinylene carbonate
VLS	vapor-liquid-solid
XPS	X-ray photoelectron spectroscopy
XRD	X-ray diffraction

LIST OF SYMBOLS

α	diffusivity, linear thermal expansion coefficient
α_{film}	linear thermal expansion coefficient of the film
$\alpha_{substrate}$	linear thermal expansion coefficient of the substrate
a	activity
A_{CC}	current collector area
$A_{electrode}$	surface area of the electrode
$A_{T,CNT}$	total carbon nanotube cross-sectional area
B	bulk density
C	specific heat
C_A	areal capacity loading
C_{VC}	factor of volume change of lithiated carbon
C_p	heat capacity
CNT_{VC}	factor of volume change of lithiated carbon nanotubes
$C_{V,CNT}$	volumetric capacity of carbon nanotubes
$C_{V,TF}$	volumetric capacity of a thin film
d	particle radius

D	diffusion coefficient
$d_{CNT-CNT}$	center-to-center distance between carbon nanotubes
$\varepsilon_{thermal}^{film}$	thermal deformation of a thin film
E_{cell}	cell potential at non-standard conditions
E_{cell}^{o}	standard cell potential
E_{oxid}^{o}	standard reduction potential of reduced species
E_{redn}^{o}	standard reduction potential of oxidized species
F	Faraday's constant
ΔG_{cell}^{o}	Gibbs free energy of a cell
ΔG_{rxn}^{o}	Gibbs free energy of a reaction
ΔH_{f}^{o}	enthalpy of formation
I_D	D band Raman intensity
I_G	G band Raman intensity
K	thermal conductivity
k_p	equilibrium constant
k_{soln}	electrolyte conductivity
l	half the length of a symmetric cell
l_a	solution length across the anode

l_c	solution length across the cathode
l_{CNT}	length of a carbon nanotube
l_s	solution length across the separator
l_{tab}	length of a current collector tab
Li^+	lithium ion
M_D	dry weight
M_S	suspended weight
M_W	saturated weight
n	number of electrons
N_{CNT}	number of carbon nanotubes per current collector area
ρ	density, electrical resistivity
ρ_{CC}	resistivity of current collector
ρ_{CNT}	density of carbon nanotube
$\rho_{CNT-composite}$	resistivity of a carbon nanotube composite material
$\rho_{electrode}$	electrical resistivity of the electrode
ρ_{H_2O}	density of de-ionized water
ρ_{Si}	density of silicon
p_i	partial pressure

P	porosity
Q_{dl}	constant phase element for the double layer
Q_{SEI}	constant phase element for the solid electrolyte interphase
r_{CNT}	radius of a carbon nanotube
R	gas constant
R_C	coefficient of the C-rate
R_{CNT}	resistance of an individual carbon nanotube
R_{ct}	charge transfer resistance
$R_{electrode}$	electrode resistance
$R_{electrode,A}$	electrode resistance per unit current collector area
$R_{interface}$	interfacial resistance between the current collector and active material
R_{SEI}	solid electrolyte interphase resistance
$R_{SEI,A}$	solid electrolyte interphase resistance per unit current collector area
R_{soln}	electrolyte solution resistance
$R_{total,a}$	total electrical resistance of the anode
$R_{total,A}$	total electrical resistance per unit current collector area
$R_{total,c}$	total electrical resistance of the cathode
$R_{total,s}$	total electrical resistance across the separator

S^o	entropy
Si_{VC}	factor of volume change of lithiated silicon
τ	tortuosity
$t_{CC,e}$	minimum current collector thickness (calculated from electrical considerations)
$t_{CC,t}$	minimum current collector thickness (calculated from thermal considerations)
$t_{electrode}$	electrode thickness
t_{Si}	Si thin film thickness
T	temperature
T_i	initial temperature
T_f	final temperature
T_{max}	maximum allowable temperature difference
ν	potential scan rate
V_{cell}	cell potential drop
V_{max}	maximum allowable potential difference
w_C	weight fraction of carbon
w_{CNT}	weight fraction of carbon nanotubes
w_{Si}	weight fraction of Si
w_{tab}	width of a current collector tab

w_{TF}	weight fraction of a thin film
Z_D	solid-state diffusion resistance

SUMMARY

Interest in high performance portable energy devices for electronics and electric vehicles is the basis for a significant level of activity in battery research in recent history. Lithium ion (Li-ion) batteries are of particular interest due to their high energy density, decreasing cost, and adaptable form factor. A common goal of researchers is to develop new materials that will lower the cost and weight of Li-ion batteries while simultaneously improving the performance. There are several approaches to facilitate improved battery system-level performance including, but not limited to, the development of new material structures and/or chemistries, manufacturing techniques, and cell management systems.

The performed research sought to enhance the understanding of structure-property relationships of carbon-containing composite anode materials in a Li-ion cell through materials and anode performance characterization. The approach focused on the development of new electrode material designs to yield higher energy and power characteristics, as well as increased thermal and electrical conductivities or mechanical strength, using techniques that could be scaled for large volume manufacturing. Here, three different electrode architectures of nanomaterial composites were synthesized and characterized. Each electrode structure consisted of a carbon substrate (graphene or carbon nanotubes (CNTs)) conformally coated with a high Li capacity material (silicon or germanium) via vapor deposition routes. The dimensionality and design for each structure was unique, with each offering different advantages. The addition of an external coating to further increase the stability of high capacity materials was also investigated.

Graphene-based composites confirmed that a reduction in specific surface area limits the formation of the solid electrolyte interphase (SEI). CNT-based electrodes, in

two-dimensional fabrics and three-dimensional vertically aligned films, demonstrated multiple orders of magnitude increases in electrical and thermal conductivities, in comparison to conventional electrode materials. Si-coated CNT fabrics also possess high strength which was retained after electrochemical testing. The specific strength of the Si-coated CNT fabric is higher than copper and aluminum, common current collector materials, due to the low density of the CNT fabrics. The electrochemical performance and calculations considering the electrical and thermal conductivities suggest that CNT fabrics can serve as a replacement to a Cu current collector when low to moderate current densities are used. 1 mm thick vertically aligned carbon nanotube films were produced. Analysis shows that as the thickness and active material of the electrode is increased, the areal capacity loading increases. There exists an upper bound on the electrode thickness which is largely specific to the electrode parameters (porosity, active material loading, conductivities) and cell operating conditions; however, calculations demonstrate that the electrolyte solution resistance dominates and limits that upper bound.

The completed studies demonstrated increases to the stability of carbon substrates can be achieved through reductions in the surface area achieved through thin film coatings, the use of electrolyte additives, and the presence of a thin overcoating of either carbon or alumina. Finally, formation of porous Si and porous Ge were demonstrated as a result of electrochemical cycling. The porous structure may have implications for the long term SEI stability on these materials.

CHAPTER 1

INTRODUCTION

1.1 Motivation

Although significant technological advances have occurred in the electronics industry, the batteries powering those devices have not improved at the same rate and the technology is often criticized for its slow growth.[1] This problem, in conjunction with increased concern over the effect of environmental pollutants from combustion power sources, has generated considerable interest in the development of environmentally benign, high energy storage and delivery electric devices.[2-5] Lithium-ion (Li-ion) battery technology is of particular interest due to its high energy and power characteristics that are adaptable to meet the needs of existing and emerging applications ranging from electronics to transportation (e.g. electric and hybrid-electric vehicles) to large-scale electrical grid stability. Batteries are a viable technology to meet these broad energy demands since they can provide consistent, reliable energy delivery and storage. Harvesting natural alternative energies (e.g. wind, solar) results in significant current intermittencies at different time scales and thus commonly require energy storage technologies in order to become broadly applicable. Batteries may aid in the further commercialization of renewable energy by allowing off-peak energy storage for later use.[6] In addition, advanced batteries are needed for mobile applications.

To facilitate further advancements in Li-ion technology, rational research and development must be conducted to increase performance, decrease cost, and extend cell lifetime to meet the design specifications of cutting-edge applications.[6] One route to increase battery specific energy and energy density is through the development of new anode materials with higher Li capacities as alternatives to conventional graphitic carbon electrodes. However, high capacity bulk materials pose a critical challenge to long battery

lifetimes due to large volume changes of the host material as a result of Li alloying/dealloying.[7-8] Rapid capacity loss results from these volume changes that cause mechanical failure though crack initiation, crack growth, and fracture.[9-10] Another source of irreversible capacity is the formation of a passive solid electrolyte interphase (SEI) that forms on the material surfaces and inhibits ion movement.[11-13] For these reasons, bulk high capacity alternatives demonstrate significant power loss during cycling.

Anodes comprised of nanomaterials have been investigated as alternatives to bulk materials since their constrained dimensions may provide increased electrochemical activity and improved mechanical stability.[5, 14-16] Nanomaterials can reduce the mass transfer resistance and allow for a higher degree of uniformity of the lithiated phase.[17] Thus far, nanomaterials have shown promise as alternatives to bulk materials. Carbon nanotubes (CNTs) have demonstrated improved power characteristics and in some cases higher specific capacities than graphite, but their large irreversible capacity limits their application.[4-5, 18] Other 1-D nanomaterials comprised of semiconducting or semi-metal elements (e.g. Si, Ge, and Sn) have shown greater promise due to their considerably higher theoretical capacity and somewhat stable performance. However, their poor mechanical properties and electrical conductivity pose a challenge. Highly structured composite electrodes may overcome the limitations of their pure 1-D counterparts and offer an attractive solution for new generation high capacity, high rate anode materials.

1.2 Thesis Format

In Chapter 2, electrochemical theory and techniques are introduced to establish a standard level of knowledge. Following, a general overview of Li-ion technology is provided. Afterwards, a review of the structure and synthesis of anode materials of interest (C, Si, Ge) is given. The focus is directed towards nanomaterials since there is overwhelming support that uniform, well-designed anodes at the nanoscale will lead to the development of high performance Li-ion batteries. A review of the prior art for these

materials in both pure and composite form is necessary in the development of a well-designed, high performing anode. Through consideration of the underlying electrochemical theory and the technological progress attained thus far, a set of research objectives and technical approaches are described in Chapter 3. The following chapters (4 – 7) detail the work performed in developing three separate composite electrode architectures and a method for further stabilization of them. In Chapter 8, the effect of synthesis conditions and electrode design affect the theoretical capacity and potential across the electrode. Factors leading to cell stability, sources of error and extensions of the work are also discussed. Lastly, in Chapter 9 the key findings of this research are summarized and suggestions for future work are discussed.

CHAPTER 2

BACKGROUND

2.1 Electrochemical Reactions and Cells

Basic electrochemical reactions are classified as either an oxidation reaction (electron loss) or a reduction reaction (electron gain) such that:

$$\text{Oxidation: } Red \rightarrow Ox + ne^- \quad (1)$$

$$\text{Reduction: } Ox + ne^- \rightarrow Red \quad (2)$$

where *n* is the number of electrons involved in the reaction. The number of electrons passing across the interface is determined stoichiometrically by the extent of chemical reaction producing them.[19] The oxidized species is the species that loses electrons and the reduced species is the species that gains electrons. Each reaction is a half-reaction and is independent of the other reaction. The net reaction of an oxidation and reduction reaction is termed a redox reaction.

The simplest electrochemical cell consists of two electrically conducting electrodes that are physically separated (to prevent electrical shorting) with an ion conducting electrolyte in contact with each. Electrodes can be metals, semiconductors, or semimetals in either liquid or solid form. Likewise, there exist several types of electrolytes including liquids (aqueous or non-aqueous), solids, or molten salts. The electrodes are called either the cathode or the anode depending on whether a reduction or oxidation, respectively, occurs at the electrode. For a reaction to proceed, the electrodes must be electrically connected with a pathway for ionic diffusion and the reactant species that can cause a spontaneous redox reaction must be present.

The cell potential (E^o_{cell}) can be calculated using the difference in standard electrode reduction potentials between a cathode and an anode versus a common reference electrode:

$$E^o_{cell} = E^o_{redn} - E^o_{oxid} \tag{3}$$

where E^o_{redn} and E^o_{oxid} are the standard reduction potentials of the oxidized species and the reduced species, respectively. Equation (3) is the Nernst equation under standard conditions (25 ^{o}C, the concentration of both the reduced or oxidizing species are equal to 1 M, partial pressure of all gases are 1 atm.). At non-standard conditions, the general cell potential (Equation 4) can be calculated from consideration of the general form of the Nernst equations (Equation 5,6) defined by:

$$E_{cell} = E_{redn} - E_{oxid} \tag{4}$$

$$E_{redn} = E^o_{redn} - \frac{RT}{nF} ln \frac{a_{red}}{a_{ox}} \approx E^o_{redn} - \frac{RT}{nF} ln \frac{[Red]}{[Ox]} \tag{5}$$

$$E_{oxid} = E^o_{oxid} - \frac{RT}{nF} ln \frac{a_{red}}{a_{ox}} \approx E^o_{oxid} - \frac{RT}{nF} ln \frac{[Red]}{[Ox]} \tag{6}$$

where a is the activity, T is the temperature at which the reaction occurs, F is Faraday's constant, and [Red] or [Ox] refers to the concentration of the particular species. A system that behaves according to the Nernst equation (or a derivative of it) is called Nerstian or electrochemically reversible.[19]

Electrochemical cells are classified as either galvanic or electrolytic. When the redox reaction occurs spontaneously (transforming chemical energy into electrical energy) as a result of the application of an external conducting path to the electrodes, the cell is defined as galvanic.[19] Galvanic cells include fuel cells and batteries (primary and

secondary during discharging). A galvanic cell will have a change in cell potential greater than zero since the Gibbs free energy is negative for spontaneous processes since cell potential is related to the Gibbs free energy (ΔG^o_{cell}) by:

$$\Delta G^o_{cell} = -nF\Delta E^o_{cell} \quad (7)$$

Conversely, if the reaction requires an applied potential to occur, the cell is called electrolytic. Electrolytic cells convert electrical energy into chemical energy and are important for processing techniques such as electrochemical synthesis, electroplating, and electrorefining.[19] It should be noted that a secondary cell is galvanic and electrolytic in nature during the discharge and charge processes, respectively. Theoretically, the potential required to drive an electrolytic cell is equal to the difference in electrode potentials under standard conditions. In practice, the applied potential will be different due to cell resistance, including the concentration polarization and the reaction overpotential.

A reduction (or cathodic) current (the flow of electrons from the electrode to the electrolyte) results when the potential (voltage) of the cell is driven to larger values (through the use of a power supply). The potential change causes the energy level of the electrons in the electrode to increase and it becomes possible for an electron to cross the electrode/electrolyte interface into a vacant site in the electrolyte.[19] Assuming no kinetic limitations, the reaction species that will be reduced first in a complete cell will (generally) be the oxidant in the half reaction with the least negative standard potential.[19] An oxidation (or anodic) current (the flow of electrons from the solution to the electrode) results when the potential of the cell is driven to more positive values. In this case, the energy level of the electrons in the electrode decrease and it becomes possible for an electron in the solution to lower its energy by crossing the interface to occupy a site in the electrode.[19]

Electrochemical reactions in which charge passes across the electrode/electrolyte interface (e.g. a reduction or oxidation current is produced) are called faradaic since the current passed is proportional to the extent of chemical reaction by Faraday's Law.[19] In addition to faradaic currents, there exist non-faradaic processes in a given electrochemical cell. Non-faradaic processes do not allow for charge-transfer (either in the range of potentials used or due to thermodynamic or kinetic limitations) but change the structure of the electrode/electrolyte interface (by ion adsorption/desorption processes, for example).

Typically, one is primarily interested in the reaction at one of the electrodes, a half reaction. When studying a half reaction, one measures the potential difference between the electrode of interest (the working electrode) in comparison to a standard electrode (the reference electrode). Several reference electrodes are commonly found throughout the literature such as normal hydrogen electrode, saturated calomel electrode, and silver-silver chloride electrode. A reference electrode has a well-defined reduction potential.[19] While an electrochemical cell can be constructed using only two electrodes, a three-electrode cell can also be used. A three-electrode cell consists of a reference, a working, and a counter electrode. In this scenario, the working electrode is the electrode of interest, the reference electrode measures and controls the potential of the working electrode, and the counter electrode controls the current flow to the working electrode. The reference electrode does not pass current.

2.2 Principles of Operation of Li-ion Batteries

Battery is a general term for a collection of electrically connected electrochemical cells (in series or parallel) that convert chemical energy into electrical energy (and vice versa) by redox reactions between the cathode and anode of each cell.[1, 5-6] There exist two major classifications of batteries: primary or secondary. Primary, or single-use, batteries are discharged once before disposal due to their inability to recharge easily whereas

secondary, or rechargeable, batteries are designed to be recharged effectively to the initial state after each discharge.

Although a commercial Li-ion battery is a so-called *full cell* (two-electrode cell comprising of an anode and a cathode), most electrode researchers perform measurements in so-called *half cells* (two-electrode cell where a working electrode is studied versus a Li metal counter electrode). However, there are some limitations to testing in half cells, such as the formation of dendrites on the Li metal surface as well as increased electrical resistance due to SEI growth on a Li surface. Despite this, two-electrode half cells are conventionally used for convenience.

The electrochemical metrics of a battery include the capacity, the energy density (specific energy), the power density (specific power), the cell shelf lifetime and cycle life, and the Coulombic efficiency (CE). The capacity is the amount of electricity able to be delivered over a time period. The units of capacity are ampere·hours (Ah; 1 Ah is equivalent to 3600 Coulombs). Normalizing by mass, geometrical area, or volume yields the gravimetric capacity (mAh/g), areal capacity (mAh/cm^2), or volumetric capacity (mAh/cm^3), respectively. Capacities and efficiencies are often reported for a given C-rate which is short-hand for stating the time, in hours, necessary for the electrode to charge/discharge to theoretical capacity at a particular current; however, in a commercial cell, the theoretical capacities would likely not be used for cycling. For example, a "1C" or "C/1" rate corresponds to the theoretical 1 hour charge time, while "0.5C" or "C/2" rate, for example, corresponds to a 2 hour theoretical charge time. Often researchers will test materials at a variety of C-rates (increasing in current density) to test power or rate capability or will test at select C-rates (often increasing in current density but there may be a decrease near the test end) for long-term stability analysis.

Cell energy and power densities are measured in Watt·hours and Watts, respectively, per volume whereas the specific energy and power are normalized per mass. Energy characteristics are indicative of the total energy able to be supplied (i.e. the ability

to do work) whereas power characteristics are indicative of how quickly that energy can be delivered (i.e. the rate at which work can be done).[6] The cell lifetime refers to the number of cycles that can be completed without significant degradation.

Coulombic efficiency is a measure of the capacity retention during cycling and is a percentage that is calculated from the ratio of the Li extraction (discharge) capacity to the Li insertion (charge) capacity. Irreversible capacity losses can be identified if the Li insertion capacity into the working electrode is greater than the Li extraction capacity. Irreversible capacity may be the result of Li losses in undesirable side reactions on the working electrode.

Batteries offer good energy and power characteristics; however, like other electrochemical energy devices, their performance cannot compare to the internal combustion engine (Figure 1).[6]

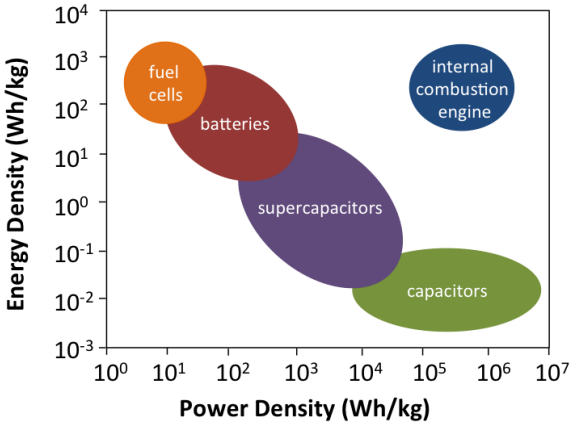

Figure 1. Ragone plot for several electrical energy devices. *Recreated from Ref. 6.*

With the exception of lithium-metal batteries which have significant safety issues, Li-ion rechargeable batteries outperform most other battery chemistries, such as lead-acid and nickel-metal hydride chemistries.[6] The high energy densities of Li-ion batteries are due to the one valence electron per lithium atom combined with the low atomic mass of Li. High energy and power characteristics of Li-ion batteries combined with a variety of

geometry configurations make them attractive for numerous applications including, but not limited to, personal electronics, military and space applications, and transportation vehicles. In addition, the cells can operate in wide temperature and potential windows for a significant number of cycles with minimal degradation.

As previously mentioned, each Li-ion cell contains a cathode and an anode, each comprised of so-called *active* materials that host Li ions. During charging, the cathode is oxidized as Li ions are extracted and subsequently inserted into the anode, which is then reduced. During discharge, the Li ions are shuttled back to the cathode and the electrons from the oxidized anode are collected by the current collector which can be utilized to operate a load (Figure 2).[2-3]

Electrodes are generally comprised of the active material, conductive additives, and polymer binders, ideally with enough porosity to achieve sufficiently fast (for the desired power characteristics) Li ion transport.[6] The electrodes are both electrically and physically connected to a current collector (copper for the anode, aluminum for the cathode) [6] that typically also serves as a substrate for electrode casting. However, there is increased interest to develop electrodes without a current collector as the metal decreases the total energy and power densities and increases material cost.

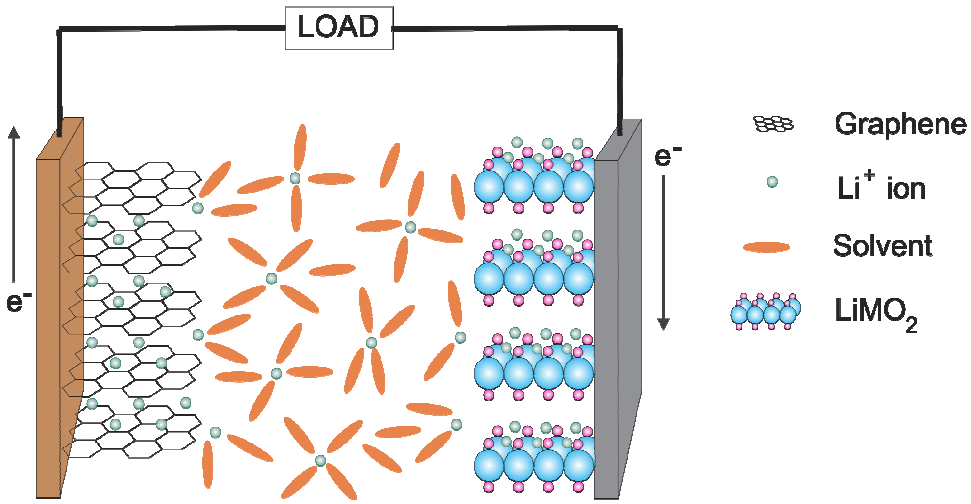

Figure 2. Schematic of a Li ion battery during discharge. *Recreated from Ref. 20.*

2.3 Electrochemical Characterization Methods

Charge/Discharge Cycling

Charge/discharge cycling simulates use as a battery in application (Figure 3). In this half cell test, a constant current is applied and the potential versus Li/Li^+ is recorded. The polarity of the current changes whether the anode is charging (reduction or negative current) or discharging (oxidation or positive current). A constant potential step is commonly used once the cell potential reaches a certain user-defined value after the constant current charging step. The constant potential step is held until the current achieves a user-defined value (e.g. 5% of the current). From the integrated area under the current versus time curve, the charge and discharge capacities, and Coulombic efficiency can be calculated.

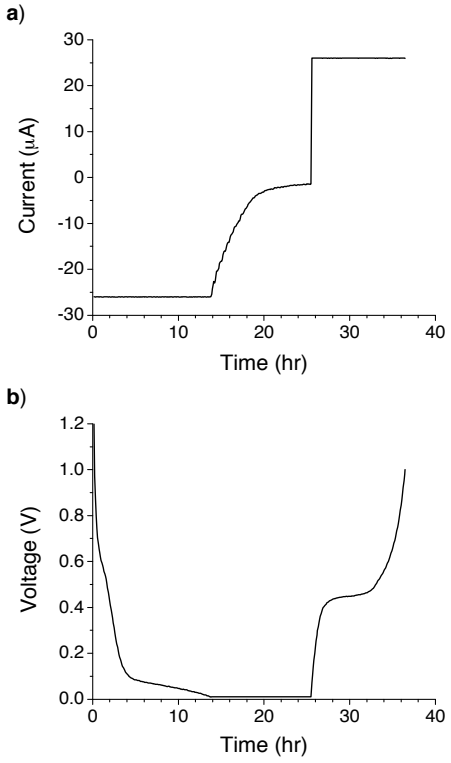

Figure 3. Representative first cycle consisting of (a) constant current and constant potential charge steps followed by a constant current discharge and (b) the corresponding potential curve.

According to the Gibbs Phase Rule for phase diagrams at constant temperature and pressure, within a single-phase region, the electric potential will vary with composition whereas it will plateau within a two-phase region when plotted against Li concentration.[7, 21] Thus, these voltage plateaus can serve as indicators of phase transformations. A potential-capacity profile which does not have any voltage plateaus indicates that the crystalline material has become amorphous during cycling thereby not forming stoichiometric alloys.[7, 21]

Cyclic Voltammetry

Cyclic voltammetery (CV) is a potential sweep method in which the potential is scanned within a user-defined potential range in both the forward and backward directions at a user-defined scan rate (ν). At potentials away from the reaction potential, only non-faradaic currents are measured.[19] As the potential is swept across the potential corresponding to reduction or oxidation, provided that the conditions for the reaction are met, the current will increase in magnitude due to faradaic reactions occurring. As the potential moves further from the reaction potential, the concentration of reactive species at the electrode surface drops and mass transfer (the current) increases.[19] Moving further still, the species at the electrode surface are depleted and the current will decrease.[19] This behavior produces a peak in an i-E curve.

Figure 4a illustrates the potential profile with respect to time for one representative complete CV cycle. CV is often used to study complicated processes (e.g. multi-component systems, multi-phase systems, coupled reactions, adsorption) to determine reaction rate constant(s), diffusion coefficient(s), and what reactions are occurring. For battery research it is primarily used to identify the potentials at which Li is (de-)inserted, the SEI is formed, the charge (discharge) capacity, and the Coulombic efficiency. It can also be used to qualitatively assess the stability of the electrode with

repeated cycling. The current can be plotted versus time (Figure 4b); however, it is more common to plot current versus potential (Figure 4c).

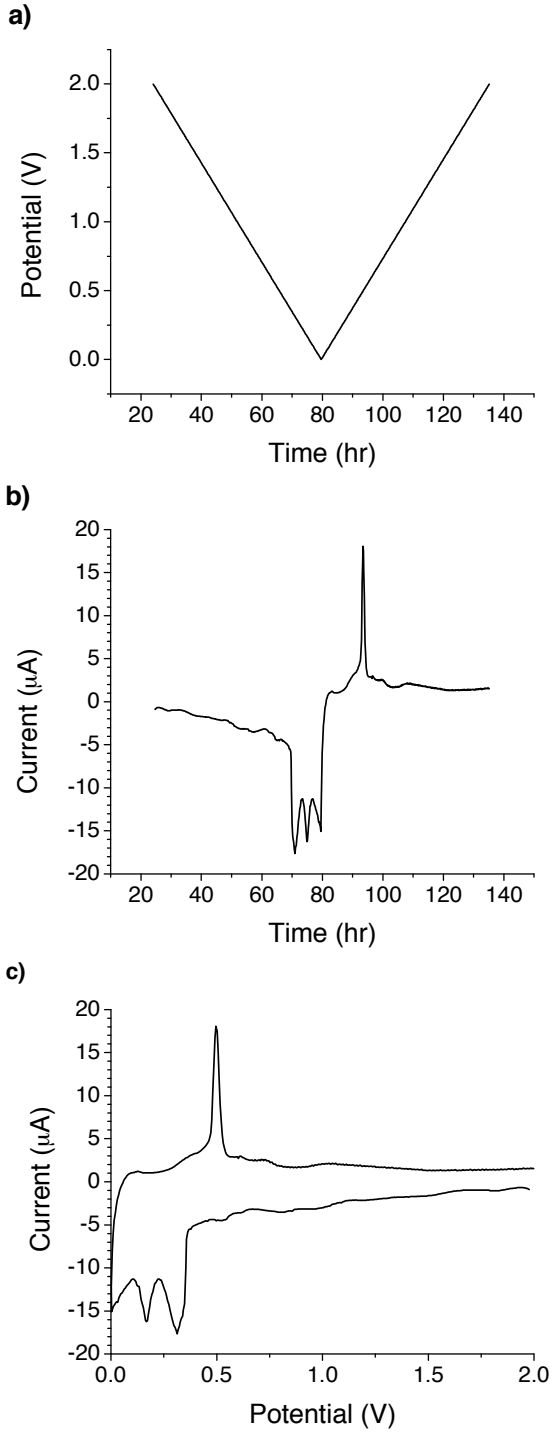

Figure 4. Evolution of a cyclic voltammogram: (a) the potential is positively and negatively swept across a defined potential range, (b) the current is measured as function of time, and (c) the cyclic voltammogram is generated.

2.3 Li-ion Battery Materials

In this section, the cathode, anode, electrolyte, and solid electrolyte interphase will be generally discussed. A more extensive review of materials for anodes is provided in Section 2.4.

Cathodes

Several criteria exist to inform cathode development. First, the cathode must reversibly react with Li to a high degree (ideally with minimal structural change) and at a high potential versus Li.[22] Secondly, the cathode must have high electronic conductivity to eliminate the need for conductive additives and high Li^+ mobility to achieve high power characteristic.[22] Ideally, the cathode can be produced at low cost from environmentally benign and abundant materials.[22]

Initially, Li metal was used as the cathode; however, due to the formation of dendrites and thermal runaway, their use in commercial batteries was ceased due to safety concerns. Titanium disulfide (TiS_2) is one of the oldest cathode materials, having been commercialized in 1977.[22] Today, a typical commercial cathode is comprised of a metal oxide such as: lithium cobalt oxide ($LiCoO_2$); lithium nickel oxide ($LiNiO_2$); mixtures of nickel, cobalt, and/or manganese ($Li(NiMnCo)O_2$, $LiMn_{3/2}Ni_{1/2}O_4$, and many others); lithium manganese spinel ($LiMn_2O_4$); and lithium iron phosphate ($LiFePO_4$).[5-6, 17, 22-23] The structure of cathode materials is typically either layered or spinel ("tunnel"). In layered cathode materials $LiCoO_2$ and $LiNi_{1-x}Co_xO_2$, the Li ions are found in between the oxygen layers. In the spinel structure $LiMn_2O_4$, the Li ions are found in one-eighth of the tetrahedral sites.

When Sony introduced Li-ion technology to the commercial market in 1990, $LiCoO_2$ was the cathode utilized. Concerns regarding its cost and toxicity (due to the cobalt) caused a shift away from its use. However, it is still commonly found in the majority of commercial cells.[5] $LiNiO_2$ is a cheaper alternative to $LiCoO_2$; however, other

problems related to safety and reproducibility has limited its use. Combinations of Co and Ni have shown promise with moderate cost and high capacities.

$LiMnO_4$ offers good rate capability, high potential (4 V), high thermal threshold, low toxicity, and low cost.[5] However, the performance of $LiMnO_4$ decreases with increased cycling due to Mn^{+2} dissolution from the electrode caused by the hydrofluoric acid (HF) produced as a byproduct in cells using lithium hexafluorophosphate ($LiPF_6$) based electrolytes.[5]

$LiFePO_4$ is commercially used in high power applications due to its moderate, stable potential (~3.5 V), low capacity fade, physical stability (no weakly bonded oxygen, no disintegration during use), and non-toxicity.[5, 22] Although electronically insulating with a low Li ion diffusivity, theoretical capacities can be achieved at low current densities or elevated temperatures (above 50 ^{o}C).[5] Electrically conductive films deposited on $LiFePO_4$ have shown increased rate performance.[22] Methods to increase the ionic conductivity include grain size reduction (to decrease diffusion length) and embedding in an ionically and electrically conductive matrix.[5]

More recently, the cathode research community has expanded its search for a high capacity material to include other compounds such as fluorides and phosphides since their multi-valent redox reactions may generate increased storage capacity.[24-26] Materials with higher potentials (near 5 V) can also boost performance; however, two challenges are present. First, electrolytes typical to Li-ion batteries are not stable at these high potentials and would decompose. Second, at high potentials, the level of oxygen partial pressure is increased and creates a stability issue that may lead to dangerous reactions, including explosion.[22]

Anodes

In 1983, the reversible nature of lithium insertion into graphite at room temperature was reported.[27] Within a decade following, Sony brought Li-ion batteries

with petroleum coke-based anodes to commercialization. Since then, carbonaceous anodes have become the industry standard due to their high degree of capacity retention and stability over many cycles without significant volume changes.[1, 4-5, 28] Although the industry standard, carbon does not have a large specific capacity as compared to many other Li hosting materials (Figure 5) with many semiconducting or semi-metal materials having theoretical specific capacities greater than carbon by up to an order of magnitude.[8] Continued success of Li-ion batteries requires new ways of increasing the capacity and cycle lifetimes to meet the needs of current and developing technology. An ideal anode would demonstrate a high reversible capacity (greater than graphite), a low irreversible capacity, good capacity retention, and long cycle life.[4] Anodes should have high conductivity and readily interact with Li^+ at a low potential versus Li so that the overall cell potential is large.

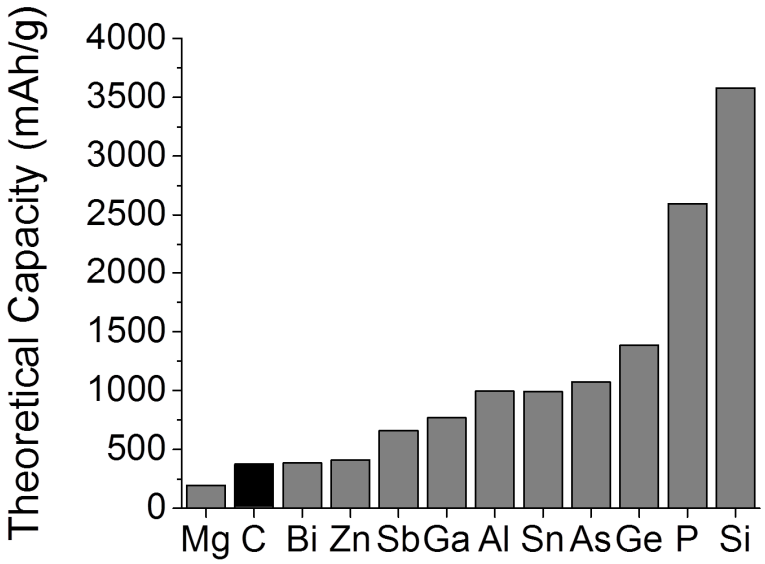

Figure 5. Theoretical capacities for several Li hosting materials. *Created from data reported by Ref 29.*

In the early 1970s, it was reported that the electrochemical alloying of Li with numerous metals (e.g. Sn, Pb, and Al) destroyed the integrity of the anode through loss of electric contact between individual particles [30] caused by the large volume changes

during Li insertion and extraction which were upwards of 300%.[7] In some anode designs, a decrease in capacity to below 50% of the initial capacity occurred in less than five cycles.[31-32]

To mitigate these destructive volume changes, three general approaches are typically considered. One attempt is to embed the high capacity particles in a 'stabilizing matrix' such as a less active material, carbon, or a polymer binder.[5, 33] Composite electrodes may better accommodate the stresses and volume changes that occur during cycling thus circumventing the challenges of utilizing high capacity materials. It has been suggested that the ability of composite electrodes to mitigate these limitations are dependent upon the electrode structure and composition and may only buffer them at low mass loadings of the high capacity material.[10, 21] Another approach is to reduce the dimensions of the high capacity particles below the theoretical critical crack length.[33] Reducing the particle size has shown to increase capacity and cycle retention but not for all anode structures. Differences in performance may be a result of the increased active material surface area which exposes more of the anode to adverse side reactions.[33] As a final approach, highly structured anodes at the nanoscale that accommodate the volume changes are considered.[34]

Use of intelligently designed highly structured electrodes consisting of high capacity materials may allow drastic improvements in cell stability.[10, 14, 16, 35] These novel electrodes would be structured so that non-destructive lithiation can occur with more sites for Li insertion available thus increasing the energy density. Despite significant research in anode materials, the materials relationship with mechanisms leading to capacity fading is not well understood.[3] Limited understanding has hindered the use of Li-alloying materials, specifically those of high capacity, as anodes in commercial applications.

The primary challenge limiting commercialization of anodes comprised of high capacity materials (e.g. Si, Ge) is the decreased capacity retention and anode degradation with cycling. This challenge originates from the large volume changes that occur during

Li alloying and dealloying which causes stress generation within and material degradation of the anode. Although lithium alloying with silicon has been heavily studied for decades, the exact contributions of various mechanisms leading to capacity fading are not fully understood.[3] Germanium is analogous to silicon in structure and properties, but it is not as heavily researched. This is largely due to the smaller theoretical capacity and higher cost, in comparison to Si.

Electrolyte

A suitable electrolyte must allow for ion diffusion (and not electron diffusion) and must be stable with respect to the electrodes and operating parameters.[6] Li-based batteries use a non-aqueous electrolyte (consisting of a Li salt and a non-aqueous solvent) due to the decomposition of water at low anode potentials. $LiPF_6$ is a popular salt due to its high conductivity ($> 10^{-3}$ S/cm) and relativity high Li^+ transference number (the current carried by Li^+ in the electrolyte, ~ 0.35) and its ability to passivate the Al current collector.[23] The disadvantages of $LiPF_6$ are that it is flammable and can readily produce HF with exposure to moisture or during cycling.[5-6] It is suggested that both HF and trace water content chemically attack the material surface and contribute to performance losses.[5, 33, 36]

Solvents are typically a mixture of carbonates such as ethylene carbonate (EC; $C_3H_4O_3$), dimethyl carbonate (DMC; $C_3H_6O_3$), and ethyl methyl carbonate (EMC; $C_4H_8O_3$), among others. Combinations are employed to tailor the solvent properties (e.g. conductivity, temperature stability, viscosity) and performance for the specific electrode materials. The conductivity of carbonate electrolytes increases with temperature and shows a concave down behavior with increasing salt concentration. Ionic liquids (room temperature molten salts) are an interesting organic electrolyte alternative with attractive properties such as non-flammability, wide operation temperature range, low vapor

pressure, and liquid state under ambient conditions.[5-6] However, some ionic liquids demonstrate high reactivity with Li and dissolution of Li intercalated in graphite.[5-6]

The use of electrolyte additives, such as vinylene carbonate (VC; C_3H_2O) and fluoroethylene carbonate ($C_3H_3FO_3$), to common carbonate based electrolytes improves SEI stability and reduces irreversible capacity.[37-38] Aurbach et al. performed an extensive study on the effect of 5 wt. % VC in an electrolyte consisting of EC and DMC on the performance of graphitic anodes.[39] Impedance data measured at several potentials after several charge/discharge cycles in electrolytes with and without VC highlighted lower resistance for VC containing electrolyte at different potentials at room temperature and at 60 ^{o}C.[39] VC is a common electrolyte additive; however, numerous other additives, including solid particles, have been researched.[37, 40]

Separator

To ensure physical separation of the electrodes, thin (< 50 μm) microporous polymer films or glass fiber membranes, known as separators, are used. The separator must be mechanically robust and wetted by and stable in the electrolyte and stable at both anode and cathode potentials. Polyethylene (PE) and polypropylene (PP) are popular materials for this application.

While Li-ion batteries are safer than their pure metal counterparts, safety is also of concern, especially at high rates of charge/discharge since the temperature increases during discharge.[5] To limit the onset of thermal runaway, a number of safety features have been considered including safety vents, thermal management systems, shutdown separators, and shutdown additives.[5, 41-42] Separator shutdown occurs when the cell temperature increases beyond the separators melting point, causing the pores to close and ion diffusion to stop.[5, 41] During this process, the separator must maintain its structural integrity to limit the two electrodes from coming into contact and initiating thermal runaway.[5] For this reason, tri-layer (PE/PP/PE) separators are often used since the layers

lead to greater structural integrity. The closure of the separator pores creates a large impedance increase that can be used by thermal management systems to stop current flow to the battery.[41]

Solid Electrolyte Interphase

One of the critical materials issues in Li-ion batteries is the formation, composition, and stability of the SEI, a passivating layer formed on an electrode that should protect the electrode from deleterious side reactions with the electrolyte media. Depending on the properties, the SEI can have an advantageous or an adverse effect on the resulting battery performance. The composition and mechanism of formation of the SEI is complex as it is highly dependent upon the electrode materials, electrolyte, and operating conditions.

In 1979, Peled introduced the SEI model to better explain electrode kinetics in non-aqueous battery systems consisting of alkali and alkaline earth metals (e.g. Li, Na, Mg).[13] Peled wrote: "This layer is formed instantly by the contact of the metal with the solution. The thickness of this freshly formed layer is determined by the electron tunneling range. This layer consists of some insoluble products of the reaction of the metal with the solution. It acts as an interphase between the metal and the solution and has the properties of a solid electrolyte, through which electrons are not allowed to pass." [13] Thus, the SEI layer is inherent to electrodes in non-aqueous systems regardless of whether the battery is undergoing cycling.

Peled's seminal paper only considered the formation and growth of the SEI at open circuit potential. However, the dynamic composition as a result of potential is a more relevant study in relation to Li-ion battery research. At high potentials, beyond the

thermodynamic stability of the electrolyte, the organic electrolyte components will decompose and form a protective SEI layer whose initial composition is determined by the electrode material and electrolyte selected.[43-45] The SEI has a strong effect on the cell performance, cycle life, power capability, and safety.[43-45] The complexity of this interphase arises not only from its formation but also from transformations during charge/discharge cycling.

During the initial cycles, the formation of the SEI layer consumes both active material and electrolyte thus the SEI produces an irreversible capacity during formation.[46] SEI formation is a concern since Li ions can become trapped within the anode material during the first charge that results in a decrease in discharge capacity. As such, a thin SEI layer is desired.[1] This irreversible incorporation of Li can occur during every electrochemical cycle which causes a continual reduction in the reversible capacity. Capacity retention over many cycles may be achieved with a stable SEI that more readily permits the diffusion of Li since the composition and structure of the SEI will not drastically change during cycling.[11]

The irreversible capacity due to SEI formation has a strong dependence on the electrode's material properties and structure, in particular its surface area and morphology.[47-48] Although the composition and formation mechanism are not well understood, it is well-accepted that the SEI is beneficial to the long-term performance of graphitic anodes.[48] The SEI hinders further electrolyte decomposition as it acts as a barrier between the active material and the electrolyte, restricting diffusion of both electrolyte solvent molecules and electrons.[46] In addition, the SEI may prevent co-intercalation of solvent molecules into the graphite which otherwise causes graphitic

exfoliation. According to a simple model, the SEI is composed of multiple components, each having its own composition and structure (Figure 6). Ideally, the SEI will protect the anode materials from further electrolyte reduction products and become electrically insulating and solvent-impermeable while still permitting Li ion transport to the anode through point defects.[46]

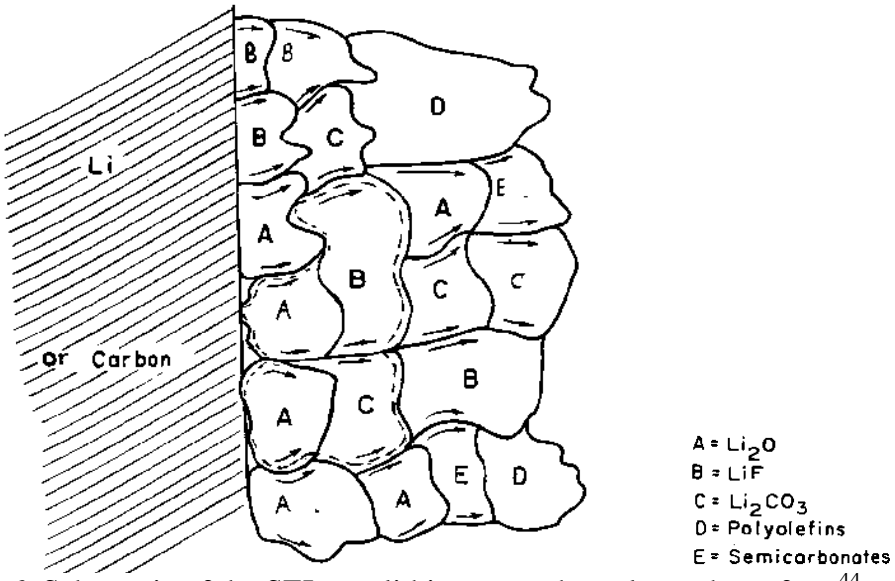

Figure 6. Schematic of the SEI on a lithium or carbon electrode surface.[44]

The formation of the SEI on high capacity active materials (e.g. Si) has not been studied as extensively as the SEI on graphite; however, several studies have illustrated its dynamic behavior during varying states of charge and discharge.[11-12] Due to volume changes oh high capacity materials during electrochemical cycling, the SEI may be broken and reformed upon each cycle which can cause both mechanical and electrochemical problems.

Mechanically, the high capacity material may contract upon discharge at a rate different than the SEI such that stresses build, the film breaks, and further decomposition occurs. When the SEI breaks, new anode material surfaces are in contact with the

electrolyte, a new SEI film forms, and the irreversible capacity losses increase (Figure 7). Due to volume changes of high capacity materials during electrochemical cycling, identifying conditions required for the stable SEI formation may be a challenge.

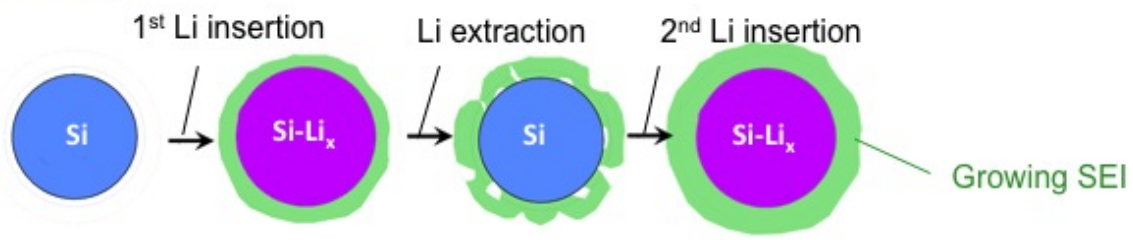

Figure 7. Schematic illustrating the growth of SEI caused by volume changes during charge and discharge of a Si particle.[29]

In addition to a number of other factors, the properties of the SEI not only depend on the elemental composition of the electrode but also its morphology. Therefore, results in the literature regarding an electrode of a particular composition may not be representative of another electrode of the same composition but different structure.

X-ray photoelectron spectroscopy (XPS) has shown that the SEI layer on a Si electrode not only changes morphologically, as demonstrated by scanning electron microscopy (SEM), but also chemically throughout cycling (Figure 8).[11] At a 0.1 V state of charge, the Si signal disappeared suggesting that at that potential the thickness of the SEI was greater than the XPS information depth which was ~10 nm in the study.[11] This type of analysis may provide estimates on the SEI thickness at a given potential on a particular type of anode. XPS may also be used to analyze the composition of the SEI at a selected state of charge/discharge by sputtering through it.[49]

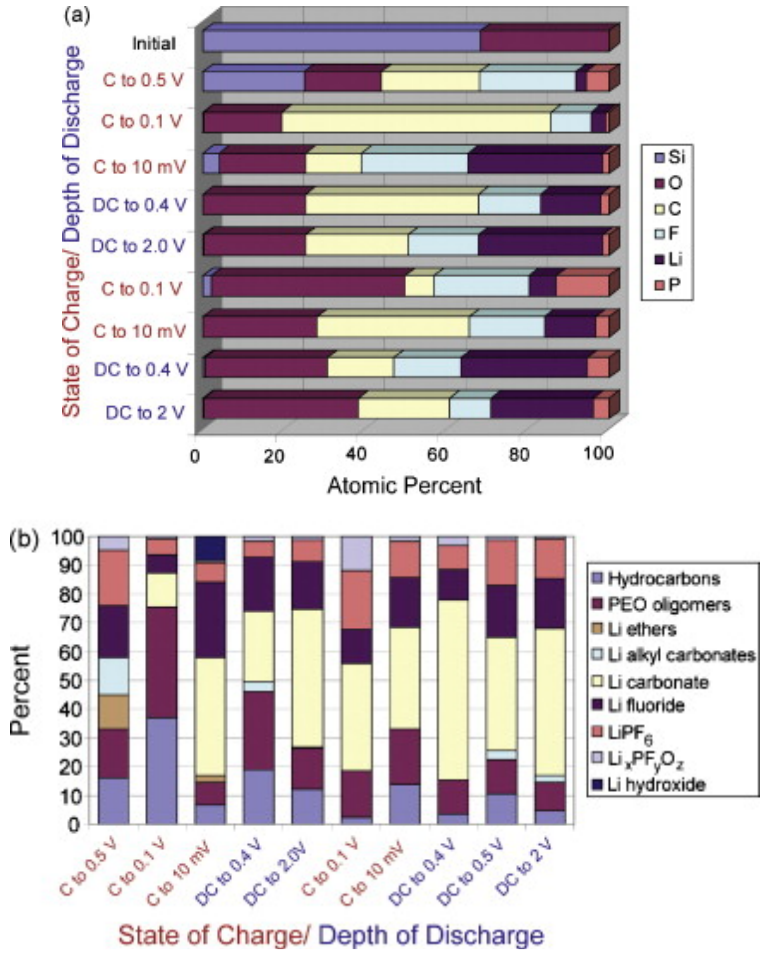

Figure 8. The SEI surface layer on Si nanowires as a function of the state of charge (C) and the depth of discharge (DC): (a) elemental composition and (b) molecular composition as determined from XPS.[11]

2.4 Materials for Li-ion Battery Anodes

Following is a review of the current state of art in Li-ion technology for conventional carbon anodes as well as pure silicon and pure germanium anodes in various electrode constructions. Background information for the relevant materials will also be discussed. Also under consideration is the use of composite anodes comprised of a high capacity material and carbon. The development of novel composite materials to replace graphite require gaining a greater fundamental understanding of the effect of composite morphology and its mechanical, electrical, chemical, and physical properties on battery performance.[20]

Carbon for Li-ion Electrodes

Background

Carbon is the most versatile of the elements, due to its ability to catenate and to form different types of covalent chemical bonds via hybridization (sp, sp^2, and sp^3).[50] Carbon is the basis of several well-known allotropes including graphene, graphite, diamond, fullerenes, carbon nanotubes, and amorphous carbon. The structure and properties of carbon materials vary as a result of the different hybridization bonding within the structure.

In 2010, Andre Geim and Konstantin Novoselov were awarded the Nobel Prize in Physics for their "groundbreaking experiments regarding the two-dimensional material graphene".[51] In 2004, Geim and Novoselov published a paper discussing the electronic properties of few layer graphene (FLG) which sparked significant interest in the utilization of graphene for a number of applications such as microelectronics, Li-ion batteries, supercapacitors, sensors, optoelectronics, and catalysis.[52-54] Although others had previously studied graphene in relation to graphite as early as the 1940s, Geim and Novoselov's work brought the material to the forefront of research since they were the first to demonstrate graphene as a free standing structure.[55] Their finding was significant since free standing atomic monolayers are thermodynamically unfavorable and had previously never been demonstrated.[53-55]

Single layer graphene (SLG) is a two dimensional sheet of carbon atoms that are arranged in a benzene ring (honeycomb) structure with sp^2 bonding and a hexagonal primitive unit cell.[54-56] In this configuration, each C atom is covalently bonded to three neighboring C atoms (Figure 9).

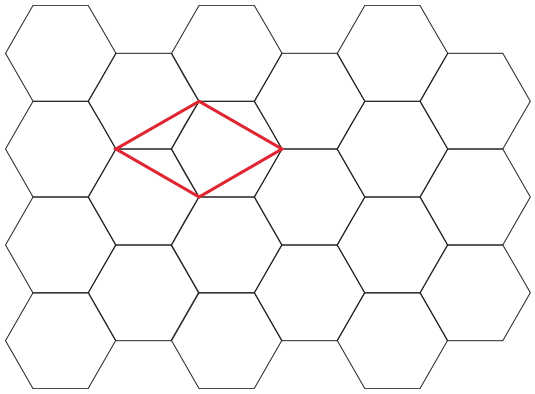

Figure 9. Depiction of the hexagonal primitive unit cell (outlined in bold red) for the graphene bond structure.

Graphene is traditionally used to describe the structure of carbon allotropes (Figure 10).[54-55] Fullerenes and carbon nanotubes can be geometrically described as different wrappings of graphene to form either a spherical or cylindrical structure. Hexagonally (or rhombohedrally) packed sheets of graphene form graphite. The distinction between graphene and graphite is the electronic structure. Partoens and Peeters mathematically demonstrated how the electronic structure of graphene changes as the number of graphene sheets is increased. The electronic structure of graphene closely resembles that of graphite at ten graphene layers and beyond.[57]

Graphite has been the predominant anode material for Li-ion batteries although many other carbon materials (graphene, carbon nanotubes, carbon black) have been used or considered for application. Graphite has a lamellar structure comprised of planar sheets of graphene. The 0.34 nm spacing of the graphene sheets is dictated by the van der Waals forces between them that causes them to stack to form a 3-D unit cell.[23, 50] Graphite is often used as a lubricant due to the interlayer bonds being much weaker than the in-plane primary bonds.[50, 58] Graphene sheets are either stacked to form hexagonal graphite (ABAB⋯) or rhombohedral graphite (ABCABC⋯) (Figure 11).[23] In disordered (turbostratic) or amorphous graphite, the stacking is highly distorted with no long-range order observed.[5, 50]

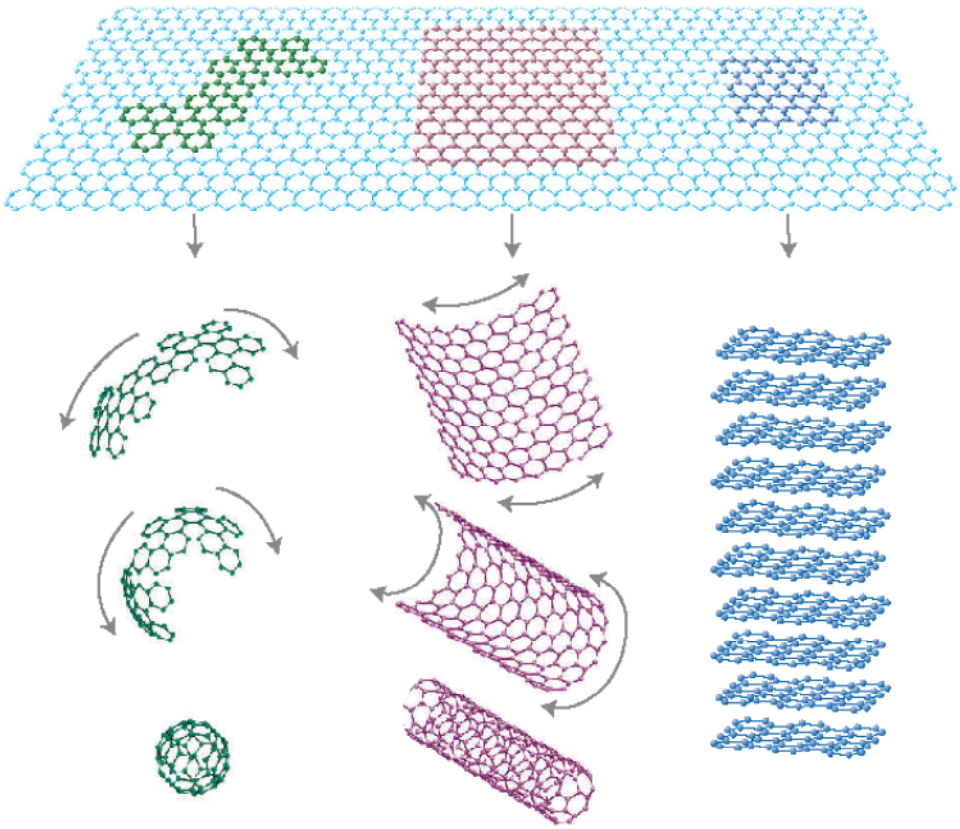

Figure 10. Graphene (light blue) can be used to describe the geometry of several carbon allotropes including buckyballs (green), carbon nanotubes (purple), and graphite (dark blue).[55]

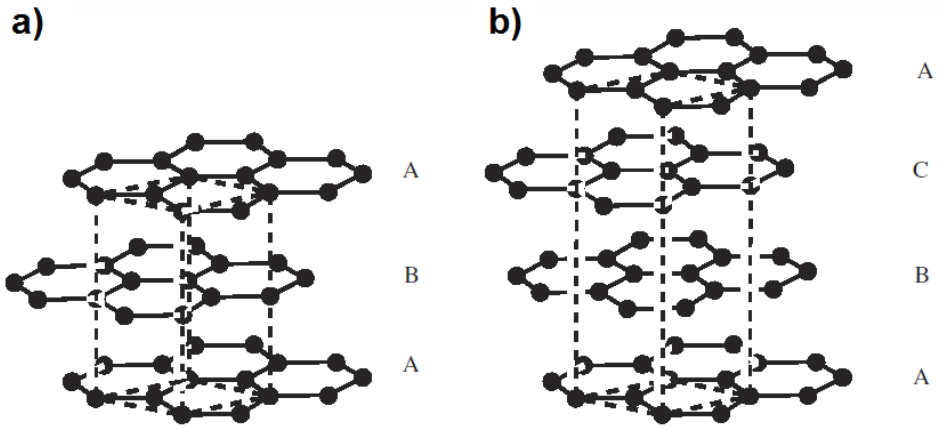

Figure 11. (a) Hexagonal and (b) rhombohedral graphite.[23]

Carbon nanomaterial synthesis

Graphitization is the process of creating the structural order of graphite from a carbon precursor or amorphous carbon. Many organic materials (coal, wood, coconut shells) can be precursors for the generation of carbon materials, but tuning the resulting microstructure is difficult. Due to the high degree of recrystallization necessary, graphitization requires very high temperatures (> 2300 ^{o}C) and thus significant energy consumption.[5, 50] Heat treatments in conjunction with transmission electron microscopy (TEM) imaging generalized the process into four steps (Figure 12).[50] In the first step, volatile components of the organic compound are removed through heat treatment (650 – 750 ^{o}C).[50] This process is called carbonization and creates very short (< 2 nm) structural units with no order between units. As the temperature increases in step two, the number of carbon layers of each unit increases and ordering begins to appear. In the third step, the units begin to coalesce and a disordered stacking arrangement ensues. During the last step, the structure becomes increasingly more graphitic as the temperature is raised.[50]

The easiest method to obtain single sheets of graphene is to use mechanical exfoliation (the "scotch-tape" technique); however, the process is not scalable.[54, 59] There are numerous other methods of which a select few will be mentioned here. Graphene nanoribbons (GNRs) can be obtained through oxidative methods that unzip multi-wall carbon nanotubes (MWCNTs).[60] TEM and X-ray diffraction (XRD) showed that the process is incomplete for some MWCNTs since some sample curvature and non-uniformity were observed. Graphene nanosheets (GNS) can be synthesized through exfoliation of bulk graphite to produce graphene stackings of four to twenty layers.[61] Through controlled reassembly of the graphene sheets produced, the sample thickness, structure, and interlayer spacing could be controlled. [61] Epitaxial growth can produce SLG on substrates such as SiC for use in the electronics industry.[62] Chemical vapor deposition (CVD) is also commonly used to produce graphene on a variety of substrates.[63] Other methods of graphene formation include pyrolysis of camphor,

exfoliation of graphitic oxide, conversion of nanodiamond, and arc evaporation of silicon carbide.[59] These methods create graphene sheets with varying crystallite sizes and number of layers (essentially graphite).[59] Graphene paper can be created via a multi-step synthesis process that includes oxidation of graphite to produce graphite oxide, multi-day purification processes, formation of graphene oxide paper, and reduction of the graphene oxide paper.[52]

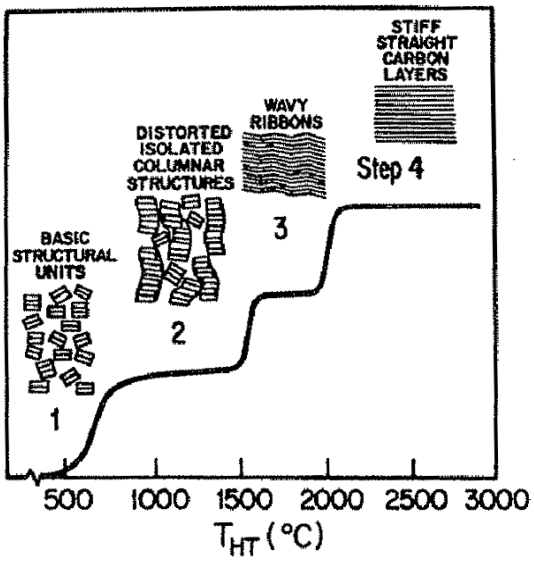

Figure 12. Evolution of the carbon structure during the four steps of the graphitization process as a function of heat treatment temperature (T_{HT}).[50]

One dimensional carbon materials were reported as early as the 1800s with work related to carbon fibers. The existence of CNTs was first speculated by Smalley in 1990 and was further theoretically discussed by Dresselhaus in 1991.[50] However, credit for the discovery of CNTs is often given to Iijima who imaged CNTs using TEM in 1991 (Figure 13) and proposed their structure.[50, 64] As a result of Iijima's paper, a boom in CNT research, both fundamental and applied, has occurred.

CNTs can be geometrically conceptualized as rolled sp^2 hybridized graphene sheets capped by a fullerene hemisphere.[50, 65] CNTs are classified as single-walled (SWCNTs) or multi-walled depending on the number of cylindrical graphene shells. When the fullerene cap is present, the tube is said to be closed. Depending on the tube

chirality, the fullerene cap will consist of six carbon heptagons and an appropriate number of carbon pentagons to completely cap the tube.[50] Conversely, when the fullerene cap is removed by chemical or thermal techniques, the tube becomes open.[66]

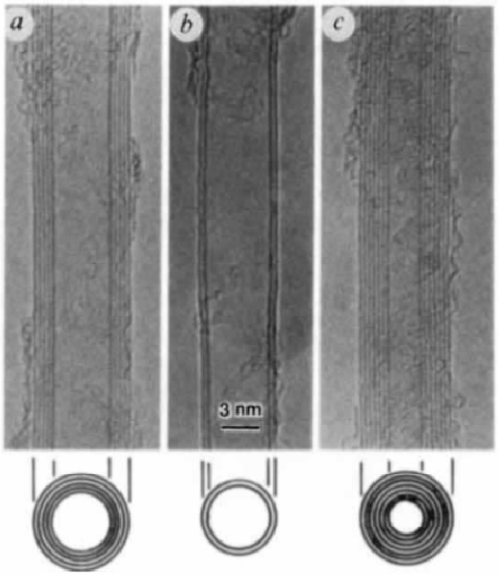

Figure 13. Iijima's revolutionary TEM images of CNTs.[64]

MWCNTs commonly exhibit a high-degree of crystallinity due to the regular 0.34 nm spacing of the tube walls (equivalent to the spacing of graphene sheets in graphite). [67] Adjacent tube layers in MWCNTs experience van der Waals forces similar to graphene sheets in graphite. Tube diameters are on the order of nanometers whereas the height can be on the order of micrometers to millimeters such that their aspect ratio makes them essentially 1-D.[50, 66]

Figure 14 illustrates the effect of the chiral angle (the angle at which the graphene sheet is "rolled") on the placement and location of C atoms. Carbon nanotubes are either metallic or semiconducting depending on their chirality.[50] It has been determined that nearly one third of possible chiralities are metallic in nature and the remainder semiconducting.[50]

While the vast majority of CNTs that are present worldwide have been synthetically produced, it is important to note that these nanostructures are naturally occurring in carbonaceous soot found as a byproduct of many processes. However, their persistence level is so low that they cannot be easily harvested for research with low cost and high purity. Early CNT growth methods were of very low yield for application. Further studies have led to procedures to grow CNTs, CNT fibers, and CNT fabrics at a large scale.[68-70] In the last twenty years, numerous synthesis methods have been utilized to create CNTs of varying purity, alignment, structure, and yield [67], including arc-discharge, laser ablation, and CVD.[66, 70-72]

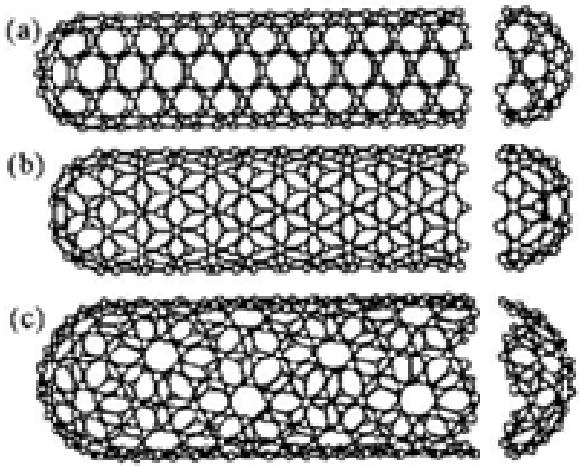

Figure 14. Schematic of CNTs illustrating (a) armchair, (b) zig-zag, and (c) chiral chirality.[50]

CVD is a general term for versatile processes that can be used with a wide array of precursors (solid, liquid, or gas) and reactor types to not only produce thin film coatings but also to facilitate CNT growth. CVD processes are utilized for controlled CNT growth and large-scale production at low cost.[65-66, 73] Parameter variations such as source gas, synthesis time, temperature, and reactor dimensions can be utilized to control the deposition rate, uniformity, purity, microstructure, and morphology of the resulting material.[66, 74] Today, CVD appears as the dominant synthesis method and is responsible

for some of the longest CNTs produced yet (with a current maximum of 55 cm [75]). While several theories to explain growth termination exist, the mechanism(s) are not universally accepted and will be substrate and system dependent. One theory is that continued growth will end once the catalyst becomes poisoned by impurities or a stable metal carbide is formed.[76] It has also been suggested that growth stops due to inaccessibility of catalyst through Ostwald ripening and/or sub-surface diffusion into the substrate.[77-78]

CVD synthesis utilizes the supersaturation of carbon on a hot surface to form a tubular structure. Commonly, a Si substrate coated with a thin layer of silica or alumina with a catalyst thin film deposited by thermal or electron-beam (e-beam) evaporation is heated in an inert atmosphere before being exposed to one or more hydrocarbons.[71, 79] Transition metals, such as iron, nickel, and cobalt are commonly used as catalysts [50, 66-67, 70-71] since carbon theoretically exhibits solubility into these metals at high temperatures, according to their phase diagrams.[67] CVD growth is somewhat related to vapor-liquid-solid (VLS) growth; however, key differences exist. The VLS model was developed in the 1960s to explain the growth of a single crystal whisker from a liquid alloy catalyst.[80] In contrast, CNTs are neither solid nor single crystal.

At an elevated temperature, the catalyst layer beads to form islands from which the nanotubes will grow. The hydrocarbon gases decompose at high temperature creating carbon atoms which react at the hot surfaces of the substrate and the furnace. Upon reaching the substrate, the atoms diffuse into the catalyst forming a supersaturated solution of the metal catalyst and carbon.[66] Once supersaturation occurs, the carbon atoms precipitate into a fullerene cap.[67] Continued precipitation creates the characteristic cylindrical nanotube shape by one of two growth process: base or tip growth.[65, 67, 71] Base growth occurs when the adhesion between the substrate and catalyst is strong so that as the nanotube grows, the catalyst island remains at the base. It has also been suggested that base growth can occur while the nanotubes end is open with increased length resulting from continued carbon absorption.[50] Tip growth is characterized by weak

interactions between the substrate and catalyst so that as the nanotube grows the catalyst rises as well. Generally, CVD synthesis temperatures within 600 – 900 ^{o}C yield MWCNTs and within 900 – 1200 ^{o}C yield SWCNTs.[67] It has been theorized that the catalyst for CNT growth does not need to be wholly liquid. Rather, the outer catalyst of the bead melts to form a liquid. Thus, lower growth temperatures, well below the bulk melting temperatures for the metal catalysts, can be used. The use of lower temperatures may also be suitable since nanomaterials have reduced melting temperatures in comparison to their bulk counterparts.[81]

The diameter of the catalyst island is affected by the surface microstructure and determines the diameter of the resulting CNTs.[67, 73, 79] Due to challenges in obtaining uniform catalyst islands, the resulting nanotubes are characterized by a diameter distribution.[18, 73, 79, 82-84] Typically, SWCNTs have diameters of 1 to 10 nm [50, 65, 76] whereas MWCNTs have diameters of 2 to 100 nm.[18, 65, 70, 76, 84] Tube diameter is difficult to control and is sensitive to the unique parameters of each synthesis. To illustrate, a previous study used e-beam evaporation to deposit a 2 nm thin film of catalyst that was subsequently heat treated without exposure to any hydrocarbon gases. The resulting catalyst island diameters were between 5 to 15 nm with an average diameter of 10 nm and a center-to-center spacing between adjacent islands of 15 nm.[79]

In 1997, methods of aligning CNTs involving physical methods post-synthesis were reported.[76] Since then CVD has facilitated the growth of vertically aligned carbon nanotube (VACNTs) films or in arrays via photolithography.[66-67, 79, 82, 84] Self-alignment is due to steric hindrance and the van der Waals forces which draw individual nanotubes together.[84] The particle density also appears to have an effect on the alignment properties, with lower densities producing unaligned CNTs.[85] Smaller catalyst particle size leads to denser arrays.[79] VACNTs height can be controlled by monitoring the synthesis time and temperature.[66, 84] However, the dependence of height on synthesis time will vary for

different reaction chambers utilizing different synthesis parameters[66, 84] and is commonly not linear.

Plasma-enhanced CVD (PECVD) is a technique that uses the electric field of the plasma to align the CNTs. Plasma ionizes the precursor gas so that the reaction can occur at lower temperatures.[86-88] An advantage of this method is that individual CNTs show better alignment and individual CNTs do not overlap. In addition, PECVD allows for a greater control of the growth since the plasma can be instantaneously turned off and diffusion of gaseous species to the substrate is limited. Similar to traditional CVD methods, PECVD requires the catalyst layer to be pre-deposited. In early work to produce CNTs, PECVD was an expensive technique although recently it has acquired more use in smaller scale laboratories.

Often, undesirable impurities are produced through CNT synthesis including residual catalyst, amorphous carbon, and other carbon nanoparticles. Some of the impurities can be removed from CNTs through filtration, chromatography, thermal treatments, and acidic treatments; however, their ability to remove impurities and retain the CNT structure and quantity vary.[50, 89]

Carbon nanotube sheets or non-woven fabrics can be formed through a variety of methods. Acid functionalization and filtration of CNTs to form a CNT sheet with limited size (Figure 15)[90] is commonly used for CNT powders. The resultant CNT fabric consists of randomly oriented CNTs. VACNT can also be used to produce CNT sheets, often of larger dimensions, by drawing the CNTs from the substrate and utilizing a rotating drum.[91] Each VACNT will draw a subsequent VACNT due to electrostatic attraction between them. Often the CNT fabrics produced through this method are anisotropic.[68]

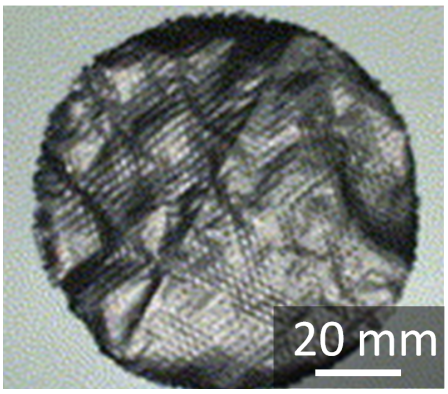

Figure 15. CNT fabric created through filtration of acid functionalized CNTs. *Adapted from Ref. 90.*

Graphitic Anodes

During charging (intercalation), Li ions diffuse into graphite via a staging mechanism where each stage number indicates the number of graphene sheets between intercalated sheets (Figure 16).[92] Each stage refers to an electrochemical reaction and can be observed via CV (as oxidation or reduction peaks) or charge/discharge cycling (as potential plateaus; Figure 17). Since only weak van der Waal bonds exist between the graphene layers, Li^+ is easily able to intercalate.[93] As the Li^+ inserts into the graphitic structure to produce the stage one fully lithiated carbon phase, LiC_6, the volume increases up to ~9.4% by volume.[5, 23, 92] LiC_6 (372 mAh/g theoretical capacity) can be described as having a Li ion sandwiched between each neighboring pair of graphene sheets where Li ions occupy all interplanar positions.[92, 94]

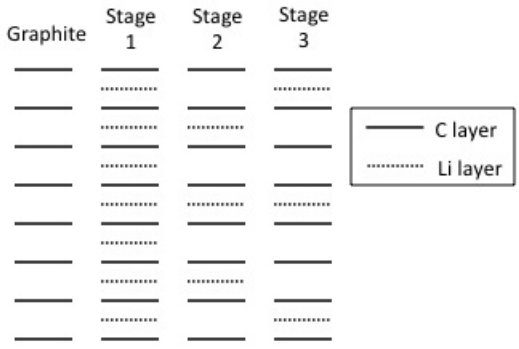

Figure 16. Schematics of the stages of lithiated graphite. *Recreated from Ref. 23.*

The structure resulting from the insertion of Li ions into graphite are termed graphite intercalation compounds and are generically represented as Li_xC_y. In this process, the graphite and the Li ions undergo a charge transfer mechanism thus causing an increase in the in-plane electrical conductivity. Graphitic anodes are commonly comprised of non-perfect graphitic materials and the electrochemical performance is highly dependent on the structure.[23, 95] Defining the stage assumes that the graphite is defect-free, a process which is not accurate in practice as defects and grain boundaries lead to inhomogeneous lithiation.[96] Amorphous carbons often exhibit higher capacities than theoretical carbon due to the lack of long-range order and presence of hydrogen content.[5] Disordered graphites exhibit a sloping potential-capacity curve since less distinct stages are formed.[23]

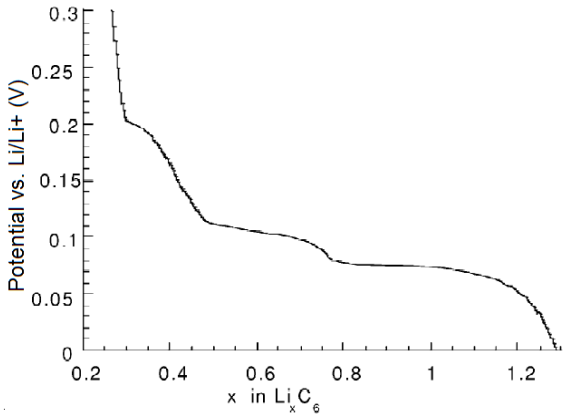

Figure 17. Potential plateaus showing the formation of Li-C stages.[4]

Graphene Anodes

Substituting graphene for graphite to increase the number of lithiation sites and gain higher capacity has been explored.[61, 97-100] Interestingly, the interactions between Li and graphene are not as well understood and differ from those observed in the Li-graphite system. Both CV and *in situ* Raman spectroscopy have been used to study the interactions of Li with SLG and FLG on different metallic substrates.[99] CV of FLG on a nickel substrate showed a large irreversible capacity on the first cycle that lessened with

increased cycling (Figure 18a). It should be noted that for both SLG and FLG, the capacities or the Coulombic efficiency were not reported. In addition, only four cycles were reported so performance trends are unknown. The behavior of SLG on copper and quartz substrates demonstrated a large irreversible capacity like the FLG; however, no reaction peaks were observed (Figure 18 b,c). Interestingly, when SLG on a quartz substrate was utilized (to remove the background current due to the copper substrate), the SLG demonstrated quasi-capacitive behavior. This suggested that SLG undergoes a different Li staging process than FLG and graphite.[99] Difference in behavior can be described by the interactions of the adsorbed Li atoms with each other and the carbon atoms.[99, 101] This phenomenon is a result of the increased metallic charge between the Li and C atoms that weakens the interactions between neighboring Li atoms and the Coulombic repulsive force between Li atoms on opposite sides of the SLG.[101] In other words, a stage one mechanism cannot be obtained for SLG.

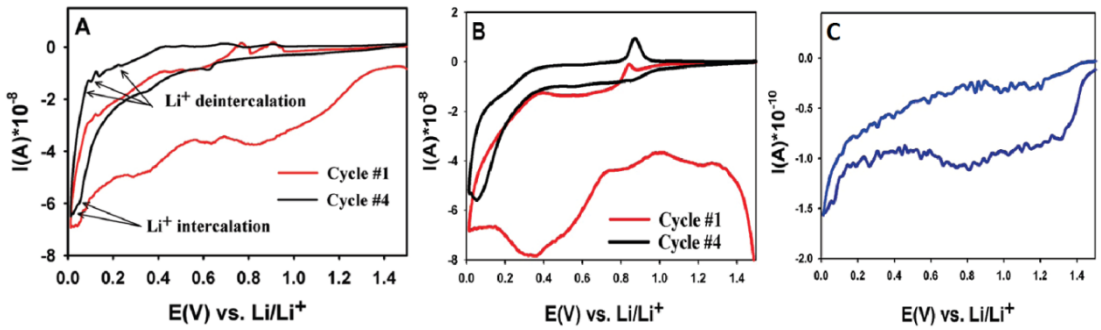

Figure 18. Cyclic voltammograms for (a) few layer and (b, c) single layer graphene on a (a) nickel, (b) copper, and (c) quartz substrate.[99]

Density functional theory has demonstrated that the GNR structure may influence the high rate and high power capabilities of graphene based electrodes for Li-ion batteries due to differences in the energy barrier for diffusion.[102] However, the model did not include effects due to SEI formation and acknowledged that SEI formation may affect Li diffusion.[102] It has also been demonstrated that the surface chemistry of the GNR also influences the electrochemical performance (capacity, Coulombic efficiency, and

capacity loss per cycle).[60] For electrochemical testing, oxidized and reduced GNRs were prepared as a slurry with a polyvinylidene difluoride (PVDF) binder and a carbon conductive additive. Mesocarbon microbeads (MCMB) and MWCNTs electrodes were created and tested in the same fashion for performance comparison. It was observed that both oxidized and reduced GNRs had high first cycle charge capacities and they also had the largest irreversible capacities. It was suggested that the larger capacities for ox-GNRs were related to the oxygen-containing surface groups contributing to the formation of a more stable SEI.[60] The authors note that the ox-GNRs have a high initial capacity loss per cycle rate that decreases with continued cycling. For the fourteen cycles reported, the GNR materials performed better than graphite and MWCNTs in terms of reversible capacity and Coulombic efficiency.

Graphene paper electrodes (Figure 19a) allow for removal of the electrochemically inactive binder from the electrode. Potential profiles of graphene paper for the first and second cycles (Figure 19b) are indicative of disordered carbon rather than graphite.[52, 99] The disordered nature of the graphene paper was confirmed by Raman spectroscopy.[52] The Coulombic efficiency of the graphene paper exceed that of the oxidized- and reduced- GNRs; however, different current rates and electrolyte compositions were utilized so direct comparison is not informative.

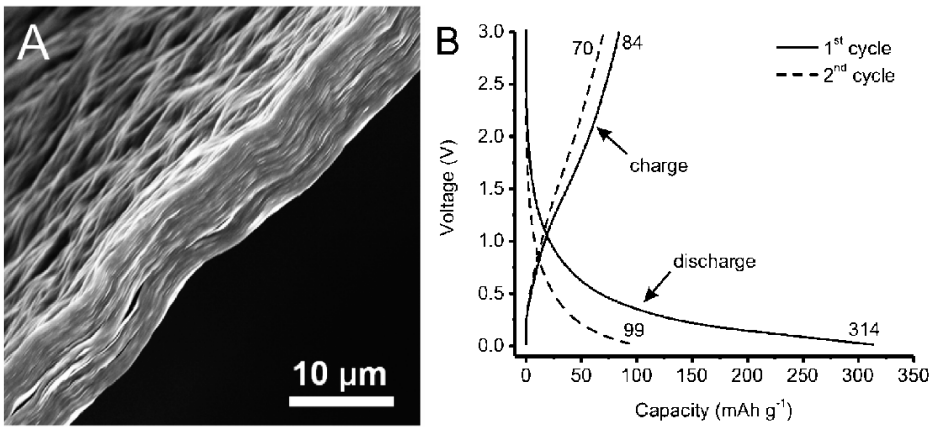

Figure 19. (a) SEM image of graphene paper and the (b) first and second charge and discharge profiles.[52]

In summary, the common shortcomings of graphene-based anodes include very high irreversible capacity losses at the first cycle, low Coulombic efficiency for subsequent cycles and limited overall stability caused by the separation of graphene layers. These shortcomings make graphene unsuitable as a replacement to the current graphite anode technology. This is surprising since graphene sheets form the basis of graphite which has been used successfully for decades. The origin is due to the different intercalation behavior between the two materials. Composite electrodes consisting of graphene nanosheets and carbon nanotubes and/or fullerenes have shown to increase the discharge capacity but failed to improve its stability to industry-usable levels.[61] Other challenges associated with graphene as electrodes, and other emerging applications, are the synthesis and handling of large quantities of graphene due to the large van der Waals energy between individual graphene sheets that causes them to assemble in graphitic structures.[53, 56] To avoid this, chemical functionalization or dispersant addition is commonly conducted.[56]

Carbon Nanotube Anodes

The ability of SWCNTs and MWCNTs to intercalate Li ions has been investigated by many researchers.[4-5, 18, 83, 103-107] Of particular interest is how the nanotube morphology and microstructure affects the intercalation of Li into CNTs and the electrochemical performance.[18, 104, 106] CNTs have multiple sites for Li intercalation, including the inner core, between concentric layers in MWCNTs, defect sites, and between neighboring SWCNTs.[5, 18, 104, 106]

Closed CNTs do not readily permit the intercalation of alkali metals into CNTs as opposed to the intercalation of graphite sheets since the inner core remains inaccessible because the Li ions cannot diffuse through the fullerene cap.[50, 104-105] In 2001, it was demonstrated that Li intercalation into the inner core has an effect on the resulting performance and cyclability.[104] During the first cycle, the capped and open CNTs showed

the same charge capacities, but very different discharge capacities, with the open CNTs achieving up to several times greater discharge capacity.[104] This result is rational since it proposes that a greater number of lithiation sites should provide a greater capacity.

Due to the increased number of cylindrical graphene sheets, MWCNTs may offer a greater capacity for hosting Li as opposed to SWCNTs. However, the intercalation of alkali metal ions into the spacing between concentric shells of a MWCNT requires the assistance of structural defects.[18, 50] The importance of defects was demonstrated in 1999, when the intercalation of alkali metals into the inter-shell van der Waals spaces of MWCNTs was achieved when the nanotubes had defects.[106] Defects in CNTs can be introduced during the formation of the fullerene cap [76] or arise from the disorder of the graphene walls. Accordingly, it has been suggested that an increase in capacity in MWCNTs is possible when not only the inter-shell spaces are available but all the interstitial sites which also include the inner tube core and defect sites[5, 18], thus making MWCNTs a potential candidate for high power anodes.[5] Apart from Li intercalation in between the shells, it has also been suggested that Li can also be doped at the surface[104], increasing the overall Li capacity of CNTs as compared to that of graphite. Intercalants have been observed in the interstices between individual SWCNTs within a CNT bundle, as observed by *in situ* XRD and electrochemical testing.[106] The intercalation of individual SWCNT bundles has also been predicted using in situ TEM and electron energy loss spectroscopy (EELS) measurements.[18]

Reports on the reversible and irreversible capacity of SWCNTs and MWCNTs show very large deviations, possibly due to different electrode preparation methods, variations in CNT microstructures, defect content, and errors in calculating the mass of the lightweight samples on relatively heavy metal substrates. For example, the values of the reversible capacity of MWCNTs was reported in the range of 100 - 1400 mAh/g.[5] Even though SWCNTs do not have the inter-shell spaces for Li intercalation, selected studies report SWCNTs to have exhibited reversible capacity of 400 – 650 mAh/g, which

is up to 50% higher than what graphite offers.[18] Unfortunately due to high surface areas, SWCNTs also demonstrated huge irreversible capacities up to 1000 mAh/g (Figure 20).[18] Previous work has illustrated the importance of electrode fabrication parameters upon the electrochemical performance.[105] While different SWCNT electrode fabrication methods were employed, there were similarities in the SWCNT synthesis. One preparation method used a slurry of SWCNT and PVDF binder (10 wt. %) and showed an extremely high irreversible capacity (~1600 mAh/g) due to a thick, porous SEI.[105] Another electrode created using a methanol dispersion of SWCNT without binder achieved a reversible charge capacity of 445 mAh/g; however, it suffered conductivity issues.[105]

Although increases in reversible capacities beyond graphite have been reported for many CNT-based anodes, a typical charge/discharge curve for these materials does not exhibit a plateau during Li extraction (Figure 20).[4, 107] In general, both SWCNTs and MWCNTs exhibit large irreversible capacities [4-5, 18] which may be a result of the increased surface area and the formation of the SEI.[18] Both of these features limit the practical application of misaligned CNT anodes.[4-5, 18]

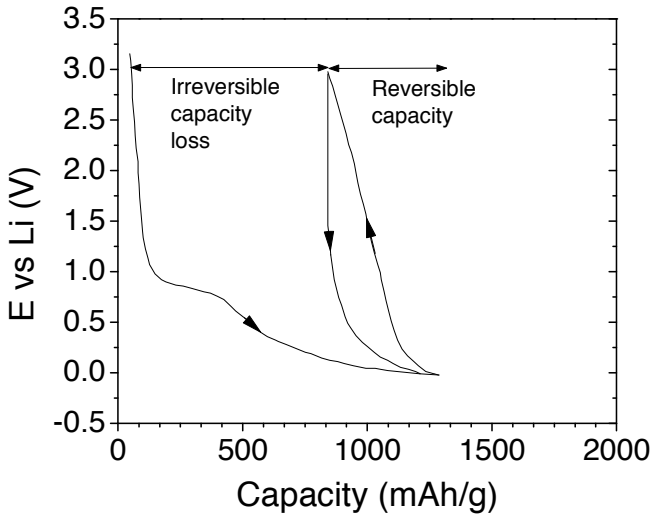

Figure 20. Charge/discharge curves for a typical CNT-based anode indicating reversible and irreversible capacities. *Recreated from Ref 4.*

Research and development of aligned CNT electrodes for highly ordered electrodes are of great interest. The primary challenge with creating aligned CNT electrodes is the development of techniques to create mechanically robust electrodes that are conductive in the horizontal direction.[5] Methods to create aligned electrodes have primarily utilized polymers to form a conducting layer or a thicker layer so that the electrode was free-standing.[5] Free-standing electrodes are of great interest since it negates the use of a copper current collector which is expensive and lowers the cell gravimetric capacity.[5]

Controlled VACNTs growth on Si substrates has been achieved [66, 84]; however, the poor conductivity of the Si wafer is a performance and/or development limiting factor. Cu foil is an ideal candidate for CNT growth due to its prevalence in electronic applications and very low resistivity, in comparison to many other metals and especially semiconducting Si.[108] VACNTs synthesis on metallic substrates has progressed, but it is not as well practiced as growth on Si wafers. VACNT growth on metallic substrates can be challenging due to inter-diffusion between the catalyst and the metallic substrate which significantly hinders CNT growth by deactivating the catalyst.[108] Accordingly, the use of diffusion barriers such as titanium nitride have been considered to eliminate this problem.[108-109] Another limiting factor is the poor adhesion between the CNTs and the substrate. For robust or electrical applications, adhesion to the substrate is imperative to prevent performance losses or electrical shorting. Post-processing steps, such as microwave exposure [110], have been shown to increase alignment and adhesion; however, such a step is likely not suitable for commercial production. Another challenge is related to the roughness of metal substrates being greater than Si or quartz since roughness has been shown to inhibit VACNTs growth.[111] It should be noted that some aligned CNTs are obtained on the Cu collector in the laser vaporization synthesis technique, but not in a sufficient quantity or obtainable manner. [50, 112]

Adhesion between CNTs and the substrate is weak for CVD processes; therefore, CNTs can be grown on a substrate and subsequently transferred onto a metal foil current collector to improve the adhesion which is imperative to maintaining electrical conductivity.[113-114] Transferring the CNTs can increase the strength of the adhesion bonds and allow for temperature sensitive processing since CVD growth occurs at elevated temperatures above which certain substrate materials may lose some of their electrical or mechanical properties.[72] The successful transfer of aligned CNTs using metals and non-metals to achieve electric conductivity has been accomplished.[5, 72, 114-115]

One method transfers VACNTs to metallic foil using a hot press and a solder of Ti and Au which is deposited on the tops of the tubes using e-beam evaporation. Preceding e-beam or concurrent with the growth process, the nanotubes are oxidized by water vapor at an elevated temperature to etch amorphous carbon, open the closed structure of the CNTs by removing the fullerene cap, and reactivate the catalyst.[72, 77] These effects further weaken the adhesion bonds between the CNTs and the Si wafer, allowing for easier removal of CNTs. The curvature of the fullerene cap, due to a high number of defects due to the arrangement of carbon heptagons and pentagons, gives rise to larger strains and increased chemical reactivity than the tube wall thus making the cap easily removable by the presence of water vapor.[72, 76] After removing the fullerene cap, the desired current collector can be placed atop the Ti-Au tipped CNTs within a heated press that allows for transfer of the CNTs.[114]

Non-metallic thin film polymers (such as PVDF and conductive poly(3,4-ethylenedioxythiophene)) have been used to create flexible and mechanically sound vertically-aligned CNT electrodes.[5, 116] In this construction, 90% of the tube length was uncoated by the polymers, allowing for a considerable surface area for intercalation.[5, 116] The initial cycle reached ~1100 mAh/g discharge capacity on the first cycle, but by the third cycle it had dropped significantly (~70%) before stabilizing ~265 mAh/g.[116]

Silicon for Li-ion Electrodes

Background

Silicon is a widely used semiconductor material. Like carbon, Si is a group IV element with four valence electrons in its outer shell and has several allotropes. The thermodynamically stable crystal structure of Si varies with temperature and pressure. At room temperature and atmospheric pressure, Si has the diamond cubic crystal structure (Figure 21) such that Si atoms are located in all FCC positions and half the tetrahedral positions [58, 117] with a lattice parameter of 0.5431 nm.[88, 117] Three other Si crystal structures can be formed at differing pressure and temperatures.[117] Silicon readily oxidizes to produce a chemically stable, native oxide (SiO_2) on the surface which can be further tailored through thermal oxidation.[118]

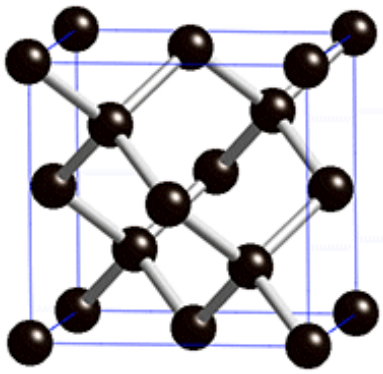

Figure 21. The diamond cubic crystal structure.

Synthesis

Bulk synthesis of Si can occur by three major routes. The Czochralski process is one method utilized to fabricate large single crystal Si ingots for wafer production for the semiconductor and microfabrication fields. Single crystal Si is also produced by the float-zone process, but the resulting Si has much higher resistivity.[118] High purity polycrystalline Si is produced from SiO_2 through a multi-step Siemens process in which

the reduced SiO_2 is reacted with hydrogen chloride to form tricholorosilane which is then decomposed.[118]

On a smaller scale, Si films can be produced via epitaxy or CVD techniques. Epitaxial growth forms a Si thin film with the same crystal orientation as the underlying substrate.[118] In contrast, the CVD decomposition of silane gas, SiH_4, can create an amorphous or polycrystalline Si thin film or deposited layer.[86-88, 119] When SiH_4 decomposition occurs between 600 – 700 ^oC, a polycrystalline layer may be achieved.[88, 120] At temperatures ~550 ^oC, amorphous Si may result and at temperatures greater than 700 ^oC non-uniform coatings may be formed as the process becomes diffusion limited.[86] Low pressure (0.5 - 1 Torr) CVD has been used to create polycrystalline Si films [88] and to hinder the homogeneous reactions to become heterogeneous in nature.[88] With careful selection of the process parameters, SiH_4 decomposition allows for controlled thickness, uniformity, adhesion, microstructure, and morphology of the Si coating.[74] It should be noted that numerous other precursors are also capable of depositing Si thin films. [86-87]

Si nanoparticles (e.g. spherical particles, nanowires) can also be formed. One method to create nano-sized Si powder is through laser induced reactions with a Si_xH_y gas.[121-122] Two disadvantages of this method for long-term commercial use exist. First, the method is of very low yield.[122] Second, due to the high surface energy associated with nanomaterials (resulting from the increased surface area to volume ratio) the particles tend to agglomerate. As such, it becomes difficult to disperse Si nanopowders effectively in various media [122] without time-consuming ball milling in an inert environment to prevent further formation of silicon oxide. Single crystal whiskers or nanowires can be produced via the VLS method (Figure 22).[14, 80] Three characteristics define the resulting nanowire. First, the nanowire is oriented along one crystal direction and does not contain dislocations. Second, a catalyst (typically gold) is necessary to begin growth and third, the catalyst is located at the top of the emerged nanowire.[80]

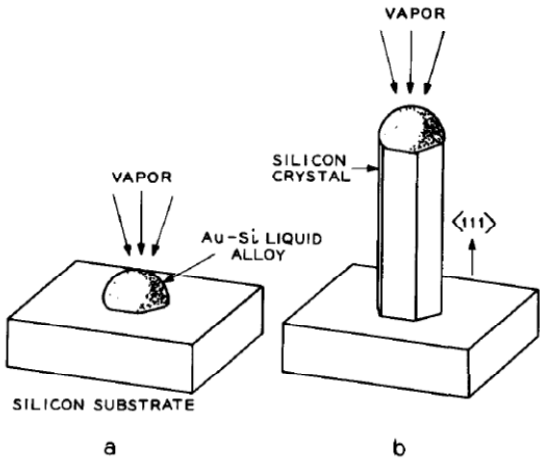

Figure 22. Two step schematic of VLS growth: precursor gas (a) saturates a liquid catalyst on the substrate surface and (b) precipitates to form a single crystal whisker.[80]

Silicon Anodes

Silicon anodes have received particular attention due to its highest gravimetric capacity for Li.[7-8, 32, 123-125] Early studies of the lithiation of silicon were conducted at high temperature (415 ^{o}C) and showed good agreement with the corresponding phase diagram.[125] At elevated temperatures, the fully lithiated phase corresponds to $Li_{22}Si_5$ with a theoretical capacity of 4200 mAh/g. The behavior is quite different at room temperature with none of the thermodynamically predicted Li-Si crystalline phases formed, but rather an amorphous Li-Si alloy [32, 123] (Figure 23). These deviations have been noted by several studies.[14, 21, 32, 123] It is also possible that the formation of metastable $Li_{15}Si_4$, not predicted by the phase diagram, can occur when the potential is less than 50 mV vs. Li/Li^+.[32, 123] $Li_{15}Si_4$ has a slightly lower theoretical capacity of 3579 mAh/g. Interestingly, the newly recrystallized phase becomes amorphous upon delithiation and remains amorphous throughout subsequent cycling.[32] It is common to find both values of theoretical capacity reported in the literature.[7]

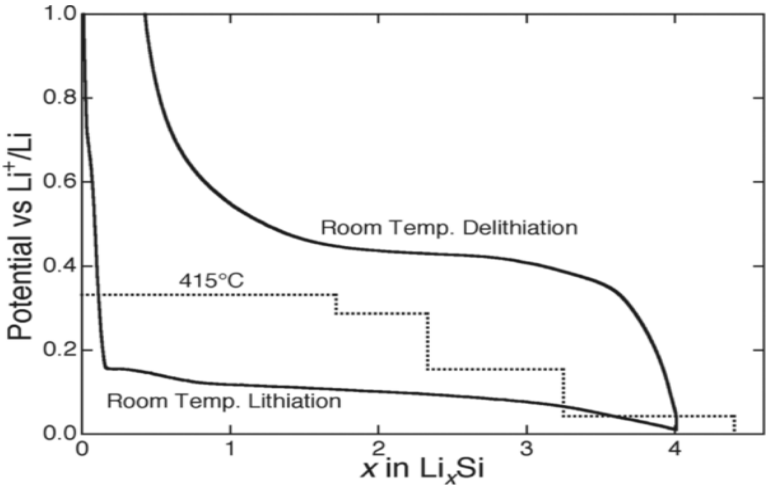

Figure 23. Comparison of the experimentally observed behavior of crystalline Si at room temperature and 415 °C as a function of Li content.[126]

The lithiation of crystalline Si is anisotropic and has been observed in several studies.[126-127] Si nanopillars of different axial orientations (<100>, <110>, and <111>) were lithiated to observe whether lithiation was preferential along certain directions. Each nanopillar exhibited different lateral and vertical growth (Figure 24).[128] From analysis, it was clear that Si lithiation is anisotropic with <110> identified as a high Li diffusion channel. The result is in keeping with the Si crystal structure as <110> has the largest atomic spacing and would thus be expected to have higher diffusion rates. Accordingly, the volume expansion along those orientations varied with expansion ratios of ~271%, ~264%, and ~243% observed along <110>, <111>, and <100>, respectively.[128] In contrast, amorphous Si lithiates isotropically due the lack of ordered crystallinity.

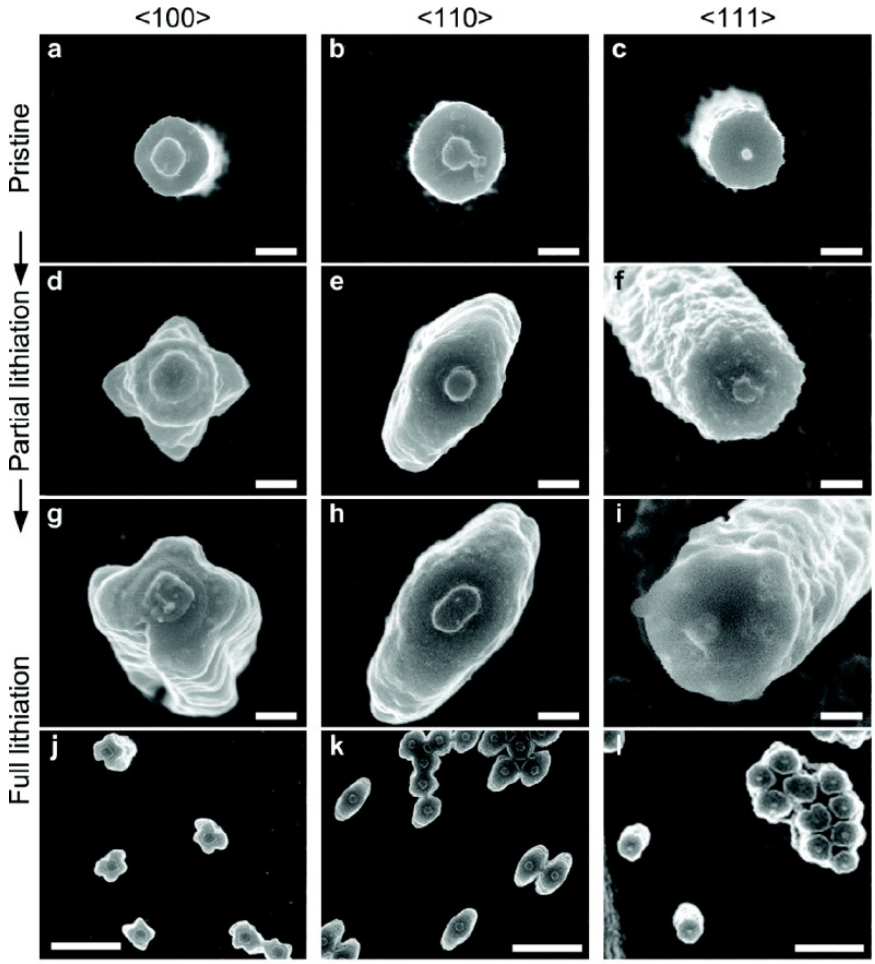

Figure 24. Top-down SEM images showing the anisotropy of the lateral expansion of crystalline Si nanopillars of different axial orientations (<100>, <110>, and <111>) at varying degrees of lithiation.[128]

The large volume (~300%) changes occuring during the Li insertion/extraction process [8, 14, 32, 124, 129-130] can generate stresses in the electrode material forming cracks and breaks in electrical conductivity.[9, 30] Irreversible capacity losses in Si electrodes may be attributed to many factors including SEI formation and loss of electric contact between active particles upon discharge [14, 32, 46, 130] which electrically isolates lithiated Si particles. Prior art studies illustrate that without sufficient space available in the electrodes for volume expansion of Si during Li_xSi_y alloy formation, significant stresses are generated and electrode failure results (Figure 25). Significant capacity losses below the initial capacity (upwards of 90%) has been reported within a very small number of cycles [17, 33,

[130] thus, the critical challenge of high capacity materials is to reduce the destructive stresses that lead to material cracking and anode disintegration.

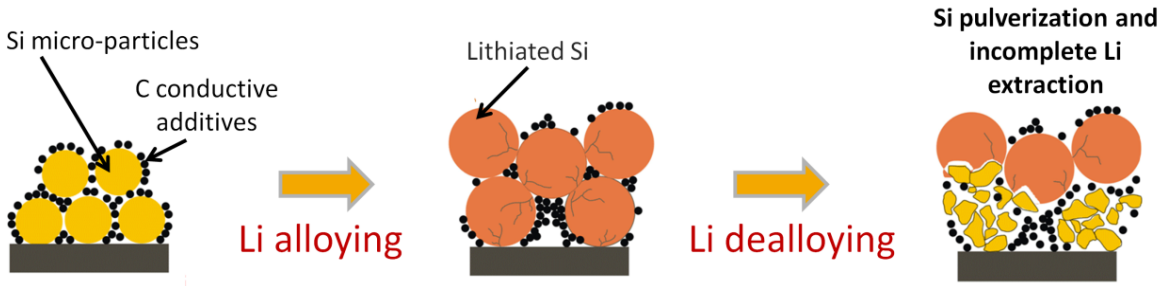

Figure 25. Schematic illustrating the degradation of an electrode created through conventional techniques utilizing micron sized Si particles.

Accordingly, strategies to reduce the rapid capacity fade have been explored, including Si thin films, micro-Si powders, nano-Si powders, combined with active and non-active materials, and novel structured nanomaterials.[3, 5, 14, 17, 33, 130-133] The use of Si nanoparticles, often combined with a high binder and C additive content [10, 134], may overcome some of these limitations at the expense of lowering the volumetric capacity.

Small particle sizes within a uniform distribution have shown to help alleviate these problems.[14, 135] Si thin films and nanomaterials have exhibited significant improvements in capacity, stability, and cyclability for several hundred up to 3000 cycles.[42, 131-132, 136-137] Several studies [42, 131-132, 136-138] have extensively researched the maximum thickness of a Si thin film which will yield high capacities and high Coulombic efficiencies. Their work demonstrated the relationship between particle size, capacity, and cyclability. For 200 cycles, a 50 nm Si film yielded a charge capacity ~3500 mAh/g and a 150 nm Si film yielded a charge capacity of 2200 mAh/g, each with high Coulombic efficiency.[136] For Si thin films deposited on pristine Ni foil, both the specific capacity and capacity retention improved as the thickness decreased.[137] For Si on roughened Ni foil, the initial charge capacity was the same as the thickness decreased; however, there was a notable increase in capacity retention for the thinner film.[137]

An amorphous 800 nm Si thin film failed after the third charge/discharge cycle whereas a thickness of 200 nm had significant capacity losses in the first 20 cycles, but eventually became stable.[33, 133] Amorphous Si thin films (430 nm thickness) exhibited a 92% efficiency relating to a charge capacity of 3000 mAh/g and a discharge capacity of 2750 mAh/g.[12] Thinner amorphous Si films (40 nm) showed stability through 50 cycles with a 2000 mAh/g capacity and with capacities as high as 3500 mAh/g initially.[33] This is in contrast with a crystalline Si thin film of the same thickness that had stable performance of 3000 mAh/g for 25 cycles.[33]

An overview of the literature indicates that further decreases in thin film thickness may be beneficial for obtaining high capacities for many cycles without material degradation.[17, 130] Recent investigations of nano-Si electrodes have shown that the reduced size limits the fracture behavior [17, 33, 130] thus leading to high capacities over many charge/discharge cycles. Overall, Si thin films (thickness < 1 μm) have shown great promise with high capacities (up to 3500 mAh/g), efficiency (> 90%), and capacity retention [17, 33, 129-130], but their applications are hindered by the small electrode thickness which leads to low energy densities when normalized by the total battery mass.[16, 129]

It is suggested that nanoparticles can provide a high reactivity with Li (due to the increased surface area) and short diffusion lengths which can increase rate capability.[5] Reports on the use of Si nanoparticles (80 nm diameter) electrically connected by 10 to 40 wt. % binders and conductive additives exhibited up to 1700 mAh/g capacity.[130] Nano-Si particles of 12 nm diameter achieved an 1100 mAh/g capacity which was reduced by half after 50 charge/discharge cycles.[33] Further confirmation that particle size reduction aids cyclability was demonstrated by lithiating spherical Si nanoparticles via *in situ* TEM.[127] The work identified a critical Si particle diameter of ~150 nm, above which Si particles formed surface cracks and eventual fracturing during lithiation. In contrast, sub-150 nm particles lithiated completely without any surface cracking or fracturing.

Aligned 1-D Si nanostructures (Figure 26) offer several advantages. First, the void space between the nanowires accommodates the volume changes that have proven detrimental to capacity retention. Second, nanowires not only increase the surface area but also the surface area to volume ratio which creates greater contact with the electrolyte and thus greater charge transport to the electrode.[15, 65] Furthermore, the open, uniform structure permits high Li diffusivity due to the short, direct diffusion paths.[14]

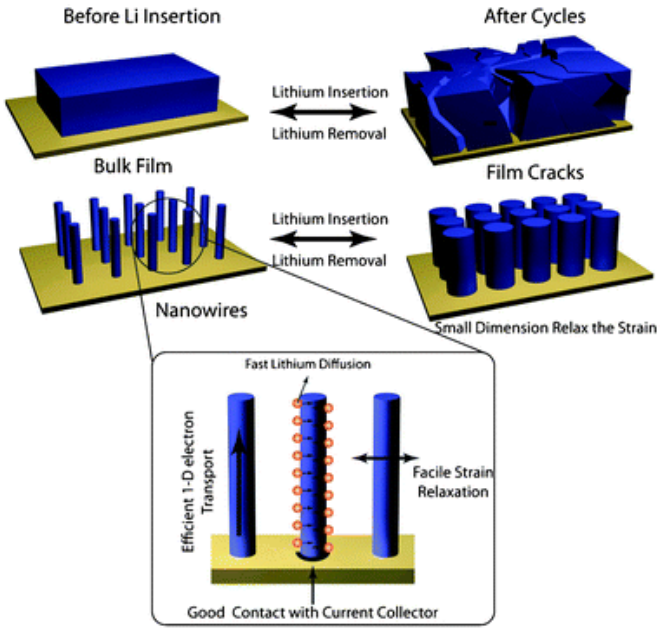

Figure 26. Schematic illustrating the proposed benefits of transitioning from bulk anodes to highly structured 1-D anodes.[34]

Previous research has shown that reductions in capacity and anode degradation can be avoided by using Si nanowires of a broad diameter range (centered around 100 nm) in a "brush"-like (1-D) structure.[14] While the particle size is greater than the nanoparticles previously discussed, the nanowires are structured such that they are in electric contact with the current collector but not directly with neighboring nanowires.[14] The one-step synthesis allowed for the removal of any binder or conductive additives. Although the electrode is fabricated in one step as compared to multi-step traditional powder methodologies, the cost is much higher due to the price of the gold catalyst

required for aligned Si nanowire growth. In addition, the technique is not currently scalable for large-scale production. Furthermore, the conductivity of the nanowires is lower than that of a 1-D carbon structure such as CNTs.

Crystalline Si nanowires underwent a transformation upon charging leading to an amorphous Si structure and increased diameter as measured using cross-sectional SEM. During the first charge, the Si nanowires achieved theoretical capacity (4200 mAh/g) and exhibited excellent reversibility, but only for ten cycles.[14]

A 3-D anode nanostructure consisting of porous Si channels electrochemically etched from a Si wafer has also been investigated.[16] CV of anodes with porous channels of different aspect ratios (pore depth/diameter) showed that there was an increase in the ability to store Li with increasing aspect ratios; however, this trend was not linear.[16] Another promising result was that the porous Si retained its structure after cycling.[16] The use of not only nanomaterials but nanostructured materials are expected to achieve high capacity without fracture thereby leading to increased capacity retention.[130]

Germanium for Li-ion Battery Electrodes

Background

Silicon and germanium are analogous in several ways. They are both group IV semiconductors with Ge having greater electron mobility.[117, 120, 139] Although Si is currently the dominant material in the microelectronics industry, Ge was more commonly used throughout the mid-1900s and was used in the first transistor.[120, 140] At atmospheric pressure and standard temperature, Ge has a diamond cubic structure with a 0.566 nm lattice constant (Figure 24).[31, 117, 141] Like Si, three other Ge crystal structures can form depending on temperature and pressure.[117] Unlike SiO_2, the native oxide for germanium (GeO_2) is soluble in water.[140]

Synthesis

Like silicon, there are several methods to produce germanium. The majority of germanium is a byproduct of other industrial processes such as smelting.[139-140] Both the Czochralski and float-zone methods can be used to create single crystal Ge. The float-zone technique used to create large Si crystals was originally developed to produce Ge for the microelectronics industry.[140] High purity polycrystalline Ge can also be formed through the reduction of GeO_2. [140]

Similar to silicon, germanium materials can be produced through both CVD and physical vapor deposition (PVD).[31, 120] CVD is common and germane, GeH_4, is the most widely used precursor although many other precursors have been explored.[88, 120, 141-143] Crystalline Ge can be deposited through low pressure CVD of germane operating between 350 – 400 ^oC.[120] At slightly higher pressures and lower temperatures, amorphous Ge can be produced. [120] CVD of germane was used to create the first single crystal Ge nanowires via VLS growth at both atmospheric and low pressures.[141, 144] The synthesis temperatures are low (> 275 ^oC) due to the presence of gold nanocrystals as a catalyst.

Germanium Anodes

Germanium may be a promising anode material since it has a higher electrical conductivity and Li diffusivity than Si. At 360 ^oC, the diffusivity of Li in Ge is fifteen times larger than in Si.[31] Using the definition of diffusivity as an Arrhenius function dependent upon an activation energy, it has been determined that the difference in room temperature diffusivity may be as large as 400 times.[31]

Ge forms a Li-Ge alloy [35] and at maximum lithiation, germanium may form the phase $Li_{22}Ge_5$, which has a theoretical capacity of 1600 mAh/g.[35] It has been observed that the phase $Li_{15}Ge_4$ (analogous to $Li_{15}Si_4$) is the fully lithiated phase with a theoretical capacity of 1385 mAh/g.[145] Interestingly, both phases have been observed to form[146] thus highlighting the lack of understanding of the lithiation of Ge.[145] Although the theoretical

capacity is not as high as silicon (due to differences in mass), it may still lead to significant advances in capacity, energy, and power, if properly designed.

Analogous to Si, large volume changes have been observed during alloying/dealloying [35] thus limiting the use of bulk Ge anodes. However, unlike Si, lithiation of Ge particles has been shown to be an isotropic process by *in situ* TEM performed on Ge nanoparticles of a broad diameter range (~100 to ~600 nm). [147] This suggests that the stability of Ge nanoparticles may be less dependent upon size than Si nanoparticles.

A comparative study of bulk Ge, crystalline Ge nanoparticles (12 nm diameter), and an amorphous Ge thin film (60 – 250 nm thick) [31] provides insight regarding the effect of the substrate on cyclability. Bulk Ge anodes were created from elemental Ge and, as expected, demonstrated very poor capacity retention even at a low charge/discharge rate of C/30 (Figure 27). Ge nanoparticles were deposited directly onto the current collector through ballistic evaporation and the thin film was deposited using thermal evaporation. Interestingly, the nanofilm and nanoparticles demonstrated a higher than theoretical charge capacity on the first cycle (Figure 27). Throughout sixty cycles, the nanofilm had charge and discharge capacities greater than theoretical. While the origins of this phenomenon are not explained, it can be hypothesized that it is due to instrumental error, native oxide lithiation, or SEI formation. The nanofilm demonstrated the highest capacity (no binder was used for the film and the nanoparticles). This result is in agreement with previously discussed research on Si thin films.[42, 131-132, 136-137]

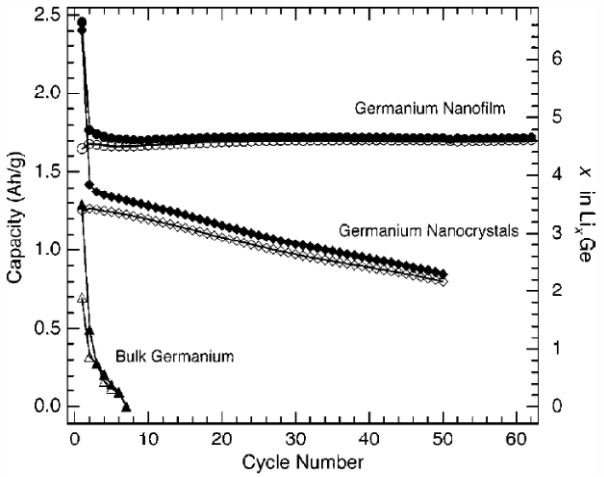

Figure 27. Charge and discharge capacities versus cycle index of multiple Ge morphologies.[31]

The 60 – 250 nm Ge thin films were deposited on a rigid substrate. Dehesion between the film and the substrate was expected due to the large strains at the interface due to lithiation of the film; however, post-mortem analysis proved that this did not occur.[31] The mechanism of operation was hypothesized as follows. Cracks were generated in the film during cycling and propagated through the film during continued cycling. These cracks separated the film into islands that were better able to accommodate the large volume expansions. It is surprising that the Ge nanoparticles did not demonstrate better cycling performance given their small size which should not allow for crack propagation.[31]

The crystal structure of the Ge anode is also of relevance. Through galvanostatic intermittent titration technique (GITT) and XRD, amorphous Ge films created by evaporation and sputtering have been shown to alloy lithium at the same potentials and to produce $Li_{15}Ge_4$ at full lithiation.[145] The authors hypothesized that the crystallization of the Li-Ge alloy to $Li_{15}Ge_4$ may be detrimental for stable long-term performance since the crystallization would generate stresses in the material. This effect may be lessened by limiting the extent of lithiation. Upon dealloying, the two films behaved differently, most likely as a result of the different initial Ge structure.[145]

Similar to prior work with aligned Si nanowires, decent capacity retention and stability at high rates of charge/discharge has been reported for aligned Ge nanowires.[35] The first cycle charge capacity for Ge nanowires had a value greater than theoretical $Li_{22}Ge_5$ (~1400 mAh/g higher), but a lower discharge capacity (~1150 mAh/g). Higher than theoretical capacities can be obtained due to the formation of the SEI consuming Li and typically give rise to large irreversible capacity loss (~1800 mAh/g for Ge nanowires).[12, 31, 35] Another possible contributing factor is the breakdown of GeO_2 to form Ge and Li_2O which would theoretically give a capacity ~1400 mAh/g. [35] The crystalline Ge nanowires undergo an amorphization process when cycled, analogous to work with crystalline Si nanowires. [14, 31, 35]

Although Ge nanowires demonstrated capacity retention for ten cycles for several high rates of charge/discharge, Ge nanowires, like their Si counterparts, require gold as a catalyst thus increasing the synthesis cost. The conductivity of germanium is higher than silicon, but it is still much lower than that of carbon. While Si or Ge nanowires may not be scaled-up for commercial production, they successfully demonstrate the architecture of the aligned one-dimensional structures as a viable route to mitigate degradation of high capacity electrodes.

Composite Materials for Li-ion Battery Anodes

As previously discussed, composite anodes are investigated to lessen the rapid performance losses observed in pure high capacity anodes. Numerous elemental and physical combinations of materials have been studied to achieve high capacity retention yet studies seeking understanding of the mechanisms of these composites is more limited with questions such as the effect of the interfaces or anode architecture on the resulting performance not addressed. Following is a sampling of highly structured nanocomposites anodes developed for high performance Li-ion batteries.

Production of composite electrodes consisting of a high capacity material (particularly Si) and various carbons which act as structural buffers have been intensely researched.[2, 10, 21, 148-150] Early Si-C composite electrodes were mostly fabricated by the decomposition of C- and Si- containing precursors or through mechanical mixing and many exhibited low performance [121, 150-153] due to limited porosity available for Si volume changes and non-uniform material properties at the nanoscale. Recent work has demonstrated that significantly better performance could be achieved if the composite materials contain uniformly distributed Si, C and interconnected pores.[10, 154-155] Improved performance may be a result of decreases in material fracture or increased conductivity.[17] The use of various binders, such as PVDF, carboxymethyl cellulose (CMC), polyacrylic acid (PAA), and alginate [156-157], have attempted to facilitate the maintenance of a conductive network during cycling and increase conductivity of semiconducting Si.[17, 123] However, the addition of binders and conductive additives decreases the energy and power densities.

Composites of nano-Si and carbon black or MCMB have given capacities of 1700 mAh/g and 1066 mAh/g, respectively.[5] While increased capacity has been achieved, mechanically mixed Si-C composites do not prevent capacity fading.[155] In contrast, C-coated Si, created via CVD, exhibited both high capacity and capacity retention. For an electrode consisting of dispersed nano-Si in a C matrix, an 11 wt. % Si composite yielded ~400 mAh/g for approximately 30 cycles.[149] An MCMB micropowder decorated with nano-Si (0.036 to 0.050 at. % Si) by CVD of SiH_4 have exhibited a modest increase in capacity of nearly 100 mAh/g; however, a large irreversible capacity during the first discharge resulted in a 45% Coulombic efficiency.[119]

A novel Si-C composite comprised of coiled CNTs grown on mechanically milled Si particles (1 - 2 μm) by CVD created a "cage" around the particles that reduced the destructive volume changes and maintained electric contact during cycling as evidenced by the 80% Coulombic efficiency over twenty cycles.[129] These composite anodes

exhibited better capacity retention than a physical mixture of Si and CNTs which may be a result of the CNTs assisting in the formation of a stable SEI as well as increasing the conductivity.[129] It was hypothesized that longer CNTs will increase the ability to enwrap the Si particles in C thus maintaining a conductive network and a continuous SEI which will help maintain high capacity over numerous cycles.[129]

A variety of methods to incorporate CNTs, Si powders, and pyrolytic carbon have been investigated.[153] First, CNTs grown on nano-Si powder were subsequently coated with C via pyrolysis at 800 ^{o}C. These composite anodes showed higher capacities and better capacity retention than mechanical mixtures of the same materials.[153] This is in contrast with a mechanical mixture of nano-Si powder, MWCNTs, and pyrolyzed carbon that had severe material degradation over 50 charge-discharge cycles with cracks larger than 1 μm and almost complete destruction of electric contact.[153] In the creation of CNTs on a Si powder via CVD, a small amount of silicon carbide was formed and helped with the contact between the two phases however, it is electrochemically inactive and does not contribute to the capacity.[153]

Similarly, efforts to combine germanium with carbon have been conducted. A mixture of C-coated Ge nanoparticles (~31 nm) and CNTs were created in which 83% of the Ge nanoparticles were inside the nanotubes.[158] The composite performance was compared at different rates of charge/discharge to a pure CNT anode. While modest increases in capacity were achieved due to the presence of Ge, the high rate performance did not improve with the capacity successively dropping to values lower than graphite with increasing rate.[158]

A layered germanium and CNT composite anode has been demonstrated; however, the results suffered from low Coulombic efficiencies and high capacity fade.[159] The Ge was deposited by e-beam evaporation onto a free-form misaligned CNT electrode. As seen in Figure 28, the Ge is not uniformly distributed throughout the electrode but, rather, is a 1 μm thick film uniformly deposited on top of the 15 μm thick

CNT fabric. Cycling performance was only shown for 10 cycles and it was unclear whether the Ge film was on the near or far side of the Li metal or $LiCoO_2$ cathode it was tested against. In those few cycles only a moderate increase beyond theoretical graphite was obtained. The authors stressed that the Coulombic efficiency increased as a result of increased Ge loading, but the claim is slightly misleading. The discharge capacity did increase, but the charge capacity decreased with increasing Ge content. The modest increases in Coulombic efficiency therefore seem somewhat artificial.

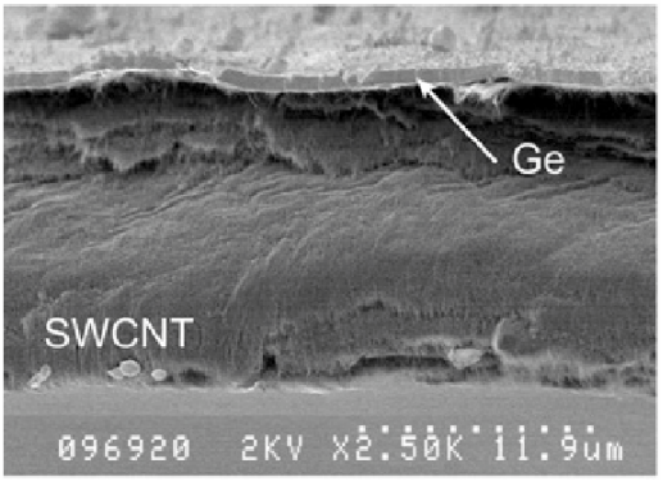

Figure 28. Cross-section SEM of a Ge film deposited onto a SWCNT misaligned film.[159]

In 2006, the formation of Ge nanowires encapsulated in graphitic C was reported. The main objective of the work was to limit the formation of germanium oxide which has poor chemical and electrical properties for electronic applications.[144] To prevent oxide formation, a technique in which the remaining Au catalyst causes C to assemble on the Ge nanowire was utilized (Figure 29). A literature review of other work by the authors suggests that they are unaware that they generated a potentially desirable material for Li-ion batteries. Even if aware, the technique is performed in the TEM; therefore, the process would produce materials at extremely low yield that would not be conducive for large scale anode use but rather fundamental studies.

The performance of a nanocomposite of Ge and Sn produced through a thermal method was compared to the performance of a physical mixture as well as pure Ge or Sn particles.[160] The nanocomposite was produced by creating $SnP_{0.94}$ particles which were mixed with Ge particles and annealed in vacuum at 400 ^{o}C for varying times. The produced nanocomposite consisted of spherical Ge and Sn (the P content was reduced during annealing) in which the Ge largely resided in between Sn particles.[160]

A physically mixed nanocomposite of Ge and Sn was difficult to obtain due to aggregation of the particles.[160] The resulting anode material demonstrated a dramatic capacity drop (~70%) over the first twenty cycles (Figure 30b). The difference in performance between the nanocomposite and the mixture indicates Ge had a significant role in promoting stable performance. TEM analysis showed that the Sn particles grew larger with cycling, similar to an Ostwald ripening event, until at a maximum particle size (undefined) the particle would pulverize. It was hypothesized that the Sn volume increase accelerated Ge pulverization to form aggregates that redistributed to provide a buffer for continued volume changes and to provide a percolation path.[160] Although the nanocomposite showed the greatest stability the discharge capacity was only ~60% of the first cycle, after fifty cycles.

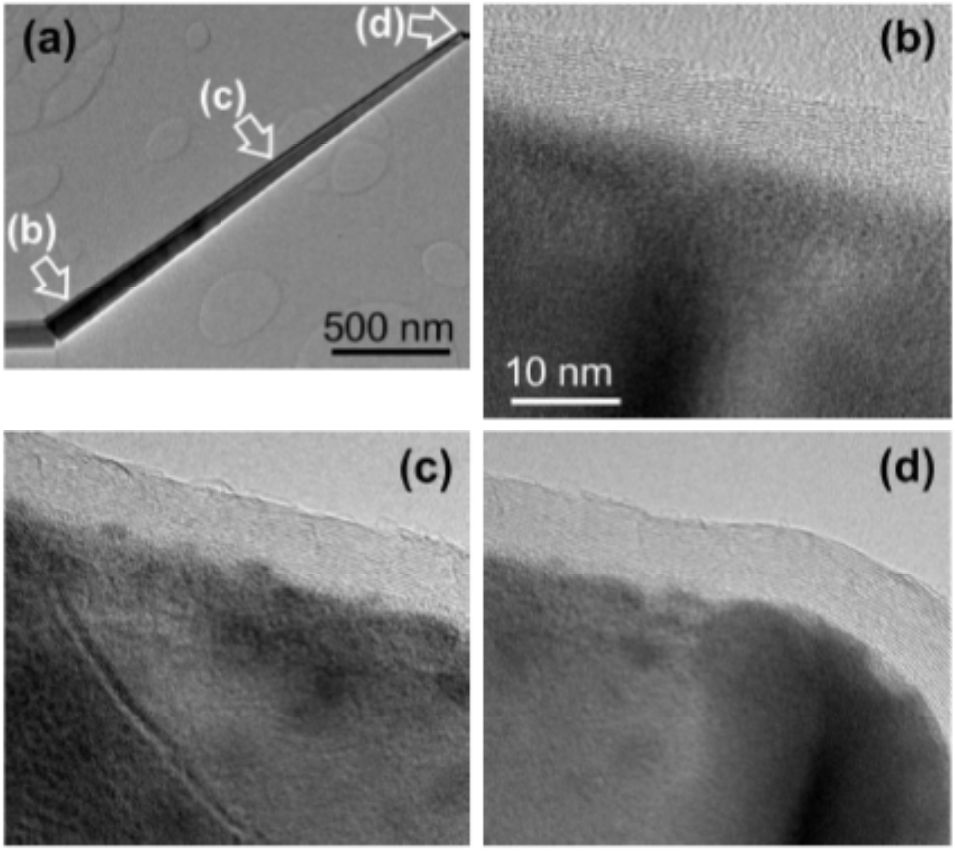

Figure 29. TEM images of the graphitic shells assembled on (a) a Ge nanowire, (b) near the nanowire base, (c) midway of the nanowire length, and (d) near the catalyst tip.[144]

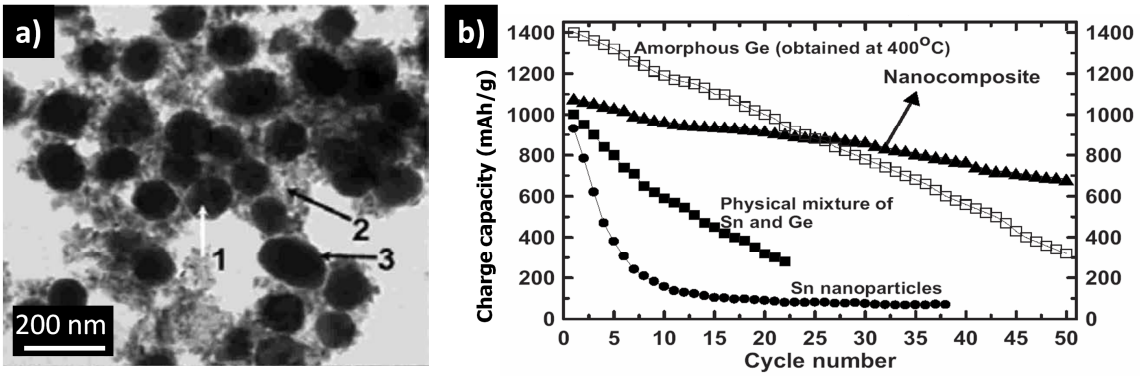

Figure 30. (a) TEM image of a Sn-Ge nanocomposite where 1: β-Sn, 2: Ge, and 3: Ge on Sn. (b) Discharge capacity as a function of cycle number for a thermally generated nanocomposite, a physically mixed nanocomposite, pure Ge nanoparticles, and pure Sn nanoparticles. *Adapted from Ref. 160.*

2.5 Vapor Deposition Techniques

PVD techniques generally describe methods to deposit thin films through a variety of methods from solid source materials. Each PVD technique is able to be completed in a variety of ways thus increasing the number of types of materials and structures achievable. Evaporation (thermal, e-beam) and sputtering (DC, RF, magnetron, reactive) are the primary PVD techniques. While a popular method for thin films on planar substrates, PVD is not always suitable for coating complex structures due to shadowing effects. In general, conformal coatings may not be achieved by PVD techniques for they allow only a line-of-sight deposition that leaves the sides and undersides uncoated.[86-87]

CVD is a general term for techniques in which reactant species are broken down in reactive (thermal, plasma) environments to generate a solid product with tunable properties onto a heated substrate.[74, 86] CVD is highly adaptable to deposit a wide variety of materials including metals, semiconductors, dielectrics, and ceramics.[86] The number and breadth of materials which can be deposited is due to the numerous system configurations and parameters as well as wide availability of precursors. Substrates are only limited by their integrity at the temperatures and pressures of the reaction and their ability to resist chemical attack by the precursors and their byproducts. In many applications (the microelectronics industry, in particular), controlled synthesis of the microstructure of the active material is desired. For this, CVD is commonly employed and is a suitable process since CVD is characterized by its ability to create thin film layers that uniformly coat both planar and complex microstructures under certain processing parameters.[74, 86, 161]

CVD systems are very complex due to many variants of reactor type, chamber pressure and temperature, and precursor selection; however a typical CVD process will consist of several steps including (Figure 31): the transport of source gases into the reaction chamber and to the substrate surface, adsorption of gaseous species onto the

heated substrate surface, diffusion and reactions of the reactants at the substrate surface to nucleate or grow, and desorption of product gases from the substrate surface. Reaction products not removed from the surface can lead to impurities in the resulting film; however, desorption is typically readily achieved, especially in vacuum systems.[74, 86, 161]

Nucleation and growth are essential within CVD processes and occur heterogeneously.[74, 88] Atoms are adsorbed onto the substrate surface and nucleate by surface diffusion and by the coalescence of impinging atoms [74, 88] to increase the nucleus density. Then, the nuclei coalesce to begin the growth process.[88] In processes dominated by surface kinetics, complex surfaces including irregularities are uniformly coated; however, in diffusion controlled processes, an uneven coating might be expected.[74]

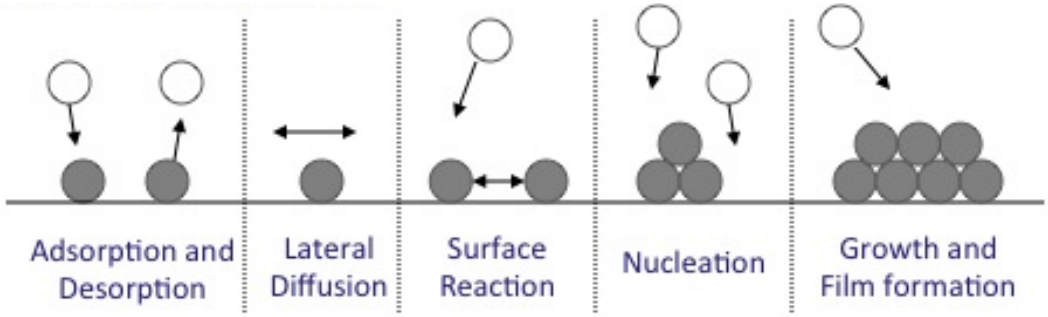

Figure 31. Schematic of the general steps of a CVD process. *Recreated from Ref. 161.*

Although CVD is a non-equilibrium process, a thermodynamic consideration of the Gibbs free energy can predict whether a deposition reaction can occur.[74, 86-88] When the change in free energy of the reaction, ΔG^o_{rxn}, is negative, the reaction is possible and deposition can take place. From first principles, it can be shown that:

$$\Delta G_i(T) = \Delta H_f^o(298) + \int_{298}^{T} C_p dT - TS^o(298) - \int_{298}^{T} \frac{C_p}{T} dT \qquad (8)$$

A direct calculation of ΔG^o_{rxn} from first principles at a temperature T requires knowledge of the enthalpy of formation (ΔH_f^o), entropy (S^o), and heat capacity (C_p) for all constituents through a range of temperatures, values which may not be well determined.[87]

An alternative method of calculating the free energy change is to consider the partial pressures of the reactants and products by [74]:

$$\Delta G^{o}_{rxn} = 2.3RT\ log k_p = 2.3RT\ log \frac{\prod_{i=1}^{n} p_{i,products}}{\prod_{i=1}^{n} p_{i,reactants}} \quad (9)$$

where R is the gas constant and k_p is the equilibrium constant which is equivalent to the ratio of the multiplicative product of the partial pressures (p_i) of the products to the reactants. These equations are merely a thermodynamic guideline developed for a closed system. Oftentimes, CVD reactions are performed in open systems in which product gases are exhausted from the system and descriptions of the reactions are quite complex.

If a reaction is thermodynamically possible, kinetics will determine the deposition rate as well as the morphology of the resulting CVD coating.[74, 86-88] Difficulty in predicting whether the rate determining step is mass transport or surface kinetics is related to variations in the sample size and porosity, reaction chamber design, and synthesis conditions such as pressure and temperature.[74] Mass transport controls the ability of the source gases to move and determines the nucleation rate. When mass transport is fast, a uniform film morphology can be obtained. When mass transport is slow, non-uniform coatings are obtained.[74]

The resulting coating morphology is primarily dependent on the vapor saturation, and the temperature of the reaction chamber, which influence the nucleation rate and growth rate, respectively.[74, 86-88] As the temperature of the reaction chamber increases, the reaction transitions from a chemically kinetic limited regime to a diffusion limited regime.[86] Figure 32 is an Arrhenius type plot for deposition rate and temperature from which the experimental activation energy can be determined from the slope of the line. At lower temperatures and pressures the deposition rate is generally surface reaction limited.[74] By increasing the temperature, diffusion increases thus leading to faster

deposition but at the risk of increased gas-phase nucleation of powder which can lead to poor uniformity and adhesion.[86-87] Lowering the pressure can reduce the homogeneous reactions to lead to more uniform deposits.[87] Furthermore, as the temperature and pressure increase, the surface reaction rate often rises exponentially, resulting in a deposition limited by mass transport.[74, 87] However, at very high temperatures, the deposition rate may decrease due to reactant depletion and/or an increased rate of desorption.[86]

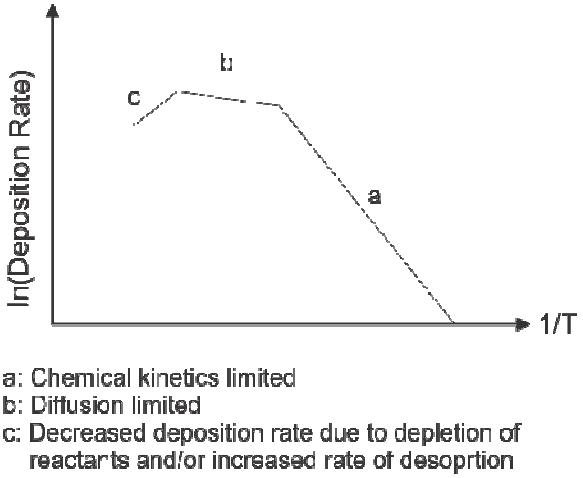

Figure 32. Generalized Arrhenius plot illustrating the rate limiting regimes. *Recreated from Ref 86*.

Atmospheric CVD processes are typically diffusion limited.[86] In contrast, low pressure CVD process facilitates diffusion and may lead to a regime in which the diffusion kinetics is greater than the surface kinetics rate.[86, 88] By utilizing lower pressures, it is possible to achieve higher deposition rates, greater uniformity and step coverage, and fewer defects than obtained at atmospheric pressure.[88]

Another factor required for coating uniformity is the uniform distribution of the gas source to all surfaces within the reaction chamber. To achieve an amorphous coating, a high saturation and low temperature are desired such that the process is dominated by

nucleation. With increasing temperature, first a columnar structure is formed and then at much higher temperatures, single-crystal growth is possible.[88]

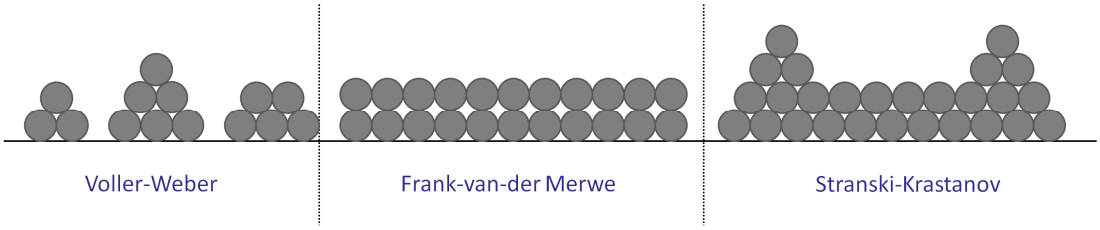

Figure 33. Schematics of the films produced by the three CVD growth models: Voller-Weber, Frank-van-der Merwe, and Stranski-Krastanov. *Recreated from Ref. 74.*

There are three types of growth models suggested for CVD processes (Figure 33): Voller-Weber, Frank-van-der Merwe, and Stranski-Krastanov.[74, 88] Voller-Weber, or island growth, occurs when the bonds between atoms in a cluster are stronger than the bonds between the atoms and the substrate. The island morphology occurs because atoms form stable clusters that nucleate on the substrate and grow in three dimensions.[74, 88] Frank-van-der Merwe, or layer growth, is commonly seen in epitaxial growth and is characterized by the planar sheets that arise.[88] In this case, atoms bond with the substrate more strongly than with each other. [74] Stranski-Krastanov growth exhibits characteristics of both island and layer growth. At first, the growth is layered; however, that mechanism becomes unfavorable and island growth takes over. This transition in growth mechanism is not well understood, but may be a result of strain energy accumulation as a result of lattice-mismatch across the interface and its release which may induce island formation.[74, 88] Continued reactions at the interface between the substrate and the coating lead to the formation of a continuous film.[74, 161] Further growth follows the same process and creates a crystalline or an amorphous coating.

CHAPTER 3

RESEARCH OVERVIEW

The motivation for this research was to create highly structured, high capacity nanocomposite anodes with novel architectures to identify the materials properties and morphologies that influence the electrochemical characteristics. Rational design of anodes allowed for the production of materials that outperform current commercially available graphitic anodes in terms of the specific capacity and capacity retention at different charge/discharge rates, resistance to the rapid degradation commonly associated with high capacity materials, thermal and electrical conductivities, and strength.

To deepen understanding in this area, three anode architectures consisting of a carbon substrate (graphene granules, CNT fabric, vertically aligned CNTs) coated with Li-ion reactive layers (Si, Ge, C) were investigated. Due to the very high electrical and thermal conductivity of graphene and CNT and short diffusion path for Li ions within thin Ge and Si, the proposed anodes demonstrated exceptionally high power characteristics and low losses during operation.

For all anode architectures, the carbon substrate has been uniformly coated with high capacity materials through CVD. Thin film thickness of the high capacity coatings reduces stresses caused by the Li concentration gradient within the coating during the rapid Li insertion and extraction. Furthermore, the pore space between graphene sheets and individual CNTs provide the necessary volume for expansion of Li during insertion. This minimization of stresses allows one to prevent cracking within high capacity anodes to allow for a high degree of lithiation with minimal degradation to improve the cycling stability. As a result, the proposed anode architectures provided stable high capacity and longer battery cycle life and improved upon the shortcomings of some of the other particle and electrode architectures previously discussed. Although high capacity coatings

were examined, the design and approaches can be considered as a platform for the future application of other coatings that enables performance gains in a wide variety of applications ranging from energy storage to chemical sensors to photovoltaics.

Understanding the relationships between materials synthesis, structure, mechanical and physical properties, and the anode performance in batteries were developed through consideration of the following objectives:

Objective 1

Develop rational methods to synthesize the proposed anode architecture with controlled microstructure including anode thickness and thickness of deposited coatings.

Objective 2

Explore whether high capacity planar coatings on graphene sheets can be used to improve the cyclability of both the high capacity material and graphene.

Objective 3

Measure the effect of repeated lithiation/delithiation cycles on the mechanical strength of a carbon substrate coated with a high capacity material. Additionally, examine the effect of tensile preloading of the nanocomposite electrode prior to electrochemical cycling on the resultant stability and capacity.

Objective 4

Evaluate whether carbon substrates coated with a high capacity material possesses higher thermal and electrical conductivities than electrodes of similar composition but produced through conventional techniques.

Objective 5

Determine the stability of the SEI layer on Ge, Si, and C and its influence on the reversible and irreversible capacity and cell lifetime.

Objective 6

Investigate the effect of surface coatings (electrically conductive and non-conductive) on the stability of high capacity electrodes.

To meet these objectives, a series of characterization and performance tests were conducted on the anode material and the anode in *half cell* configurations, as described in the following chapters.

CHAPTER 4

TWO DIMENSIONAL GRAPHENE COMPOSITE ELECTRODES

4.1 Overview

The common shortcomings of graphene-based anodes include very high irreversible capacity losses at the first cycle, low CE in subsequent cycles and limited overall stability caused by the separation of graphene layers. These shortcomings make graphene unsuitable as a replacement to the current graphite anode technology. Composite electrodes consisting of graphene nanosheets and carbon nanotubes and/or fullerenes have shown to increase discharge capacity, but failed to improve its stability to industrially useful levels.[61]

Several studies analyzed the performance of graphene mixed with high capacity nanoparticles of Sn [162] or Si [163-164] using physical mixing or solution-based methods. In spite of the noticeable improvements over the pure graphene performance, these studies demonstrated several shortcomings. The high surface area led to very large irreversible capacity losses and low CE at the first (<73%) and the subsequent 30 cycles (80 – 94%). The anode stability was moderate with ~30% losses during the first 30 – 100 cycles. In the case of Sn, the capacity improvements were also moderate, ~500 mAh/g after 100 cycles[162], only a slight increase beyond theoretical capacity for graphite and less than the proposed theoretical capacity of graphene (744 mAh/g).

4.2 Approach

In contrast to prior work on graphene mixed with Si [163-164], an alternative method to synthesize porous nanosilicon- and graphene-containing nanocomposites was utilized. Vapor deposition methods employed in this synthesis allowed for reduction of the graphene specific surface area to limit the available surface for SEI formation.

The synthesis route and the developed architecture of three-dimensional porous particles composed of curved two-dimensional nano-sized layers provides unique benefits. The prior work on thin film batteries [130, 136, 165] showed that during Li insertion large area Si films mostly accommodate the volume changes via variation in thickness. Therefore, the changes in the external surface area during cycling can be minimized and, thus, stabilization of the SEI should be easier to achieve than in Si nanoparticles or nanowires, which experience very large external surface area changes during insertion/extraction of Li. Additionally, the high specific surface area of graphene allows for rapid Si deposition, which is important for practical applications. Finally, the tunable spacing between individual graphene layers permits for Si film depositions of various thicknesses and thus optimization of the composite for either high energy or high power applications. While only a Si-containing composite is demonstrated, the synthesis techniques are applicable for other high capacity materials that can be conformally coated on graphene.

4.3 Experimental Methods

Graphene was produced from natural graphite via a multi-step process by Argonne National Laboratory. First, a natural graphite powder (Sigma Aldrich, USA) was immersed in concentrated sulfuric acid (Sigma Aldrich, USA) for two hours. The product was dried and then subjected to thermal shock treatment at 1000 °C for 30 seconds to obtain exfoliated graphite worms. The graphene layers can be tuned by varying the exfoliation parameters. The exfoliated graphite worms were then dispersed in deionized water and subjected to extensive ultrasonication to break down the graphite flakes and separate the graphene sheets. The dried product, graphene oxide, was reduced at 800 °C in a H_2 stream for one hour to obtain the graphene powder.

Low-pressure decomposition of a high purity SiH_4 (5 wt. % in He balance; Airgas, USA) at 500 °C was utilized to deposit Si onto graphene. A thin layer of

amorphous carbon was then deposited on the Si coated graphene via atmospheric pressure decomposition of high purity propylene (C_3H_6, Airgas, USA) at 700 °C for 45 minutes in a custom-built hot wall furnace. The flow rate of the propylene was controlled at 20 sccm. The system was purged with Ar gas prior to heating to the deposition temperature and during system cooling. A mineral oil bubbler was placed in line with the gas exhaust. For both processes, samples were removed from the system (i.e. exposed to atmosphere) at room temperature. The produced composite contained ~60 wt. % Si. The Si and C contents were calculated via mass change measurements after the corresponding depositions and verified using thermogravimetric analysis (TGA).

The material morphology was examined by SEM (Hitachi 4700, Japan) and TEM (JEOL 100 CX, Japan). SEM images were taken using a 10 kV accelerating voltage and a 5 – 7 mm working distance. TEM studies were performed at an accelerating voltage of 100 kV. XRD (PANalytical X'Pert PRO Alpha-1, USA, Cu Kα source) and Raman spectroscopy (Horiba Jvon spectrometer, USA, 532 nm laser) were utilized for elemental and structural analysis. The XRD parameters were as follows: 45 kV accelerating voltage, 40 mA current, 0.033° 2θ-step size, and 120 second record time. Materials Data, Inc. Jade version 8 with ICDD PDF-4 database was utilized for analysis. For Raman spectroscopy, an exposure time of five seconds with a 0.6 filter, 400 μm hole, 100 μm slit and 600 grating was used. N_2 gas physisorption (Micromeritics TriStar II 3020, USA) at –196 °C allowed for the determination of the specific surface area of the initial and coated materials. Each sample was degassed in N_2 gas at 100 °C and 300 °C for at least 30 minutes and 8 hours, respectively, prior to the measurements. The Brunauer-Emmett-Teller method was used to calculate the surface area.

The carbon and silicon coated graphene electrodes were prepared from a water-based slurry containing PAA (15 wt. %) binder. After casting, the electrode was dried in a conventional oven at 70 °C for two hours and in a vacuum oven at 70 ^{o}C for 8 hours. Electrodes were spot-welded to the 2016-type coin cell and then assembled into half cells

with a Li foil counter electrode (battery grade; Alfa Aesar, USA) in an Ar filled glovebox (<1 ppm H_2O, O_2). A commercially blended electrolyte solution (Novolyte Technologies, USA) consisting of 1.0 M $LiPF_6$ in DMC:EC:DEC (1:1:1 by volume) carbonates with 8 wt. % VC was used. Charge/discharge cycling was performed on an Arbin SB2000 (Arbin Instruments, USA) between 10 mV and 1 V with a constant potential step at 10 mV to 20% of the initial current. The Coulombic efficiency was calculated by taking a ratio of the capacity after Li dealloying to the capacity after Li alloying. Differential capacity values for select cycles in the potential range of 0.0 to 1.2 V at a rate of 0.014 mV/s were also calculated.

4.4 Results and Discussion

Figure 34 shows the process flow for the formation of the nanocomposite powder. First, graphene is produced via exfoliation of natural graphite followed by ultrasonic shearing. While mechanical exfoliation produces graphene of very high quality, the process is not very scalable. Ultrasonic treatment allows scalable graphene production with significantly higher yield. Second, the produced graphene was uniformly coated with Si and C via the aforementioned methods, as determined by TEM and SEM observations. Carbon coating was deposited to reduce Si oxidation and improve anode stability.[10, 154, 157]

SEM and TEM images show the evolution of the composite material morphology (Figure 35). The deposited Si nanoparticles uniformly coat the smooth graphene sheets (Figure 35 a,b) forming a rough continuous surface (Figure 35 c,d). No crystallites were observed in the TEM images, indicating amorphous structure of Si. The carbon layer uniformly coats the Si surface reducing the surface roughness (Figure 35e). The produced composite particles (Figure 35f) retain the original 10 – 30 μm size of the graphene agglomerates.

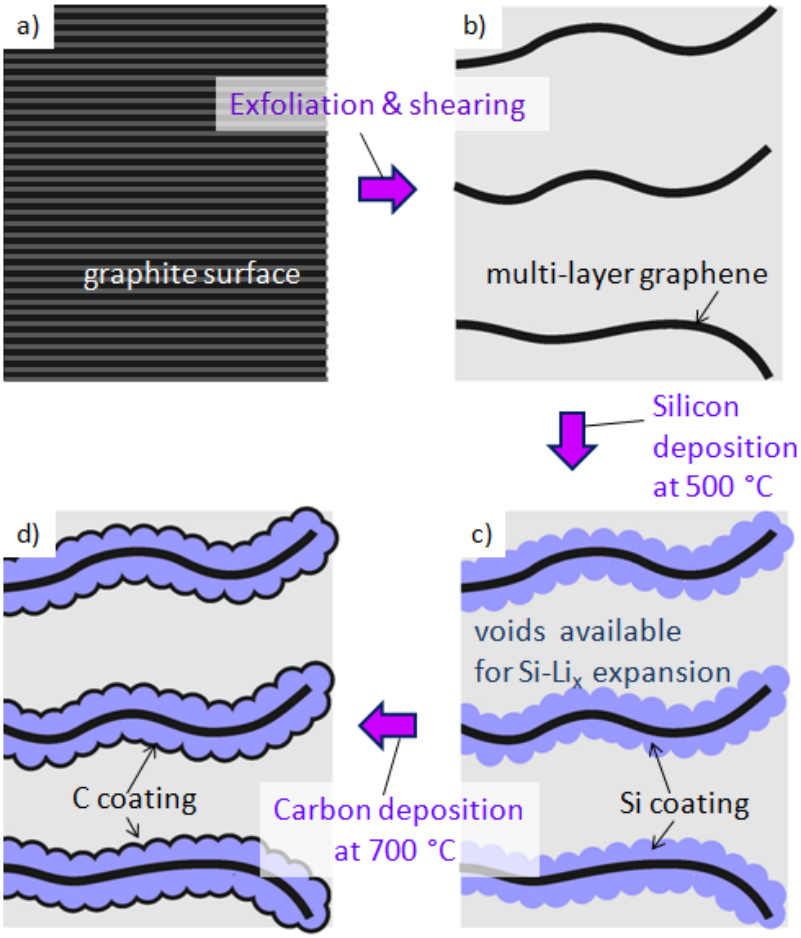

Figure 34. Schematic of C-Si-graphene composite formation: (a) natural graphite is transformed to (b) graphene and then (c) coated by Si nanoparticles and (d) a thin C layer.

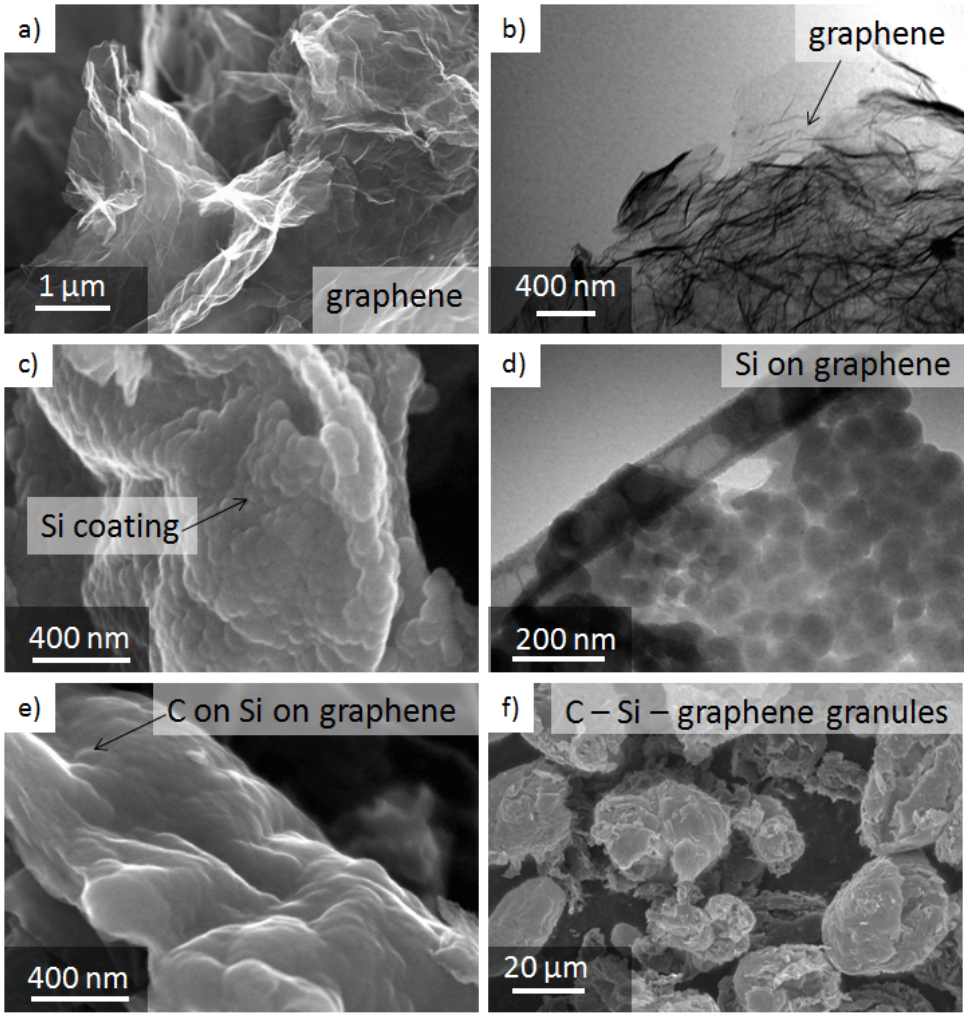

Figure 35. Structure of the graphene-Si materials. (a, c, e, f) SEM and (b, d) TEM micrographs of (a, b) graphene, (c, d) Si-coated graphene, and (e, f) graphene granules coated with Si and C.

Raman spectroscopy (Figure 36a) revealed the synthesized graphene to show nearly the same spectra as commercially available purified exfoliated graphite (PEG), suggesting that a large portion of the produced graphene has more than 5 layers.[166] Characteristic Raman peaks for carbon materials are the induced D band at ~1350 cm^{-1}, the graphitic G band at ~1580 cm^{-1}, the second order G' band (also known as the 2D band) at ~2700 cm^{-1} and D" (also known as the D+G band) at ~2900 cm^{-1}.[166-167] The large D peak and the small relative intensity of the 2D peak indicate a high concentration of defects, dangling bonds, and structural disorder present.[166, 168-169] These defects likely served as nucleation sites for Si nanoparticle deposition and allowed uniform coating formation (Figure 35). Raman spectroscopy verified the deposition of Si (~520 cm^{-1}). The lack of carbon peaks in the Si-coated sample (Figure 36a) indicates conformal Si deposition, supporting SEM and TEM measurements (Figure 35). The C deposition was confirmed by the reappearance of D and G peaks (Figure 36a). The small shift in the Si band suggests stresses caused by the difference in the thermal expansion of Si and C.

XRD studies (Figure 36b) provided additional information about the structural changes accompanying the synthesis steps. The XRD pattern of graphene showed weak graphite peaks ~26° and ~43°. Those peaks were suppressed after Si coating. The very broad Si peaks indicate amorphous structure of Si on the graphene surface. Carbon deposition at a higher temperature caused crystallization of Si, as evidenced by the formation of diffraction peaks (Figure 36b).

Analysis of the N_2 sorption isotherm of the produced graphene (Figure 36c) indicated its very high specific surface area (940 m^2/g) and the presence of micropores. The Si and C deposition eliminated the smallest pores and reduced the surface area of the produced composite to ~5 m^2/g.

First cycle electrochemical performance of the produced composite recorded at the low current density of 140 mA/g showed a high reversible discharge capacity of ~2300 mAh/g (1080 mAh/cm^2) (Figure 37a). This reversible capacity is over six times

greater than the theoretical capacity of graphite, indicating a high degree of Li alloying with Si. Increasing the current density to 1400 mA/g resulted in the reduction of the average specific reversible capacity to ~1060 mAh/g. Stability of the produced electrodes for 150 cycles (Figure 37a) is promising considering that the Li insertion capacity and the resulting Si expansion were not limited. Another positive attribute of the produced composite is the high CE (99.00 ± 1.96%, on average for all cycles), which is likely due to the low composite surface area (Figure 36c), planar Si geometry, and its good cycle stability.

The potentials at which Li (de-)alloying occur were identified through consideration of the differential capacity (Figure 37b). Broad lithiation peaks were observed at 0.08 and 0.22 V vs. Li/Li^+, consistent with our earlier studies on C-coated Si.[10] The Li was extracted from Si at 0.49 V. The peak height slightly increased after the second cycle, indicating improved cycling kinetics. Carbon delithiation occurs at potentials lower than Si and corresponding peaks are not evident in the differential capacity curves due to the significantly larger Li capacity of Si. Charge/discharge voltage profiles (Figure 37c) show transformations in the electrode during cycling. The shapes of the profiles are similar to the profiles previously reported in literature for other Si electrodes.[10] With increasing cycling number the Li extraction profiles become more horizontal and exhibit slightly smaller overpotential, suggesting a gradual improvement in the discharge kinetics.[170]

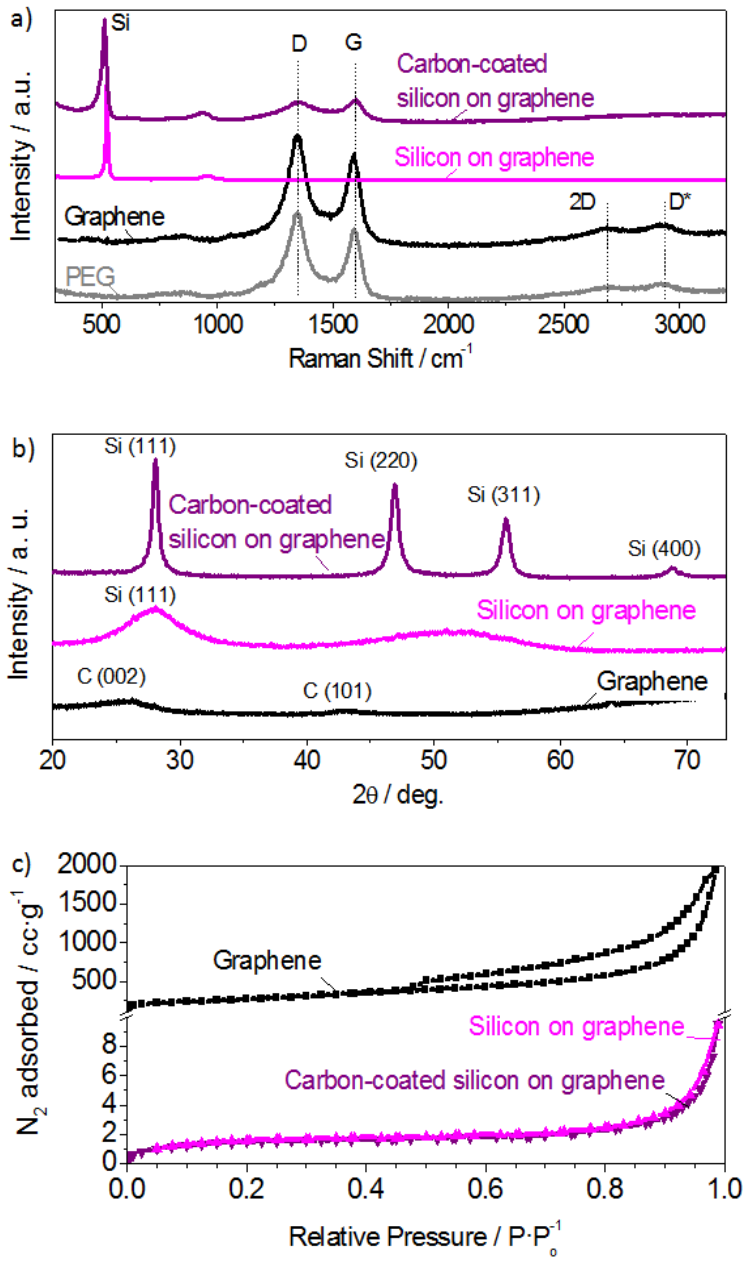

Figure 36. Characterization of the graphene and graphene-based materials by (a) Raman spectroscopy, (b) X-ray diffraction, and (c) N_2 physisorption.

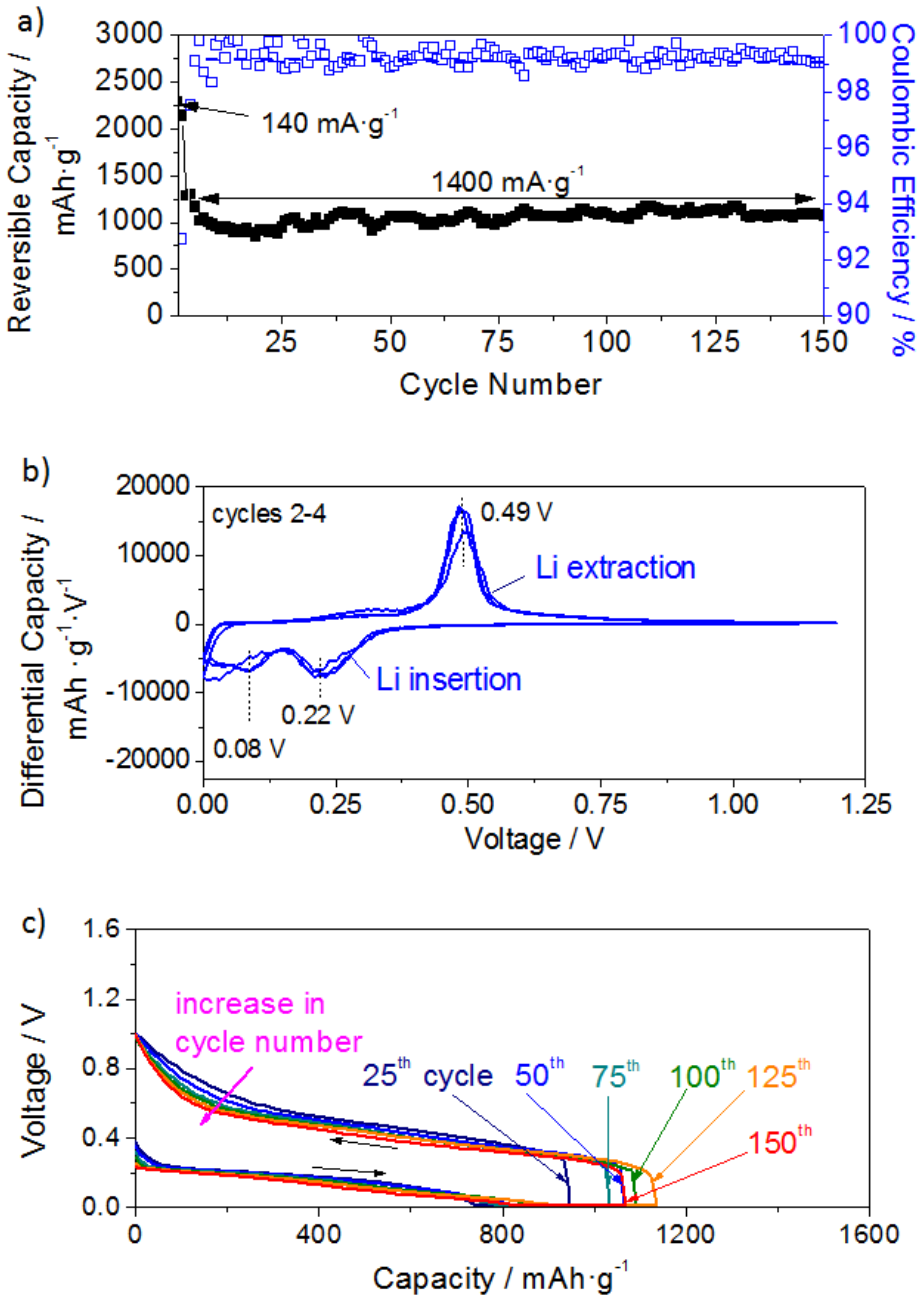

Figure 37. Electrochemical performance of the graphene-Si-C electrode: (a) capacity (per mass of the composite) and Coulombic efficiency as a function of cycle number at current densities of 140 mA/g and 1400 mA/g, (b) differential capacity plot, and (c) charge/discharge profiles for select cycles.

4.5 Conclusions

In summary, it was demonstrated that uniform Si and C coatings can be deposited on high surface area graphene via vapor decomposition routes. The produced Si and C-coated graphene granules exhibit specific surface area of ~5 m^2/g and an average size of ~25 μm. The anode composed of the nanocomposite particles exhibited specific capacity in excess of 2000 mAh/g at the current density of 140 mA/g and good stability for 150 cycles, significantly exceeding the theoretical capacity of graphite and graphene. The low surface area of the composite resulted in an average Coulombic efficiency of 99%. Although the calculated CE is significantly higher than has been reported for other graphene composite electrodes it is not yet sufficient for commercial applications (Section 8.2). Testing the produced composite material against a matching cathode would further reveal the stability and efficiencies of the electrochemical performance. The proposed architecture of 3D porous particles composed of curved two dimensional layers may provide unique benefits for a number of Li alloying materials. Further, the developed fabrication route is suitable to generate other high capacity composite electrodes.

CHAPTER 5

TWO DIMENSIONAL CARBON NANOTUBE COMPOSITE ELECTRODES

5.1 Overview

Multifunctional materials capable of providing an energy storage ability coupled with a load bearing ability are attractive for applications in which reducing the overall mass and volume of equipment is important such as unmanned or aerospace vehicles [171-174] and high performance equipment for commercial, professional, and military applications. Flexible Li-ion batteries with load bearing abilities could be attractive candidates for these applications due to their high energy and power densities. As a first step towards realization of such a battery design one needs to develop scalable synthesis routes to produce structural and flexible anodes and cathodes.

The traditional technique to fabricate electrodes requires mixing of the active particles with carbon conductive additives and a polymer binder and then casting of the mixture onto metal foil or mesh current collectors (Figure 38a). Due to numerous point contacts between the individual particles, the electrical and thermal conductivities of such traditional electrodes are quite limited.[175] The tensile strength of traditional electrodes is primarily dominated by the mechanical properties of the metal foil current collectors (Cu, Al) because the particles in the electrode are weakly bonded. Another disadvantage of traditional electrodes is the significant weight of the metal current collectors that further limits the gravimetric capacities of the battery cells. For example, while commercial graphites exhibit capacities in the range of 300 - 360 mAh/g and the weight of the binder and carbon additives is limited to only 10 - 15 wt. %, the effective capacities of Li-ion battery anodes is commonly less than 200 mAh/g if all the materials including heavy Cu foil are taken into account. Indeed, the weight of the Cu foil accounts for over 35% of the

total weight. If high capacity Li-alloying materials such as Si are used to improve the gravimetric energy density of Li-ion batteries [10, 14, 30, 150, 156, 175-183], then the relative weight of the Cu foil may account for up to 80 wt. %.

Various approaches to fabricate structural electrodes to enhance the mechanical properties have been reported in the literature. Following traditional electrode fabrication techniques, a previous study combined $LiCoO_2$ particles, carbon additives, and polymer binder into a slurry and measured a maximum tensile strength < 5 MPa, a value which may limit widespread applicability of this technique to provide structural support due to the low strength and low content of the polymer binder.[172] Sintered composite particle-based electrodes demonstrated increased strength (~90 MPa); however, the capacity retention over 10 cycles was very poor with only 85% of the theoretical capacity retained.[173] In addition, the sintered electrodes are not flexible which may limit some of their multifunctional applications.

Flexible electrodes comprised of graphene or CNTs offer excellent thermal, electrical, and mechanical properties.[184] Graphene paper electrodes have demonstrated very high tensile strength of up to 290 MPa; however, such electrodes suffer from poor cycling ability, very low first cycle CE of ~12%, and low reversible capacity of ~55 mAh/g, metrics much lower than traditional graphite electrodes.[94, 185] Insertion of electrolyte solvent molecules in between the individual graphene sheets and their decomposition may explain the observed rapid degradation.[52, 98, 182, 186] One may further expect that mechanical properties of such electrodes should also degrade dramatically after electrochemical cycling. Although tensile tests of individual MWCNTs have previously shown tensile strengths > 11 GPa [187], this value is several orders of magnitude higher than the tensile strengths observed for nonwoven CNT fabrics and CNT-polymer composites.[68, 188-190] Commonly reported methods of forming CNT fabrics or buckypapers rely on vacuum filtration of acid-treated CNTs [90, 190], impregnation with a polymer [189, 191], or the addition of surfactant [188] to form a fabric with limited size,

typically less than a few inches in diameter. In those approaches, the ability to produce continuous rolls of the CNT fabric/paper with good mechanical strength is very limited and the batch-to-batch variability makes large scale applications difficult. Furthermore, the insertion of electrolyte solvent molecules between the individual CNTs will likely result in high irreversible capacity losses and low CE at the first cycle combined with rapid degradation of such CNT electrodes if used as Li-ion battery anodes.

5.2 Approach

Here, a route to produce flexible anodes with significantly higher strength and specific capacity than state of the art is reported. According to the approach, a high-strength binder-free CNT–based electrically conductive non-woven fabric is produced and then coated with a uniform layer of a high capacity material (Figure 38) such as Si.

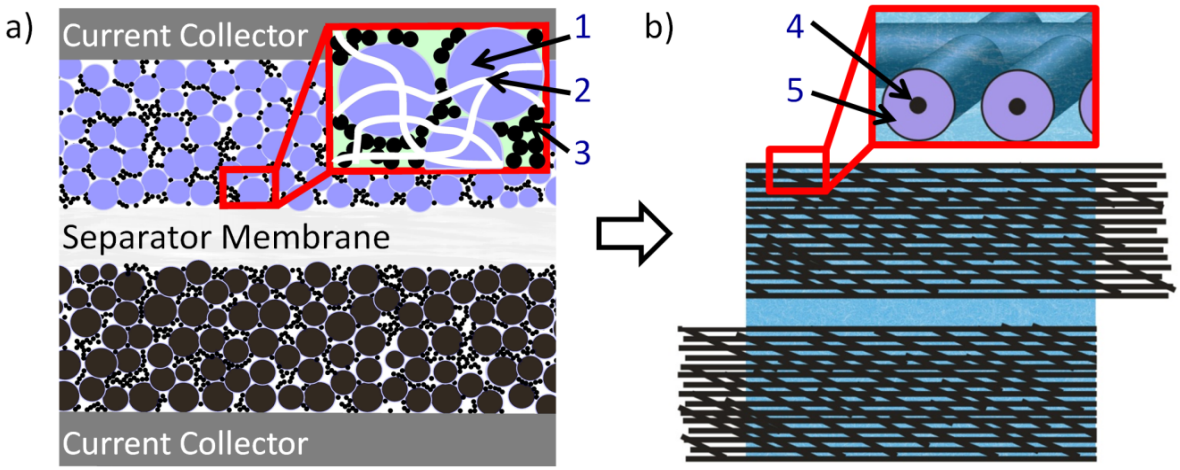

Figure 38. Schematics of an elementary Li-ion battery unit for (a) traditional and (b) proposed architectures. In a traditional architecture, the electrodes, composed of (1) active powders, (2) polymer binder, and (3) conductive carbon additives, are cast on metal current collector foils. In a proposed architecture, (4) the CNT fabric (5) coated with active material layers serves as lightweight multi-functional current collectors for both anodes and cathodes.

Deposition of an active material on a pre-formed fabric shall allow one to maintain the high electrical and thermal conductivities of the composite because of the elimination of the highly resistive particle-to-particle contacts.[175] In contrast to common CNT fabric assembly methods, a commercial-scale continuous CVD process was utilized. This method allows for the scalable production of multifunctional structural materials of various geometries. The deposited Si coating is impermeable to solvent molecules and protects the individual CNT-CNT junctions from failure during cycling. Furthermore, the amount of inserted Li ions was limited to prevent mechanical electrode degradation.

5.3 Experimental Methods

Carbon nanotube material was produced by floating catalyst CVD with ethanol as the primary carbon source. Ferrocene dissolved in the fuel served as the source for iron catalyst particles. Sulfur was added as a catalyst conditioner. The fuel mixture was injected into the furnace in the presence of hydrogen. The vaporized fuel mixture is taken through carefully controlled thermal gradients to produce a narrow distribution of the proper size catalyst particles and to crack the ethanol to create a carbon source for the nanotubes. Nanotube growth continues through the furnace. Upon exiting the furnace hot zone, the CNT material is collected onto a moving drum until the required dimensions are obtained. Afterwards the CNT sheet may be treated to enhance electrical and/or mechanical properties. Large-format CNT fabrics were produced through this proprietary method (Figure 39) by Nanocomp Technologies (USA).

The nonwoven CNT fabric was cut into strips (100 mm x 25 mm) and into rounds (12.7 mm diameter) for testing in Li-ion pouch and 2016-type coin cells, respectively. The CNT fabrics were then coated with Si via low pressure (600 mTorr) CVD of SiH_4 (5% in He balance; Airgas, USA) at 500 ^{o}C. The produced composite contained 47 ± 2 wt. % Si. The Si and C contents were calculated using mass change measurements on a balance with 0.01 mg accuracy after Si deposition.

Figure 39. Example of Nanocomp's large-format CNT fabric capability.

Micrographs of the material morphology and structure were taken by SEM (Hitachi S-4700, Japan). Images were taken with a 10 kV accelerating voltage and working distances of 5.6 – 8.0 mm. Energy-dispersive X-ray spectroscopy (EDS) mapping was performed at 20 kV. Raman spectroscopy (WITec Instruments Corp., Germany) was performed using a 785 nm laser, 50x objective, and 600 grating density with a 10 second integration time for 5 accumulations to identify chemical bonds associated with Si and C.

XPS surface characterization of the synthesized and annealed CNT fabrics was performed on a Thermo K-Alpha instrument (Thermo Scientific, USA) using Al Kα radiation. All tests were conducted under vacuum (< 10^{-8} Torr) with a 200 μm spot size and energy resolutions of 1 eV and 0.1 eV for the survey scans and the high resolution elemental scans, respectively. An electron flood gun was used to minimize surface charging. TGA analysis was performed on a TA Instruments Q50 (TA Instruments, USA) between room temperature and 800 ^{o}C at 5 ^{o}C/min in N_2 gas flow. All samples were dried in vacuum at 80 ^{o}C prior to TGA and XPS analysis.

Thermal conductivity was measured at room temperature using a Huskeflux THISYS (Huskeflux Thermal Sensors, Netherlands) calibrated to operate without glycerol. Pyrex, brass, and copper standards were utilized for system calibration.

The linear electrical resistivity was measured using a custom-built 4-point probe system in which a 5 cm x 1 cm sample is clamped across four metal strips. The outer probes applied a constant 1 mA current. The voltage was measured by the inner probes which were separated by 2.0 cm.

Electrochemical performance of the CNT fabric-based electrodes was evaluated in two-electrode cells. Prior to assembly in an Ar filled glove box (< 1 ppm H_2O, O_2; Innovative Technologies, USA), all electrodes were treated at 70 ^oC in vacuum overnight. All electrodes were tested in an electrolyte (Novolyte Technologies, USA) composed of 1M $LiPF_6$ dissolved in a mixture of carbonates DMC:EC:DEC (1:1:1 by volume) with 10 wt. % VC.

Cyclic voltammetry measurements were performed using a multi-channel potentiostat (Solartron Analytical, USA). The capacity was not limited in the cyclic voltammetry measurements. Charge/discharge testing was conducted on a multi-channel Arbin potentiostat (Arbin Instruments, USA). After testing, cells were dealloyed at 1 V until the current was less than 5% of the C/5 current. The electrodes were removed from the pouch cells and rinsed with anhydrous dimethyl carbonate (Sigma Aldrich, USA) to remove residual $LiPF_6$ salt.

Tensile test specimens were cut using a Hermes LS500XL CO_2 laser (GravoTech, Inc, USA) to form 100 mm x 5 mm CNT fabric rectangular strips and the edges were visually inspected for cracks. Thickness measurements were made using a micrometer to control for variations in the fabric thickness and provide accurate stress measurements. After cutting, the samples were mounted on disposable aluminum mounts to avoid damage during loading on the test frame providing a gauge length of 60 mm. Tensile test measurements were conducted on a MTS Insight 2 test frame (MTS Systems

Corporation, USA) using screw action vice grips with double serrated faces in accordance with ASTM D882 – 10 and using a MTS 100N load cell sampling at 45 Hz. The electrodes were loaded in uniaxial tension at a strain rate of 10 %/min until failure. Electrodes stressed prior to charge/discharge cycling were loaded at a constant 25 MPa.

Densities of the CNT fabrics were measured in accordance with ASTM C830 in which the samples are infiltrated with a liquid to calculate the bulk density of a porous sample. Deionized (DI) water was used for this study. According to the standard, three different weights are recorded: the dry weight M_D, the suspended weight M_S, and the saturated weight M_W. Test specimens were dried by heating at 70 °C in vacuum for over 2 hours. Following, the samples were weighed in air (not submerged in liquid) to determine M_D. Samples are sufficiently dry when the mass reaches a constant value after prolonged drying. The suspended weight is the weight of the sample after saturation in DI water. M_S was measured while suspended in liquid. The sample holder was a wire mesh basket and the balance was tared with the same amount of liquid depth as performed during the actual measurement. Care was taken to remove bubbles/micro-bubbles from the mesh basket before measurement. The saturated weight is the weight of the liquid saturated sample after light blotting measured in air (not submerged in the liquid). The samples were saturated using vacuum infiltration. Blotting was performed using lint free wipers to avoid excess surface liquid withdrawal. The bulk density B of the sample (g/cm^3) can then be calculated by:

$$B = \frac{M_D}{M_W - M_S} * \rho_{H2O} \tag{10}$$

where ρ_{H2O} is the density of the DI water.

5.4 Results and Discussion

The as-produced large format, flexible CNT fabric consists of randomly oriented MWCNTs as observed via SEM (Figure 40). A conformal layer of ~30 nm thick Si was deposited on individual CNTs throughout the fabric (Figure 40b) via the thermal decomposition of SiH_4. EDS mapping indicates a thin coating is uniformly deposited throughout the fabric (Figure 41). The CNT fabric retained its flexibility after Si deposition (Figure 40 c,d). Although the CNT fabric is relatively thin (~20 μm), the energy density and specific energy of the battery will not be significantly compromised due to the incorporation of high capacity Si and the absence of a metal current collector.

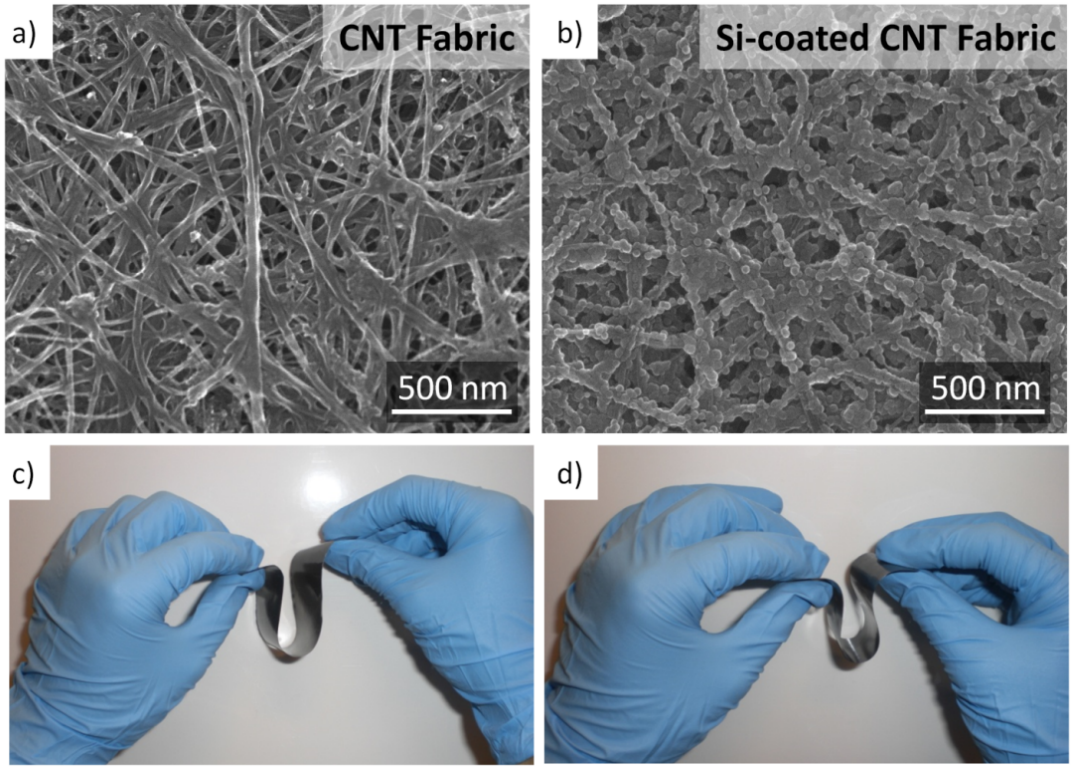

Figure 40. (a,b) SEM micrographs and (c,d) photographs of the CNT fabric (a,c) before and (b,d) after Si coating.

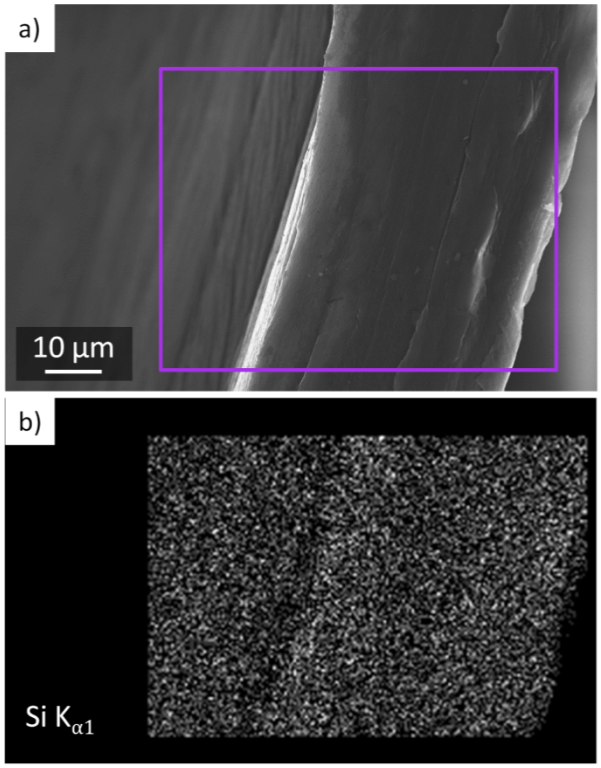

Figure 41. Cross-section of the Si-coated CNT fabric showing uniform Si deposition throughout the fabric: (a) SEM micrograph, (b) mapping of Si distribution in the selected area using EDS capability.

Raman spectroscopy was performed on the CNT fabric before and after Si coating (Figure 42). The initial CNT fabric exhibits two strong Raman peaks ~1320 cm^{-1} and ~1590 cm^{-1}, corresponding to the D band originating from disordered carbon and the G-band from graphitic carbon, respectively.[192-193] The low value of the ratio of the integrated intensities of the D and G bands, the I_D/I_G ratio, of 0.14, indicates a low defect density in the CNTs.[169, 192-193] The slight asymmetry of the G band is attributed to the D' band ~1620 cm^{-1} and is present in all sample types analyzed.[192] To reveal the effect of thermal annealing during Si deposition, the CNT fabric was annealed in Ar under temperature and pressure conditions replicating Si deposition but in the absence of SiH_4. The annealed CNT fabric was found to maintain a very low I_D/I_G value (0.18) indicating that significant changes to the microstructure due to thermal energy do not occur (Figure 42). After Si coating, a broad Raman band ~480 cm^{-1} associated with hydrogenated

amorphous Si emerges [194-195] and the I_D/I_G ratio significantly increases to 0.82. The increased concentration of defects in CNTs is attributed to the free hydrogen produced as a SiH_4 decomposition product which is known to induce surface defects in carbon at elevated temperatures. Some defects may additionally form at the interface between the CNT and the Si coating upon cooling to relieve stress at the interface due to differences in thermal expansion coefficients. Both of these effects would give rise to higher intensity of the D band.

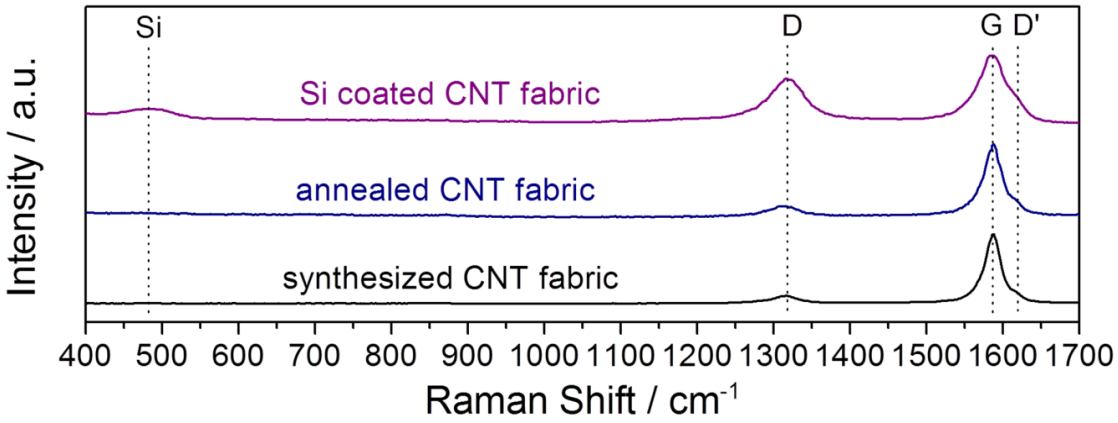

Figure 42. Raman spectra for the synthesized, annealed, and Si coated CNT fabric.

Electrochemical measurements of the CNT fabric-based electrodes were performed in both pouch and 2016-type coin cell configurations against a metallic Li foil counter electrode in the voltage range from 0.01 - 1 V vs. Li/Li^+ with a 500 mAh/g (985 mAh/g_{Si}, LiSi average composition) Li insertion capacity limit (Figure 43). The moderately high Li insertion capacity was selected as a compromise between high energy storage capability and good mechanical stability of the produced electrodes. Stable performance at C/5 was achieved for > 150 cycles, suggesting good integrity of the composite anode. An average dealloying capacity of 494 mAh/g, when normalized by the total mass of CNT and Si, and an average CE (for cycles 2 - 150) of 98.43 ± 2.15% was observed (Figure 43a, Figure 44). The measured capacity is over 2.5 times higher than that of commercial electrodes based on graphite-binder mixtures deposited on Cu foils.

The rate capability tests (Figure 45), however, showed very moderate performance at high current densities. These results suggest that in the current configuration the produced fabrics should primarily be used at medium-to-slow discharge rates.

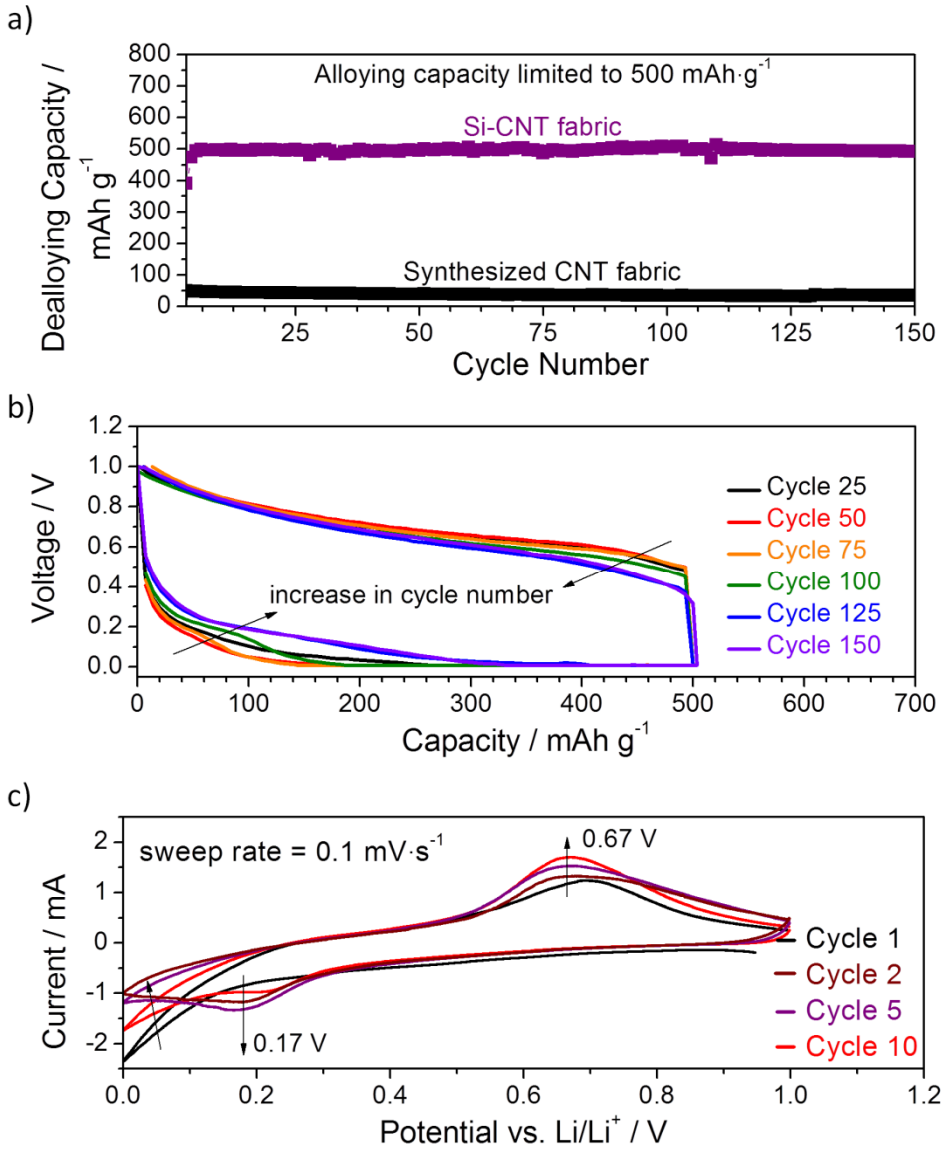

Figure 43. Electrochemical performance of Si-coated CNT fabric: (a) reversible de-alloying (Li extraction) capacity versus cycle number in comparison to the synthesized CNT fabric, (b) changes in the charge and discharge profiles with cycle number, and (c) cyclic voltammograms.

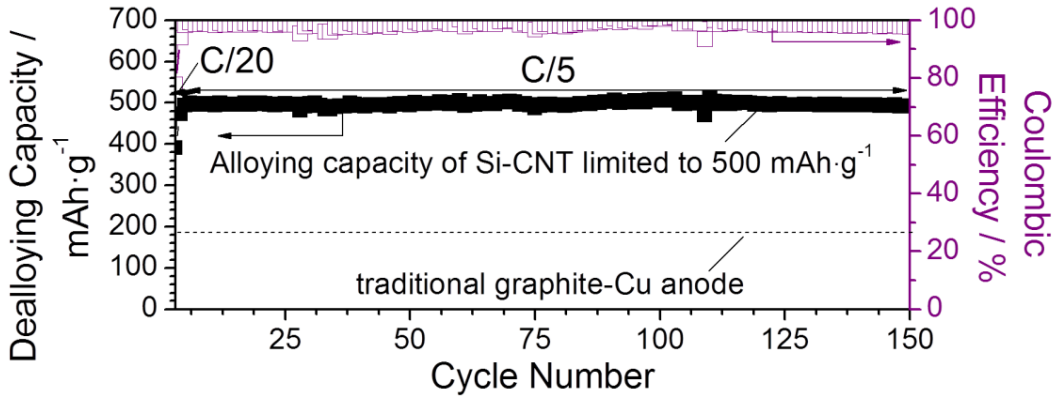

Figure 44. Reversible de-alloying (Li extraction) capacity and Coulombic efficiency versus cycle number for Si-coated CNT fabric.

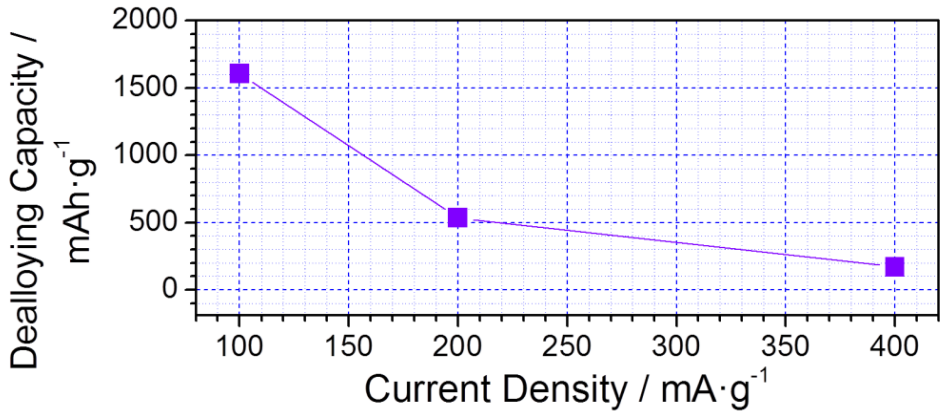

Figure 45. Capacity retention of the Si-coated CNT fabric electrode at increasing current densities.

Charge/discharge voltage profiles of the Si-coated CNT fabric (Figure 43b) show transformations in the electrode during cycling. With increased cycling (> 75 cycles), lower overpotentials were observed, indicating an improvement in cycling kinetics. Similarly, CV was performed to further examine the potentials at which Li (de-)alloying occurs (Figure 43c). A peak at 0.17 V and 0.67 V emerged during lithiation and delithiation, respectively. These values are consistent with previous nanoscale Si-based composite anodes and indicate a high degree of alloying with Si. CV does not show peaks corresponding to intercalation of Li into CNTs; however, they are likely masked due to the significantly larger Li capacity of Si since the capacity is not limited in CV experiments and the CNT fabric (without Si) can only offer limited capacity (< 10%)

(Figure 43a). CV performed at a slower scan rate showed a slight shift in peak potentials, thus indicating that kinetics are not yet optimized for this structure (Figure 46).

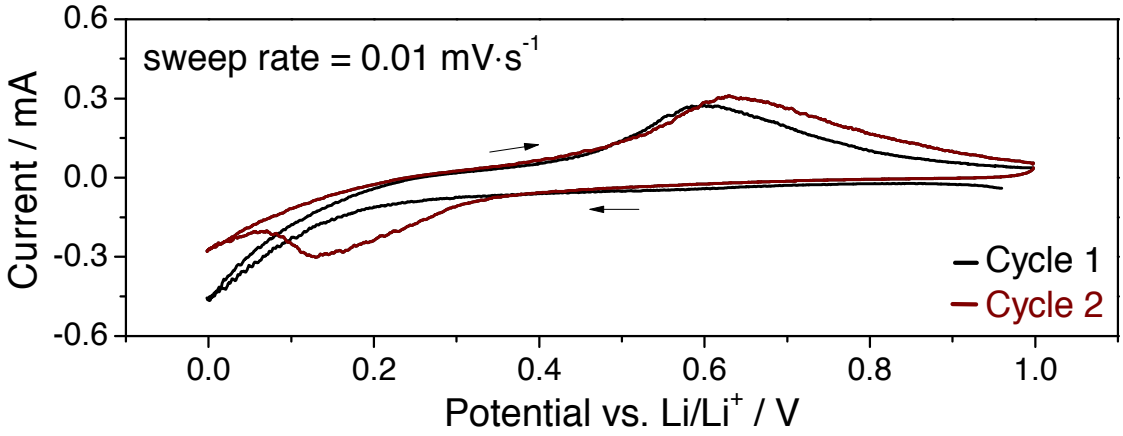

Figure 46. First two cycles of a cyclic voltammogram (scan rate of 0.01 mV/s) for Si-coated CNT fabric.

Uniaxial tensile test experiments were conducted on the CNT fabrics before and after battery cycling. The initial CNT fabric revealed very high maximum elongations of over 30% and UTS value in excess of 150 MPa, comparable to that of cast iron, copper and aluminum alloys [196] (Figure 47a) and up to 5 times higher than previously reported CNT sheets with [189-190] and without polymer [68, 188] throughout. It should be noted, however, that because of the limited porosity available within the produced fabrics for silicon expansion, cycling without insertion capacity limitation resulted in rapid mechanical and electrochemical degradation (Figure 48). Therefore, a balance between the utilized capacity and the desired mechanical properties shall be carefully considered when designing multifunctional electrodes for future applications.

As the Si deposition process subjects the electrodes to 500 ^{o}C it is important to study the impact of the heating process on the mechanical properties of the CNT fabric. Annealing the fabric at 500 ^{o}C in Ar reduces the maximum elongation to an average value of 6% and the UTS to ~90 MPa. Longer annealing time does not reduce the fabric

mechanical properties any further. 500 °C is sufficiently high to de-functionalize CNTs and possibly cause different pull-out behavior due to CNT re-alignment.

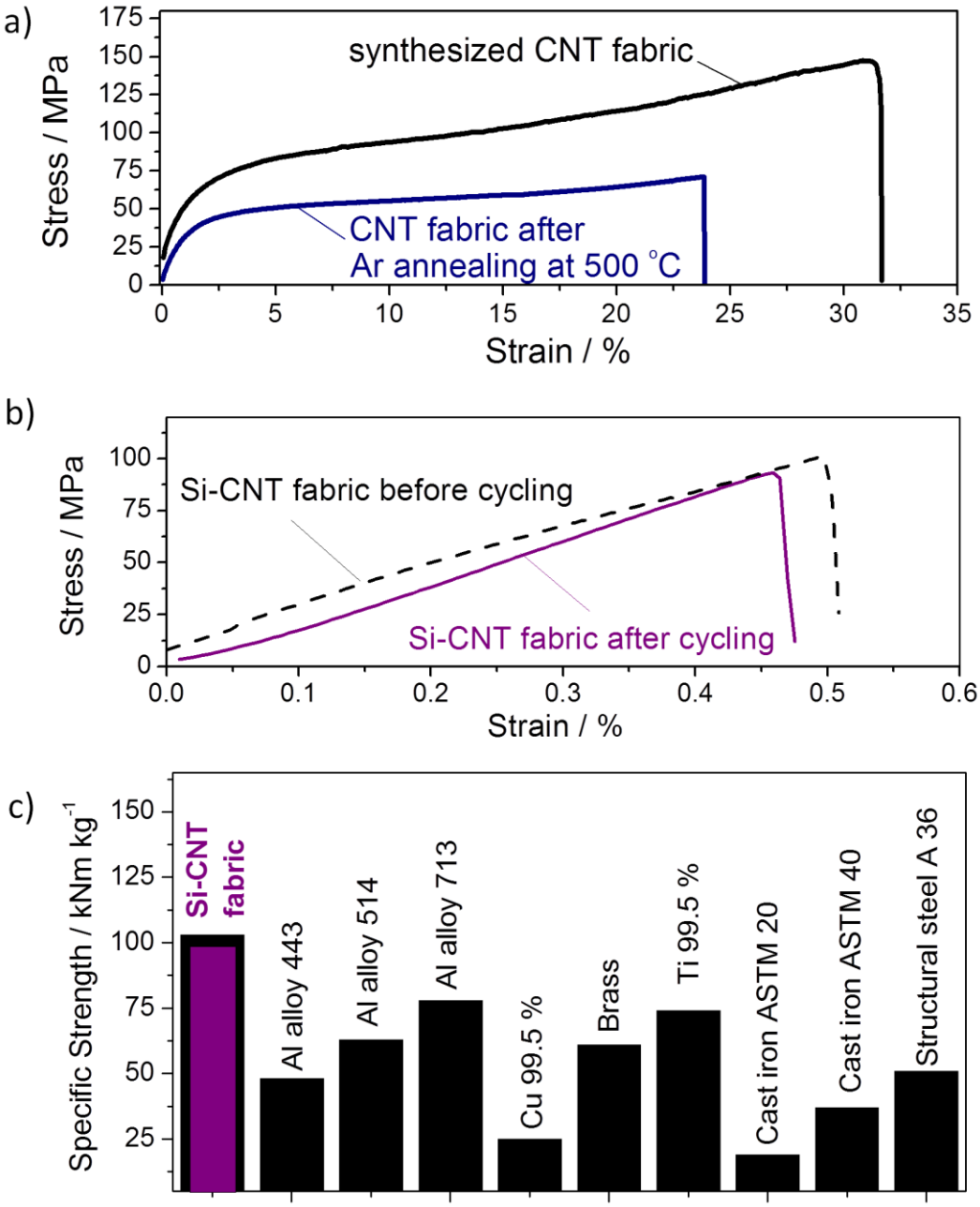

Figure 47. Mechanical characterization of the produced samples: (a) typical tensile tests on CNT fabric before and after annealing in Ar, (b) typical tensile tests on Si-coated CNT fabric before and after cycling, and (c) comparison of the specific strength of the multifunctional Si-coated CNT fabric with that of other common materials.

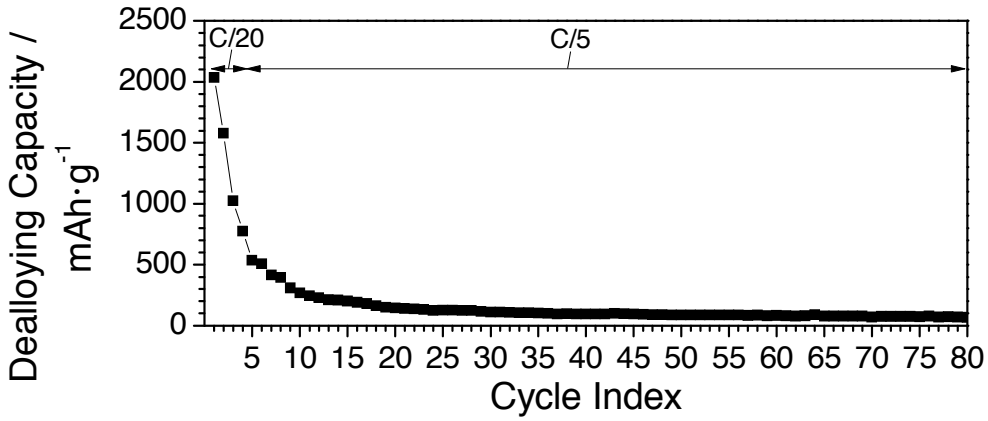

Figure 48. Electrochemical performance of Si-coated CNT fabric (with slightly higher wt. % Si than Figure 45) cycled at constant current without capacity limits.

TGA and XPS were performed on synthesized and annealed CNT fabrics to confirm removal of functional groups. Analysis of the TGA derivative curve (Figure 49) for the synthesized CNT fabric shows significant mass losses occurring at temperatures below 400 ^{o}C (that can be associated with de-functionalization[197]) and that are not seen in the annealed CNT fabric. This result is in good agreement with the XPS survey and high resolution scans that show dramatic reductions in the O1s and N1s spectra after annealing (Figure 50). Comparison of the O/C and N/C atomic % ratios before and after annealing reveal reductions from 0.094 to 0.009 and 0.001 to 0, respectively. Removing the functional groups from the CNT surface leaves behind defects which may reduce the axial strength of the individual tubes.[197] In addition, removing these functional groups reduces the van der Waals interactions between the tubes which lowers both the maximum elongation and the UTS of the CNT fabric.

Si deposition onto the CNT fabric has little effect on the UTS, but decreases its maximum elongation. While selected Si-coated CNT samples demonstrated UTS up to 150 MPa and maximum elongation up to 0.8%, the average values for the UTS and maximum elongations were ~ 100 MPa and 0.5%, respectively (Figure 47b). In the as-produced CNT fabric, the high maximum strain (Figure 47a) and the resultant high fracture toughness was achieved by the energy dissipation during continuous sliding of

the van der Waals bonded individual tubes relatively to each other. Due to the covalent nature of the atomic bonds in Si and its resultant brittle behavior, formation of continuous amorphous Si coating on the internal surface of the CNT fabric could be expected to significantly reduce its ductility. But, the experimentally measured composite fabric ductility and the UTS (Figure 47) were relatively high. Indeed, the non-uniformities observed within amorphous Si coatings (Figure 41b) and the pores within the Si-CNT fabric should act as pre-existing cracks, lowering both the ultimate strength and the maximum elongation achievable in such a composite. SEM studies of the fracture surface (Figure 51) revealed that the high UTS of the Si-CNT fabrics could be attributed to realignment and the pull-out behavior of CNTs. The fracture edge of the Si-CNT fabric specimens has a clear transition from the randomly oriented CNT fabric to highly aligned CNTs (Figure 51a, b). It is expected that the degree of plastic deformation of the composite fabric could be greatly increased by using active materials having higher ductility than Si (such as Sn or Mg). It is further hypothesized that the reduction of the deposition temperature could favor achieving better mechanical properties (Figure 47a).

Despite volumetric changes of Si during insertion and extraction of Li [7, 124], the mechanical properties of the Si-CNT fabric did not degrade significantly after cycling (Figure 47b), thus demonstrating multifunctional properties of the synthesized fabric. Both the UTS and maximum elongation was reduced by only ~10% after 150 cycles. The cycled Si-CNT fabric electrodes demonstrated similar pull-out behavior (Figure 51 c, d). The retention of the fabric's mechanical properties could be a result of limiting the extent of Li insertion into the individual tubes (Figure 43 b,c).

To further demonstrate the robustness of the Si-CNT fabric, the samples were statically loaded at 25 MPa prior to electrochemical testing. The pre-stressed Si-CNT fabrics also demonstrate good cycling stability with an average dealloying capacity ~480 mAh/g and good cycle stability (Figure 52).

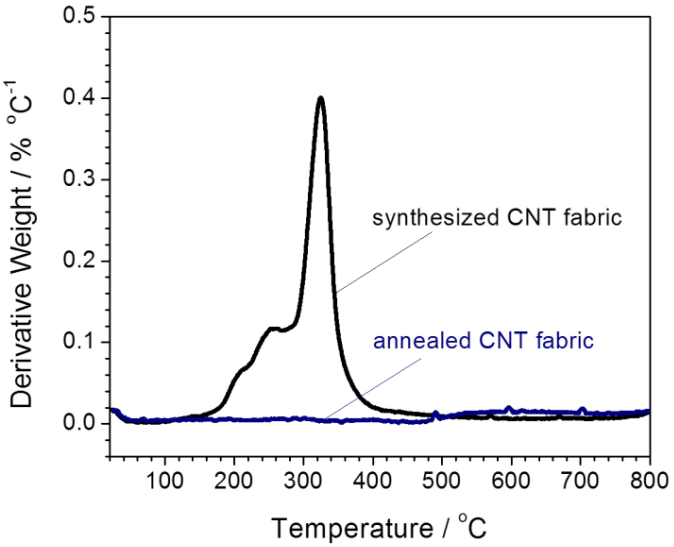

Figure 49. Derivative weight loss curves obtained from TGA of the synthesized and annealed CNT fabrics.

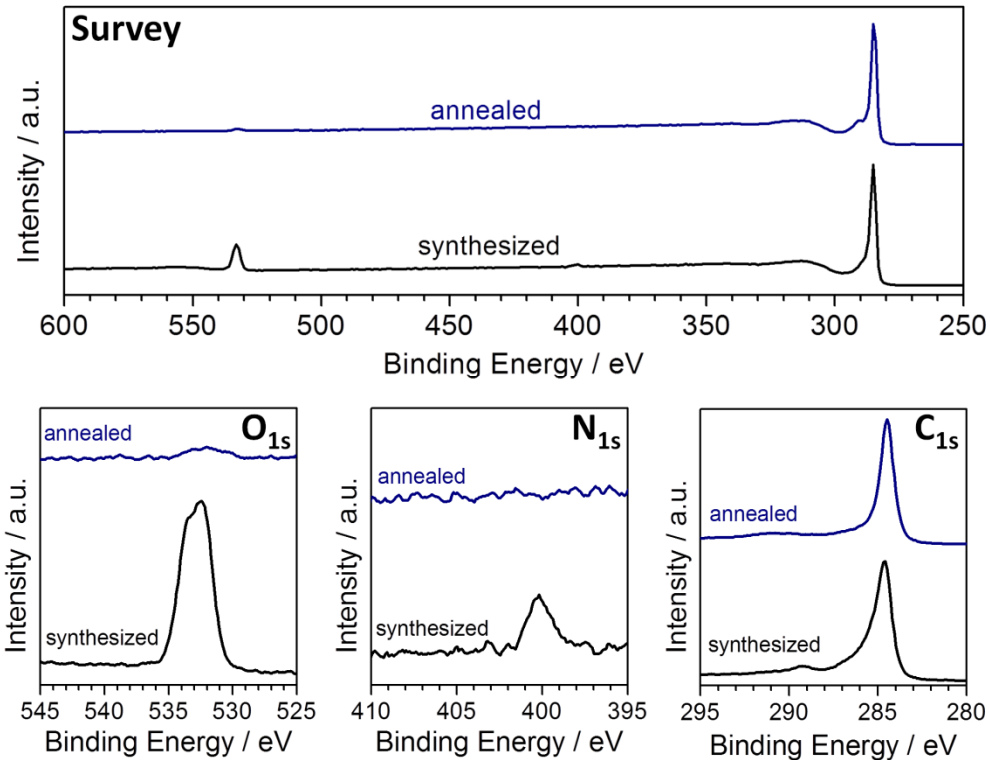

Figure 50. XPS spectra of the CNT fabric before and after annealing.

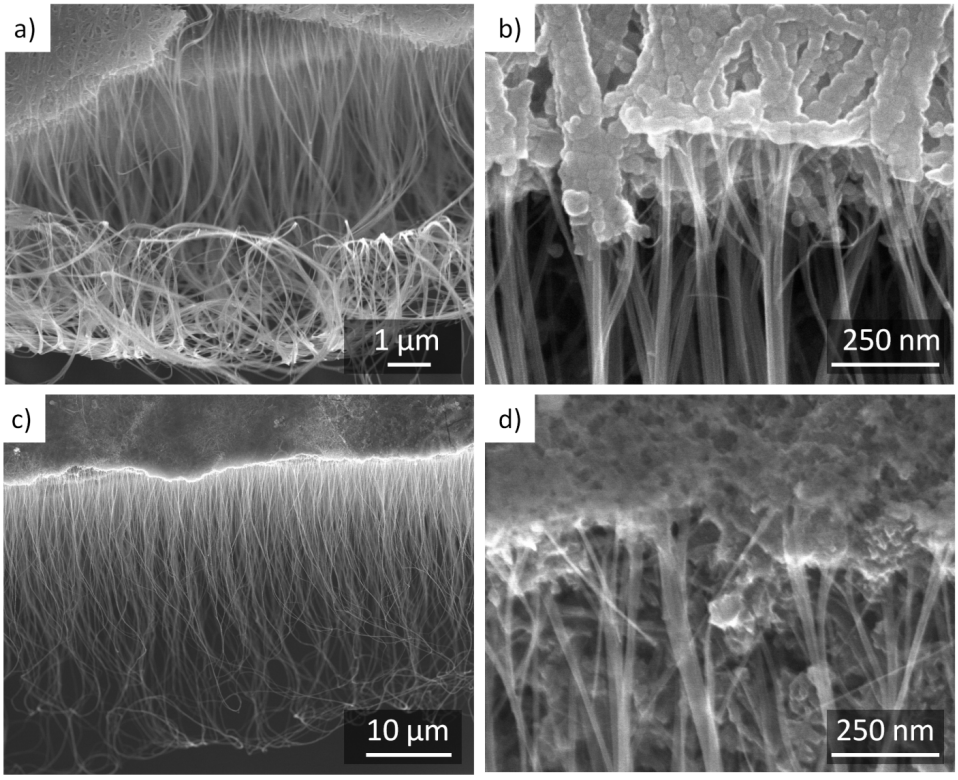

Figure 51. SEM micrographs of the fracture surface of the Si-coated CNT fabric edge after tensile measurements (a, b) before and (c, d) after electrochemical testing.

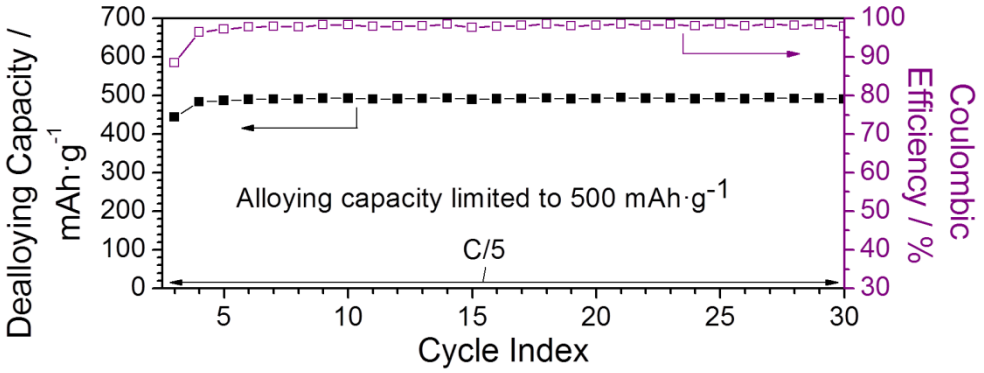

Figure 52. Reversible de-alloying (Li extraction) capacity and Coulombic efficiency versus cycle number for a Si-CNT fabric electrode intentionally bent and pre-stressed to 25 MPa.

High values of the achieved UTS combined with the low density of Si and C favors the use of the multifunctional Si-CNT fabrics in applications where high specific capacity (Table 1) and specific strength is desired. Indeed, the specific strength of the synthesized electrodes exceed that of both Cu and Al, conventional current collectors for anodes and cathodes, respectively (Figure 47c). It further exceeds the specific strength of multiple Al alloys, Ti, cast iron, and even selected types of structural steel (Figure 47c).

Table 1. Areal and volumetric capacities for CNT fabric based electrodes tested with a 500 mAh/g alloying limit.

	Areal Capacity	**Volumetric Capacity**	**Density**
	mAh/cm^2	mAh/cm^3	g/cm^3
CNT fabric	0.09	38	1.0
Si-coated CNT fabric	1.16	642	1.3

Localized thermal and electrical gradients have been demonstrated to cause unbalanced charging and discharging which leads to premature aging of the battery.[198-199] In a traditional powder based electrode, heat flows through the electrode to the current collector in the cross-plane direction.[200] For applications in which the current collector is removed, high in-plane thermal and electrical conductivities of the active material become critically important. Thus the in-plane thermal and electrical conductivities for the CNT fabric before and after Si coating were measured (Table 2). In comparison to traditional powder based electrodes based on Si nanopowder or graphite [175, 200-201], the thermal and electrical conductivities of CNT fabric based electrodes show a 1 – 2 order of magnitude improvement in thermal conductivity and up to 5 orders of magnitude reduction in electrical resistivity.

Table 2. Electrical resistivity and thermal conductivity of the CNT fabric before and after Si coating compared to values found in literature.[175, 200, 202]

	$\boldsymbol{\rho}$ 1×10^{-3} Ω·cm	$\boldsymbol{K}$ W/m·K
CNT fabric	1.17 ± 0.11	29.72 ± 3.59
Si-coated CNT fabric	2.93 ± 0.34	17.59 ± 2.32
Compressed Si nanopowder electrode	327,500 ± 22,000	0.40
Graphite electrode	5.0	1.04

Li-ion cells experience variations in temperature as a result of charge/discharge cycling and their environment. Although values of electrical and thermal conductivity are dependent upon temperature, the variations in cell temperature are not expected to dramatically affect the current collector performance as the variations in thermal and electrical conductivity are less than an order in magnitude over a broad operating temperature range (-20 to 50 ºC).[184, 203-205] Thus, the following considerations of the practicality of a CNT fabric current collector assume constant thermal and electrical conductivities.

The CNT fabric demonstrates moderately higher electrical and thermal conductivities than Si and graphite electrodes but lower than that of Cu. Using the conductivities, the minimum current collector thickness was calculated for cells of a broad range of sizes tested at multiple C-rates to evaluate the practicality of a CNT fabric current collector.

The minimum current collector thickness ($t_{CC,e}$, cm) necessary to limit the potential drop across the current collector tab to a maximum value (V_{max}, V) can be calculated by:

$$t_{CC,e} = \frac{\rho \, l_{tab} A_{CC} C_A R_C}{1000 V_{max} w_{tab}} \tag{11}$$

where ρ is the resistivity of the current collector (Ω·cm), l_{tab} is the length of the current collector tab (cm), A_{CC} is the current collector area (cm^2), C_A is the areal capacity loading (mAh/cm^2), R_C is the coefficient of the C-rate (e.g. a 10C rate would have R_C = 10), and w_{tab} is the width of the current collector tab (cm). The calculation assumes that the highest current will be at the current collector tab and calculates the minimum current collector tab thickness to achieve a potential drop equal to V_{max}. From the minimum thickness, the total mass of material for the entire current collector can be calculated using the density of each material. As a sample calculation, the following parameters were selected: l_{tab}= 1 cm, C_A = 3 mAh/cm^2, V_{max} = 0.1 V, w_{tab} = 0.2 cm, and R_C of 1 and 10.

From Figure 53 and Figure 54 it can be seen that the minimum CNT fabric thickness is always greater than for a Cu foil due to the lower electrical resistivity of Cu. However, much thicker Cu foils than the minimum value are used for practical purposes as Cu foils at least 10 μm thick are used. Further, the total electrode thickness includes both the thickness of the current collector and the active materials. For a traditional electrode cast on Cu foil, the total thickness may be at least 100 μm, if only one side of the current collector is coated. In contrast, a CNT fabric allows for the deposition of active material within it. Increases in thickness (up to 50%) due to material deposition within the pore should not be problematic for small total current collector area when tested at moderate C-rates. For example, a 20 μm thick Cu foil will have approximately the same mass as a 200 μm CNT fabric. However, at higher C-rates, the disparity between the conductive properties of the materials becomes more apparent and significantly thicker current collectors are required. This finding and the poor measured high rate capability (Figure 45) suggest that only low to moderate C-rates should be used for CNT fabric current collectors.

Similarly, the minimum thickness for the current collector ($t_{CC,t}$) was analyzed using the thermal conductivities (K_{CC}) and can be generally written as:

$$t_{CC,t} = \frac{w_{tab} V_{max} A_{CC} C_A R_C}{1000 T_{max} K_{CC} l_{tab}} \quad (12)$$

where T_{max} is the maximum allowable temperature difference (K) across the current collector tab. In this model, the heat is conducted through one of the long-edges (l_{tab}) of the current collector tab such that a thermal gradient would be produced along the width (w_{tab}). It is assumed that the long-edge is in contact with ambient air which acts as a heat sink such that the edge will equilibrate to room temperature. As a sample calculation, the following parameters were selected: l_{tab}= 1 cm, C_A = 3 mAh/cm^2, V_{max} = 0.1 V, w_{tab} = 0.2 cm, and R_C of 1 and 10. T_{max} was defined as 5 K across the width of the tab.

From Figure 55 and Figure 56, it can be seen that the minimum CNT fabric thickness is always greater than for a Cu foil due to the lower thermal conductivity of the CNT fabric. However, the Cu foil thickness is thinner than the minimum thickness necessary for practical purposes. Again, recall that the nearly 9x higher density of Cu allows for thicker CNT fabrics with equal mass. In addition, the overall thickness of the current collector and active material will increase more for the Cu foil current collector than the CNT fabric, due to casting of the active material on top of the Cu foil. However, the order of magnitude difference in thermal conductivity necessitates thicker current collectors which become impractical at higher current collector areas and higher C-rates. These calculations further confirm that the CNT fabric is better suited for small cells at low to moderate C-rates.

5.5 Conclusions

In summary, this work demonstrated that fabrication of CNT fabric coated with active (Li-ion hosting) materials for use as electrodes in multifunctional Li-ion batteries with high mechanical strength, flexibility, conductivities, and capacity coupled with good cycle stability can be achieved. The investigated example of Si-CNT fabric fabricated via

vapor deposition routes demonstrated 2.5 times higher specific capacity than state of the art anodes and stable electrochemical performance for >150 cycles with the capability to retain over 90% of its original strength after cycling. The lightweight, good structural stability, and high electrical and thermal conductivities of CNTs may allow CNT fabrics to serve as a platform for novel flexible batteries with enhanced properties and functionalities. It is expected that future studies with other active material coatings and deposition methods may allow further optimization of their performance and achieve even better mechanical and electrochemical properties of the flexible CNT-based electrodes, contributing to the development of high power, flexible and structural batteries.

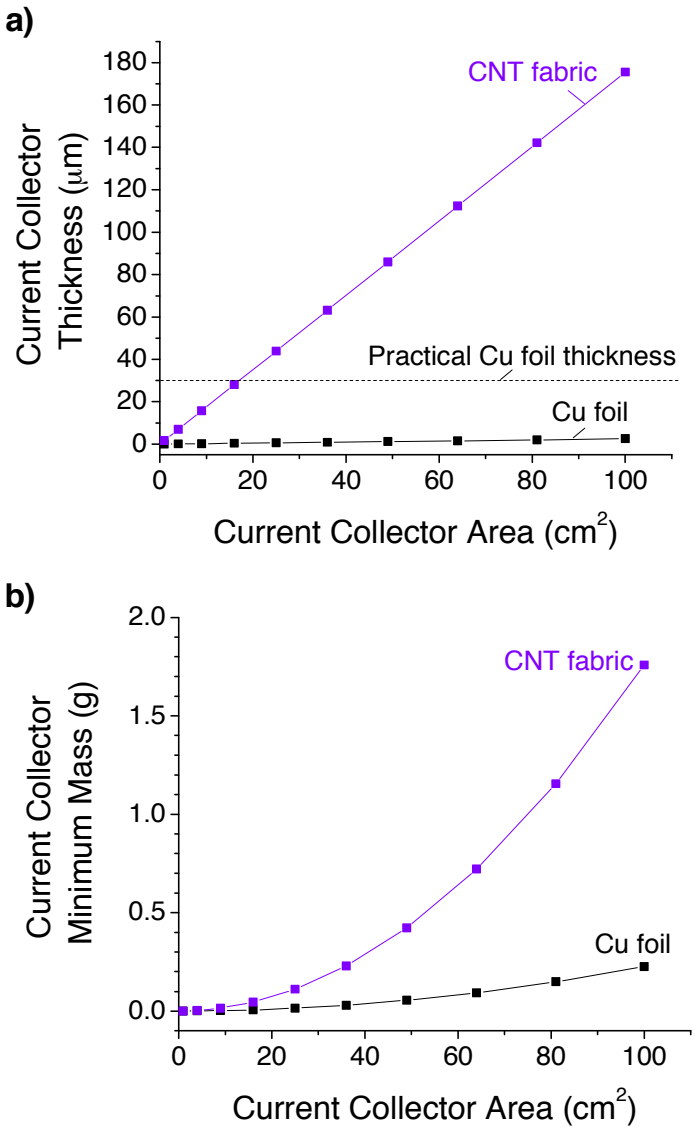

Figure 53. Assuming a maximum allowable potential drop of 0.1 V across the current collector tab at a rate of "1C" for a 3 mAh/cm^2 electrode, the minimum current collector (a) thickness and (b) corresponding mass can be calculated.

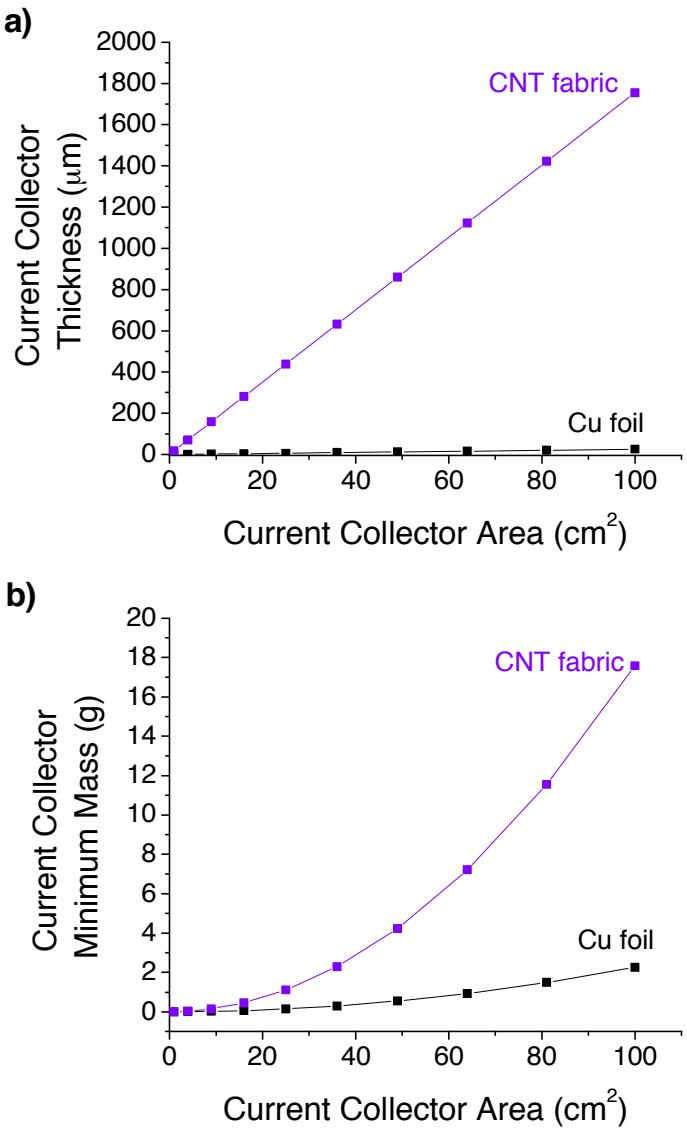

Figure 54. Assuming a maximum allowable potential drop of 0.1 V across the current collector tab at a rate of "10C" for a 3 mAh/cm^2 electrode, the minimum current collector (a) thickness and (b) corresponding mass can be calculated.

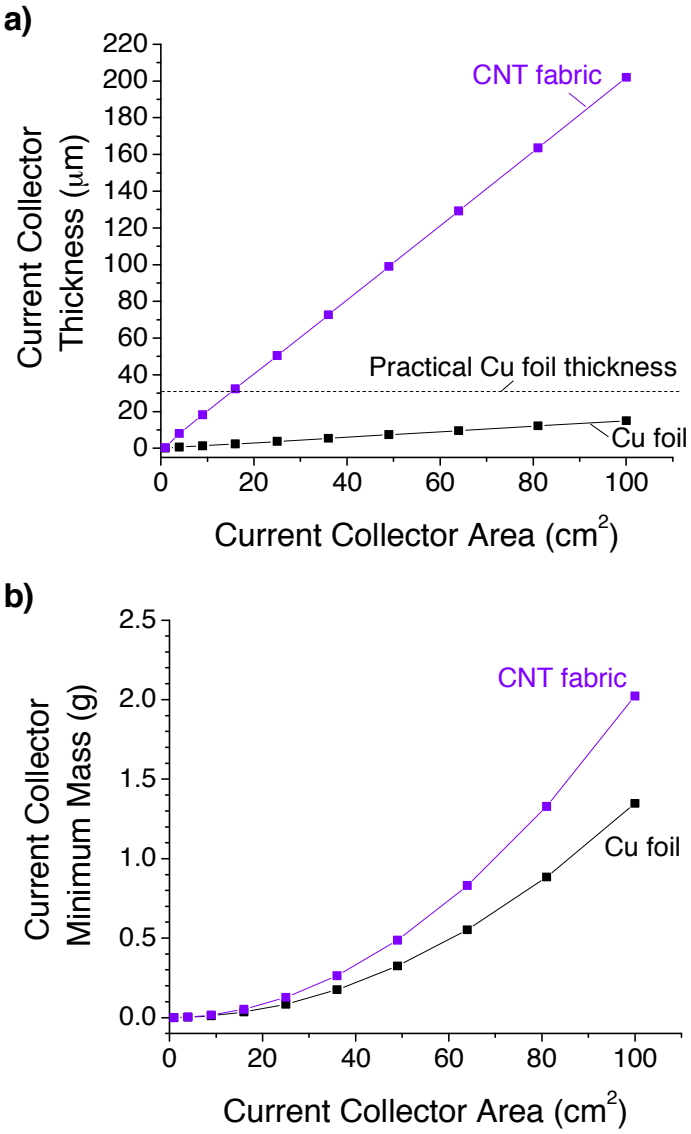

Figure 55. Assuming a maximum allowable potential drop of 0.1 V and temperature gradient of 5 K across the current collector tab at a rate of "1C" for a 3 mAh/cm^2 electrode, the minimum current collector (a) thickness and (b) corresponding mass can be calculated.

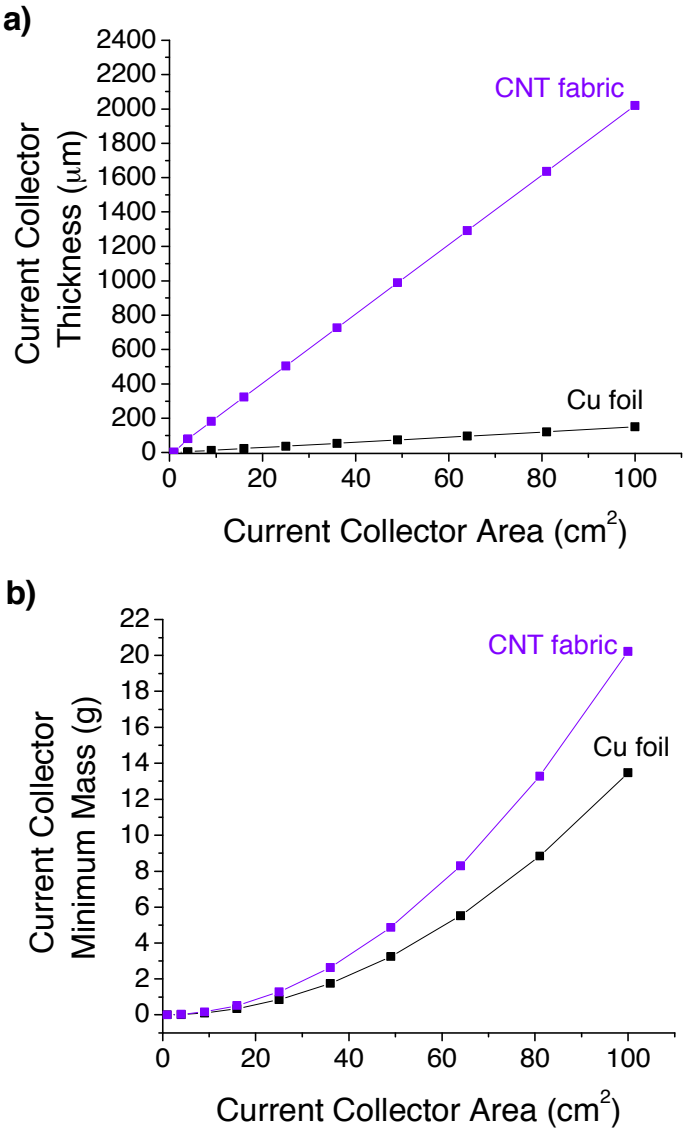

Figure 56. Assuming a maximum allowable potential drop of 0.1 V and temperature gradient of 5 K across the current collector tab at a rate of "10C" for a 3 mAh/cm^2 electrode, the minimum current collector (a) thickness and (b) corresponding mass can be calculated.

CHAPTER 6

THREE DIMENSIONAL CARBON NANOTUBE COMPOSITE ELECTRODES

6.1 Overview

Increasing the specific capacity of battery electrodes and minimizing the relative weight and volume of inactive components (separators and metal foils)[206] by increasing the thickness of electrodes from the currently used 50–100 μm to hundreds of micrometers and above are attractive and complimentary routes to achieve higher energy density of Li-ion batteries.

Conventional electrodes contain active material mixed with conductive additives and a polymer binder. They commonly suffer from poor control over the resulting porosity, tortuous electrolyte diffusion paths, , inhomogeneity [207] and high electrical and high thermal resistance caused by point contacts between individual particles. These issues become particularly critical for nanopowder or thicker electrodes. Other challenges that need to be overcome for increasing the electrode thickness include formation of cracks within electrodes during the slurry drying process caused by slow and uneven solvent evaporation throughout the thick layer, poor adhesion between the thick electrodes and metal current collectors, and the brittle behavior of thick electrodes. As a result, the overall progress on the development of thick electrodes has been limited.[207]

Several interesting routes have been reported to decrease the electrode resistance by changing the current collector or electrode architecture. For example, the three-dimensional battery architecture [208-211] overcomes most of the limitations of the conventional technology, but its applications may likely be limited to microbatteries. Electrodeposited Cu or Al nanorods/nanowires have been successfully used as conductive supports for anodes [212-213] and cathodes [211]. The use of vapor-deposited nanowires[14] have

also shown potential for reduced electrode resistance and improved stability. However, the relatively high cost of these processes and slow nanowire growth rates impose some limitations on these technologies for thick electrode formation. Highly conductive vertically aligned carbon nanorods and C-Si nanotubes produced by pyrolysis of photoresist [214] and template-assisted vapor depositions [154], respectively, have shown promising electrochemical behavior. However, the overall electrode thickness and the cost of the proposed process could similarly be a limiting factor for large size battery applications.

6.2 Approach

Here, an alternative scalable method to produce ultra-thick, yet highly conductive and stable, Li-ion battery electrodes using VACNTs uniformly coated with a vapor-deposited active material layer was pursued (Figure 57) The recent developments in the rapid growth of VACNTs [70, 215] allow low-cost formation of 1 mm or longer highly conductive tubes within minutes. The vapor deposition of anode (e.g. Si) [154] and cathode (e.g., LiV_2O_5) [216] materials may allow for the formation of uniform coatings on the CNT surface. The proposed architecture may offer unique benefits for the scalable formation of ultra-thick electrodes, such as: 1) straight and aligned pores for rapid ion transport, 2) high thermal and electrical conductivity for high stability and long cycle life, 3) high structure uniformity combined with precise control over the dimensions of individual coated CNTs for predictable and reproducible performance, 4) a very smooth electrode surface which allows for thinner separators, 5) control over the electrode porosity achieved by electrode compression for the optimization of volumetric capacity and power characteristics, and 6) the absence of binder giving rise to improvements to the specific capacity and power performance.

Further, the nano-dimensions of the Li–Si alloy coating minimize mechanical stresses.[9, 130] In addition, the pores remaining within the VACNT electrode are needed for

Si expansion during Li insertion. In contrast to a prior work on short VACNT-coated electrode[217], enhanced stability was demonstrated.

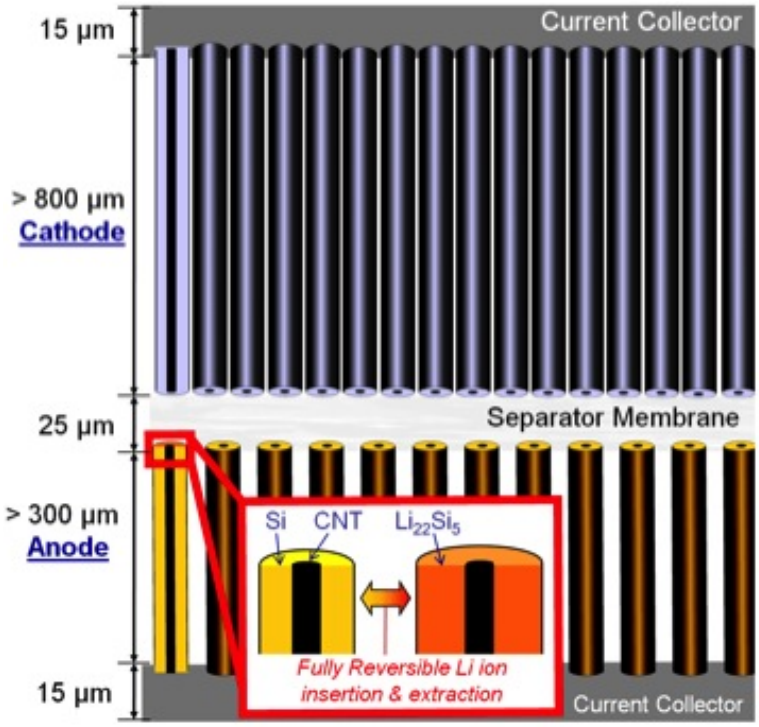

Figure 57. Schematic illustrating the use of long, individually coated VACNT for both the cathode and the anode.

6.3 Experimental Methods

For growth of VACNT on quartz substrates, a procedure similar to Ref. 215 was employed. In this custom-built low-pressure CVD method, no catalyst pre-deposition on substrates is necessary. Here, iron (II) chloride powder, placed inside the quartz tube at ambient conditions is vaporized during heating to 820 °C. During heating, the iron (II) chloride deposited on all surfaces acts as nucleation sites for VACNT growth. The gas-feed for growth was 200 sccm acetylene. With a growth rate ~0.1 mm/min, this system is capable of quickly producing long VACNTs. The length of the VACNT was tuned by adjusting the time of acetylene gas exposure.

Silicon was deposited at 500 ^{o}C in a temperature-controlled custom-built hot wall furnace using low pressure (~500 mTorr) CVD of silane gas diluted to 5% in He (Airgas, USA). The flow rate of the SiH_4 mixture was controlled at 50 sccm. The system was purged with Ar gas prior to heating to the deposition temperature and during system cooling. Samples were removed from the system (i.e. exposed to atmosphere) at room temperature to minimize oxidation of the deposited silicon.

Carbon was deposited by the atmospheric decomposition of propylene at 700 ^{o}C in a temperature-controlled custom-built hot wall furnace. The flow rate of the propylene was controlled at 20 sccm. The system was purged with Ar gas prior to heating to the deposition temperature and during system cooling. A mineral oil bubbler was utilized to maintain atmospheric pressure during the process. Samples were removed from the system (i.e. exposed to atmosphere) at room temperature.

Micrographs of the material morphology were captured by SEM (LEO 1530 and 1550, Germany; Hitachi S-4700, Japan) and TEM (JEOL 100 CX, Japan). SEM images were taken using accelerating voltages of 3 – 10 kV and working distances 4 – 12 mm. An accelerating voltage of 100 kV was used for TEM imaging. For elemental and structural characterization Raman spectroscopy (WITec Instruments Corp., Germany) and XRD (PANalytical X'Pert PRO Alpha-1, USA) were utilized. Raman spectroscopy was performed using a 514 nm laser, 20x objective, and 600 grating with a 10 second integration time for 15 accumulations. XRD studies were conducted with a Cu Kα source with a monochromator using the following parameters: 45 kV accelerating voltage, 40 mA current, 0.033^{o} 2θ step size, and 80 – 90 s record time. For diffraction analysis Materials Data, Inc. Jade version 8 software with ICDD PDF-4 database was used.

The electrical measurements utilized a two probe technique in the cross-plane direction of the electrode (parallel to the VACNTs axis) using an Agilent B1500A analyzer. Tungsten metal probes with a tip radius of 0.5 μm were used. The electrical

measurements were taken as a function of temperature by sweeping the voltage from -1 V to 1 V in 20 mV increments.

The thermal conductivities of VACNT–based electrodes were measured using a noncontact optical laser flash technique. According to the established protocol, a xenon flash lamp produced shots with an energy of 10 J/pulse on the sample surface while the temperature rise was measured at the other end with a nitrogen-cooled InSb infrared detector. The thermal-wave travel time allowed measurement of the thermal diffusivity α. The thermal conductivity K is related to α as $K = \alpha\rho C$, where ρ and C are the mass density and specific heat of the material, respectively. Details of the experimental setup and measurements procedures were reported elsewhere.[218-220] The system used for this study was calibrated with other techniques for measuring thermal conductivity such as transient planar source and 3-omega techniques.[219] The K values measured for given samples are associated with the thermal conductivity along the VACNT–Si–C length and perpendicular to the electrode plane. Thermal conduction via CNT arrays dominates all other contributions to thermal transport owing to the extremely high intrinsic thermal conductivity of CNTs.[184] The heat losses via air are negligible for the transient method of measurements used in this work.

Si nanoparticles (98+%; US Research Nanomaterials, Inc., USA), MWCNTs (Arkema, USA) and PVDF (Sigma Aldrich, USA) were mixed by mortar and pestle and formed into a pellet using a pellet die (International Crystal Laboratories, USA) and hydraulic press (Carver Inc., USA) operating at ~ 8 Ton (applied pressure ~ 0.5 GPa). Each pellet contained Si:C:PVDF at the weight ratio of 7:2:1 with an average thickness of ~1 mm. Pellets of equivalent composition and thickness consisting of Si nanoparticles, Pure Black (Superior Graphite, USA), and PVDF were also formed using the previously described technique.

To adhere the VACNTs onto conductive current collectors, the VACNT were removed from the quartz by a razor blade to produce a free-standing VACNT film.

Following deposition of any active materials, the VACNT film was cut and adhered to copper foil rounds that had been coated with a layer of PVDF through a thermal adhesion process.

The ratio of Si to C for the electrodes was calculated from mass differences after each CVD reaction using a balance with 0.01 mg accuracy. Electrodes were spot-welded to 2016-type coin cells and degassed under vacuum at 70 ^{o}C overnight prior to assembly into half cells with a Li foil counter electrode (battery grade; Alfa Aesar, USA) in an Ar filled glovebox (< 1 ppm H_2O, O_2). A commercially blended electrolyte solution (Novolyte Technologies, USA) consisting of 1.0 M $LiPF_6$ in DMC:EC:DEC (1:1:1 by volume) with 10 wt. % VC was used. The cells were cycled between 10 mV and 2 V for Si-VACNTs and 10 mV and 1 V for C-Si-VACNTs on an Arbin BT2000 (Arbin Instruments, USA). The charge/discharge procedure utilized both constant current and constant voltage (at 10 mV to 5% of the initial current) regimes on the alloying step to ensure high degree of lithiation. The Coulombic efficiency was calculated as the percent ratio of the capacity after Li dealloying to after Li alloying. Cyclic voltammetry measurements were performed at a scan rate of 0.1 mV/s using a multi-channel potentiostat (Solartron Analytical, USA).

6.4 Results and Discussion

Cross-section SEM images show the high degree of alignment of the as-produced VACNTs at both low and high magnification (Figure 58 a,b). Representative SEM and TEM images show that the resulting Si forms rather uniform ~70 nm coating along the CNT length (Figure 58 c,d). The deposited Si is amorphous, as indicated by the absence of crystallites in the TEM images (Figure 58d). Following, a thin C outer coating was deposited on the Si-coated VACNTs (Figure 58e) to improve the high rate performance, stability, and the SEI layer. The importance of an outer C layer to achieve stable performance has been reported elsewhere.[10, 157, 221] TEM images of the C and Si coated

VACNTs show the formation of crystallites in the Si structure (Figure 58f). A schematic illustrating the final morphology and composition of individual nanotubes within the VACNTs film is shown in (Figure 58g). The final Si:C composition and thickness ratios can be tailored to meet design requirements (Section 8.3) by adjusting the reaction time for both deposition processes.

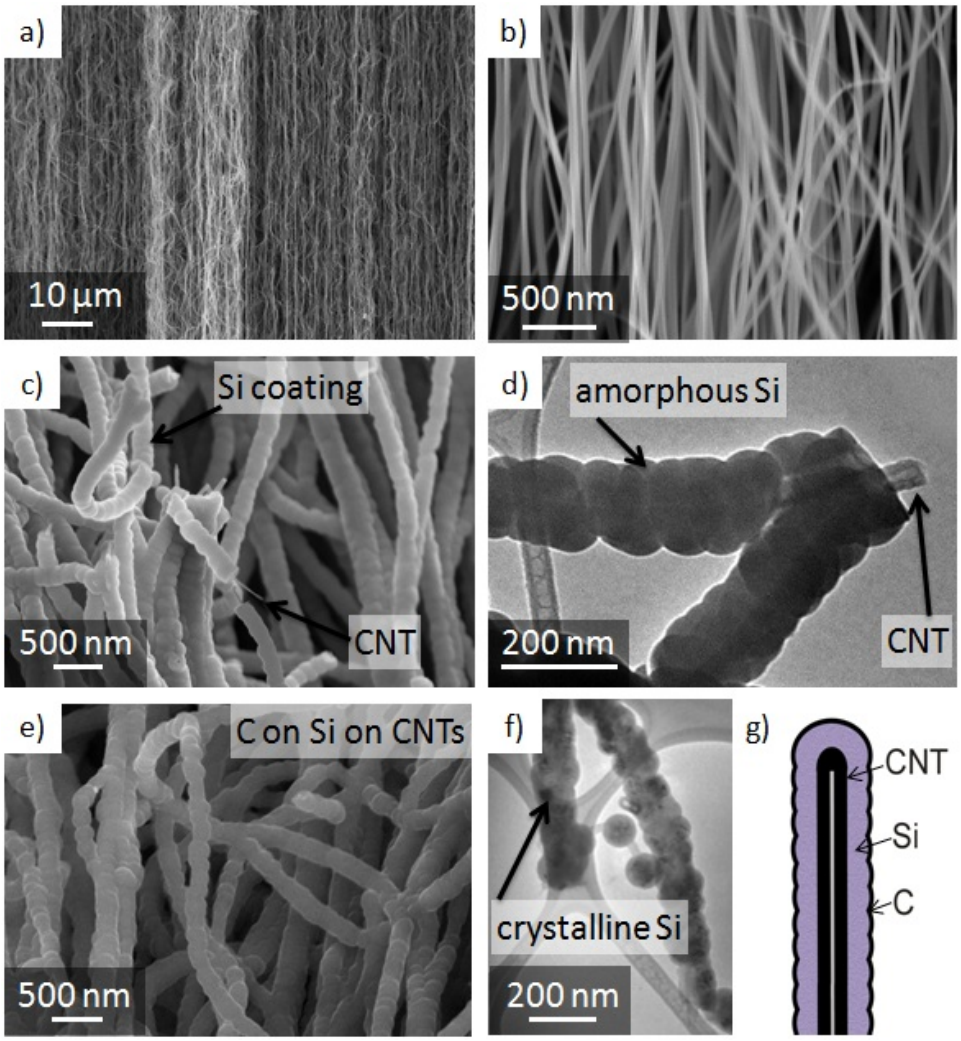

Figure 58. (a, b, c, e) Cross-sectional SEM and (d, f) TEM images of: (a, b) synthesized VACNTs, (c, d) Si coated VACNTs, and (e, f) C and Si coated VACNTs. (g) A schematic of the final morphology of an individual tube.

Raman spectroscopy (Figure 59) and XRD (Figure 60) studies followed the sample evolution. The Raman spectra of the as-produced VACNTs showed the

characteristic G and D peaks with a low D band intensity thus indicating a small number of defects are present.[192, 222] After Si deposition, a peak corresponding to Si emerged. After C coating, the Si band was still observable; however, the relative intensity in comparison with the D and G bands decreased thus confirming deposition (Figure 59).

The XRD pattern of the as-produced VACNTs showed peaks corresponding to graphitic materials. After Si coating, the distinct graphitic peaks were no longer visible, but rather broad peaks attributed to amorphous Si were observed (Figure 60) in agreement with the TEM observations (Figure 58d). Following C coating, the XRD pattern showed sharp peaks associated with crystalline Si and weaker peaks corresponding to C were visible (Figure 60).

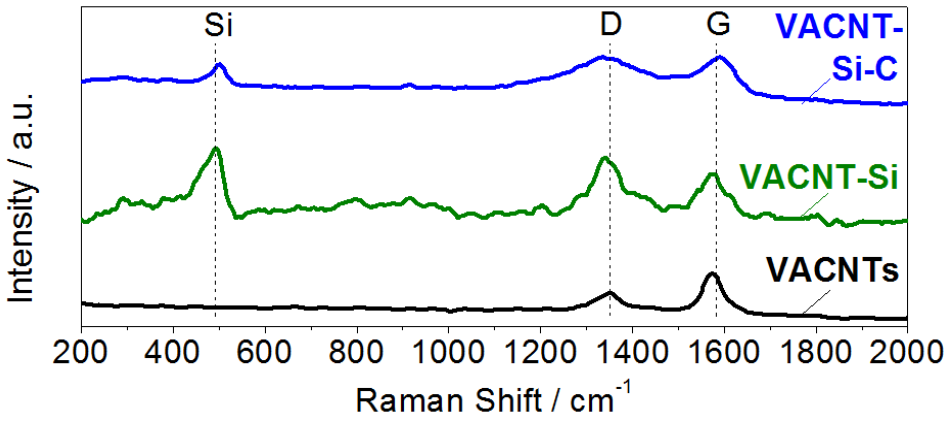

Figure 59. Raman spectroscopy analyses of the VACNT: as-produced, after Si coating and after C coating. Spectra normalized by the intensity of the G band.

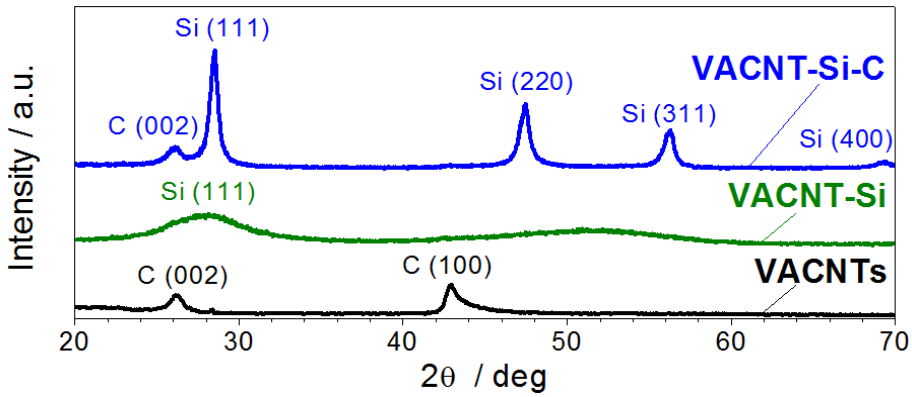

Figure 60. X-ray diffraction analyses of the VACNT: as-produced, after Si coating, and after C coating.

High thermal and electrical conductivity of electrodes is desired for the majority of applications because most of the battery degradation mechanisms are thermally activated and related to processes on individual particles within electrodes, such as metal dissolution in cathodes or degradation of the SEI on the anodes.[198, 223-224] Therefore, local heating caused by moderately high current pulses may severely diminish the battery cycle life, particularly if thick and more resistive electrodes are utilized.[198, 223, 225]

Additionally, localized thermal and electrical gradients within electrodes give rise to highly undesirable unbalanced charging and discharging that may lead to faster degradation and under-utilization of the available electrode capacity.[198-199] The importance of heat removal and thermal management of the batteries has been extensively discussed in recent literature.[198-199] Sophisticated methods of thermal management that employ microfluidic channels incorporated within the battery to transport cooling fluids were proposed to address this issue. These approaches, unfortunately, dramatically increase the cost and complexity of the battery production. Therefore, designing thick electrodes with very high thermal conductivity is of critical importance.

Figure 61 shows the results of the thermal conductivity measurements for the coated VACNT-based electrodes as a function of temperature compared with the conventional electrode of similar thickness composed of densely packed Si (<80 nm) and CNT powder bonded with PVDF.

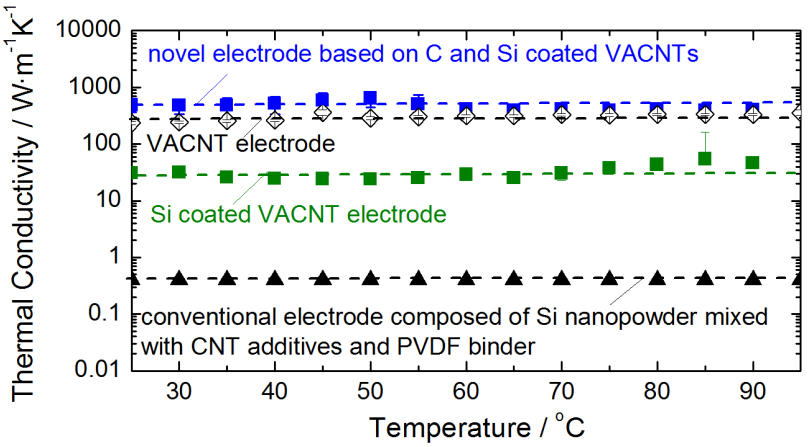

Figure 61. Comparison of the thermal conductivities of conventional and VACNTs-enabled thick electrodes.

Although Si electrodes with porosity insufficient to accommodate Si expansion upon electrochemical alloying with Li show rapid degradation [157], comparison of the novel electrodes with that of a dense sample which was called "reference"(Figure 62) having a very high thermal conductivity achievable for conventional electrode preparation methods was performed. The effective thermal conductivity determined for the CNT-containing reference powder electrode is ~0.4 W/m·K. In sharp contrast, the VACNT–Si–C electrode shows a three-order of magnitude improvement with K values in excess of 400 W/m·K. The increase in K translates to ~1000 times reduction of the thermal resistance $t_{electrode}/K$ of the electrode (here $t_{electrode}$ is the electrode thickness). The key reason for such a major improvement in the thermal properties of the electrodes is the extremely high intrinsic thermal conductivity of CNTs, which was reported to exceed 2000 W/m·K and approach that of graphene.[226] The high degree of MWCNT alignment, their extension over the whole electrode thickness and the C shell coating the Si surface likely contribute to the very high thermal conductivity achieved. Electrical measurements using a two-probe technique revealed ~100 times reduction of the electrical resistance of the VACNT-based electrode compared to the reference electrode (Figure 63).

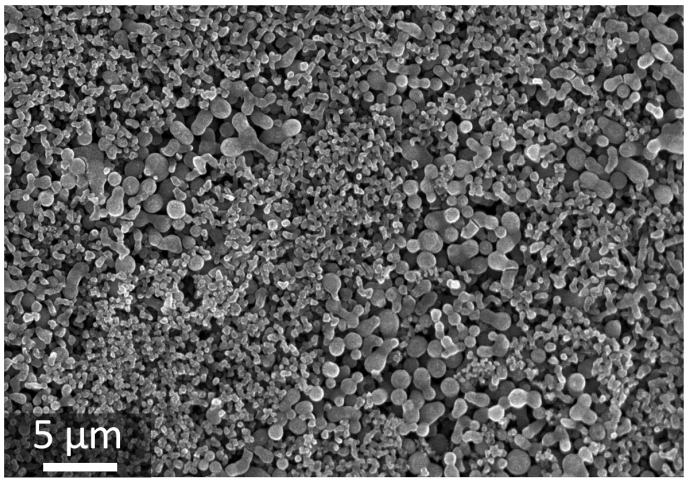

Figure 62. Top-down SEM micrograph of the Si nanopowder "reference" electrode used for conductivity measurements.

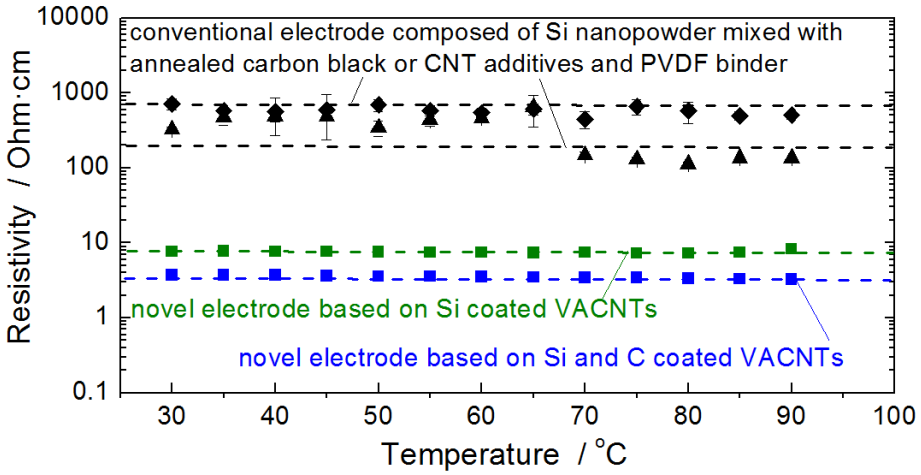

Figure 63. Comparison of electrical resistivity of Si-based electrodes: conventional electrode produced by compaction of Si and C nanopowder and Si and C coated VACNT electrode.

Prior to cell assembly the active materials were adhered to a thin copper foil (Figure 64a) through thermal processes that created a conductive carbon interface with good adhesion. The VACNT–Si–C anode demonstrated good stability for over 250 cycles (Figure 64b) and high specific capacity approaching theoretical limits (4200 mAh/g_{Si}), which indicates efficient electrical connectivity within the electrode and access of the electrolyte to all the deposited Si. The average values of dealloying capacities of the electrode at C/5 and C/2 were ~3300 mAh/g_{Si} and ~2000 mAh/g_{Si}, respectively (Figure

64b). The average CE for the first 100 cycles was 99.92 ± 4.61%. The shape of the charge/discharge profiles (Figure 65a) and cyclic voltammograms (Figure 65b) of VACNT–Si–C electrode were very similar to prior observations in various nanoSi-based anodes.[10, 154, 157, 221]

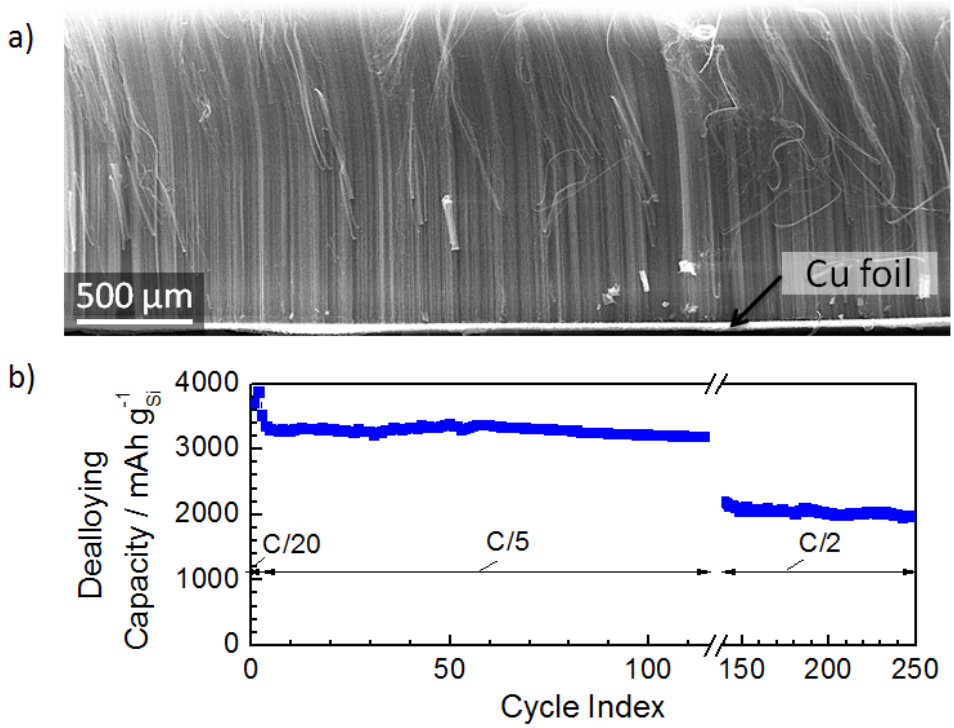

Figure 64. (a) Cross-section SEM image of a VACNT-based thick electrode adhered onto a thin copper foil. (b) Dealloying capacity versus cycle number for the VACNT-Si-C electrode at three different current densities. The capacity is reported for the Si contribution only.

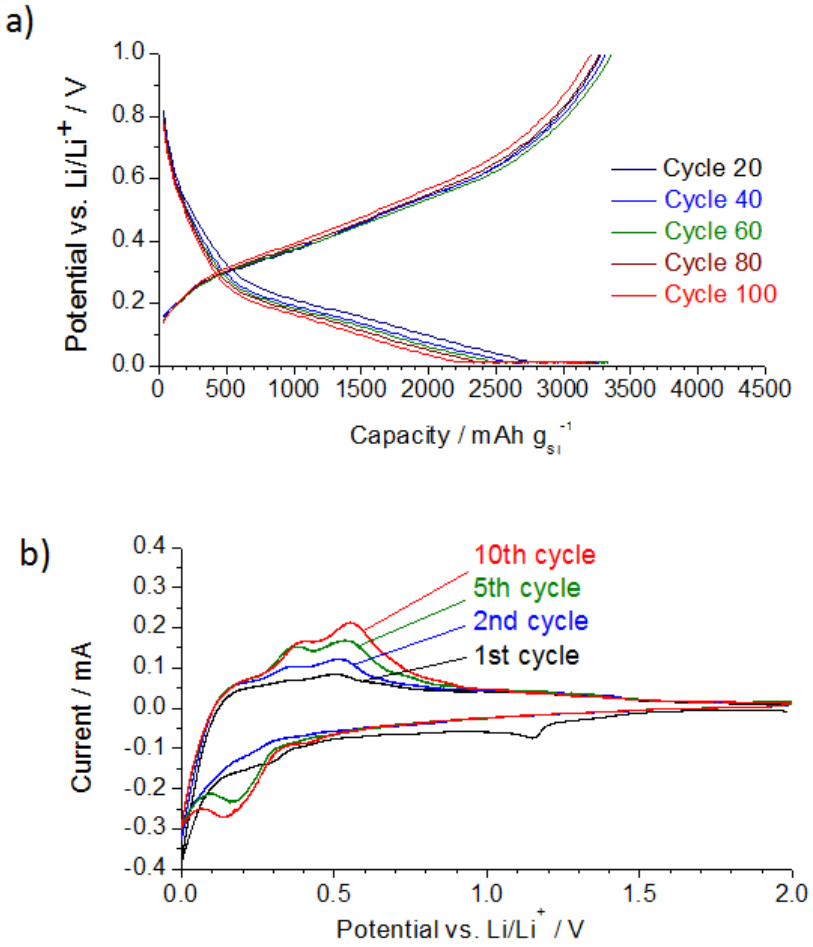

Figure 65. Electrochemical characterization of VACNT electrodes coated with Si and protective C layer: (a) charge/discharge profiles and (b) cyclic voltammetry.

In addition, it was found that a C overcoating on the Si surface is critical to achieving good capacity retention and high Coulombic efficiencies (Figure 66), confirming prior studies.[10, 154, 157, 221] Without the C layer, Si-coated VACNT electrodes showed a noticeable decline in specific capacity at the rate of ~1% per cycle. In addition, the unprotected Si showed relatively low values of CE to 97.58 ± 0.14%, after the formation cycles. In contrast, the CE steadily increased to 99.52 ± 0.71% after the formation cycles for C-coated electrodes.

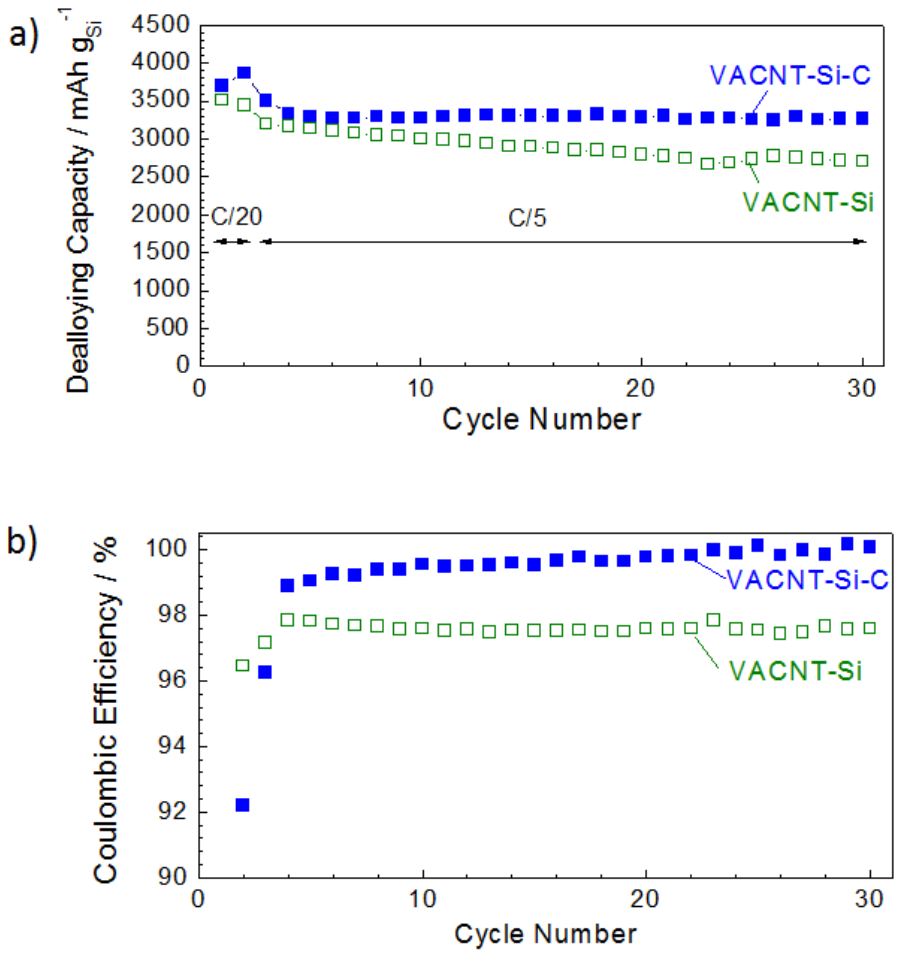

Figure 66. Electrochemical characterization of VACNT electrodes coated with Si with and without protective C layer: (a) specific capacity and (b) Coulombic efficiency versus cycle number.

6.5 Conclusions

Ultra-thick electrodes that utilize VACNTs as a structured nanoscale platform with unique performance advantages were synthesized and characterized. The application of the VACNT architecture resulted in three and two orders of magnitude improvements in the electrodes' thermal and electrical conductivities, respectively. In addition, VACNTs can be considered as an attractive substrate for the deposition of other high capacity or low electrical or thermal conductivity materials to provide high energy and power characteristics, high electrical and thermal conductivities, and stable cycling for both cathodes and anodes.

It was also demonstrated that ultra-thick Si-coated VACNTs electrodes, when protected with a C overcoating, can produce stable performance at multiple current densities with reversible capacities significantly greater than graphite. However, the CE of the produced electrodes is not high enough for commercial cells. Although the observed rate capability of the 1 mm thick electrode was not very high, it is expected that patterning of the electrode (for the formation of small interpenetrating channels for faster electrolyte access) as well as the modification of the electrolyte solvent may improve the high current/high power performance. In addition, it is expected that substitution of Li foil with an actual cathode may further improve the rate capability. Furthermore, testing the produced composite material against a matching cathode would further reveal the stability and efficiencies of the electrochemical performance.

CHAPTER 7

SURFACE COATINGS FOR STABILIZATION OF HIGH CAPACITY ELECTRODES

7.1 Overview

Several approaches can be pursued to stabilize high capacity electrodes including, but not limited to, re-designing the electrode architecture to generate increased porosity and varying the electrolyte composition to produce a stable SEI layer. New electrode architectures are the basis of this research and numerous other studies (Section 2.3). Similarly, there is research activity in stabilizing the SEI through electrolyte additives (Section 2.3). However, another approach to stabilize high capacity electrodes may be through the deposition of an overcoating. Previous research revealed that that the addition of an outer C coating on the Si surface is critical to achieving good capacity retention and high CE for VACNT-Si electrodes. Without the C layer, Si-coated VACNT electrodes showed a noticeable decline in specific capacity at the rate of ~1% per cycle. In contrast, C-coated electrode showed higher CE with no signs of degradation. This effect was attributed to the increased thermal and electrical conductivities of the electrodes and improved structural integrity of the surface layer close to the SEI; however, morphological changes of individual coated VACNTs were not investigated in detail.

Although C may evidently provide increased conductivities and enhanced structural stability to the SEI, other coatings may likely improve SEI stability as well. For example, nanoscale coatings of alumina (Al_2O_3) have improved the cycle stability for a variety of electrode materials including C, $LiCoO_2$, MoO_2, S, and Si, among others [227-230]; however, a detailed and unambiguous explanation of such performance improvements has yet to be determined.

7.2 Approach

In this study, alumina thin films were deposited on different high capacity VACNT-based electrodes:

1) VACNT-Ge

2) VACNT-Si and VACNT-Si-C.

Coatings on CNTs are typically either smooth thin films, thin films consisting of coalesced particle deposits, or discrete particles, with the latter two producing composite materials with higher surface roughness. Differences in coating morphology can be attributed to a number of factors such as the substrate surface (e.g. defects, functional groups, crystal structure) and deposition conditions. It is hypothesized that materials with higher surface roughness will have higher local stress concentration sites. If an externally deposited thin film can sustain repeated non-uniform stress gradients within it, then it shall also be able to sustain uniform stress gradients.

A prior study on the lithiation of Al nanowires with a 4 – 5 nm thin native oxide reported the formation of a robust 6 – 10 nm Li-Al-O surface solid electrolyte upon lithiation.[231] The formed Li-Al-O glass underwent elastic and plastic deformation as the Al nanowire volumetrically expanded by 100% with no evidence of fracture.

In this study, Al_2O_3 was selected as a proof-of-concept electrically insulating overcoating to test the hypothesis that an alumina thin film coated onto a high capacity material could improve cycling by serving as an artificial SEI. ALD was selected as the deposition method as the technique is well understood, produces high quality films, and allows for tight (often 0.1 nm) control of the film thickness. Further, as a vapor deposition technique, ALD allows for conformal deposition of alumina on complex electrode geometries. The ALD used to deposit alumina is a shared system that can deposit a variety of other coatings. For this reason, thermal ALD, instead of plasma ALD, was chosen to reduce sample contamination from other thin films deposited within the same process chamber.

To understand the role of alumina on the produced electrodes, lithiation and delithiation of individual particles of the produced materials was performed by *in situ* TEM. TEM measurements allowed for observation of the dilating and thinning of the active materials in response to lithiation and delithiation and the formation of pores or cracks. To validate the TEM observations, electrochemical cycling of electrodes of the same composition and structure was performed. After cycling, the cells were disassembled and the active materials were investigated through TEM for comparison with the *in situ* results.

7.3 Experimental Methods

For direct growth of VACNT on metallic substrates, a layered stack of catalyst and catalyst supports were utilized including layers of Ti, Al, and Fe deposited via e-beam (Ti, Fe) and thermal (Al) evaporation on nickel foil. Low-pressure thermal CVD (Black Magic, Aixtron) at 825 ^{o}C utilizing a hydrogen and acetylene mixture (7:1 by flow rate) was utilized. The length of the VACNT was tuned by adjusting the time of hydrogen and acetylene gas exposure. The resulting VACNT were well-aligned on the foil substrates and did not require additional post-synthesis alignment techniques.

Germanium was deposited from pure, electronic grade germane gas at 400 ^{o}C at pressures ~750 mTorr in a commercial system (EasyTube 3000, FirstNano). The system is a cold-wall reactor in which the samples are resistively heated while on the quartz stage. The flow rate of the GeH_4 was controlled at 5 sccm during the growth period. The system was purged with Ar gas prior to heating to the deposition temperature and during system cooling. Samples were removed from the system (i.e. exposed to atmosphere) at room temperature to minimize oxidation of the deposited germanium.

Preparation of silicon and carbon coated VACNT electrodes was conducted according to the experimental procedures described in Chapter 6.

ALD (CambridgeNanoTech, USA) was utilized to deposit alumina on select VACNT-Ge-based and VACNT-Si-based materials. The precursors for ALD were trimethylaluminum (TMA) and high purity water. For these experiments, a deposition temperature of 150 ^{o}C with a precursor pulse time of 0.6 seconds and a purge time of 20 seconds for both the TMA and de-ionized water were utilized (Figure 67). The temperature of both precursors was 22 ^{o}C.

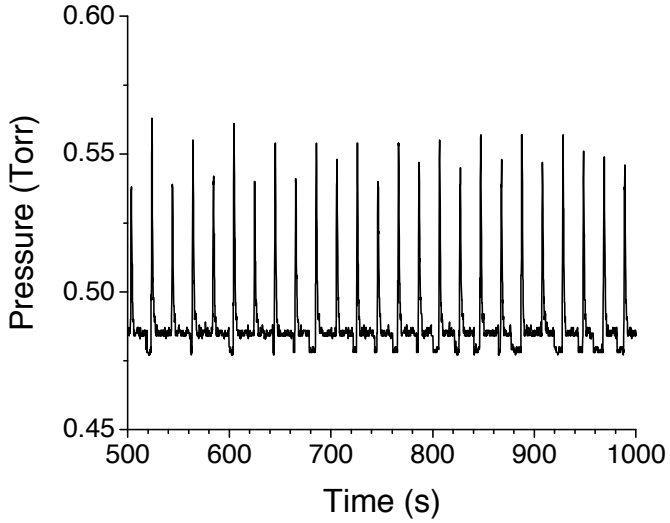

Figure 67. A representative pressure profile for multiple ALD cycles for alumina deposition.

Mass measurements using a balance with 0.01 mg accuracy were used to determine the ratio of Si to C. EDS mapping was performed at 15 kV to determine the chemical composition of the VACNT-Ge samples. Mass measurements were not used for the Ge-based electrodes as Ge was deposited on the underside of the metal foil, thus giving inaccurate composition measurements by mass change alone. All electrodes were spot-welded to 2032-type coin cells prior to assembly into half cells with a Li foil counter electrode (battery grade; Alfa Aesar, USA) in an Ar filled glovebox (< 1 ppm H_2O, O_2). A commercially blended electrolyte solution (BASF, USA) consisting of 1.0 M $LiPF_6$ in DMC:EC:DEC (1:1:1 by volume) with battery-grade 10 wt. % VC was used. The cells were cycled between 10 mV and 2 V for Ge-based electrodes and 10 mV and 1 V for Si-

based electrodes on an Arbin BT2000 (Arbin Instruments, USA). The charge/discharge procedure utilized both constant current and constant voltage (at 10 mV to 5% of the initial current) regimes on the alloying step to ensure high degree of lithiation. The Coulombic efficiency was calculated as the percent ratio of the capacity after Li dealloying to after Li alloying. Cyclic voltammetry measurements were performed on a multi-channel potentiostat (Solartron Analytical, USA). VACNT-Si-based electrodes were tested at a scan rate of 0.1 mV/s between 0 and 1 V. VACNT-Ge-based electrodes were tested at a scan rate of 0.01 mV/s between 0 and 2 V.

TEM studies were performed on a Tecnai F30 (FEI, USA) with an accelerating voltage of 300 kV. For *in situ* TEM, the Li/Li_2O electrode can be driven to contact individual sample particles to construct a nanobattery through the piezo-manipulation of a Nanofactory TEM-scanning tunneling microscope holder. Upon applying a potential between the nanowire and Li/Li_2O counter electrode, (de)lithiation can be initiated. ImageJ software was employed to measure the film thicknesses.

As synthesized CNT-based materials were prepared for TEM by sonication in anhydrous ethanol (Sigma Aldrich, USA). Post-mortem TEM samples were prepared by sonication in battery-grade DMC (BASF, USA). The TEM grids containing lithiated materials were transported to the TEM in air-tight containers filled with Ar.

7.4 Results and Discussion

VACNT-Ge anodes

Cross-sectional SEM shows the high degree of alignment of the VACNTs coated with Ge particles (Figure 68). Individual ~90 nm Ge particles were distributed along the CNT surface. A nanoscale coating of Al_2O_3 was deposited onto the VACNT-Ge via ALD. TEM images (Figure 69) show that Al_2O_3 conformally coats the crystalline Ge particles. Much smaller Al_2O_3 particles along the CNT outer surface were expected and

observed in both SEM and TEM. Non-functionalized carbon nanotubes have highly inert surfaces that limit the reaction of TMA and H_2O thus nanoparticles, rather than films, are often formed on the CNT surface via ALD.[232]

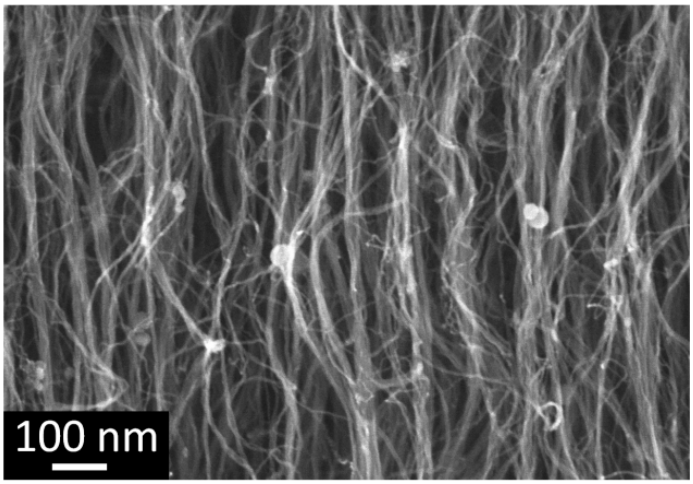

Figure 68. Cross-section SEM image of VACNT-Ge.

Images of as-synthesized Al_2O_3-coated Ge particles undergoing lithiation were recorded using *in situ* TEM methods (Figure 70). The investigated area observed the evolution of three Ge particles during repeated lithiation and delithiation. TEM images of the initial material suggest that at least two of the Ge particles are highly crystalline and faceted (Figure 70a). The initial Al_2O_3 thickness was ~6.7 nm. After the first lithiation, each of the particle diameters increased to form more spherical particles (Figure 70b). The thickness of the Al_2O_3 layer on each particle decreased to ~3.9 nm with a thin SEI layer visible. No cracks in the Ge particle or in the Al_2O_3 layer were observed. Upon delithiation, the Al_2O_3 film thickened to ~7.5 nm and pores within a Ge particle were observed (Figure 70c).

During the second lithiation, the Ge particles increased in diameter and the Al_2O_3 layer decreased in thickness (Figure 70d), similar to the first lithiation. After the second lithiation, a slightly thicker SEI layer was observed. Interestingly, the voids present after the first delithiation appear to shrink. However, after the second delithiation, a significant

number of pores within the Ge particles were observed (Figure 70e). Additionally, the Ge particles did not return to the dimensions prior to the second lithiation. The Ge particles were subsequently lithiated a final time (Figure 70f). Similar to the second lithiation, voids present within the Ge particle shrunk and there was a slight increase in Ge particle diameter.

The formation of porous Ge has been previously reported in Ge nanowires cycled by similar methods.[233] In that work, the formation of porous Ge was hypothesized to contribute to increased cycling stability. However, Ge nanoparticles (100 nm and larger) did not exhibit pore formation.[147] The Ge nanoparticles investigated here are of similar dimension and were tested under the same conditions; therefore, the difference in lithiation behavior might be attributed to the presence of the alumina film, initial differences in crystal structure, or retained hydrogen from the CVD process.

Comparison of the *in situ* cycling of Al_2O_3-coated Ge particles with uncoated particles could not be performed. Without the Al_2O_3 coating, the Ge particles on the CNT detached from the CNT surface during TEM sample preparation, with clusters of Ge particles and bare CNTs observed. Adhesion was likely weak due to the small area of contact between the Ge particle and the CNT due to the high radius of curvature of both. Deposited Al_2O_3 increased adhesion of the Ge particle to the CNT substrate. Future work to increase adhesion through CNT surface modification or thermal treatment may allow for *in situ* investigation of the lithiation/delithiation behavior of Ge particles without Al_2O_3.

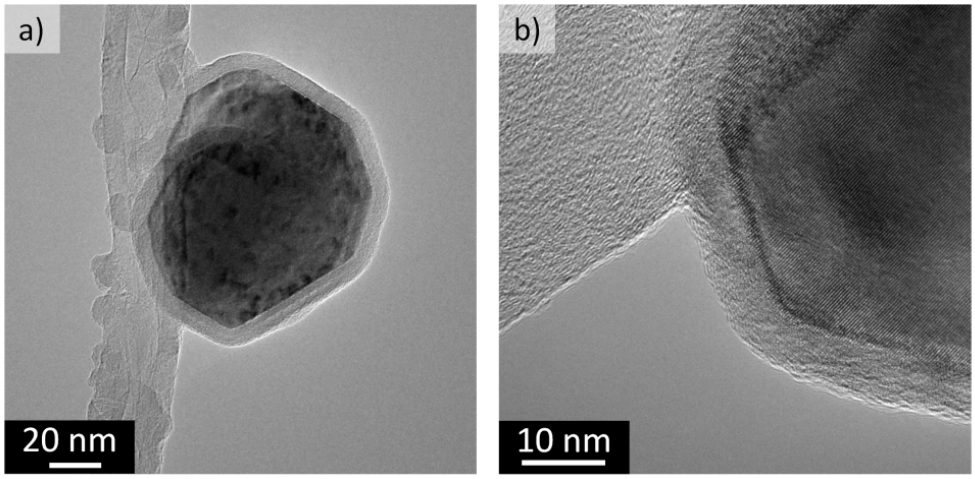

Figure 69. TEM micrographs of an individual Ge particle coated with a layer of alumina adhering to a CNT.

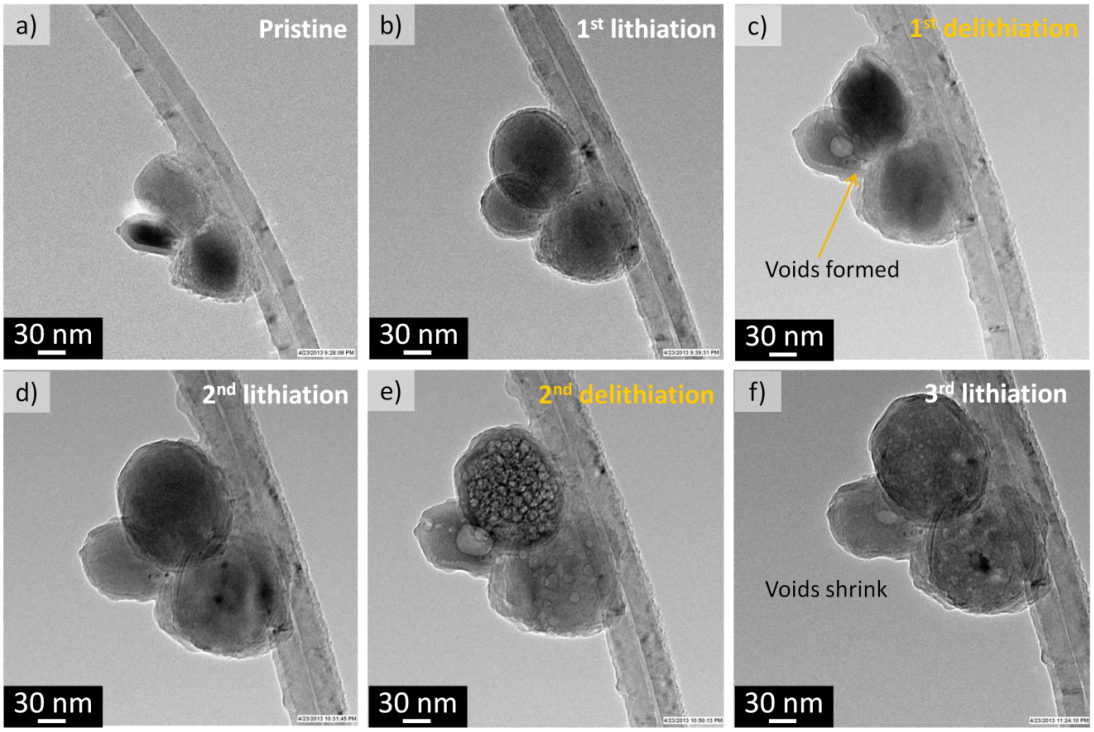

Figure 70. TEM micrographs of (a) pristine CNT-Ge-Al_2O_3 undergoing multiple (b, d, f) lithiation and (c, e) delithiation cycles *in situ*.

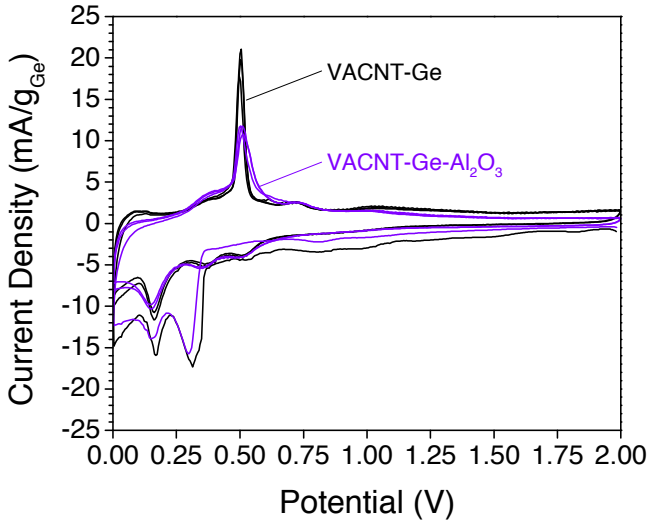

Figure 71. Cyclic voltammograms for VACNT-Ge and VACNT-Ge-Al_2O_3 electrodes.

The reaction potentials for the alumina coated electrodes are broader, indicating that the alumina likely affects the diffusion of Li to the Ge particles. Alumina films created via ALD often are free of pinholes thus its presence on the external surface of the active material likely impedes the diffusion of Li ions to the active material. Experimental or simulated values of the diffusivity at room temperature could not be found in existing literature. Density functional theory calculated the diffusivity of Li in high-temperature (~325 ^{o}C) amorphous alumina to be ~10^{-9} cm^2/s.[234] This diffusivity value is two orders of magnitude smaller than experimentally measured Li diffusivity in Ge at similar temperatures.[235]

Cycled VACNT-Ge particles imaged by TEM (Figure 72) show both crystalline and porous Ge. The formation of porous Ge is counter to previously reported *in situ* TEM lithiation of Ge particles.[147] The difference may be attributed to the initial crystal structure of the Ge particles. In the previously reported study, the Ge particles were single crystal and produced from a Ge wafer. Here, the particles were produced via CVD with no thermal treatment step performed to induce a high degree of crystallinity.

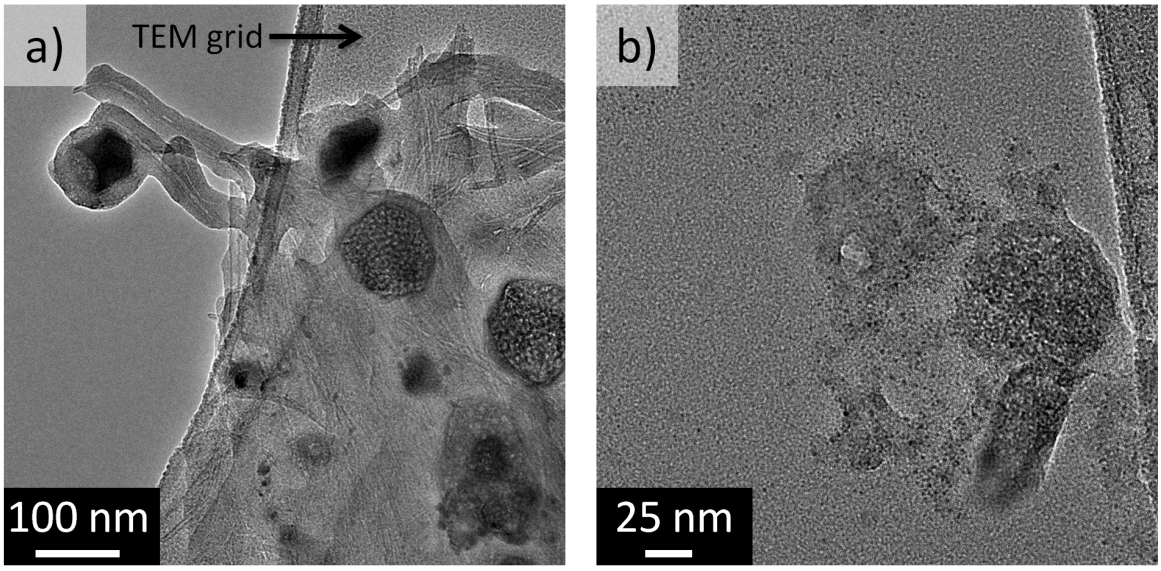

Figure 72. (a, b) Post-mortem *ex situ* TEM micrographs for VACNT-Ge after three cycles.

The lithiated Ge particles appear to remain adhered to the CNT surface; however, due to the dense clustering of CNTs it is difficult to observe points of contact clearly (Figure 72a). Further sonication to isolate the CNTs appears to have a negative impact on the VACNT-Ge as porous Ge likely cannot withstand cavitation as burst porous Ge particles were observed (Figure 72b). Clusters of Ge particles were also observed. The destruction of porous Ge and the weak CNT-Ge adhesion limit clear observations of the post-mortem morphology and crystal structure of VACNT-Ge through *ex situ* techniques alone.

Post-mortem TEM analysis of cycled VACNT-Ge-Al_2O_3 particles also revealed the formation of porous Ge with the surface layer of Al_2O_3 still visible Figure 73, in agreement with *in situ* results. Interestingly, burst porous Ge particles were not observed *ex situ*. Thus, the presence of alumina is attributed to not only maintaining Ge adhesion to the CNT surface but also retaining the resultant Ge structure after cycling during TEM sample preparation techniques.

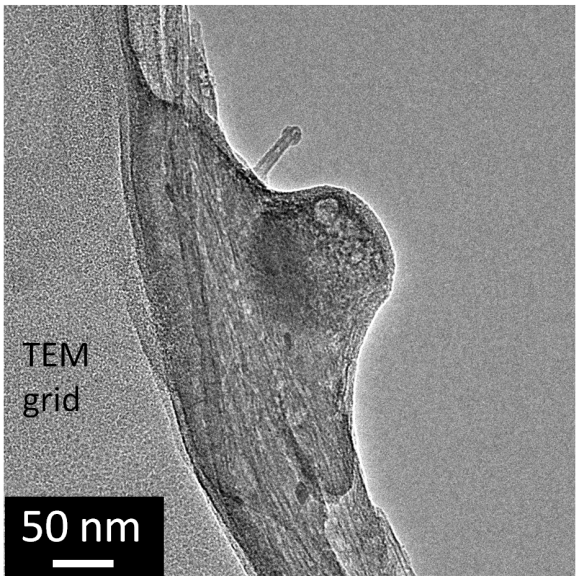

Figure 73. Post-mortem *ex situ* TEM micrograph for VACNT-Ge-Al_2O_3 after three cycles.

Uncoated and Al_2O_3-coated VACNT-Ge were tested in coin cells to compare the effect of the Al_2O_3 coating on cycling performance.

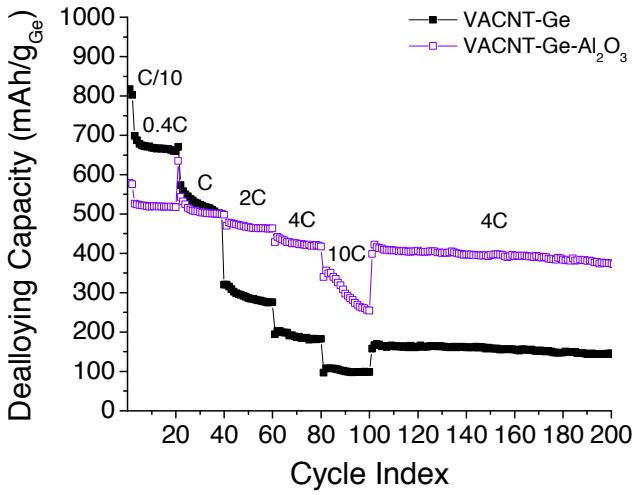

Figure 74 shows the dealloying capacity for the produced materials at varying C-rates. During the initial cycles, the uncoated VACNT-Ge electrodes demonstrate higher dealloying capacity. This is likely due to the electrically insulative nature of the Al_2O_3 limiting the combination of Li ions and electrons. As the number of cycles increases, the uncoated electrode performs stably at higher C-rates, but the dealloying capacity at each

is lower. This may be a result of the loss of weakly adhered Ge nanoparticles detaching from the CNT surface as the particles expand and contract. Detachment of Ge would electrically isolate the particles such that the active material content would slowly decline with repeated cycling. In contrast, the performance of the Al_2O_3-coated materials remains rather constant as the C-rate increases. The exception is at a C-rate of 10C in which the capacity slowly fades over the course of twenty cycles. However, when the C-rate is decreased, the capacity increases and is stable.

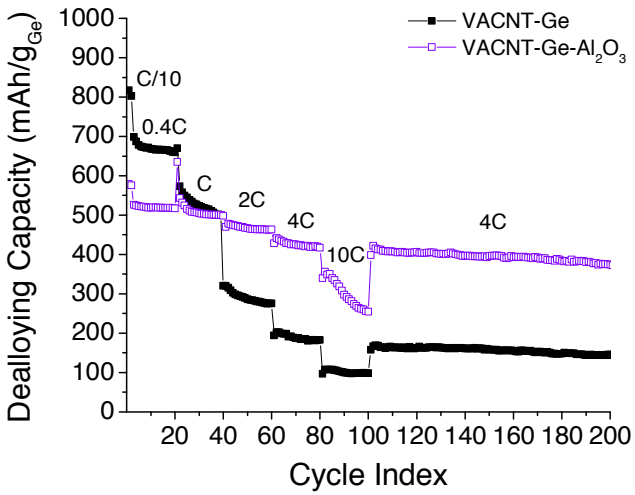

Figure 74. Dealloying capacity versus cycle index measured at multiple C-rates for VACNT-Ge and VACNT-Ge-Al_2O_3. The capacity is reported for the Ge contribution only.

The average CE for the last 100 cycles for VACNT-Ge was 99.69 ± 2.34% and ~99.74 ± 3.15% for VACNT-Ge-Al_2O_3 (Figure 75). The CE for each electrode type drops by as much as ~50% when transitioning between C-rates. A reduction of this effect is observed for samples that have been alumina coated; however, it remains too large for commercial applications in which the rate changes frequently.

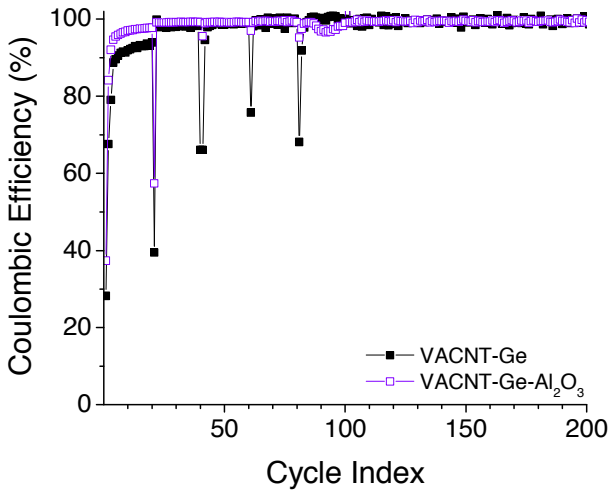

Figure 75. Coulombic efficiency versus cycle index measured at multiple C-rates for VACNT-Ge and VACNT-Ge-Al_2O_3.

VACNT-Si and VACNT-Si-Al_2O_3 anodes

VACNT-Si with a Si coating thickness of 30 - 35 nm were produced. A nanoscale coating (~19.2 nm) of Al_2O_3 was deposited onto the VACNT-Si via ALD. TEM images (Figure 76) show that a layer of amorphous Al_2O_3 conformally coats the deposited Si.

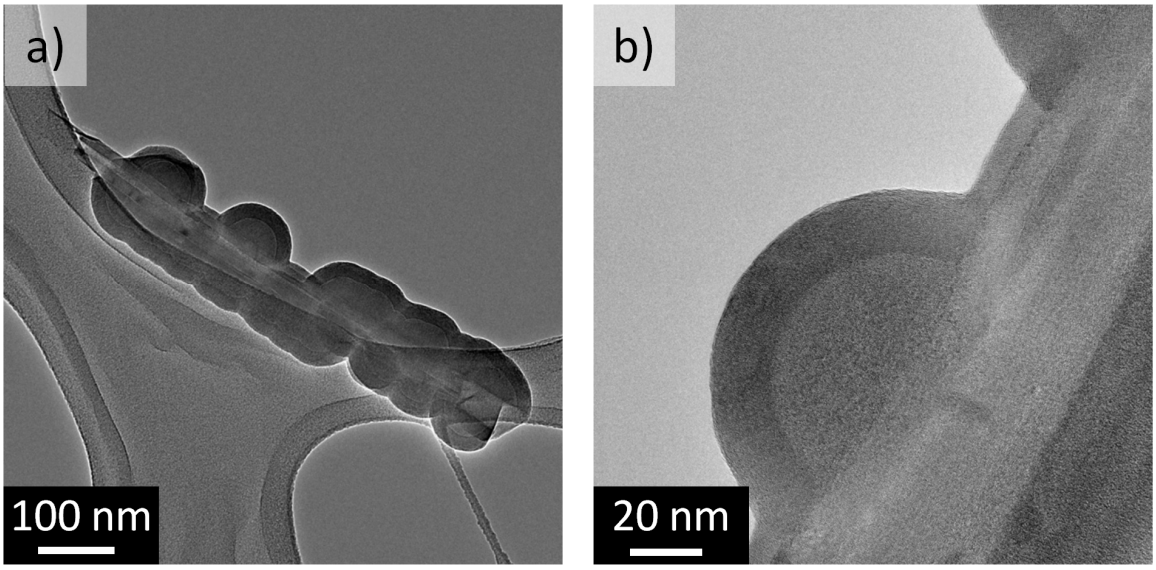

Figure 76. TEM images of VACNT-Si-Al_2O_3.

Images of VACNT-Si-Al_2O_3 undergoing lithiation were recorded using *in situ* TEM methods (Figure 77). Lithiation proceeded primarily in the axial direction due to the

increased electrical conductivity along the CNT axis than radially. As the lithiation front travelled, the thickness of the Si and Al_2O_3 film increased. At 114 seconds, a surface crack in the Al_2O_3 layer was observed. Still quite remarkably, in spite of the very significant volume changes a large portion of the Al_2O_3 layer plastically deformed and did not form cracks or delaminated areas.

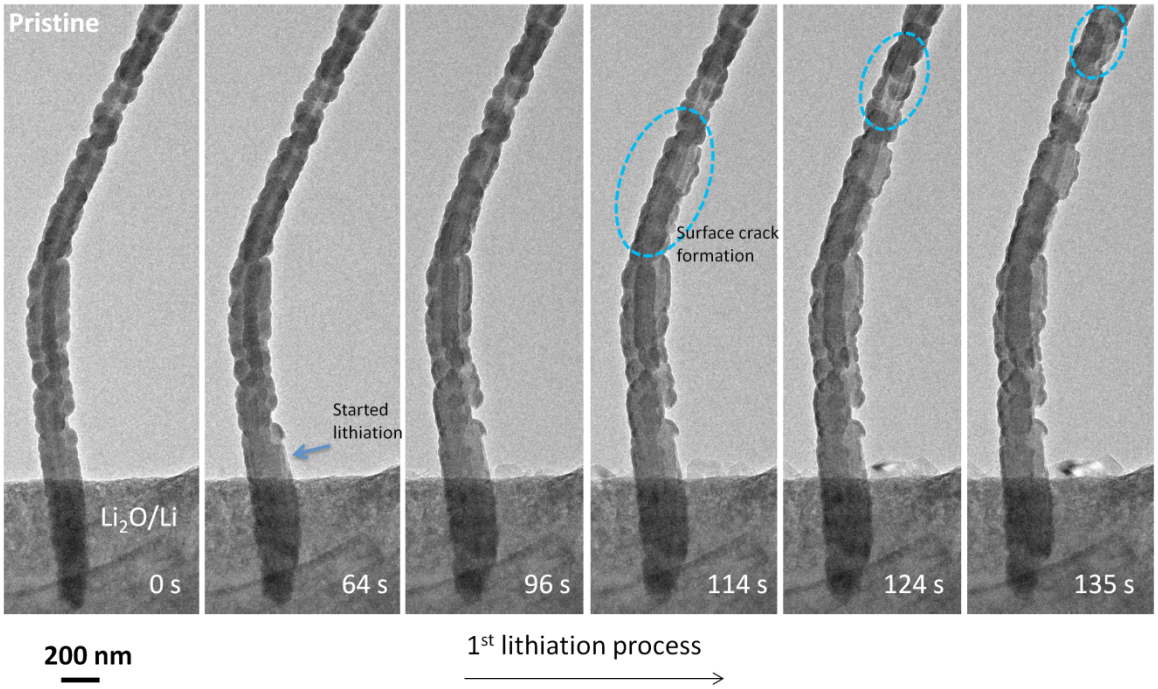

Figure 77. TEM micrographs of *in situ* lithiation of CNT-Si-Al_2O_3 with time.

Unfortunately, the CNT-Si-Al_2O_3 could not be fully delithiated before the CNT burned under the high applied potential (20 V). No morphological changes were observed (Figure 78b) before the end of the test. It was hypothesized that the electrical resistivity and length (500 μm) of the lithiated CNT-Si-Al_2O_3 was too large for this technique.

Based on the thermal and electrical conductivity results (Figure 61, Figure 63) for ultra-thick VACNT electrodes, it was hypothesized that the addition of C would increase conductivity such that delithiation could be successfully performed *in situ*.

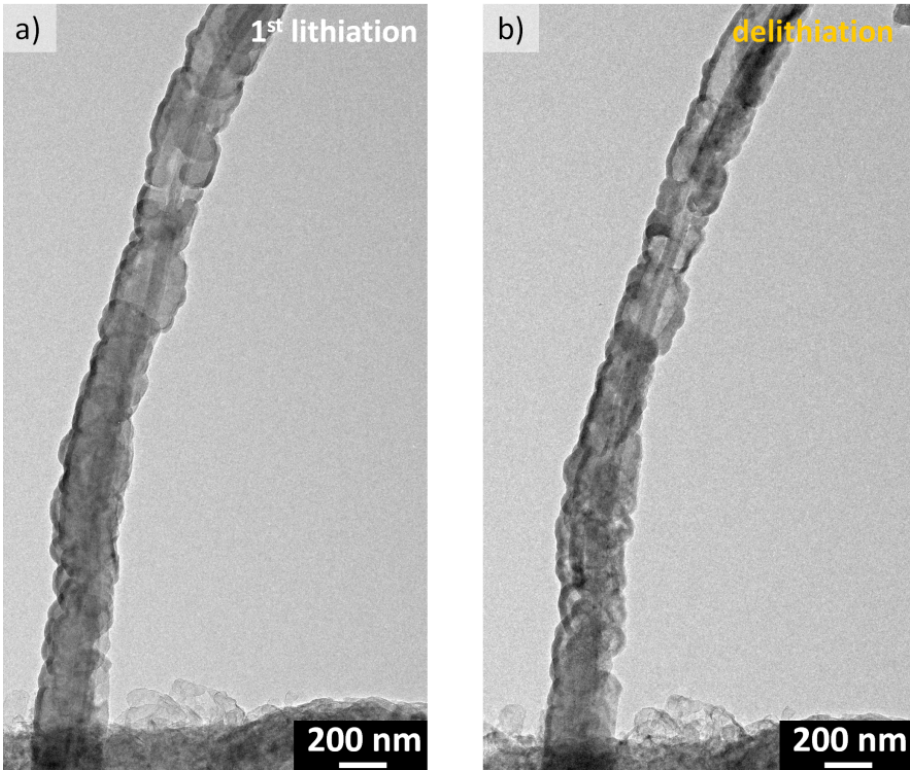

Figure 78. TEM micrographs for the (a) lithiated CNT-Si-Al_2O_3 and (b) the same CNT undergoing *in situ* delithiation.

TEM images of the produced VACNT-Si-C-Al_2O_3 (Figure 79a) show that the C deposition process induces some Si crystallization, in agreement with prior results (Figure 58, Figure 59, Figure 60). During the first lithiation of VACNT-Si-C-Al_2O_3 (Figure 79 b,c), an increase in tube diameter, due to the increase in Si and Al_2O_3 film thickness, was observed. A small fracture in the VACNT-Si-C-Al_2O_3 coating is also observed. Further, the Si crystallites, upon lithiation, became amorphous, in agreement with prior literature.[32] VACNT-Si-C-Al_2O_3 was able to be delithiated and the TEM study shows the formation of porous Si (Figure 79d). This is in agreement with prior work reported in the literature for the development of porous Si in Si nanowires tested as Li-ion battery anodes.[236] Formation of internal pores in Si minimizes the volume changes during cycling and thus should be advantageous for SEI stabilization.

Upon continued lithiation and delithiation (Figure 80), the closure of voids within porous Si upon lithiation and their subsequent reappearance upon delithiation were

observed. Upon each lithiation the CNT-Si-C-Al_2O_3 resembled the dimensionality and crystallinity as after the first lithiation. On the fourth delithiation (Figure 80f), the CNT itself fractured. The fracture site was an area in which the original coating layers were not continuous along the CNT axis and likely experienced local stress concentration. Fracture at a non-uniformity emphasizes the necessity for continuous layers on all active material surfaces.

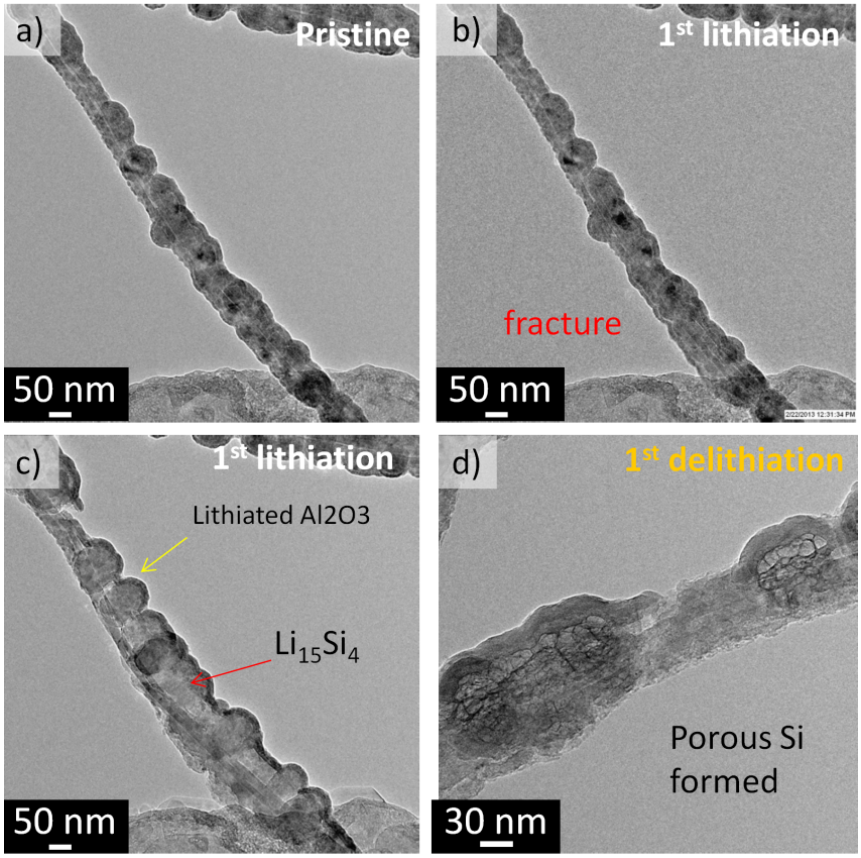

Figure 79. TEM micrographs for the (a-c) lithiated CNT-Si-C-Al_2O_3 and (d) the same CNT after *in situ* delithiation.

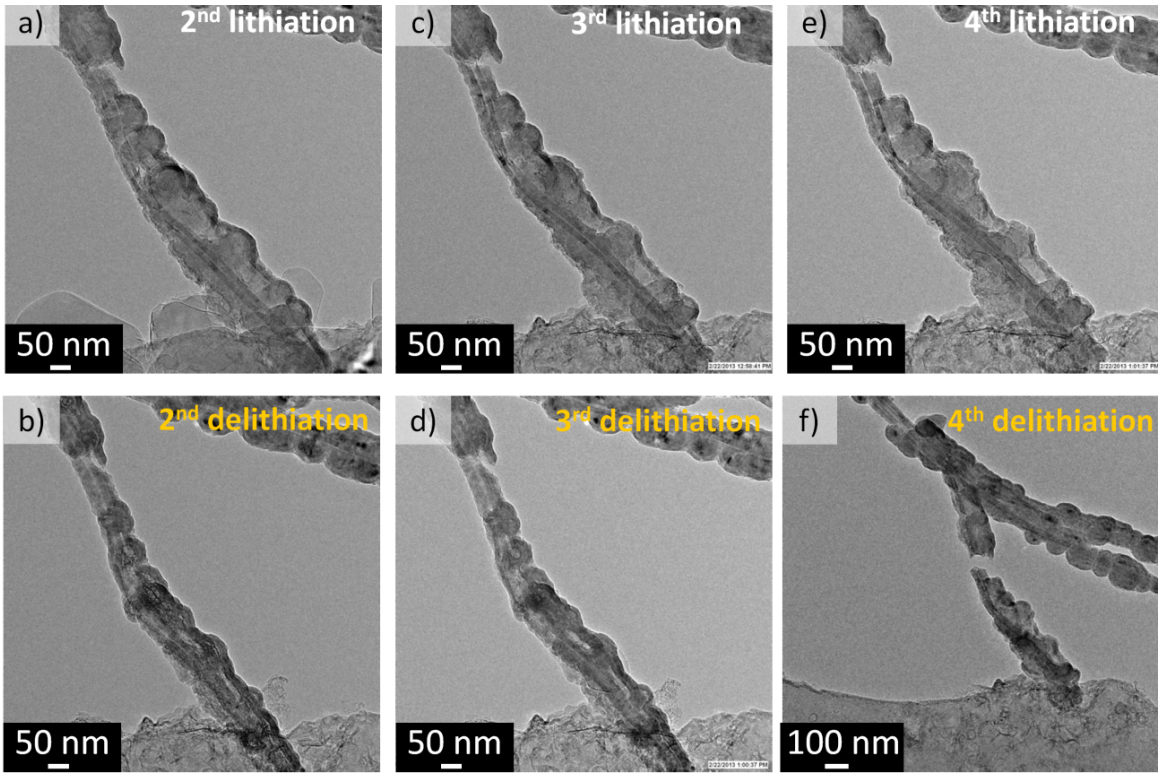

Figure 80. TEM micrographs of CNT-Si-C-Al2O_3 undergoing multiple (a, c, e) lithiation and (b, d, f) delithiation cycles *in situ*.

To verify the *in situ* TEM results, coin cells consisting of the same active VACNT materials were produced and each were cycled once (Figure 81). Al_2O_3, an electrical insulator, likely reduces the active material electrical conductivity because the side contacts between the individual tubes (in the compressed electrode) become more resistive. For these reasons, it was expected that the VACNT-Si-Al_2O_3 electrode would have the lowest first cycle reversible capacity.

Introduction of C increases the electrical and thermal conductivities of the VACNT-Si electrode and provides a higher Li diffusive material (in comparison to Si and Al_2O_3) thereby allowing for faster rate performance and higher capacity utilization (Figure 66). Since the presence of Al_2O_3 reduces the overall rate capability in comparison to a VACNT-Si-C electrode, it is expected that the capacity of VACNT-Si-C should be

higher than that of VACNT-Si-C-Al_2O_3. Lastly, VACNT-Si electrodes do not have a limiting Al_2O_3 layer so it was expected to have the highest first cycle reversible capacity.

Experimentally, the dealloying capacity for the VACNTs coated with combinations of Si, C, and/or Al_2O_3 show similar potential-capacity curves in regards to their potential hysteresis; however, their capacities differ. As expected, the uncoated VACNT-Si electrode demonstrates the highest first cycle dealloying capacity (~4100 mAh/g_{Si}), near the theoretical capacity of Si, followed by VACNT-Si-C (~3890 mAh/g_{Si}), VACNT-Si-C-Al_2O_3 (~3650 mAh/g_{Si}), and VACNT-Si-Al_2O_3 (~1430 mAh/g_{Si}). mAh/g_{Si}. Differences are attributed to the irreversible Li consumption upon the reaction of Li with Al_2O_3 over larger surface areas. Also, the conductivity of the alumina coated materials are likely lower and prior results with Ge (Figure 71) indicate that the presence of alumina leads to lower first cycle capacities.

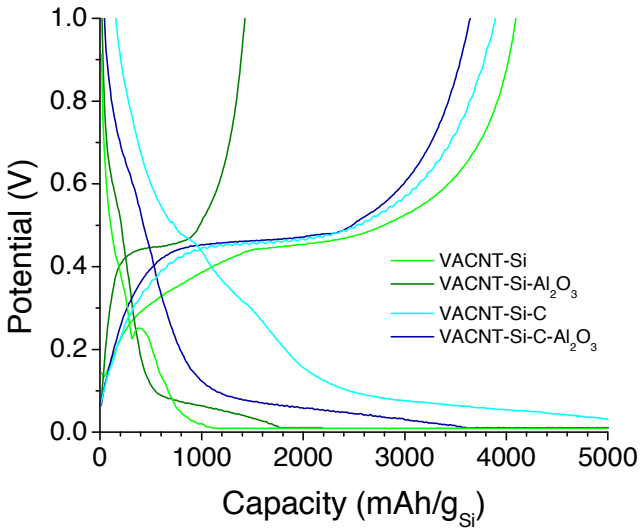

Figure 81. Potential-capacity curves for several different VACNT-Si based electrodes.

From the TEM micrographs obtained post-mortem (Figure 82), it was observed that the delithiated Si has formed porous Si contained within a thick (~22.5 nm) SEI layer. No dehesion of the Si from the CNT surface was observed. EFTEM (Figure 83 a - c) shows the composition of the CNT material via elemental mapping. The distribution of

C (Figure 83a) and Si (Figure 83b) are in good agreement with the structure of the synthesized VACNT-Si. It is hypothesized that the residual Li observed (Figure 83c) is due to the trapped Li in the SEI. The collected plasmon image (Figure 83d) is in good agreement with expected variation in densities of the layers in VACNT-Si.

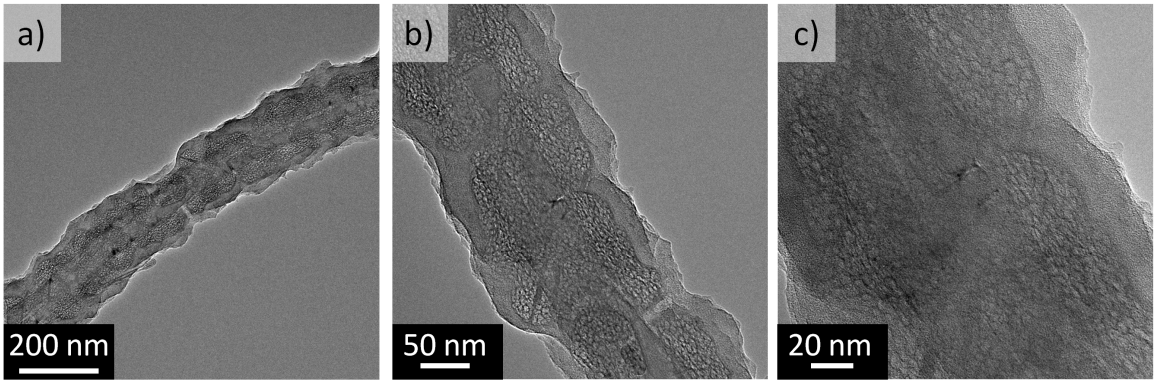

Figure 82. Post-mortem *ex situ* TEM micrographs for VACNT-Si.

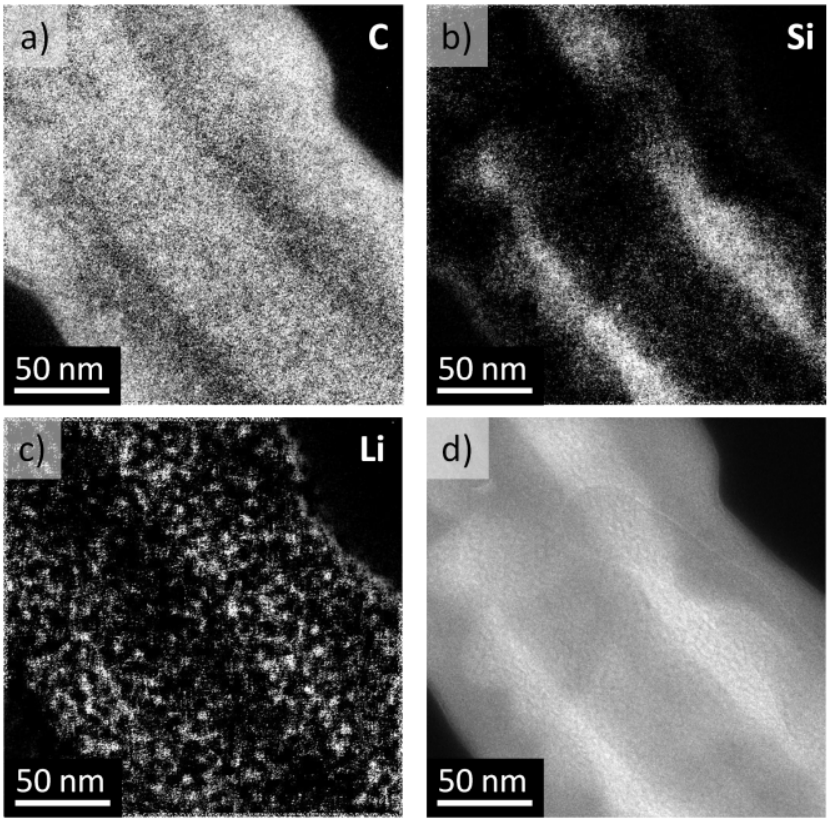

Figure 83. Post-mortem *ex situ* (a - c) EFTEM elemental mapping and (d) plasmon micrographs for VACNT-Si.

VACNT-Si-Al_2O_3 also formed porous Si (Figure 84 a,b) after the first delithiation step with no dehesion of Si from the CNT surface observed. Again, a thin SEI layer was observed. No cracking or separation of the alumina coating from Si was observed, in agreement with the lithiation of native alumina on an Al nanowire.[231]

VACNT-Si-C material also formed porous Si (Figure 85 a,b) after the first delithiation step with no dehesion of Si from the CNT surface observed. The post-mortem TEM images also showed that the C coating allowed for the formation of a very smooth SEI layer. This result suggests that the presence of C does help in the formation of a stable SEI on Si, in agreement with charge/discharge results (Figure 65 and Figure 66).

In agreement with the *in situ* TEM micrographs, the formation of porous Si in VACNT-Si-C-Al_2O_3 electrodes was observed in post-mortem analysis (Figure 86 a,b). As with the VACNT-Si-Al_2O_3materials, no dehesion of Si from the CNT surface or alumina cracking was observed. Further, a thin SEI layer was similarly observed.

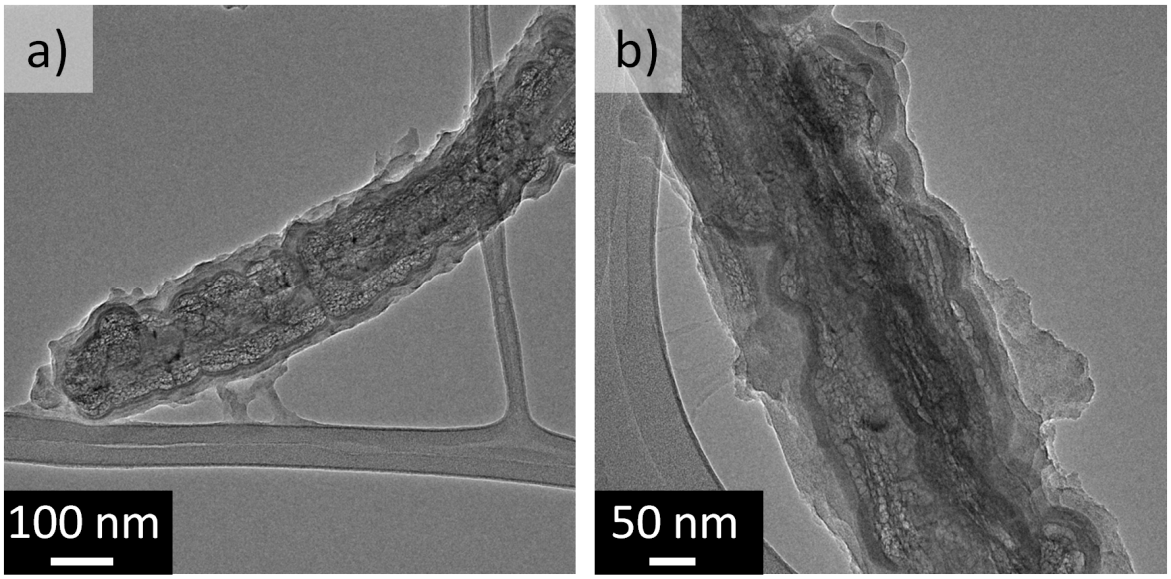

Figure 84. Post-mortem *ex situ* TEM micrographs for VACNT-Si-Al_2O_3.

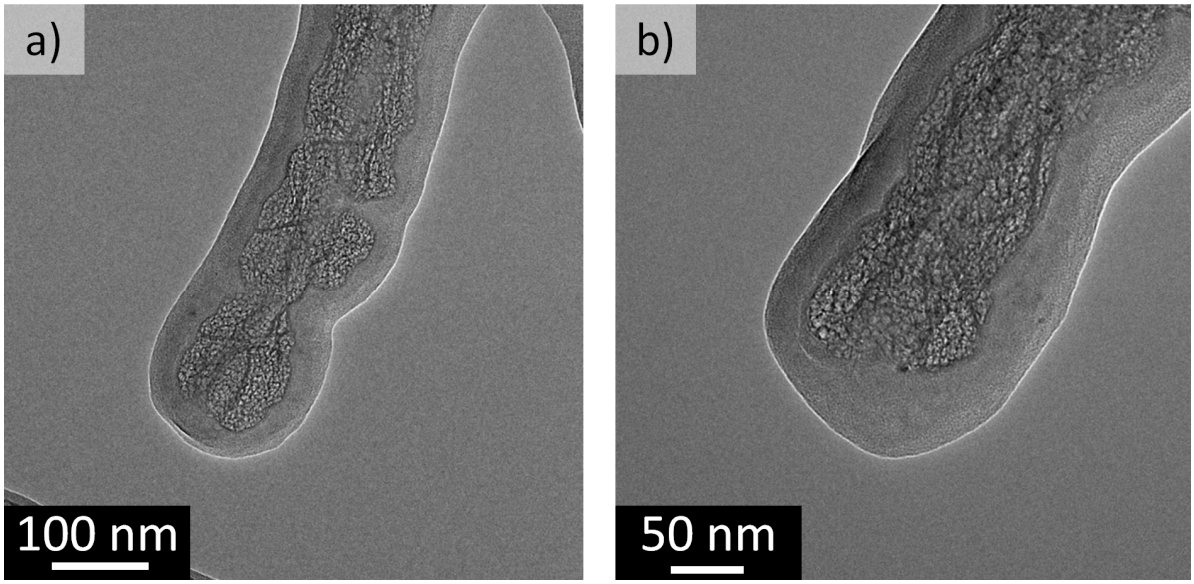

Figure 85. Post-mortem *ex situ* TEM micrographs for VACNT-Si-C.

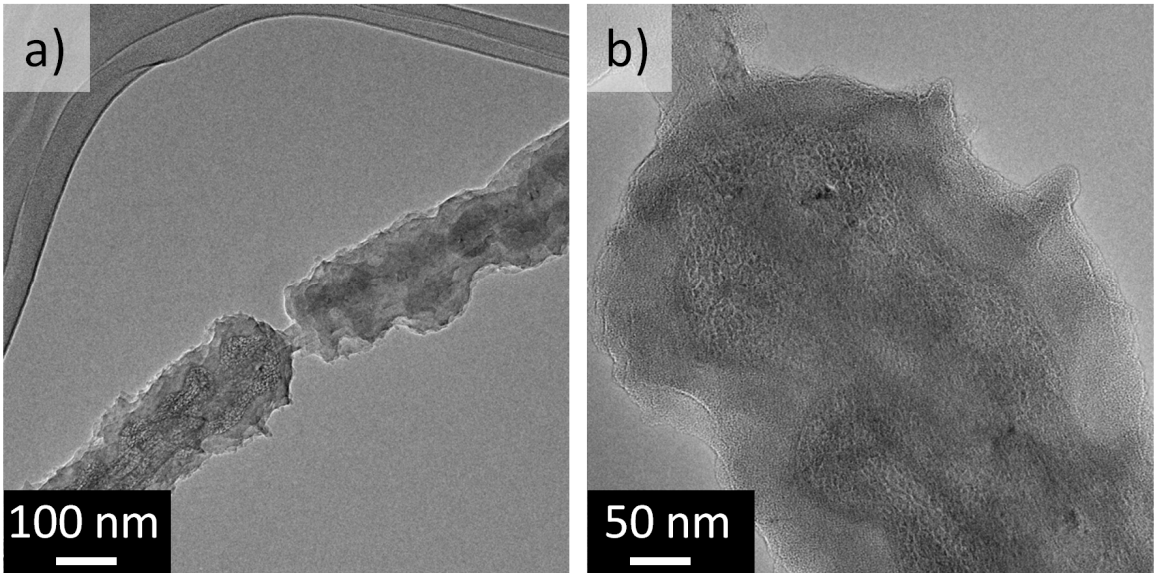

Figure 86. Post-mortem *ex situ* TEM micrographs for VACNT-Si-C-Al_2O_3.

Cyclic voltammetry was performed on VACNT-Si with and without alumina. All voltammograms have similar shapes. The first cycle of VACNT-Si and VACNT-Si-Al_2O_3 show a lithiation peak around 0.30 V which shifts to 0.17 V at later cycles with a delithiation peak potential (~0.60 V) for all cycles (Figure 87a). All peak currents are higher for the uncoated VACNT-Si than for the coated VACNT-Si, suggesting that the presence of alumina slightly decreases the electrical conductivity of the active materials. However, comparison of the peak potentials for a particular cycle for each type of material shows that there is no polarization effect due to the alumina.

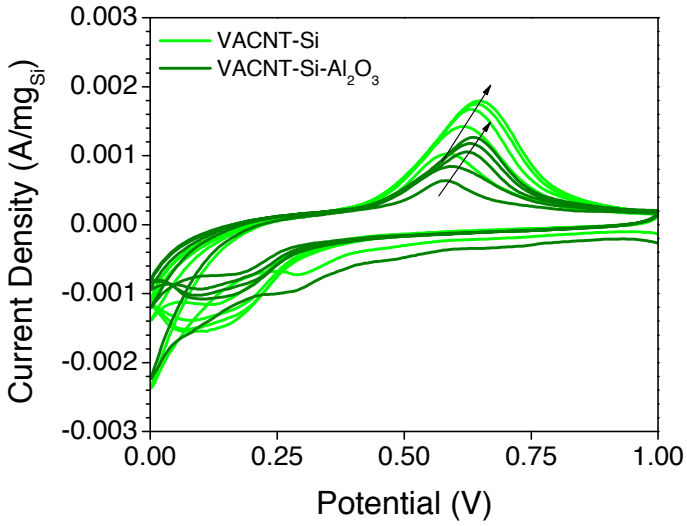

Figure 87. Cyclic voltammograms for VACNT-Si with and without Al_2O_3.

7.5 Conclusions

VACNT-Ge coated with alumina demonstrated better stability and capacity retention at multiple higher C-rates than VACNT-Ge without the alumina overcoating. *In situ* TEM showed that the alumina coated Ge nanoparticles were securely attached to the CNT surface throughout multiple cycles without fracture or cracking of the alumina layer. It is concluded that without the alumina coating, the integrity of the initial electrode morphology may be compromised due to active material loss. This may be a specific

feature of the VACNT-Ge studied here as the adhesion between the CNT and Ge is likely poor since sonication removes the Ge particles from the CNT surface. Loss of Ge particles at high rate may explain the lower measured capacities for VACNT-Ge. Unfortunately, *in situ* TEM investigation of VACNT-Ge (without alumina) could not be performed for those samples to confirm this hypothesis.

To complement the VACNT-Ge work, TEM studies and initial electrochemical behavior measurements of VACNT-Si based electrodes were performed. All investigated VACNT-Si electrodes exhibited the formation of porous Si as a result of cycling. *In situ* TEM allowed for the observation of the high deformability of the alumina coating without surface cracking or dehesion from the underlying Si or C.

Therefore, the electrochemical data and TEM observations suggest that thin surface layers of C or Al_2O_3 may contribute to increased cycling stability of high capacity thin films and particles with large curvature. It is likely that the thickness of the alumina film has an effect on the cycling behavior of the encapsulated material due to the low conductivity and Li diffusivity of alumina.

Although not explored here, other metal oxide coatings (TiO_2, ZrO_2) [237-238] have also been demonstrated to improve cycling performance, suggesting that multiple types of materials can serve to create a stable artificial SEI. However, the ability for a surface layer to improve the stability of battery materials may not be wholly dependent upon the coating composition but rather its mechanical properties at the nanoscale. Bulk alumina is extremely hard yet at the nanoscale, when lithiated, it can easily, and unexpectedly, deform and accommodate volumetric expansions. This difference in behavior is likely due to nano-thick alumina's ability to accommodate lithiation stresses without cracking. It is speculated that depending on the nature of the stresses generated by lithiation, there could be a critical film thickness beyond which the alumina thin film would crack. However, that thickness may be beyond practical limitations due to the poor conductivity and Li diffusivity of alumina.

CHAPTER 8

SUMMARY OF PERFORMED RESEARCH

8.1 Synthesis Considerations

Selection of Si Film Thickness

With continued cycling of large volume expansion materials, cracks and material fracture [124] can initiate and cause: 1) loss of electrical contact between particles and with the current collector and 2) exposure of the fresh surface to electrolyte and formation of a new SEI.[46] Diffusion induced stresses result from Li concentration gradients in the particle give rise to non-uniform volume changes. If the volume changes in a particle due to lithiation occur uniformly throughout, internal stresses will not be generated thus fracture may be avoided.[9]

Nanomaterials have shorter paths for diffusion and may accommodate the stresses without fracture.[23, 31] In addition, small size of particles or thin films yields short diffusion relaxation times as the relaxation time scales with the square of the diffusion distance.[31] Short relaxation times correspond to fast dissipation of strains due to much more uniform lithiation at a constant current density.[5, 7, 130] Therefore, the generated stresses can be lessened and resulting fracture could be avoided in smaller (nano-) size particles and coatings.[9] The aforementioned theoretical observations were the basis of significant research to understand the effect of lithiation on volume expansion, stress evolution, and structural and morphological changes of nano-Si. From those studies, a critical particle size, below which a particle will not crack, can be approximated. In general, the effect of diffusion induced stresses on the particle can vary depending upon the particle's crystallinity, size, and morphology.

For example, *in situ* TEM microscopy observations reveal that Si nanowires of several hundred nanometers in diameter did not fracture as a result of alloying and dealloying, despite the volume changes.[239] An analysis of the fracture mechanics of a Si nanowire determined that Si nanowires with diameters less than 300 nm would not fracture, even if large pre-existing cracks are present. *In situ* TEM studies of spherical crystalline Si particles suggest a critical particle size of 150 nm.[127] In contrast, larger hydrogenated amorphous spherical particles of diameter up to 870 nm were cycled without fracture.[240] Two-dimensional Si thin films of thicknesses greater than 250 nm fracture [241]; however, delamination and fracture of 50 nm thick Si films was not observed.[131] In addition to the thickness of the Si films, the substrate and the adhesion of the Si film to it affects the fracture and delamination behavior.

Through consideration of the literature and the type of C substrate, approximations for maximum suitable Si thin films were assumed as 50 nm thick Si for graphene-based electrodes and 300 nm total diameter for CNT-Si electrodes. However, as C substrates exist within a complex network with other particles, these values may not be practical for all pore structures.

For example, one can calculate the minimum porosity of a VACNT-Si-C electrode based on the CNT radius and coatings thicknesses by calculating the minimum spacing between individual VACNTs using the cross-sectional surface areas of the VACNT and current collector.

Here, it is assumed that all VACNTs are perfectly aligned 1-D cylinders each of which are the same radius (r_{CNT}) and length (l_{CNT}) and uniformly coated with the same thickness of Si (t_{Si}) and C (t_C). Further, it is assumed that all VACNTs are well-adhered to the current collector with negligible interfacial resistance.

The total CNT cross-sectional surface area ($A_{T,CNT}$) will be equal to the cross-sectional surface area of an individual coated CNT multiplied by the number of CNTs per current collector surface area (N_{CNT}):

$$A_{T,CNT} = \pi N_{CNT}(CNT_{VC} r_{CNT} + Si_{VC} t_{Si} + C_{VC} t_C)^2 \quad (13)$$

where CNT_{VC}, Si_{VC}, and C_{VC} correspond to the volume change of CNT, Si, and C with lithiation, respectively. For example, a 300% volume change in Si corresponds to Si_{VC} of 4. Determination of the volume change in nanocomposite systems may not be equivalent to the volume change in particles of single composition due to mechanical constraints from neighboring layers.

The minimum center-to-center distance between CNTs ($d_{CNT-CNT}$) can be calculated as:

$$d_{CNT-CNT} = 2(CNT_{VC} r_{CNT} + Si_{VC} t_{Si} + C_{VC} t_C) \quad (14)$$

The percent porosity (P) of the electrode remaining after volume expansion for a specified VACNT-Si-C electrode is equal to:

$$P = \frac{A_{CC} - A_{T,CNT}}{A_{CC}} \cdot 100 \quad (15)$$

The porosity will decrease as the number of coated VACNTs increase per current collector surface area and as the total radius increases (Figure 88). There is a limit to both the number and radius of CNTs, especially for CNTs coated with high volume expansion materials. For increased areal capacities, the remaining porosity after lithiation should be as low as possible.

Through consideration of the pore structure and cell requirements, such as energy density and rate capability, the optimal thickness of Si will vary. Discussion describing

how to correlate the areal capacity of an electrode to the thickness of Si is provided in Section 8.2 for VACNT-based anodes.

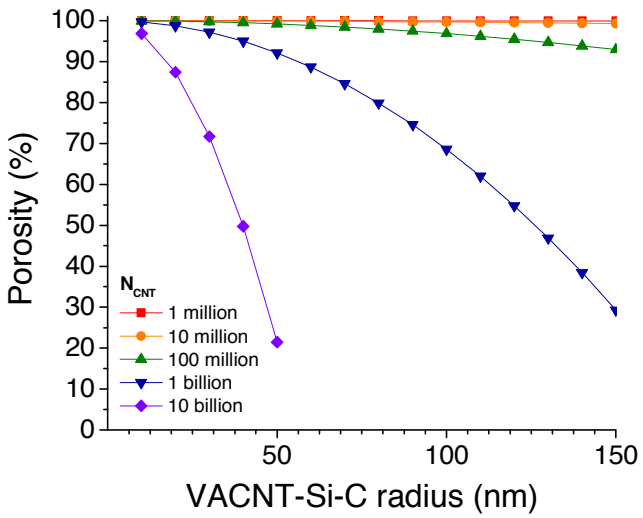

Figure 88. Percent porosity versus total coated VACNT radius for multiple number densities of carbon nanotubes per current collector surface area.

Selection of Thin Film Deposition Process

Initial research considered both CVD and PECVD as viable processes to deposit Si thin films on C substrates. The advantage of PECVD is that deposition can occur at lower temperatures (200 – 300 ^{o}C) than CVD which requires slightly higher temperatures depending on the crystallinity and coverage required. While PECVD of SiH_4 has been utilized to coat VACNTs with Si, the plasma penetration depth into the VACNTs is limited by the density of CNTs with higher density leading to a shallower plasma penetration depth (Figure 89). With further investigation of the PECVD parameters (pressure, temperature, plasma power), it may be possible to achieve uniform coatings on porous, thick substrates (> 500 μm); however, they have not been determined yet. Lastly, the PECVD system used non-adjustable high gas flow rates (1000 sccm) thus limiting the ability to coat powder material without significant material loss. For these reasons, thin Si coatings on both graphene and CNT substrates were achieved using low-pressure CVD

decomposition of SiH_4. Ge was deposited on VACNTs via low-pressure CVD of GeH_4. PECVD of Ge films was not considered for this research for the same reasons as for Si films and due to lack of availability of suitable equipment.

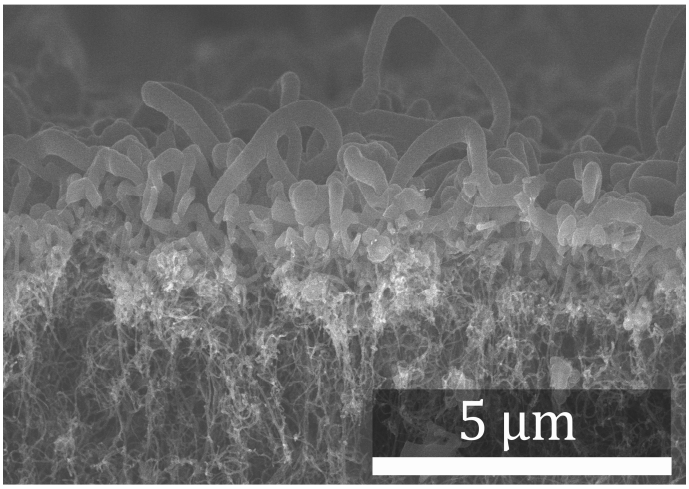

Figure 89. Cross-section SEM image of VACNTs coated with Si deposited via PECVD.[195]

Selection of Thin Film Deposition Process Parameters

To achieve a uniform coating on the complex electrode geometry via thermal CVD, the coating should be deposited in a kinetically controlled regime so that sufficient time for the atoms to diffuse throughout the structure is obtained. Both low pressure and low reaction temperature can aid in developing a surface-kinetics rate limiting step.[74] Through control of the process parameters, the resulting deposition rate, crystal structure, and coating uniformity are tunable. The thickness of the deposited material at a given temperature and pressure can be controlled by monitoring the deposition time. For example, the diameter of deposited Ge nanoparticles (Figure 90) or Si thin films (Figure 91) can be controlled through variation in synthesis time for the same temperature and pressure. The crystallinity of the material can also be controlled as higher temperatures yield greater crystallinity.

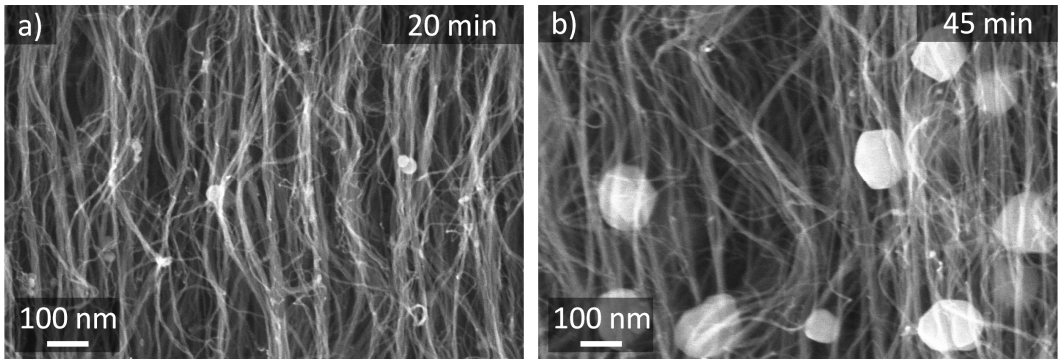

Figure 90. Cross-sectional SEM images of VACNTs coated with Ge via CVD deposition with growth times of (a) 20 and (b) 45 minutes at 400 °C.

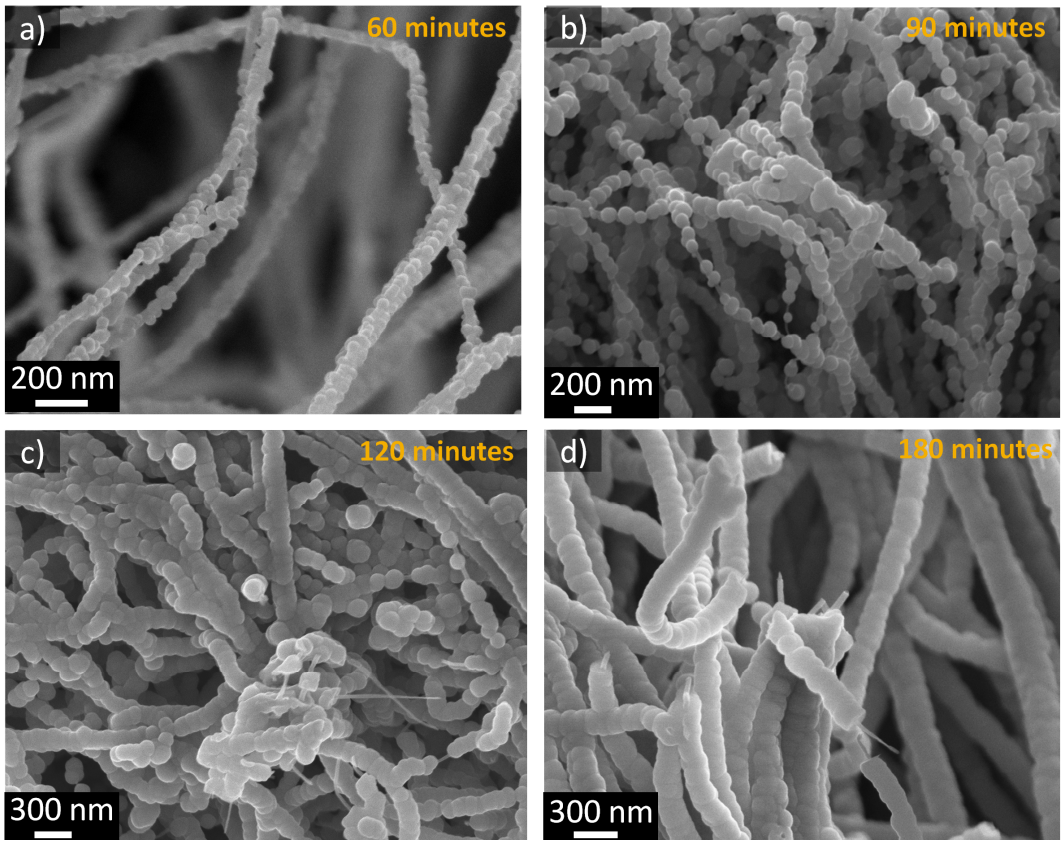

Figure 91. Cross-sectional SEM images of VACNTs coated with Si via CVD deposition with growth times of (a) 60, (b) 90, (c) 120, and (d) 180 minutes at 500 °C.

The quality of the mechanical properties and adhesion of the resulting film are highly substrate dependent due to the stresses generated at the film-substrate interface. These stresses reside in the material even when the system is not under a load.[88]

Differences in thermal expansion coefficients of the film and the substrate lead to the production of thermoelastic stresses as the temperature is changed (most commonly resulting from cooling of the substrate from the reaction temperature).[88, 242] The thermoelastic stresses cause film deformation, $\varepsilon_{thermal}^{Film}$, calculated by:

$$\varepsilon_{thermal}^{Film} = \int_{T_i}^{T_f} [\alpha_{Substrate}(T) - \alpha_{Film}(T)]dT \quad (16)$$

where T_i and T_f are the initial and final temperature, respectively, and $\alpha_{Substrate}$ and α_{Film} are the coefficients of thermal expansion (CTE) of the substrate and film, respectively.[242]

Applying equation (16) to Si deposited on graphene sheets or MWCNTs allows for calculation of the expansion/contraction of Si after cooling from the deposition temperature using known CTE values (Table 3). For all C substrates, Si deposition occurred at 500 ^{o}C and the samples were cooled to room temperature (22 ^{o}C). Under these conditions, using the values from Table 3, the Si films contract ~0.45% and up to ~3.1% on graphene and MWCNT substrates, respectively. During cooling, the contraction of Si coupled with the expansion of the C substrates (due to their negative CTE) will generate compressive forces on the C substrate from Si. Graphene and CNTs serve as good substrates as they can withstand compression without fracture.[243-244] Higher deposition temperatures and differences in CTE significantly increase the thermoelastic deformation.[242] Thus, the adhesion between two different materials is highly dependent upon the processing temperatures used to create them.

There is significant scatter in the values for CTE in the radial direction of MWCNTs with variations in tube diameter. However, in scenarios in which the CTE of the C substrate is less than that of the deposited film, the deposited film will compress the C substrate by a factor related to the difference in CTE and the compressibility of the C substrate. It has been suggested that radial compression of CNTs can lower their thermal

conductivity [245] so optimization of deposition temperature to achieve a well-adhered coating without sacrificing thermal conductivity should be explored.

Cracking and delamination of the deposited films were not observed in SEM and TEM micrographs recorded throughout the synthesis process of the composite materials. SEM and TEM studies indicate that the bonding between Si and C in VACNT-based electrodes is strong as no delamination is observed.

Not only is the Si-C interface subject to inherent stresses from processing, stresses are commonly generated during the lithiation process due to corresponding changes in volume. The stresses will vary in magnitude due to volume changes occurring in multiple Li ion interacting materials and possibly the overall material's curvature. The combination of these stresses may contribute to different levels of degradation at different rates of cycling.[154] However, delamination between layers after charge/discharge was not observed in the performed TEM studies (Section 7.4).

For composite anodes, the differences in volume expansion during cycling may pose a significant problem because of the danger of interfacial fracture caused by stresses resulting from the battery cycling.[9] Maintaining electrical conductivity across all interfaces is a crucial factor in capacity retention. Due to different volume changes in C and Si during battery operation and mechanical constraint from neighboring layers, stresses at the interface may lead to battery failure. The adhesion between the coating and the substrate during CVD growth may also affect the adhesion during cycling. In this work, C substrates are externally coated with Si and the volume changes of lithiated Si films should occur via variations in film thickness outward from the C surface.

Consideration of the interface between the various layers in multilayer C-based composite electrodes and the effect on the fracture mechanics and cycling stability would be useful in the design of future nanocomposite materials for Li-ion cells. It is expected that the high conductivities of the CNT and their high growth rates will allow for higher power capabilities for VACNT-Si electrodes in comparison to Si nanowire electrodes.

However, there may be limitations to the degree of lithiation of composite materials or in the layer thicknesses due to interfacial effects between the layers.

Table 3. Linear thermal expansion coefficients for selected materials at 25 °C.[88, 242, 246-251]

Material	α (x 10^{-6} $°C^{-1}$)
Alumina	5.4
Germanium	5.75
Graphene	-8
Graphite	8
Hydrogenated amorphous carbon	1.5 to 7
Hydrogenated amorphous silicon	1
MWCNT (radial)	-64.8 to -23.7
MWCNT (axial)	-13

8.2 Pore Formation in Lithiated Si

In this research, Si films and Ge particles on CNTs were observed to form porous Si or Ge as a result of electrochemical cycling. This phenomenon has also been observed in other studies for both Si and Ge materials of 1-D and spherical morphologies.[233] Interestingly, porosity was found in all samples that were exposed to free hydrogen during synthesis through either vapor deposition of SiH_4, GeH_4, or C_2H_2. Lithiation of particles or morphologies created from single crystal wafers did not show porosity after cycling. To the author's knowledge, lithiation induced porosity has not been observed in non-hydrogenated Si or Ge. Fourier transform infrared spectroscopy (FTIR) studies showed that the amount of retained hydrogen in VACNTs coated with amorphous Si deposited by PECVD of SiH_4 varies with synthesis temperature and the area of the CNT coating covered (Figure 92).[195] Higher temperature deposition or PECVD methods may enhance the amount of retained hydrogen. Models to explain the formation of pores have been proposed, but they do not consider the effect of retained hydrogen.

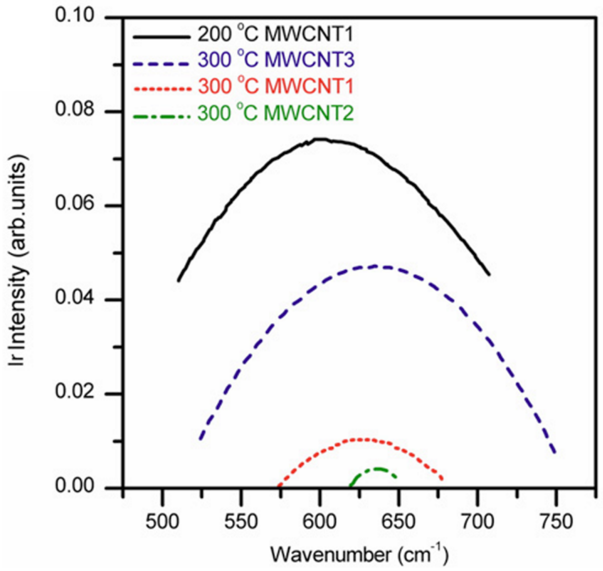

Figure 92. Gaussian fitted FTIR peaks for different VACNTs samples coated with a-Si:H at different temperatures.[195]

Si-coated CNTs, produced through methods similar to in this work, generated pores when the active materials were tested between 0.17 – 1.0 V vs. Li/Li^+ yet pores were not observed when the delithiation cut-off was lowered to 0.6 V vs. Li/Li^+ (Figure 93).[252] More extensive pore formation was observed post-mortem for CNT-Si tested between 0.05 – 1.0 V. These results suggest that the extent of pore formation can be limited by the cycling conditions. Limiting the potential window for charge/discharge cycling will limit the capacity but may reduce capacity fading.[252]

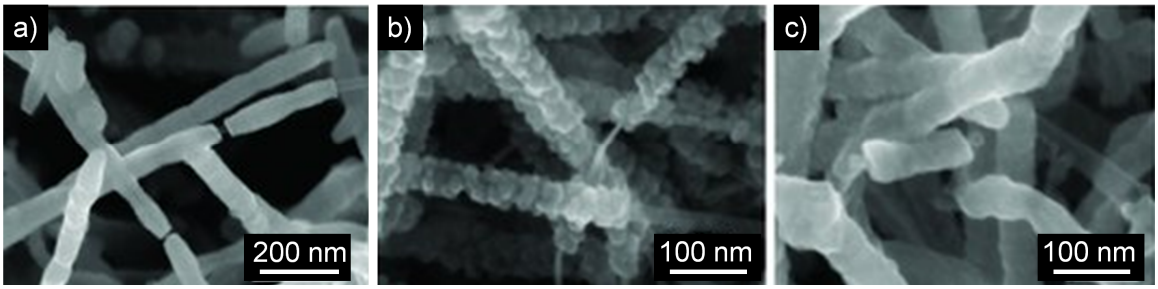

Figure 93. SEM images of CNT-Si: (a) as synthesized, (b) after battery cycling between 0.17 – 1.0 V vs. Li/Li^+, and (c) after battery cycling between 0.17 – 0.6 V vs. Li/Li^+. *Adapted from* [252].

A model was generated to explain the evolution of pores in Si films on CNTs.[252] In this model, the Si coating was assumed to be well-adhered to a rigid CNT core. Experimental observations of Si remaining attached to the CNT surface during cycling (Section 7.4) as well as the theoretical calculations of thermal stresses (Section 8.1) suggest that a well-adhered Si film is a reasonable assumption.

In the reported model, both elastic and plastic contributions to the strain rate were considered. From the analysis, it was determined that the lithiated Si shell extends radially during lithiation since axial expansion is constrained by the CNT. Previous work on Si nanopillars and nanowires show that 1-D Si will expand axially if unconstrained or weakly adhered to a substrate.[14, 128] When weakly adhered, the porous Si will delaminate from the substrate. Delamination was not seen in previously reported work [252-253] or the research performed here for Si-coated CNTs, further confirming the strong bonding between the CNT and the Si coating. Since the stresses during lithiation are compressive, it was hypothesized that voids would not form during Li alloying; however, those stresses are tensile during delithiation and act as the driving force for pore nucleation and growth.[252] This hypothesis is consistent with the *in situ* observations in this research that showed void formation upon delithiation only (Section 7.4).

Further, it was hypothesized that low Li concentration (corresponding to a more brittle Li-Si material) aids in the formation of pores within Si. Another identified contribution was that, for higher Li concentrations, the SEI will generate additional tensile stresses which will help nucleate pores.[252] However, the described model does not mathematically account for the SEI layer (or any film on the Si surface). As the SEI, or any overcoating, imparts additional stresses on the Li-Si film, the effect of such layers should be extended for this model, assuming that the change in mechanical properties due to lithiation of such layers can be identified.

To elucidate the mechanical properties, studies to perform nanoindentation of lithiated alumina films were initiated. However, due to the requirements of

nanoindentation sample thickness and the poor conductivity of such thick films, lithiation of the alumina layer was not observed. Future work to investigate the effect of overcoatings should include performing electrochemical-mechanical studies to incorporate the mechanical properties as a function of Li concentration. Consideration of the chemical environment of the lithiated Si particle may further contribute to a complete understanding of the Li-Si system. For example, HF, a by-product of side reactions in fluorine containing electrolytes, may also etch unlithiated regions of Si.

8.3 VACNT-based Anode Design

In this section, the parameters of the electrode that affect the areal capacity of and the voltage drop across VACNT-based structures will be discussed. Although the treatments will focus on Si and C, the methods employed can be adapted for VACNTs coated with other Li-alloying materials. Through determination of the relevant factors contributing to performance characteristics, generalizations regarding the synthesis of the electrodes can be stated.

Factors contributing to the areal capacity of VACNT-based electrodes

The areal capacity of a VACNT coated with a Li alloying material can be approximated by:

$$C_A = \frac{l_{CNT}(C_{V,CNT}w_{CNT} + C_{V,TF}w_{TF})}{A_{CC}} \quad (17)$$

where $C_{V,CNT}$ is the volumetric capacity of CNTs (mAh/cm^3), w_{CNT} is the weight fraction of CNTs, $C_{V,TF}$ is the volumetric capacity of the thin film coating (mAh/cm^3), and w_{TF} is the weight fraction of the thin film coating. Equation 17 can be easily extended for multi-layer coatings by adjusting the numerator to account for the volumetric capacity and

weight ratio of all the layers. In Equation 17 and subsequent equations concerning the length of the CNT, it is assumed that the thickness of the electrode is equal to the CNT length:

$$t_{electrode} = l_{CNT} \tag{18}$$

As a sample calculation, the areal capacity loading as a function of VACNT length, weight fraction Si, and volumetric capacity was considered. The theoretical volumetric capacity for Si (2190 mAh/cm^3) and C (756 mAh/cm^3) [29] was adjusted by assuming a porous electrode (40% porosity for C and 50% porosity for Si) on a 1 cm^2 current collector. It should be noted that achieving theoretical volumetric capacity for CNTs is unrealistic; however, the value is used here for qualitative analysis.

Figure 94 shows that VACNTs of 1 mm have significantly high areal capacity loadings even without Si. Typical commercial areal capacity loadings are ~3 mAh/cm^2.[29] Development of very high areal capacity loadings (>> 3 mAh/cm^2) are very challenging. First, from a manufacturing perspective, the creation of high areal capacity electrodes through increases in thickness faces several limitations (Section 6.1). VACNTs may aid in the development of high capacity materials, but further studies investigating practical limitations of VACNT-based electrodes should be performed. Second, research of high areal capacity electrodes may prove difficult since new electrode materials are commonly tested versus a Li counter electrode. For example, an electrode with an areal capacity of 30 mAh/cm^2 will have a 1C current density of 30 mA/cm^2. At current densities above 1 mA/cm^2, the formation of dendrites and the SEI resistance on Li increase [29] and electrodes with high areal capacity loadings exhibit unstable performance. Third, an equally high capacity loading for the cathode would be necessary to accommodate high capacity loading of the anode. If a cathode has a lower areal coating, Figure 94 indicates

that significant reductions in the VACNT height for VACNT-Si can be used to allow for increased thicknesses of the cathode, if the total cell volume is constant.

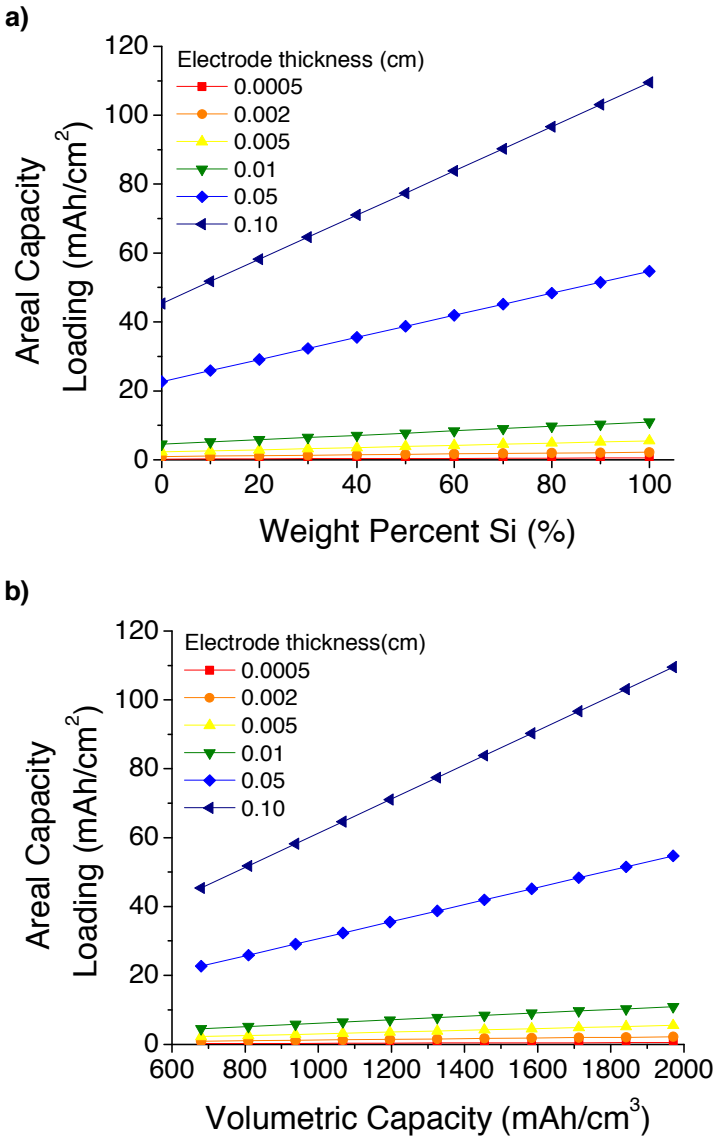

Figure 94. The areal capacity loading of a VACNT-based electrode for varying VACNT lengths as a function of the (a) weight percent of Si and (b) the volumetric capacity.

From examination of Figure 94, one can identify the weight percent of Si necessary for a specific application. Determination of t_{Si} corresponding to a particular w_{Si} for VACNT-Si electrodes can be approximated by:

$$t_{Si} = \sqrt{\frac{w_{Si}\rho_{CNT}r_{CNT}^2}{\rho_{Si}(1-w_{Si})} + r_{CNT}^2} - r_{CNT} \quad (19)$$

where ρ_{Si} is the Si density (g/cm^3) and $\rho_{CNT}$is the CNT density (g/cm^3). For example, if the CNT diameter is 50 nm, then the thickness of the Si coating to achieve a 80 wt. % Si would be ~21 nm.

Representative Si film thickness values for varying CNT diameters are shown in Figure 95. When the diameter of coated VACNTs approaches that of the critical crack dimension (assumed as 300 nm), the Si weight percent is extremely high (Figure 96). Further, such thick coatings would require a high degree of porosity within the VACNT structure. Rearranging equation (19), w_{Si} can be calculated by varying t_{Si} via:

$$w_{Si} = \frac{(t_{Si}^2 + 2r_{CNT}t_{Si})\rho_{Si}}{r_{CNT}^2\rho_{CNT} + (t_{Si}^2 + 2r_{CNT}t_{Si})\rho_{Si}} \quad (20)$$

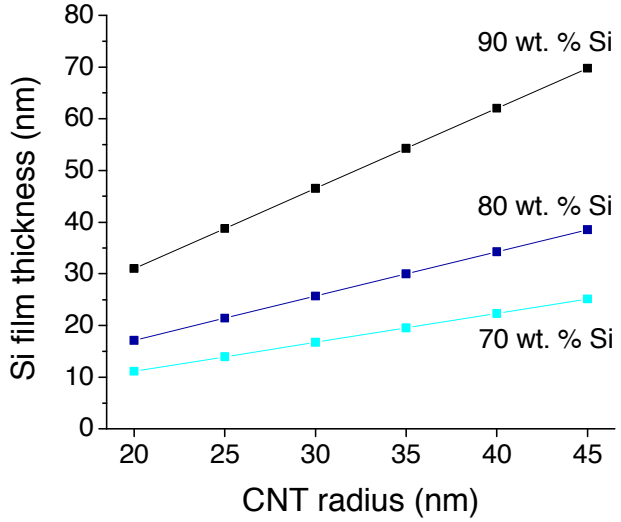

Figure 95. The Si film thickness needed to create a desired Si weight percent for a VACNT-Si electrode for varying CNT radii.

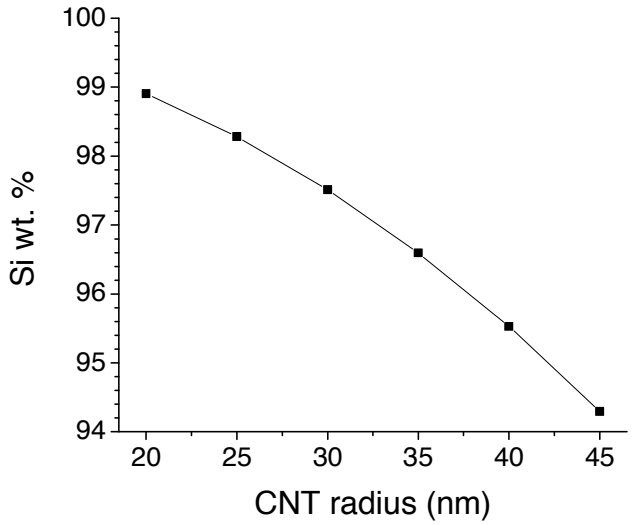

Figure 96. The weight percent of Si for varying CNT radii coated with the maximum thickness of Si such that the total coated VACNT radius is less than 150 nm.

Factors contributing to the voltage drop across VACNT-based electrodes

The performed research demonstrated that 1 mm VACNT-based electrodes do not significantly degrade when tested in half cells versus Li metal at low to moderate C-rates. However, investigation of the dependency between VACNT length and performance was not conducted. Here, analysis of the dependency of VACNT length on the potential drop V_{cell} (V) across the cell is discussed. V_{cell} is related to the resistance of the cell (R_{cell}, Ω) and the current (I, A) passed by:

$$V_{cell} = IR_{cell} \tag{21}$$

R_{cell} is the sum of electrical resistances across the cathode ($R_{total,c}$), the separator ($R_{total,s}$), and the anode ($R_{total,a}$) such that:

$$R_{cell} = R_{total,c} + R_{total,s} + R_{total,a} \tag{22}$$

The electrical resistance across the separator is related to the solution resistance through its thickness. Assuming a constant separator thickness, $R_{total,s}$ will be constant as the thickness of the cathode and anode increase with VACNT length and was neglected in the following calculations. The total resistance for an electrode is dependent upon several factors including the electrode resistivity and the resistance of any surface films. VACNTs coated with a cathode material were not synthesized in this research; therefore, the resistivity of such a cathode is not known. However, the contribution of the anode to the cell potential drop will be the same for the same current so the contributions from the cathode are ignored in this treatment. Further, for simplicity, electrical resistance changes due to charge and discharge of the anode were not considered.

Analysis of the equivalent circuit of a VACNT-based anode can approximate the practical maximum VACNT length for a given application. Figure 97 is a schematic of an equivalent circuit that can be used to describe the electrical contributions of the anode. It consists of several key components: the electrolyte solution resistance (R_{soln}), the charge transfer resistance for the anode (R_{ct}), the electrode resistance for the anode ($R_{electrode}$), the current collector/active material interfacial resistance for the anode ($R_{interface}$), the resistance of the SEI on the anode (R_{SEI}), a capacitance from the double layer (Q_{dl}) and for the SEI (Q_{SEI}), and a Warburg element (Z_D) for solid-state diffusion through the active material.

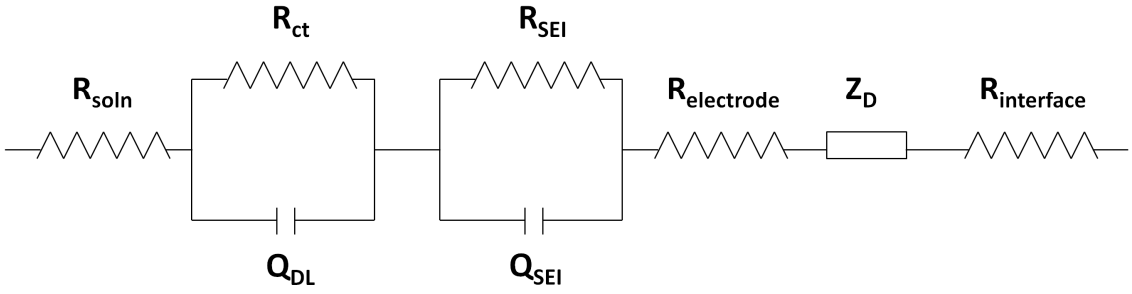

Figure 97. Equivalent circuit for a Li-ion electrode.

Assuming a constant N_{CNT}, the interfacial resistance will not vary as it is dependent on the number of CNTs in electrical contact with the current collector and the resistance of that point contact, rather than the CNT length. In general, it is assumed that the interfacial resistance will be very small such that it can be ignored even as N_{CNT} changes. Likewise, the Warburg element for solid-state Li diffusion throughout the CNT is dependent upon the composition and crystal structure of the coated-CNT and is independent of the CNT length. Here, constant phase elements are used rather than an ideal capacitor for the double layer and SEI to account for surface roughness of the particle.[254] Commonly, generating an equivalent circuit that models the measured impedance data relies upon fitting elements such as constant phase elements. For the purposes of approximating the voltage drop along the CNT length the capacitive behavior of these elements is ignored. The charge transfer resistance is also ignored in the calculation as it is dependent upon the temperature and exchange current across the electrolyte/electrode interface and is independent of the CNT length.[19] Therefore, as the VACNT length varies, only R_{soln}, R_{SEI}, and $R_{electrode}$ should be affected and a simplified equivalent circuit can be drawn (Figure 98).

Figure 98. A reduced equivalent circuit based on length-dependent elements for an electrode.

The potential drop across the electrode thickness should be minimized to achieve uniform lithiation throughout. An increase in electrode thickness will correspond to an increase in the electrode resistance per unit surface area of the current collector since:

$$R_{electrode,A} = \frac{\rho_{electrode} t_{electrode}}{A_{electrode}} \quad (23)$$

where $\rho_{electrode}$ is the resistivity of the electrode (Ω·cm) and $A_{electrode}$ is the superficial surface area of the electrode active material (cm^2). For VACNT-based electrodes, $R_{electrode}$ can be determined by multiplying the electrical resistivity of the VACNT-based composite material ($\rho_{CNT-composite}$) by the electrode thickness and then multiplying by the electrode porosity and normalizing by current collector mass:

$$R_{electrode,A} = \frac{\rho_{CNT-composite} t_{electrode}}{A_{CC}} P \quad (24)$$

where $\rho_{CNT-composite}$ is the resistivity of the VACNT-Si-C composite (Ω·cm) and is dependent upon the thicknesses of Si and C.

The SEI resistance can be calculated from experimental values of the resistance and the thickness of the SEI. For the following example calculation, a 10 nm thick SEI with a resistance of 100 Ω·cm^2 was used.[46] Here, the SEI resistance of a single nanotube was calculated and then divided by N_{CNT} to calculate the total resistance of the SEI per unit surface area ($R_{SEI,A}$). The solution resistance can be calculated by [19]:

$$R_{soln} = \frac{l}{\kappa_{soln} A} \quad (25)$$

where κ_{soln} is the conductivity of the electrolyte (S/cm), l is the thickness of the electrode (cm), and A is the effective surface area of the current collector (cm). A is determined by:

$$A = A_{CC} - A_{T,CNT} \quad (26)$$

l is traditionally defined as the distance between two electrodes (Figure 99) and can be defined as:

$$l = l_c + l_s + l_a \quad (27)$$

where l_c is the cathode thickness, l_s is the separator thickness, and l_a is the anode thickness. In reality, for electrodes with tortuosity, the values of the various length parameters will be longer than the electrode thickness. As an example, for an electrode with tortuosity (τ):

$$l_{electrode} = \tau t_{electrode} \quad (28)$$

To calculate l, one must know the thickness of each electrode which is dependent upon the areal capacity loading and electrode composition. As the contributions to the potential drop across the cell from the cathode and the solution resistance across the separator are not considered in this treatment, a value of l that equals the electrode thickness was used. In such a case, $\tau = 1$.

From the reduced equivalent circuit (Figure 98), the total contributions to $R_{total,A}$ can be written as:

$$R_{total,A} = R_{soln} + R_{SEI,A} + R_{electrode,A} \quad (29)$$

Ohm's Law can then be used to calculate the potential drop across the electrode at specified currents.

For the following calculations, the change in resistivity for a broad range of CNT diameter and Si and C coating thicknesses were ignored as the variation in coating

thickness on the electrical resistivity was not experimentally measured or simulated. An electrolyte conductivity of 1 mS/cm for a 1M $LiPF_6$ in a 1:2.7:6.3 by volume mixture of PC:EC:DMC was used.[255]

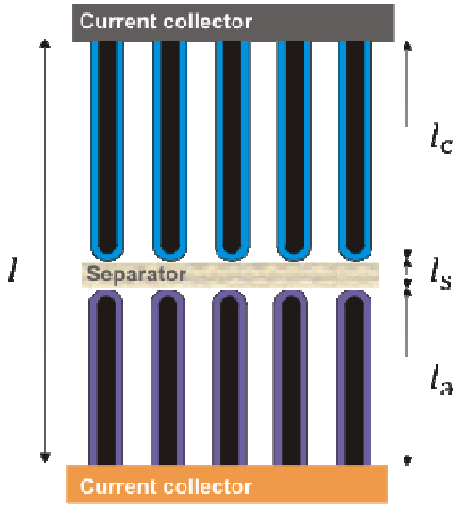

Figure 99. Schematic of a single Li-ion cell consisting of VACNT-based electrodes. The length of the electrodes and the separator are identified in relation to the total separation distance between electrodes.

Calculation of potential drop across the anode assuming a constant number of VACNTs per superficial current collector area:

Constant N_{CNT} equates to constant electrode porosity. The porosity of a VACNT film may be controlled by repeatedly controlling the catalyst and synthesis conditions such that with increased synthesis time only the length of VACNTs changes. As the electrode thickness increases with constant porosity, the areal capacity loading increases (Figure 100). Thus, thicker electrodes of the same porosity will have higher currents than thinner electrodes for the same C-rate.

The first calculation considers an electrode with ~34% porosity. Values for relevant parameters in this calculation are listed in Table 4. Analysis shows that as the length of the electrode increases, the voltage drop increases (Figure 101). The potential drop changes with the square of the electrode thickness as both the current and resistance

follow a linear relationship with the thickness. The individual contributions to the total resistance from the SEI, electrolyte, and the electrode are not equivalent though with the solution resistance dominating (Figure 102). Thus, thick electrodes are not limited by the resistance of the electrode but by the solution resistance. The voltage drop across the electrode also increases as the C-rate increases due to the associated higher currents.

The effect of decreasing N_{CNT} was also investigated in a second calculation for which the electrode was ~73% porous. Values for relevant parameters in this calculation are listed in Table 5. As N_{CNT} decreases, the porosity increases and the areal capacity loading decreases. The potential drop across the anode (Figure 103) is lower, despite the increased electrode resistance (Figure 104) due to the lower currents corresponding to the lower area capacity loading (Figure 100). Again, the potential drop changes with the square of the electrode thickness as both the current and resistance follow a linear relationship with the thickness. Thus, for VACNT-based electrodes with ultra-high porosity, the use of thick electrodes is dominated by the electrode resistance. The solution resistance for highly porous electrodes is lower than denser electrodes due to the increased value of A.

For both cases, the data shows that VACNT-based materials, under the assumed conditions, may only be suitable for low-to-moderate C-rates if the electrode thickness is large (Figure 101, Figure 103). Also, as the electrode becomes more porous, the voltage drop across the electrode is much lower than denser electrodes; however, this advantage is at the expense of significantly reduced areal capacity loadings (Figure 100). The calculations also demonstrate that tuning the VACNT synthesis method to yield electrodes of varying porosity affects the voltage drop across the electrode and the areal capacity loading.

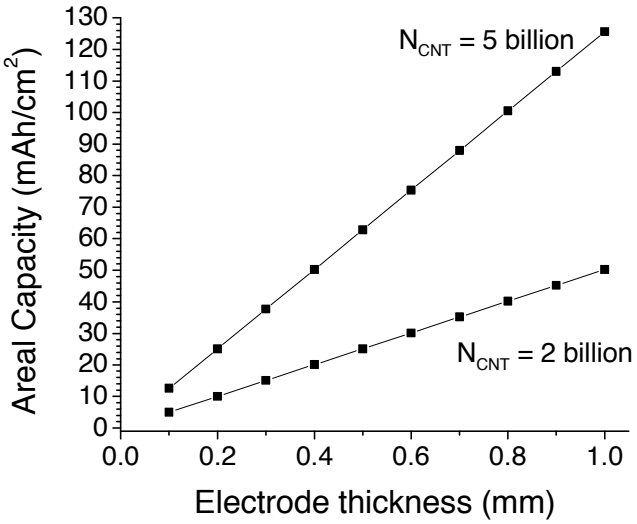

Figure 100. Areal capacity as a function of electrode thickness when the number density of VACNT was constant for two different scenarios. Additional assumptions are listed in Tables 4 and 5.

Table 4. Parameter values for the calculation of $R_{total,A}$ and the potential drop across a VACNT-Si-C anode as plotted in Figure 101 and Figure 102.

Parameter	Value	Units
N_{CNT}	5 x 10^9	
CC_A	1	cm^2
w_{Si}	0.3575	
w_C	0.6425	
κ_{soln}	0.01	S/cm
$\rho_{VACNT-Si-C}$	3.76	Ω·cm
ρ_{SEI}	100	Ω·cm^2
t_{SEI}	1.0 x 10^{-6}	cm
r_{CNT}	2.5 x 10^{-6}	cm
t_{Si}	2.0 x 10^{-6}	cm
t_C	2.0 x 10^{-6}	cm
P	33.63	%

Table 5. Parameter values for the calculation of $R_{total,A}$ and the potential drop across a VACNT-Si-C anode as plotted in Figure 103 and Figure 104.

Parameter	Value	Units
N_{CNT}	2 x 10^9	
CC_A	1	cm^2
w_{Si}	0.3575	
w_C	0.6425	
κ_{soln}	0.01	S/cm
$\rho_{VACNT-Si-C}$	3.76	Ω·cm
ρ_{SEI}	100	Ω·cm^2
t_{SEI}	1.0 x 10^{-6}	cm
r_{CNT}	2.5 x 10^{-6}	cm
t_{Si}	2.0 x 10^{-6}	cm
t_C	2.0 x 10^{-6}	cm
P	73.45	%

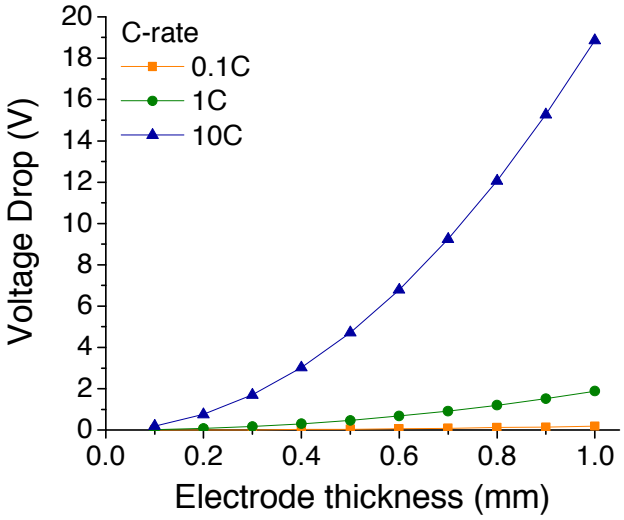

Figure 101. The voltage drop per unit area of the current collector across the electrode thickness at multiple C-rates. The number density of VACNT was constant. Additional assumptions are listed in Table 4.

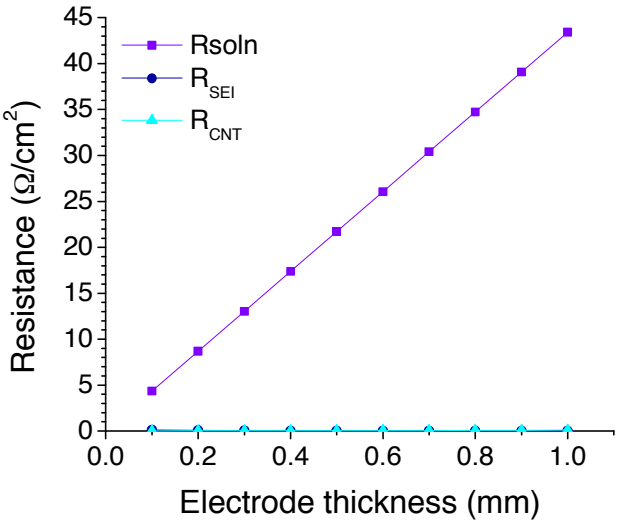

Figure 102. The change in resistance of select resistive elements per unit area of the current collector as a function of electrode thickness. The number density of VACNT was constant. Additional assumptions are listed in Table 4.

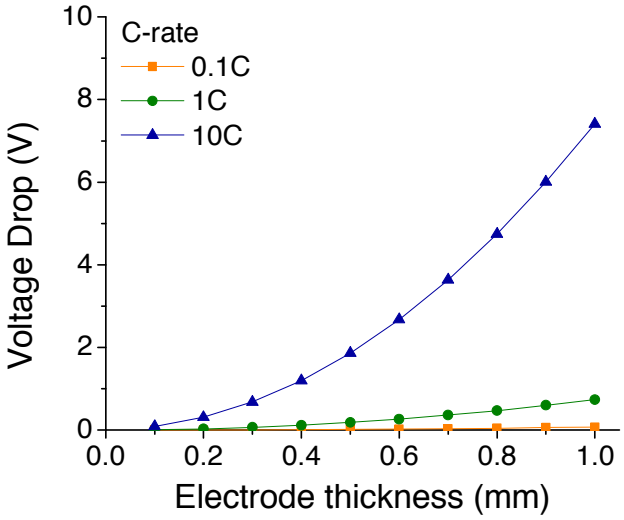

Figure 103. The voltage drop per unit area of the current collector across the electrode thickness at multiple C-rates. The number density of VACNT was constant. Additional assumptions are listed in Table 5.

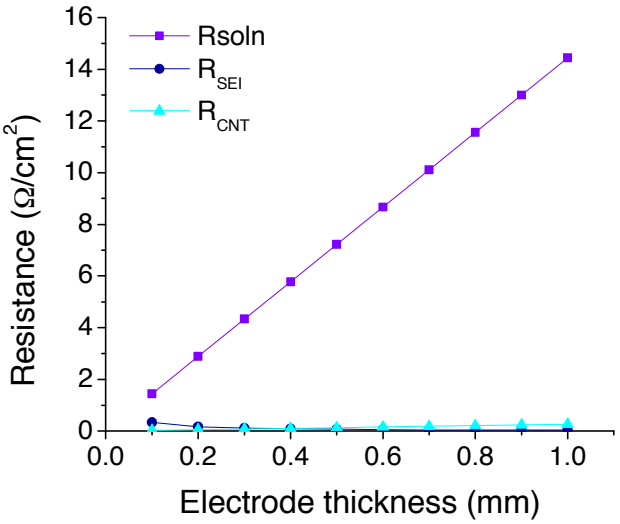

Figure 104. The change in resistance of select resistive elements per unit area of the current collector as a function of electrode thickness. The number density of VACNT was constant. Additional assumptions are listed in Table 5.

8.4 Comparison of Researched Anodes

The performed research investigated three distinct structures consisting of a carbon substrate coated with high capacity Si. In some designs, the Si layer was coated with an overcoating of carbon. Despite the similar description of the anodes, each offers unique advantages and limitations in regards to electrochemical stability, as have been previously described. The researched electrode architectures also differ in their readiness for commercial applications. The Si-coated graphene materials may be considered as a drop-in replacement for graphite particles for anodes created through conventional methods; however, optimization and increased electrochemical stability is needed before the material could be considered as a true replacement technology. The synthesis techniques and structure of Si-coated CNT fabrics and VACNTs are considerably different than those conventionally used for electrodes. To warrant investment in such novel technologies, further optimization and increased electrochemical stability are necessary for these designs as well.

In general, for the electrode structures to be used in commercial cells, the materials must possess the ability to be produced at commercial scale with low cost, demonstrate high Coulombic efficiencies, and other application specific metrics. In a majority of applications, long cycle lifetimes are very important. Electrodes for these applications would ideally exhibit a Coulombic efficiency of 100% without fading. In reality, the Coulombic efficiency will always be less than 100% as a result of numerous phenomena including, but not limited to, SEI formation, side reactions, unbalanced cycling, and thermal degradation. Lower Coulombic efficiencies lead to faster capacity fading. Assuming a constant CE, the number of cycles before a threshold percentage of the initial capacity is reached can be calculated. Figure 105 shows that even at a “high” CE of 99.9%, the maximum percent of the initial capacity available decreases rapidly with only 80% available after 223 cycles.

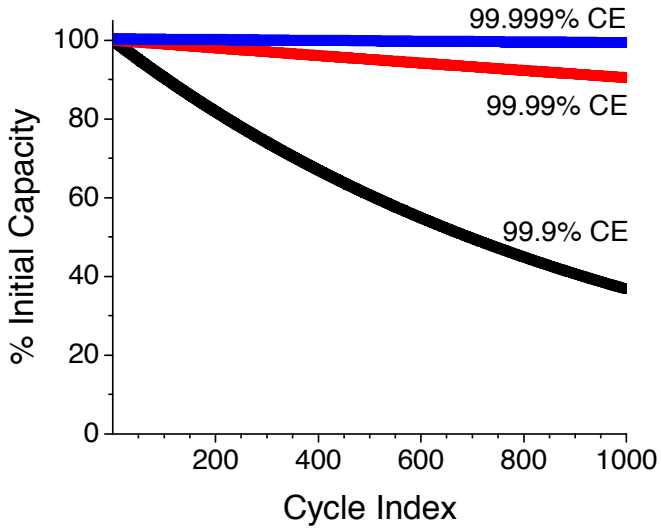

Figure 105. Capacity fade profiles for multiple Coulombic efficiencies.

.

The same analysis can be used to compare the cycle stability of the researched electrode structures (Table 6). The VACNT-Si-C possessed the highest average CE and, as such, demonstrates longer capacity retention, assuming a constant CE. It was expected that VACNT-based electrodes would have the best stability, of the electrode structures researched in this study, as the structure does not include polymer binder or conductive additives, possesses 1-D porosity, and possesses high thermal and electrical conductivities. Rapid fading of Si-coated graphene and CNT fabric electrodes highlight the need for further investigation of these structures to understand the factors contributing to capacity fading. It should be noted that all materials studied in this research were tested versus Li metal and that the CE values for each will likely be different when tested versus a matching cathode. Further, the nanocomposite structures have not yet been optimized for high capacity and stable efficiencies.

Table 6. The number of cycles until the capacity falls below a percentage of the initial capacity, assuming a constant Coulombic efficiency.

Number of Cycles	**Graphene-Si-C**	**CNT-Si (fabric)**	**VACNT-Si-C**
To 90% initial capacity	11	7	132
To 80% initial capacity	23	15	279

8.5 Factors Contributing to Stable Performance

To reduce oxide formation and improve the SEI properties, Si-coated CNT and graphene substrates were uniformly coated with a thin amorphous carbon overcoating. This approach has also been successful in previous work utilizing C-coated Si-C composite anodes.[10, 153] A thin layer of C (5 – 10 nm) was desired such that the diffusion of Li ions penetrates beyond the outer C layer to the high capacity material at high C-rates. Further, even a thin C overcoating can greatly increase the overall weight percent of C due to the increased surface area of deposition after Si coating so determination of the minimum C coating will allow for higher Si loading. From visual inspection of the SEI layer on VACNT-Si and VACNT-Si-C materials, it was observed that the SEI on the C overcoating was smoother (Figure 85). This observation, in combination with electrochemical performance and conductivity comparisons (Section 6.4), suggests that the C overcoating can play a critical role on the cell stability.

Investigation of an electrically insulative coating was also considered for VACNT-Si and VACNT-Ge based electrodes. The data collected thus far suggests that the alumina coating may allow for increased stability of a high capacity material; however, an understanding of the changes in properties of lithiated alumina is not yet known. It can be concluded though that the presence of the alumina may have limited rate capability due to the decreased Li^+ diffusivity, in comparison to C. Stabilization effects are also likely dependent upon the alumina thickness on a particular high capacity geometry and may reveal relationships between the high capacity material curvature, crystallinity, and dimensions. A systematic approach to identify the optimal alumina thickness and properties should be investigated in future studies. It should also be noted that the decision to use a carbon overcoating or an alumina coating may also be dependent upon the cell requirements for the material (e.g. mass loading, conductivity), processing capabilities, and operation requirements (e.g. high power).

To demonstrate the importance of the electrolyte on cell stability, VACNT-Si and VACNT-Si-C with the same thickness of Si were tested with and without 10 wt. % VC additive. It was found that incorporating VC electrolyte additive helped achieve good capacity retention and high Coulombic efficiencies, in agreement with prior studies.[37-39] Figure 106 shows that without VC additive, the Si-coated VACNT electrodes showed a steady decline in specific capacity at an average rate of ~1.5% per cycle with an average CE of 93.78 ± 3.54%. With the VC additive, the VACNT-Si electrodes still exhibited capacity fading of an average rate of 0.87% per cycle, but at a rate lower than without the VC additive. The CE for the VC containing electrolyte was slightly better with an average of 96.82 ± 3.96%.

Similar findings were observed for VACNT-Si-C electrodes tested in electrolyte with and without VC (Figure 107). Here, the average capacity fading for VACNT-Si-C without VC was 1.68% with a CE of 97.13 ± 2.49%. With VC, the VACNT-Si-C had an average capacity fading of 1.23% with a CE of 97.09 ± 4.62% .The lower CE for VC containing electrolyte is attributed to the lower first cycle CE. Comparing the average CE at the C/5 rate (after the initial formation cycles) of the VACNT-Si-C with and without VC, the CE without VC is 97.57 ± 0.57% and with VC is 98.01 ± 0.48%. This suggests that very modest gains in CE can be achieved with VC containing electrolyte for C coated Si.

The capacity fading and CE values of VACNT-Si and VACNT-Si-C in Figure 106 and Figure 107 differ from Figure 66 due to a higher weight percent of Si in the VC additive study. However, qualitatively, the results indicate trends that should hold at other Si weight percents.

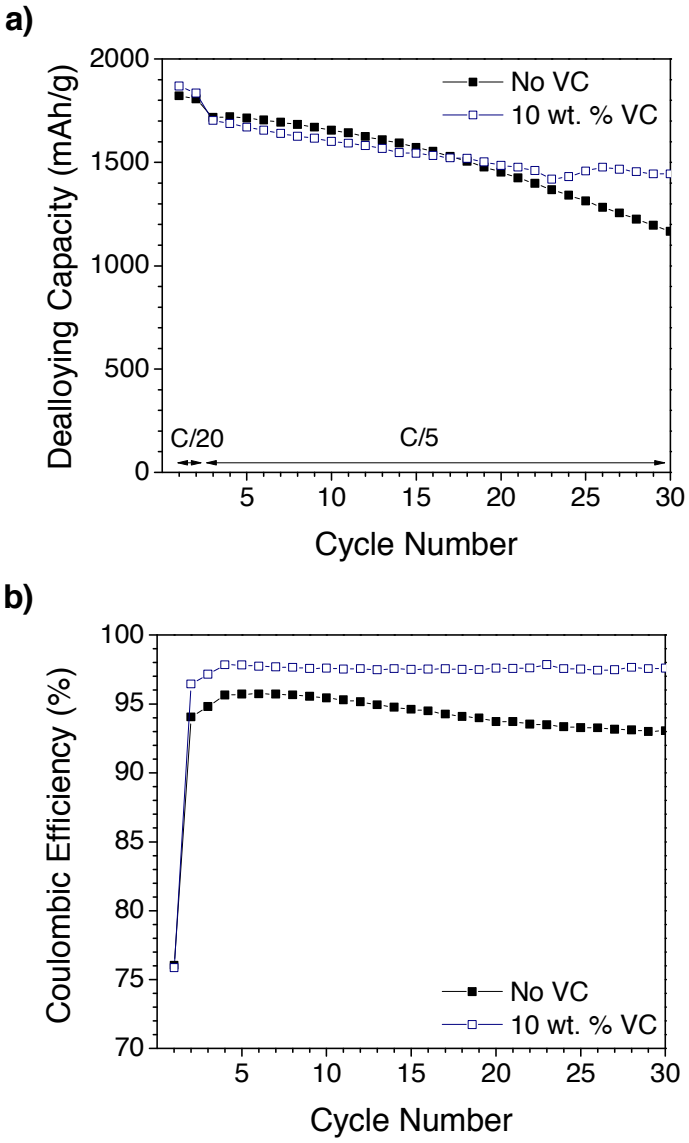

Figure 106. Electrochemical characterization of VACNT electrodes coated with Si tested with and without VC electrolyte additive: (a) specific capacity and (b) Coulombic efficiency versus cycle number. Capacity is normalized by the total mass of Si and C.

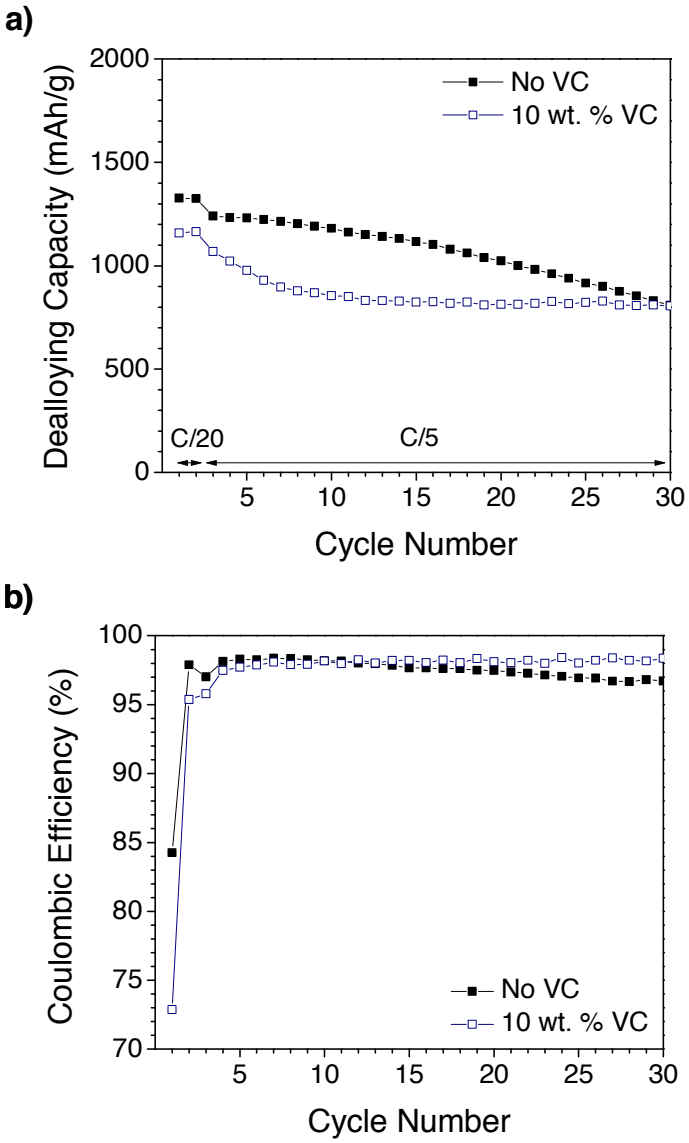

Figure 107. Electrochemical characterization of VACNT electrodes coated with Si and C overcoating tested with and without VC electrolyte additive: (a) specific capacity and (b) Coulombic efficiency versus cycle number. Capacity is normalized by the total mass of Si and C.

Electrolyte wetting of the anode is another important consideration for stable performance. Poor electrolyte wetting limits the ability of ions to diffuse to the anode and electrochemical reactions cannot proceed. For VACNTs electrodes, anomalies in the electrochemical performance such as significant, sudden capacity drops that rebound after one to several cycles (Figure 108) suggested that incomplete electrolyte wetting was an issue. Gas bubbles in the electrode create non-conducting pathways that limit the resulting performance. The lack of incomplete wetting may originate from an insufficient volume of electrolyte was deposited on the anode material. Visual inspection confirmed the presence of gas bubbles within relatively thick (> 500 μm) VACNTs-based electrodes. To ensure full wetting, a vacuum electrolyte infiltration system was developed and utilized. To limit the evaporation of the electrolyte solvent, the time of vacuum filling is short (< 30 seconds). After this modification to the cell assembly process, drastic capacity drops at a constant C-rate were not observed.

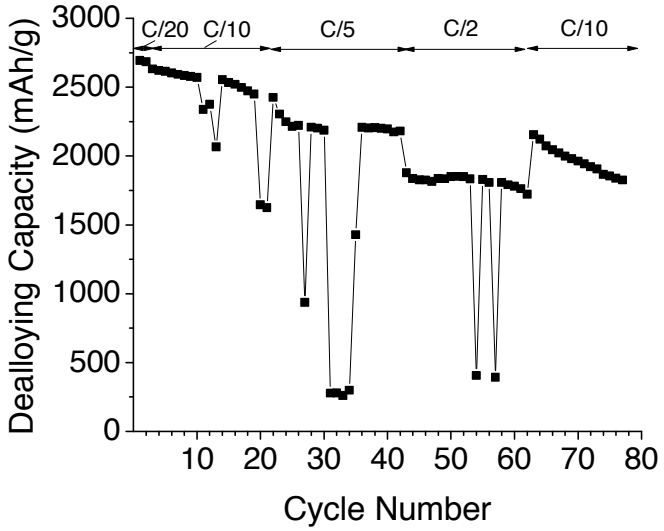

Figure 108. Dealloying capacity for VACNT-Si-C showing sudden capacity drops during cycling at multiple C-rates.

8.6 Sources of Error

Accurate mass measurements are critical for calculation of the gravimetric capacity. The error of the balance used to weigh the samples is ± 0.005 mg. The minimum sample mass across all samples in this study was ~0.20 mg. The minimum sample mass would be the most affected by instrument error. As a sample calculation, at a mass loading of 0.20 mg, the measurement error corresponds to ± 2.5%. The error in gravimetric capacity increases as the absolute capacity increases. Assuming theoretical capacity of Si, as it has the highest theoretical capacity, the error in calculating the theoretical gravimetric capacity is ±90 mAh/g.

The error in calculating the weight percent of materials in the composite is also dependent upon mass measurement error. The thin film deposition processes utilized can deposit as little as one milligram to as much as tens of milligrams of material, depending on the synthesis conditions and substrate surface area. As the mass of the material increases, the percent error in the measurement decreases. For example, a 1 mg sample will have an error of 0.5% whereas as a 10 mg sample will have an error of 0.05%. For a substrate coated with a thin film, the total error will be dependent upon the measured values for the substrate and thin film contributions. The maximum error for calculating a weight percent for a C-Si composite is thus 0.87%, as no samples weighing less than 1 mg were coated. As an example, assuming theoretical capacity of Si, the error in calculating the theoretical gravimetric capacity is ±31 mAh/g. The variation in gravimetric capacity will decrease as the theoretical capacity decreases.

Tensile test sample preparation also gives rise to sources of error in measurement of the sample width, the condition of the sample edge, and the loading of the sample in the instrument grips. Sample imperfections, such as a pre-existing crack, irregular edges, and non-parallel edges will act as stress concentrators and will reduce the strength of the sample. These samples can be identified through observation of the fracture location

since a perfect sample should fracture at the midpoint of the sample. In addition, if the sample is not securely held by the grips, the sample may slip during testing and affect the value for strain to failure. This behavior, if significant, can be seen as a jagged plateau in the stress-strain curve. Lastly, if the sample is too securely held by the grips, the sample may fracture closer to the grips. For these studies, the results of samples that indicated poor sample preparation were discarded.

Low sample-to-sample variability was observed for materials of the same type tested under the same conditions. The potentiostats used for charge/discharge testing have three settings for different current ranges such as ± 100 μA, ± 1 mA, and ± 10 mA. Even after calibration, the currents used for charge/discharge testing are subject to instrument error that propagate as error in the calculation of the Coulombic efficiency and can be quantified as:

$$\% \, Error = \frac{8 \, x \, 10^{-4} (Current \, range)}{Current} \cdot 100 \tag{30}$$

where the current range and the current must be in the same units. Using this calculation, the limits of error in CE are 0.08% to 8%. The smaller the current used for a particular setting, then the larger the percent error.

Error in thermal conductivity measurements of CNT-fabric electrodes were due to several factors including machine accuracy (± 6%), measurement of the thickness (± 7.9%), and calibration for narrow samples (± 3.9%). Variation in recorded measurements for the CNT fabric and Si-coated CNT fabric were 3.16% and 2.1%, respectively. The instrument error in the electrical measurements was 0.70% as determined through calibration with a known resistance. For conductivity measurements without clear quantifiable sources of error, calibration and multiple tests for multiple samples were performed. The presented data shows the standard deviation of those measurements.

8.7 Extensions of This Work

Carbon substrates serve as a platform for the deposition of coatings for not only energy storage electrodes but also for solar cells and gas sensors, among other areas. Si and Ge were explored in this research; however, other studies performed by the Yushin group have built upon some of the findings of this work and have illustrated the variety of materials that can be utilized.

For example, vanadium oxide was deposited on CNT fabrics via ALD of deionized water and vanadium tri-*n*-propoxide oxide (Figure 109a).[256] The resultant smooth coating caused a linear increase in CNT tube diameter with respect to the number of ALD cycles. Multiple thicknesses of vanadium oxide coated on CNT fabrics were tested as symmetric supercapacitors. All of the coated CNT fabrics showed increased high capacitance and capacitance retention, in comparison to the uncoated CNT fabric (Figure 109b).

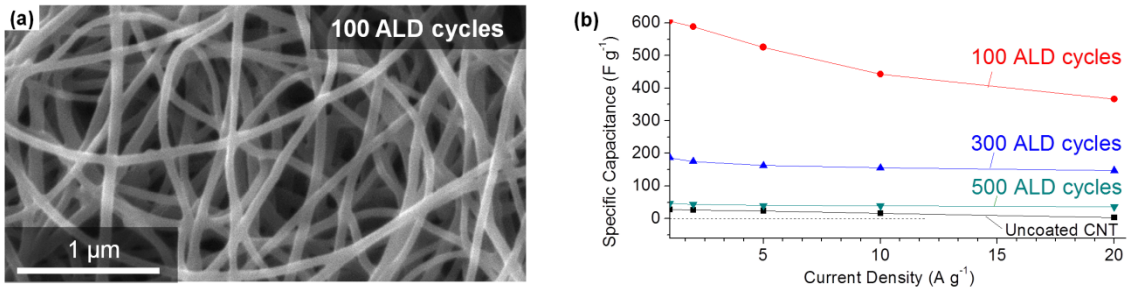

Figure 109. (a) SEM image of a CNT fabric coated with vanadium oxide after 100 ALD cycles. (b) Specific capacitance retention for the composite electrodes.[256]

Non-vapor routes to conformally coat CNT fabrics were also explored. Electrically conductive polyaniline (PANI) was electrochemically deposited on the surface of individual CNTs in a CNT fabric (Figure 110a) and tested as a symmetric supercapacitor.[257] Similar to the presented two-dimensional Si-coated CNT fabrics, the

mechanical (Figure 110b) and energy storage (Figure 110c) characteristics were measured. The CNT-PANI composite had high tensile strength and modulus of toughness that may enable its use as a robust structural energy storage composite. This particular composite also demonstrated applicability for water desalination.[257]

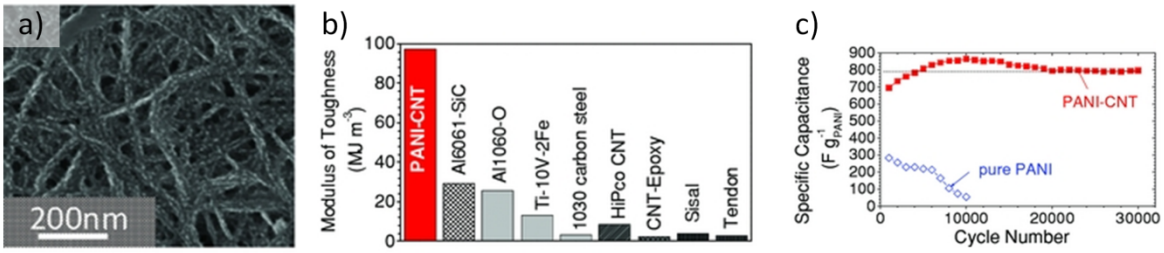

Figure 110. (a) SEM image of a CNT fabric coated with electro-deposited PANI. (b) The modulus of toughness for the CNT-PANI composite in comparison with other materials. (c) Cycle stability of a PANI-CNT electrode in comparison with that of pure PANI (chemically synthesized) electrode.[257]

Low cost, high capacity sulfur-based cathodes are attractive for Li-ion batteries; however, stable utilization of sulfur's high capacity plagues current research. High capacity and rapid capacity degradation can be partly explained by the high solubility of polysulfides in electrolytes and the inherent low electrical conductivity of sulfur. Sulfur vapor infiltrated VACNT electrodes (Figure 111 a – c) have been shown to resist rapid degradation at multiple testing temperatures (Figure 111d).[258]

Although the three extensions briefly described are designed for energy storage applications, it is clear that a variety of materials can be conformally deposited through multiple techniques onto the surfaces of CNTs. Thus, CNTs are an attractive substrate for the deposition of other high capacity or low electrical or thermal conductivity materials to provide high energy and power characteristics, high electrical and thermal conductivities, and stable cycling for both cathodes and anodes. Further, the structure itself is amenable to fundamental studies as the structure is not complicated by conductive additives or binder and thus may provide valuable insight that will lead to further advancements in multiple areas of research.

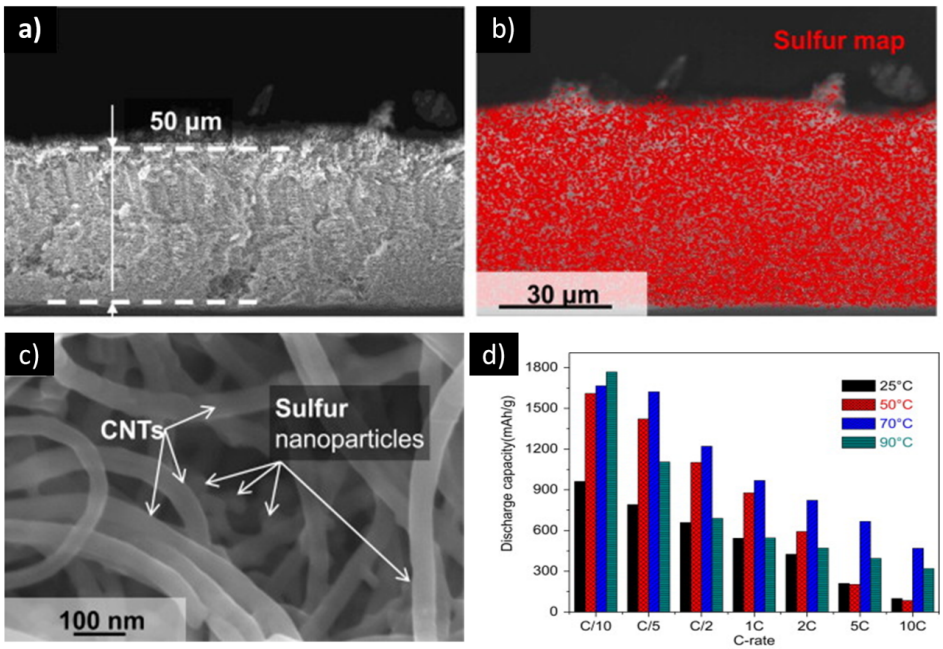

Figure 111. Cross-section SEM micrograph highlighting (a) the VACNT electrode thickness and (b) uniformity of the deposited sulfur via EDS mapping. (c) SEM micrograph showing the distribution of sulfur nanoparticles throughout the electrode. (d) Discharge capacity (normalized by the sulfur mass) for the CNT-S electrode at multiple C-rates and testing temperatures.[258]

CHAPTER 9

CONCLUSIONS

9.1 Impact of Research

The research presented here has contributed to the existing body of knowledge in battery research. The key findings of the research are as follows:

1. Graphene granules coated with Si decrease the graphene specific surface area by 100x to reduce the surface area for SEI formation to yield decent CE (99%)
2. Carbon nanotube based electrodes offer up to multiple orders of magnitude increases in electrical and thermal conductivities, depending upon their configuration, in comparison to electrodes of similar composition created through traditional methods
3. The first demonstration of the specific strength of electrodes before and after charge/discharge cycling showed only a slight reduction in UTS for Si-coated CNT fabrics
4. The experimentally measured specific strength of Si-coated CNT fabric (~100 kN·m/kg) is higher than the specific strength of common current collector materials (Cu, Al)
5. Analysis of the electrical and thermal conductivities of CNT fabrics indicates that at low to moderate C-rates, it is possible for CNT fabrics to serve as a replacement for the Cu current collector for smaller cells
6. Vertically aligned carbon nanotube electrodes allow for the formation of 1 mm thick, high areal capacity electrodes

7. C and/or Al_2O_3 overcoatings on high capacity materials and VC as an electrolyte additive decreases the capacity fade and increases the Coulombic efficiency
8. The thickness of VACNT-based electrodes is limited by the solution resistance (for high VACNT number density per area) and the high areal capacities which may not have a matching electrode
9. Proper electrolyte filling in thick electrodes is critical to stable cycling
10. Porous Si and porous Ge are formed via electrochemical cycling of 30 – 35 nm thick Si and 90 nm diameter Ge particles deposited on CNTs, in the presence and absence of overcoatings

9.2 Recommendations for Future Work

This research has demonstrated that highly structured C-based composite anodes can be created through vapor deposition techniques. All of the proposed anode structures demonstrated higher capacity than traditional graphite, often with additional benefits such as higher thermal and electrical conductivities or mechanical strength. A surface coating of carbon and/or alumina to further stabilize C-composite electrodes was also explored.

Continued investigation of the researched electrode architectures will yield an increased understanding of the complex relationship between microstructure, material properties, and electrochemical performance. Recommendations for future work to aid in the further development of electrode materials include:

1. For all composite materials, conduct further research to understand the effect of the electrode structure and properties to increase the Coulombic efficiencies
2. The tunable spacing between individual graphene layers permits coatings of varying thickness to be deposited. Variations in coating thickness can be

studied for high energy or high power applications through conductivity and electrochemical measurements

3. Perform electrochemical measurements against a capacity-matched counter electrode in a full cell configuration for all electrodes and compare to half cell data
4. Examine the effect of the CNT fabric porosity, coating thickness and composition on the electrochemical performance, mechanical strength, capacity, and cycle stability
5. Develop and synthesize a flexible, strong cathode and a flexible, solid electrolyte for use with multi-functional flexible electrodes to not only increase cell safety but also advance realization of a strong flexible battery
6. Reveal the effect of varying the thickness of the alumina coating on high capacity thin films and particles to determine 1) if the formation of porous Si or Ge is primarily an effect of particle/film size or crystal structure and 2) at what thickness an alumina coating becomes performance limiting
7. Develop a computational model for the alumina coated CNT materials that reflects known material properties and lithiation behavior to compare with both *in situ* and *ex situ* TEM studies

REFERENCES

1. Tarascon, J. M.; Armand, M., Issues and challenges facing rechargeable lithium batteries. *Nature* 2001, 414, 359-367.

2. Brodd, R. J., Recent developments in batteries for portable consumer electronics applications. *Electrochemical Society Interface* 1999, 21-21.

3. Daniel, C., Materials and Processing for Lithium-Ion Batteries. *JOM* 2008, 60, 43-48.

4. Frackowiak, E.; Beguin, F., Electrochemical storage of energy in carbon nanotubes and nanostructured carbons. *Carbon* 2002, 40, 1775-1787.

5. Shukla, A. K.; Kumar, T. P., Materials for Next Generation Lithium Batteries. *Current Science* 2008, 94, 314-331.

6. Whittingham, M. S., Materials Challenges Facing Electrical Energy Storage. *MRS Bulletin* 2008, 33, 411-420.

7. Boukamp, B. A.; Lesh, G. C.; Huggins, R. A., All-Solid Lithium Electrodes with Mixed-Conductor Matrix. *Journal of The Electrochemical Society* 1981, 128, 725-729.

8. Obrovac, M. N.; Christensen, L.; Ba Le, D.; Dahn, J. R., Alloy Design for Lithium-Ion Battery Anodes. *Journal of The Electrochemical Society* 2007, 154, A849-A855-A849-A855.

9. Huggins, R. A.; Nix, W. D., Decrepitation model for capacity loss during cycling of alloys in rechargeable electrochemical systems. *Ionics* 2000, 6, 57-63.

10. Magasinski, A.; Dixon, P.; Hertzberg, B.; Kvit, A.; Ayala, J.; Yushin, G., High-performance lithium-ion anodes using a hierarchical bottom-up approach. *Nature Materials* 2010, 9, 353-358.

11. Chan, C. K.; Ruffo, R.; Hong, S. S.; Cui, Y., Surface chemistry and morphology of the solid electrolyte interphase on silicon nanowire lithium-ion battery anodes. *Journal of Power Sources* 2009, 189.

12. Lee, Y. M.; Lee, J. Y.; Shim, H.-T.; Lee, J. K.; Park, J.-K., SEI Layer Formation on Amorphous Si Thin Electrode during Precycling. *Journal of The Electrochemical Society* 2007, 154, A515-A519-A515-A519.

13. Peled, E., The Electrochemical Behavior of Alkali and Alkaline Earth Metals in Nonaqueous Battery Systems - The Solid Electrolyte Interphase. *Journal of The Electrochemical Society* 1979, 126, 2047-2051.

14. Chan, C. K.; Peng, H.; Liu, G.; McIlwrath, K.; Zhang, X. F.; Huggins, R. A.; Cui, Y., High-performance lithium battery anodes using silicon nanowires. *Nature Nano* 2008, 3, 31-35.

15. Kim, J. H.; Khanal, S.; Islam, M.; Khatri, A.; Choi, D., Electrochemical characterization of vertical arrays of tin nanowires grown on silicon substrates as anode materials for lithium rechargeable microbatteries. *Electrochemistry Communications* 2008, 10, 1688-1690.

16. Shin, H. C.; Corno, J. A.; Gole, J. L.; Liu, M., Porous silicon negative electrodes for rechargeable lithium batteries. *Journal of Power Sources* 2005, 139, 314-320.

17. *Advances in Lithium-Ion Batteries*. Kluwer Academic/Plenum Publishers: 2002.

18. Ajayan, P. M.; Zhou, O. Z., Applications of Carbon Nanotubes. *Topics in Applied Physics* 2001, 80/2001, 391-425.

19. Bard, A. J.; Faulkner, L. R., *Electrochemical Methods: Fundamentals and Applications*. John Wiley & Sons, Inc.: 2001.

20. Goodenough, J. B.; Abruna, H. D.; Buchanan, M. V., Basic Research Needs for Electrical Energy Storage. Report of the Basic Energy Sciences Workshop on Electrical Energy Storage, April 2-4, 2007. 2007.

21. Huggins, R. A., Lithium alloy negative electrodes. *Journal of Power Sources* 1999, 81-82, 13-19.

22. Whittingham, M. S., Lithium Batteries and Cathode Materials. *Chemical Reviews* 2004, 104, 4271-4302.

23. Ehrlich, G. M., Lithium-Ion Batteries. In *Handbook of Batteries*, Linden, D., Ed. McGraw-Hill: 1995; pp 35.1 - 35.94-35.1 - 35.94.

24. Wang, F.; Robert, R.; Chernova, N. A.; Pereira, N.; Omenya, F.; Badway, F.; Hua, X.; Ruotolo, M.; Zhang, R.; Wu, L.; Volkov, V.; Su, D.; Key, B.; Whittingham, M. S.; Grey, C. P.; Amatucci, G. G.; Zhu, Y.; Graetz, J., Conversion Reaction Mechanisms in Lithium Ion Batteries: Study of the Binary Metal Fluoride Electrodes. *Journal of the American Chemical Society* 2011, 133, 18828-18836.

25. Boyanov, S.; Annou, K.; Villevieille, C.; Pelosi, M.; Zitoun, D.; Monconduit, L., Nanostructured transition metal phosphide as negative electrode for lithium-ion batteries. *Ionics* 2008, 14, 183-190.

26. Pralong, V.; Souza, D. C. S.; Leung, K. T.; Nazar, L. F., Reversible lithium uptake by CoP3 at low potential: role of the anion. *Electrochemistry Communications* 2002, 4, 516-520.

27. Yazami, R.; Touzain, P., A reversible graphite-lithium negative electrode for electrochemical generators. *Journal of Power Sources* 1983, 9, 365-371.

28. Patil, A.; Patil, V.; Shin, D.; Choi, J.; Paik, D.; Yoon, S., Issues and challenges facing rechargeable thin film lithium batteries. *Materials Research Bulletin* 2008, 43, 1913-1942.

29. Nitta, N.; Yushin, G., High-Capacity Anode Materials for Lithium-Ion Batteries: Choice of Elements and Structures for Active Particles. *Particle & Particle Systems Characterization* 2013, n/a-n/a.

30. Kasavajjula, U.; Wang, C.; Appleby, A. J., Nano- and bulk-silicon-based insertion anodes for lithium-ion secondary cells. *Journal of Power Sources* 2007, 163, 1003-1039.

31. Graetz, J.; Ahn, C. C.; Yazami, R.; Fultz, B., Nanocrystalline and Thin Film Germanium Electrodes with High Lithium Capacity and High Rate Capabilities. *Journal of The Electrochemical Society* 2004, 151, A698-A698.

32. Hatchard, T. D.; Dahn, J. R., In Situ XRD and Electrochemical Study of the Reaction of Lithium with Amorphous Silicon. *Journal of The Electrochemical Society* 2004, 151, A838-A838.

33. Aifantis, K. E.; Hackney, S. A., Nanoscale Engineering for the Mechanical Integrity of Li-Ion Electrode Materials. In *Nanostructured Materials in Electrochemistry*, Eftekhari, A., Ed. Wiley: 2008.

34. Liu, R.; Duay, J.; Lee, S. B., Heterogeneous nanostructured electrode materials for electrochemical energy storage. *Chemical Communications* 2011.

35. Chan, C. K.; Zhang, X. F.; Cui, Y., High Capacity Li Ion Battery Anodes Using Ge Nanowires. *NANO LETTERS* 2008, 8, 307-309.

36. Lux, S. F.; Lucas, I. T.; Pollak, E.; Passerini, S.; Winter, M.; Kostecki, R., The mechanism of HF formation in LiPF6 based organic carbonate electrolytes. *Electrochemistry Communications* 2012, 14, 47-50.

37. Zhang, S. S., A review on electrolyte additives for lithium-ion batteries. *Journal of Power Sources* 2006, 162, 1379-1394.

38. Xu, K., Nonaqueous Liquid Electrolytes for Lithium-Based Rechargeable Batteries. *Chemical Reviews* 2004, 104, 4303-4418.

39. Aurbach, D.; Gamolsky, K.; Markovsky, B.; Gofer, Y.; Schmidt, M.; Heider, U., On the use of vinylene carbonate (VC) electrolyte solutions for Li-ion as an additive to batteries. *Electrochimica Acta* 2002, 47, 1423-1439.

40. Komaba, S.; Ishikawa, T.; Yabuuchi, N.; Murata, W.; Ito, A.; Ohsawa, Y., Fluorinated Ethylene Carbonate as Electrolyte Additive for Rechargeable Na Batteries. *ACS Appl. Mater. Interfaces* 2011, 3, 4165-4168.

41. Uchida, I.; Ishikawa, H.; Mohamedi, M.; Umeda, M., AC-impedance measurements during thermal runaway process in several lithium/polymer batteries. *Journal of Power Sources* 2003, 119-121, 821-825.

42. Zhang, T.; Fu, L. J.; Takeuchi, H.; Suzuki, J.; Sekine, K.; Takamura, T.; Wu, Y. P., Studies of the structure of vacuum deposited silicon films on metal substrates as anode materials for Li-ion batteries. *Journal of Power Sources* 2006, 159, 349-352.

43. Balbuena, P. B.; Wang, Y., Preface. Balbuena, P. B.; Wang, Y., Eds. Imperial College Press: 2004.

44. Peled, E.; Golodnitsky, D.; Ardel, G., Advanced Model for Solid Electrolyte Interphase Electrodes in Liquid and Polymer Electrolytes. *Journal of The Electrochemical Society* 1997, 144, L208-L210-L208-L210.

45. Yen, Y.-C.; Chao, S.-C.; Wu, H.-C.; Wu, N.-L., Study on Solid-Electrolyte-Interphase of Si and C-coated Si Electrodes in Lithium Cells. *Journal of The Electrochemical Society* 2009, 156, A95 - A102-A95 - A102.

46. Peled, E.; Golodnitsky, D., SEI on lithium, graphite, disordered carbons and tin-based alloys. Balbuena, P. B.; Wang, Y., Eds. Imperial College Press: 2004.

47. Eshkenazi, V.; Peled, E.; Burstein, L.; Golodnitsky, D., XPS analysis of the SEI formed on carbonaceous materials. *Solid State Ionics* 2004, 170, 83-91.

48. Ratnakumar, B. V.; Smart, M. C.; Surampudi, S., Effects of SEI on the kinetics of lithium intercalation. *Journal of Power Sources* 2001, 97-98, 137-138.

49. Lee, J. T.; Nitta, N.; Benson, J.; Magasinski, A.; Fuller, T. F.; Yushin, G., Comparative study of the solid electrolyte interphase on graphite in full Li-ion battery cells using X-ray photoelectron spectroscopy, secondary ion mass spectrometry, and electron microscopy. *Carbon* 2013, 52, 388-397.

50. Saito, R.; Dresselhaus, G.; Dresselhaus, M. S., *Physical Properties of Carbon Nanotubes*. Imperial College Press: London, 1998.

51. The 2010 Nobel Prize in Physics - Press Release. http://nobelprize.org/nobel_prizes/physics/laureates/2010/press.html.

52. Abouimrane, A.; Compton, O. C.; Amine, K.; Nguyen, S. T., Non-Annealed Graphene Paper as a Binder-Free Anode for Lithium-Ion Batteries. *The Journal of Physical Chemistry C* 2010, 114, 12800-12804.

53. Chen, D.; Tang, L.; Li, J., Graphene-based materials in electrochemistry. *Chemical Society Reviews* 2010, 39, 3157-3157.

54. Novoselov, K. S.; Geim, A. K.; Morozov, S. V.; Jiang, D.; Zhang, Y.; Dubonos, S. V.; Grigorieva, I. V.; Firsov, A. A., Electric field effect in atomically thin carbon films. *SCIENCE* 2004, 306, 666-669.

55. Geim, A. K.; Novoselov, K. S., The rise of graphene. *Nat Mater* 2007, 6, 183-191.

56. Li, D.; Kaner, R. B., Materials science - Graphene-based materials. *Science* 2008, 320, 1170-1171.

57. Partoens, B.; Peeters, F. M., From graphene to graphite: Electronic structure around the K point. *Physical Review B* 2006, 74, 075404-075404.

58. Schaffer, J. P.; Saxena, A.; Antolovich, S.; Sanders, J. T.; Warner, S., *Science and Design of Engineering Materials/Second Edition*. M: 1999.

59. Subrahmanyam, K. S.; Vivekchand, S. R. C.; Govindaraj, A.; Rao, C. N. R., A study of graphenes prepared by different methods: characterization, properties and solubilization. *Journal of Materials Chemistry* 2008, 18, 1517-1517.

60. Bhardwaj, T.; Antic, A.; Pavan, B.; Barone, V.; Fahlman, B. D., Enhanced Electrochemical Lithium Storage by Graphene Nanoribbons. *Journal of the American Chemical Society* 2010, 132, 12556-12558.

61. Yoo, E.; Kim, J.; Hosono, E.; Zhou, H.; Kudo, T.; Honma, I., Large reversible Li storage of graphene nanosheet families for use in rechargeable lithium ion batteries. *Nano Letters* 2008, 8, 2277-2282.

62. Ruan, M.; Hu, Y.; Guo, Z.; Dong, R.; Palmer, J.; Hankinson, J.; Berger, C.; de Heer, W. A., Epitaxial graphene on silicon carbide: Introduction to structured graphene. *MRS Bulletin* 2012, 37, 1138 - 1147.

63. Zhang, Y.; Zhang, L.; Zhou, C., Review of Chemical Vapor Deposition of Graphene and Related Applications. *Accounts of Chemical Research* 2013, 46, 2329-2339.

64. Iijima, S., Helical microtubules of graphitic carbon. *Nature* 1991, 354, 56-58.

65. Endo, M.; Hayashi, T.; Ahm Kim, Y.; Terrones, M.; Dresselhaus, M. S., Applications of carbon nanotubes in the twenty–first century. *Philosophical Transactions A* 2004, 362, 2223-2223.

66. Shanov, V. N.; Miskin, A.; Jain, S.; He, P.; Schulz, M. J., Advances in Chemical Vapor Deposition of Carbon Nanotubes. Schulz, M. J.; Kelkar, A. D.; Sundaresan, M. J., Eds. CRC - Press: 2005; pp 125-125.

67. Ando, Y.; Zhao, X.; Sugai, T.; Kumar, M., Growing Carbon Nanotubes. *Materials Today* 2004, 7, 22-29.

68. Inoue, Y.; Suzuki, Y.; Minami, Y.; Muramatsu, J.; Shimamura, Y.; Suzuki, K.; Ghemes, A.; Okada, M.; Sakakibara, S.; Mimura, F.; Naito, K., Anisotropic carbon nanotube papers fabricated from multiwalled carbon nanotube webs. *Carbon* 2011, 49, 2437-2443.

69. Martin, C., A Carbon Nano-wired World. *R & D Magazine* 2010, pp 40-40.

70. Shanov, V. N.; Yun, Y.-H.; Schulz, M. J., Synthesis and Characterization of Carbon Nanotubes Materials (Review). *Journal of the University of Chemical Technology and Metallurgy* 2006, 41, 377-390.

71. Vinciguerra, V.; Buonocore, F.; Panzera, G.; Occhipinti, L., Growth mechanisms in chemical vapour deposited carbon nanotubes. *Nanotechnology* 2003, 14, 655-655.

72. Zhu, L.; Sun, Y.; Hess, D. W.; Wong, C. P., Well-aligned open-ended carbon nanotube architectures: an approach for device assembly. *Nano Lett* 2006, 6, 243-247.

73. Liu, J.; Fan, S.; Dai, H., Recent Advances in Methods of Forming Carbon Nanotubes. *MRS Bulletin* 2004, 29, 244-250.

74. Pattanaik, A. K.; Sarin, V. K., Basic Principles of CVD Thermodynamics and Kinetics. In *Chemical Vapor Deposition*, ASM International: 2001; Vol. 2.

75. Zhang, R.; Zhang, Y.; Zhang, Q.; Xie, H.; Qian, W.; Wei, F., Growth of Half-Meter Long Carbon Nanotubes Based on Schulz–Flory Distribution. *ACS Nano* 2013, 7, 6156-6161.

76. Ajayan, P. M.; Ebbesen, T. W., Nanometre-size tubes of carbon. *Reports on Progress in Physics* 1997, 60, 1025-1025.

77. Kim, S. M.; Pint, C. L.; Amama, P. B.; Hauge, R. H.; Maruyama, B.; Stach, E. A., Catalyst and catalyst support morphology evolution in single-walled carbon nanotube supergrowth: Growth deceleration and termination. *Journal of Materials Research* 2010, 25, 1875-1885.

78. Kim, S. M.; Pint, C. L.; Amama, P. B.; Zakharov, D. N.; Hauge, R. H.; Maruyama, B.; Stach, E. A., Evolution in Catalyst Morphology Leads to Carbon Nanotube Growth Termination. *Journal of Physical Chemistry Letters* 2010, 1, 918-922.

79. Zhu, L.; Xu, J.; Xiu, Y.; Sun, Y.; Hess, D. W.; Wong, C. P., Growth and electrical characterization of high-aspect-ratio carbon nanotube arrays. *Carbon* 2006, 44, 253-258.

80. Wagner, R. S.; Ellis, W. C., VAPOR-LIQUID-SOLID MECHANISM OF SINGLE CRYSTAL GROWTH. *Applied Physics Letters* 1964, 4, 89-89.

81. Wronski, C. R. M., The size dependence of the melting point of small particles of tin. *Br. J. Appl. Phys.* 1967, 18, 1731.

82. Dai, H., Carbon Nanotubes: Synthesis, Integration, and Properties. *Accounts of Chemical Research* 2002, 35, 1035-1044.

83. Hu, C.; Zhang, Y.; Bao, G.; Liu, M.; Wang, Z. L., Diameter-dependent voltammetric properties of carbon nanotubes. *Chemical Physics Letters* 2006, 418, 524-529.

84. Turano, S. P.; Ready, J., Chemical vapor deposition synthesis of self-aligned carbon nanotube arrays. *Journal of Electronic Materials* 2006, 35, 192-194.

85. Liu, X.; Bigioni, T. P.; Xu, Y.; Cassell, A. M.; Cruden, B. A., Vertically Aligned Dense Carbon Nanotube Growth with Diameter Control by Block Copolymer Micelle Catalyst Templates. *The Journal of Physical Chemistry B* 2006, 110, 20102-20106.

86. Choy, K. L., Chemical vapour deposition of coatings. *Progress in Materials Science* 2003, 48, 57-170.

87. Creighton, J. R.; Ho, P., Introduction to Chemical Vapor Deposition (CVD). In *Chemical Vapor Deposition*, ASM International: 2001; Vol. 2.

88. Ohring, M., *Materials Science of Thin Films, Second Edition*. Academic Press: 2001.

89. Karousis, N.; Tagmatarchis, N.; Tasis, D., Current Progress on the Chemical Modification of Carbon Nanotubes. *Chemical Reviews* 2010, 110, 5366-5397.

90. Morris, R. S.; Dixon, B. G.; Gennett, T.; Raffaelle, R.; Heben, M. J., High-energy, rechargeable Li-ion battery based on carbon nanotube technology. *Journal of Power Sources* 2004, 138, 277-280.

91. Lepró, X.; Lima, M. D.; Baughman, R. H., Spinnable carbon nanotube forests grown on thin, flexible metallic substrates. *Carbon* 2010, 48, 3621-3627.

92. Dresselhaus, M. S.; Dresselhaus, G., Intercalation compounds of graphite. *Advances in Physics* 1981, 30, 139-139.

93. Sangster, J., C-Li (Carbon-Lithium) System. *Journal of Phase Equilibria and Diffusion* 2007, 28, 561-570.

94. Dahn, J. R.; Zheng, T.; Liu, Y.; Xue, J. S., Mechanisms for Lithium Insertion in Carbonaceous Materials. *SCIENCE* 1995, 270, 590-593.

95. Endo, M.; Kim, C.; Nishimura, K.; Fujino, T.; Miyashita, K., Recent development of carbon materials for Li ion batteries. *Carbon* 2000, 38, 183-197.

96. Noel, M.; Santhanam, R., Electrochemistry of graphite intercalation compounds. *Journal of Power Sources* 1998, 72, 53-65.

97. Liang, M.; Zhi, L., Graphene-based electrode materials for rechargeable lithium batteries. *Journal of Materials Chemistry* 2009, 19, 5871-5871.

98. Pan, D.; Wang, S.; Zhao, B.; Wu, M.; Zhang, H.; Wang, Y.; Jiao, Z., Li Storage Properties of Disordered Graphene Nanosheets. *Chemistry of Materials* 2009, 21, 3136-3142.

99. Pollak, E.; Geng, B.; Jeon, K.-J.; Lucas, I. T.; Richardson, T. J.; Wang, F.; Kostecki, R., The Interaction of Li+ with Single-Layer and Few-Layer Graphene. *Nano Letters* 2010, 10, 3386-3388.

100. Liang, M.; Zhi, L., Graphene-based electrode materials for rechargeable lithium batteries. *Journal of Materials Chemistry* 2009, 19, 5871-5878.

101. Ataca, C.; Akturk, E.; Ciraci, S.; Ustunel, H., High-capacity hydrogen storage by metallized graphene. *Applied Physics Letters* 2008, 93.

102. Uthaisar, C.; Barone, V., Edge Effects on the Characteristics of Li Diffusion in Graphene. *Nano Letters* 2010, 10, 2838-2842.

103. Shin, H. C.; Liu, M.; Sadanadan, B.; Rao, A. M., Electrochemical insertion of lithium into multi-walled carbon nanotubes prepared by catalytic decomposition. *Journal of Power Sources* 2002, 112, 216-221.

104. Yang, Z. H.; Wu, H., Electrochemical intercalation of lithium into carbon nanotubes. *Solid State Ionics* 2001, 143, 173-180.

105. Mukhopadhyay, I.; Touhara, H., Different methods of preparing electrode from single-wall carbon nanotubes and their effect on the Li ion insertion process. *Journal of Solid State Electrochemistry* 2007, 12, 715-720.

106. Gao, B.; Kleinhammes, A.; Tang, X. P.; Bower, C.; Fleming, L.; Wu, Y.; Zhou, O., Electrochemical intercalation of single-walled carbon nanotubes with lithium. *Chemical Physics Letters* 1999, 307, 153-157.

107. Frackowiak, E.; Gautier, S.; Gaucher, H.; Bonnamy, S.; Beguin, F., Electrochemical storage of lithium in multiwalled carbon nanotubes. *Carbon* 1999, 37, 61-69.

108. Garcia-Cespedes, J.; Thomasson, S.; Teo, K. B. K.; Kinloch, I. A.; Milne, W. I.; Pascual, E.; Bertran, E., Efficient diffusion barrier layers for the catalytic growth of carbon nanotubes on copper substrates. *Carbon* 2009, 47, 613-621.

109. Nguyen, J. J.; Turano, S.; Ready, W. J., The Synthesis of Carbon Nanotubes Grown on Metal Substrates: A Review. *Nanoscience and Nanotechnology Letters* 2012, 4, 1123-1131.

110. Nguyen, J. J.; Bougher, T. L.; Pour Shahid Saeed Abadi, P.; Sharma, A.; Graham, S.; Cola, B. A., Postgrowth Microwave Treatment to Align Carbon Nanotubes. *Journal of Micro and Nano-Manufacturing* 2013, 1, 014501-014501.

111. Huang, J.-Q.; Zhang, Q.; Xu, G.-H.; Qian, W.-Z.; Wei, F., Substrate morphology induced self-organization into carbon nanotube arrays, ropes, and agglomerates. *Nanotechnology* 2008, 19, 435602-435602.

112. Guo, T.; Nikolaev, P.; Rinzler, A. G.; Tomanek, D.; Colbert, D. T.; Smalley, R. E., Self-Assembly of Tubular Fullerenes. *The Journal of Physical Chemistry* 1995, 99, 10694-10697.

113. Chiu, C.-C.; Tsai, T.-Y.; Tai, N.-H., Field emission properties of carbon nanotube arrays through the pattern transfer process. *Nanotechnology* 2006, 17, 2840-2844.

114. Cross, R. Processing Vertically Aligned Carbon Nanotubes for Heat Transfer Applications. Georgia Institute of Technology, Atlanta, GA, 2008.

115. Zhang, H.; Cao, G. P.; Yang, Y. S., Using a cut–paste method to prepare a carbon nanotube fur electrode. *Nanotechnology* 2007, 18, 195607-195607.

116. Chen, J.; Liu, Y.; Minett, A. I.; Lynam, C.; Wang, J.; Wallace, G. G., Flexible, Aligned Carbon Nanotube/Conducting Polymer Electrodes for a Lithium-Ion Battery. *Chemistry of Materials* 2007, 19, 3595-3597.

117. King, H. W., Crystal Structures and Lattice Parameters of Allotropes of the Elements. In *CRC Handbook of Chemistry and Physics*, Haynes, W. M., Ed. CRC Press, Taylor & Francis Group: Boca Raton, FL, 2010.

118. Elshabini-Riad, A., Active Component Fabrication. In *Electronic Materials Handbook: Packaging*, Minges, M. L., Ed. ASM International: 1989; Vol. 1, pp 191-202.

119. Xie, J.; Cao, G. S.; Zhao, X. B., Electrochemical performances of Si-coated MCMB as anode material in lithium-ion cells. *Materials Chemistry and Physics* 2004, 88, 295-299.

120. Pierson, H. O., *Handbook of Chemical Vapor Deposition*. Noyes Publications: 1992.

121. Dimov, N.; Kugino, S.; Yoshio, M., Carbon-coated silicon as anode material for lithium ion batteries: advantages and limitations. *Electrochimica Acta* 2003, 48, 1579 - 1587.

122. Li, H., A High Capacity Nano-Si Composite Anode Material for Lithium Rechargeable Batteries. *Electrochemical and Solid-State Letters* 1999, 2, 547-547.

123. Key, B.; Bhattacharyya, R.; Morcrette, M.; Seznéc, V.; Tarascon, J.-M.; Grey, C. P., Real-Time NMR Investigations of Structural Changes in Silicon Electrodes for Lithium-Ion Batteries. *Journal of the American Chemical Society* 2009, 131, 9239-9249.

124. Obrovac, M. N.; Christensen, L., Structural Changes in Silicon Anodes during Lithium Insertion/Extraction. *Electrochemical and Solid-State Letters* 2004, 7, A93-A93.

125. Wen, C. J.; Huggins, R. A., Chemical diffusion in intermediate phases in the lithium-silicon system. *Journal of Solid State Chemistry* 1981, 37, 271-278.

126. McDowell, M. T.; Lee, S. W.; Nix, W. D.; Cui, Y., 25th Anniversary Article: Understanding the Lithiation of Silicon and Other Alloying Anodes for Lithium-Ion Batteries. *Advanced Materials* 2013, 25, 4966-4985.

127. Liu, X. H.; Zhong, L.; Huang, S.; Mao, S. X.; Zhu, T.; Huang, J. Y., Size-Dependent Fracture of Silicon Nanoparticles During Lithiation. *ACS Nano* 2012, 6, 1522-1531.

128. Lee, S. W.; McDowell, M. T.; Choi, J. W.; Cui, Y., Anomalous Shape Changes of Silicon Nanopillars by Electrochemical Lithiation. *Nano Letters* 2011, 11, 3034-3039.

129. Shu, J.; Li, H.; Yang, R.; Shi, Y.; Huang, X., Cage-like carbon nanotubes/Si composite as anode material for lithium ion batteries. *Electrochemistry Communications* 2006, 8, 51-54.

130. Graetz, J.; Ahn, C. C.; Yazami, R.; Fultz, B., Highly Reversible Lithium Storage in Nanostructured Silicon. *Electrochemical and Solid-State Letters* 2003, 6, A194-A194.

131. Takamura, T.; Ohara, S.; Uehara, M.; Suzuki, J.; Sekine, K., A vacuum deposited Si film having a Li extraction capacity over 2000 mAh/g with a long cycle life. *Journal of Power Sources* 2004, 129, 96-100.

132. Takamura, T.; Uehara, M.; Suzuki, J.; Sekine, K.; Tamura, K., High capacity and long cycle life silicon anode for Li-ion battery. *Journal of Power Sources* 2006, 158, 1401-1404.

133. Moon, T.; Kim, C.; Park, B., Electrochemical performance of amorphous-silicon thin films for lithium rechargeable batteries. *Journal of Power Sources* 2006, 155, 391-394.

134. Beattie, S. D.; Larcher, D.; Morcrette, M.; Simon, B.; Tarascon, J. M., Si Electrodes for Li-Ion Batteries—A New Way to Look at an Old Problem. *Journal of The Electrochemical Society* 2008, 155, A158-A158.

135. Luo, Z.; Fan, D.; Liu, X.; Mao, H.; Yao, C.; Deng, Z., High performance silicon carbon composite anode materials for lithium ion batteries. *Journal of Power Sources* 2009, 189, 16-21.

136. Ohara, S.; Suzuki, J.; Sekine, K.; Takamura, T., A thin film silicon anode for Li-ion batteries having a very large specific capacity and long cycle life. *Journal of Power Sources* 2004, 136, 303-306.

137. Uehara, M.; Suzuki, J.; Tamura, K.; Sekine, K.; Takamura, T., Thick vacuum deposited silicon films suitable for the anode of Li-ion battery. *Journal of Power Sources* 2005, 146, 441-444.

138. Fu, L. J.; Endo, K.; Sekine, K.; Takamura, T.; Wu, Y. P.; Wu, H. Q., Studies on capacity fading mechanism of graphite anode for Li-ion battery. *Journal of Power Sources* 2006, 162, 663-666.

139. Adams, J. H.; Thomas, D., Germanium and Germanium Compounds. In *Kirk-Othmer encyclopedia of chemical technology*, John Wiley & Sons, Inc.: New York, 1994; Vol. 12, pp 548-564.

140. Butterman, W. C.; Jorgenson, J. D. *Germanium*; U.S. Geological Survey: 2005.

141. Wang, D.; Dai, H., Low-Temperature Synthesis of Single-Crystal Germanium Nanowires by Chemical Vapor Deposition. *Angewandte Chemie International Edition* 2002, 41, 4783-4786.

142. Baxter, D. V.; Chisholm, M. H.; Gama, G. J.; Hector, A. L.; Parkin, I. P., Low pressure chemical vapor deposition of metallic films of iron, manganese, cobalt, copper, germanium and tin employing bis(trimethyl)silylamido complexes, M(N(SiMe3)2)n. *Chemical Vapor Deposition* 1995, 1, 49-51.

143. Dittmar, K.; Jutzi, P.; Schmalhorst, J.; Reiss, G., Cyclopentadienyl Germanes as Novel Precursors for the CVD of Thin Germanium Films. *Chemical Vapor Deposition* 2001, 7, 193-193.

144. Sutter, E.; Sutter, P., Au-Induced Encapsulation of Ge Nanowires in Protective C Shells. *Advanced Materials* 2006, 18, 2583-2588.

145. Baggetto, L.; Notten, P. H. L., Lithium-Ion (De)Insertion Reaction of Germanium Thin-Film Electrodes: An Electrochemical and In Situ XRD Study. *Journal of The Electrochemical Society* 2009, 156, A169-A175-A169-A175.

146. Yoon, S.; Park, C. M.; Sohn, H. J., Electrochemical characterizations of germanium and carbon-coated germanium composite anode for lithium-ion batteries. *Electrochemical and Solid State Letters* 2008, 11, A42-A45-A42-A45.

147. Liang, W.; Yang, H.; Fan, F.; Liu, Y.; Liu, X. H.; Huang, J. Y.; Zhu, T.; Zhang, S., Tough Germanium Nanoparticles under Electrochemical Cycling. *ACS Nano* 2013, 7, 3427-3433.

148. Khomenko, V. G.; Barsukov, V. Z.; Doninger, J. E.; Barsukov, I. V., Lithium-ion batteries based on carbon-silicon-graphite composite anodes. *Journal of Power Sources* 2007, 165, 598-608.

149. Wilson, A. M.; Dahn, J. R., Lithium Insertion in Carbons Containing Nanodispersed Silicon. *Journal of The Electrochemical Society* 1995, 142, 326-332.

150. Wilson, A. M.; Way, B. M.; Dahn, J. R.; van Buuren, T., Nanodispersed silicon in pregraphitic carbons. *Journal of Applied Physics* 1995, 77, 2363-2363.

151. Cao, A.; Veedu, V. P.; Li, X.; Yao, Z.; Ghasemi-Nejhad, M. N.; Ajayan, P. M., Multifunctional brushes made from carbon nanotubes. *Nature Materials* 2005, 4, 540-545.

152. Dimov, N.; Fukuda, K.; Umeno, T.; Kugino, S.; Yoshio, M., Characterization of carbon-coated silicon: Structural evolution and possible limitations. *Journal of Power Sources* 2003, 114, 88-95.

153. Zhang, Y.; Zhao, Z. G.; Zhang, X. G.; Zhang, H. L.; Li, F.; Liu, C.; Cheng, H. M., Pyrolytic carbon-coated silicon/Carbon Nanotube composites: promising application for Li-ion batteries. *International Journal of Nanomanufacturing* 2008, 2, 4-15.

154. Hertzberg, B.; Alexeev, A.; Yushin, G., Deformations in Si–Li Anodes Upon Electrochemical Alloying in Nano-Confined Space. *Journal of the American Chemical Society* 2010, 132, 8548-8549.

155. Zhang, X. W.; Patil, P. K.; Wang, C.; Appleby, A. J.; Little, F.; others, Electrochemical performance of lithium ion battery, nano-silicon-based, disordered carbon composite anodes with different microstructures. *Journal of Power Sources* 2004, 125, 206-213.

156. Kovalenko, I.; Zdyrko, B.; Magasinski, A.; Hertzberg, B.; Milicev, Z.; Burtovyy, R.; Luzinov, I.; Yushin, G., A Major Constituent of Brown Algae for Use in High-Capacity Li-Ion Batteries. *Science* 2011, 334, 75-79.

157. Magasinski, A.; Zdyrko, B.; Kovalenko, I.; Hertzberg, B.; Burtovyy, R.; Huebner, C. F.; Fuller, T. F.; Luzinov, I.; Yushin, G., Toward Efficient Binders for Li-Ion Battery Si-Based Anodes: Polyacrylic Acid. *ACS Applied Materials & Interfaces* 2010, 2, 3004-3010.

158. Cui, G. L.; Gu, L.; Kaskhedikar, N.; van Aken, P. A.; Maier, J., A novel germanium/carbon nanotubes nanocomposite for lithium storage material. *Electrochimica Acta* 2010, 55, 985-988.

159. DiLeo, R. A.; Ganter, M. J.; Landi, B. J.; Raffaelle, R. P., Germanium–single-wall carbon nanotube anodes for lithium ion batteries. *Journal of Materials Research* 2010, 25, 1441-1446.

160. Kim, M. G.; Cho, J., Nanocomposite of Amorphous Ge and Sn Nanoparticles as an Anode Material for Li Secondary Battery. *Journal of The Electrochemical Society* 2009, 156, A277-A277.

161. Vedula, R.; Kaza, S.; Desu, S., Chemical Vapor Deposition of Polymers: Principles, Materials, and Applications. In *Chemical Vapor Deposition*, ASM International: 2001; Vol. 2.

162. Wang, G. X.; Wang, B.; Wang, X. L.; Park, J.; Dou, S. X.; Ahn, H.; Kim, K., Sn/graphene nanocomposite with 3D architecture for enhanced reversible lithium storage in lithium ion batteries. *Journal of Materials Chemistry* 2009, 19, 8378-8384.

163. Chou, S.-L.; Wang, J.-Z.; Choucair, M.; Liu, H.-K.; Stride, J. A.; Dou, S.-X., Enhanced reversible lithium storage in a nanosize silicon/graphene composite. *Electrochemistry Communications* 2010, 12, 303-306.

164. Lee, J. K.; Smith, K. B.; Hayner, C. M.; Kung, H. H., Silicon nanoparticles–graphene paper composites for Li ion battery anodes. *Chemical Communications* 2010, 46, 2025-2025.

165. Yoshimura, K.; Suzuki, J.; Sekine, K.; Takamura, T., Evaluation of the Li insertion/extraction reaction rate at a vacuum-deposited silicon film anode. *Journal of Power Sources* 2005, 146, 445-447.

166. Ferrari, A. C.; Meyer, J. C.; Scardaci, V.; Casiraghi, C.; Lazzeri, M.; Mauri, F.; Piscanec, S.; Jiang, D.; Novoselov, K. S.; Roth, S.; Geim, A. K., Raman Spectrum of Graphene and Graphene Layers. *Physical Review Letters* 2006, 97, 187401-187401.

167. Ferrari, A., Raman spectroscopy of graphene and graphite: Disorder, electron–phonon coupling, doping and nonadiabatic effects. *Solid State Communications* 2007, 143, 47-57.

168. Beyssac, O.; Goffe, B.; Petitet, J. P.; Froigneux, E.; Moreau, M.; Rouzaud, J. N., On the characterization of disordered and heterogeneous carbonaceous materials by Raman spectroscopy. *Spectrochimica Acta Part A - Molecular and Biomolecular Spectroscopy* 2003, 59, 2267-2276.

169. Ferrari, A. C.; Robertson, J., Interpretation of Raman spectra of disordered and amorphous carbon. *Physical Review B* 2000, 61, 14095-14095.

170. Chandrasekaran, R.; Magasinski, A.; Yushin, G.; Fuller, T. F., Analysis of Lithium Insertion/Deinsertion in a Silicon Electrode Particle at Room Temperature. *Journal of The Electrochemical Society* 2010, 157, A1139-A1139.

171. Anton, S. R.; Erturk, A.; Inman, D. J., Multifunctional self-charging structures using piezoceramics and thin-film batteries. *Smart Materials and Structures* 2010, 19, 115021-115021.

172. Liu, P.; Sherman, E.; Jacobsen, A., Design and fabrication of multifunctional structural batteries. *Journal of Power Sources* 2009, 189, 646-650.

173. Sun, L.; Karanjgaokar, N.; Sun, K.; Chasiotis, I.; Carter, W. C.; Dillon, S., High-strength all-solid lithium ion electrodes based on Li4Ti5O12. *Journal of Power Sources* 2011, 196, 6507-6511.

174. Thomas, J. P.; Qidwai, M. A., The design and application of multifunctional structure-battery materials systems. *JOM* 2005, 57, 18-24.

175. Evanoff, K.; Khan, J.; Balandin, A. A.; Magasinski, A.; Ready, W. J.; Fuller, T. F.; Yushin, G., Towards Ultrathick Battery Electrodes: Aligned Carbon Nanotube – Enabled Architecture. *Advanced Materials* 2012, 24, 533-537.

176. Kim, H.; Cho, J., Superior Lithium Electroactive Mesoporous Si@Carbon Core–Shell Nanowires for Lithium Battery Anode Material. *Nano Lett*. 2008, 8, 3688-3691.

177. Park, M.-H.; Kim, M. G.; Joo, J.; Kim, K.; Kim, J.; Ahn, S.; Cui, Y.; Cho, J., Silicon Nanotube Battery Anodes. *Nano Lett*. 2009, 9, 3844-3847.

178. Bridel, J. S.; Azais, T.; Morcrette, M.; Tarascon, J. M.; Larcher, D., Key Parameters Governing the Reversibility of Si/Carbon/CMC Electrodes for Li-Ion Batteries. *Chem. Mater*. 2010, 22, 1229-1241.

179. Guo, J. C.; Wang, C. S., A polymer scaffold binder structure for high capacity silicon anode of lithium-ion battery. *Chem. Commun*. 2010, 46, 1428-1430.

180. Mazouzi, D.; Lestriez, B.; Roue, L.; Guyomard, D., Silicon Composite Electrode with High Capacity and Long Cycle Life. *Electrochemical and Solid State Letters* 2009, 12, A215-A218.

181. Hertzberg, B.; Benson, J.; Yushin, G., Ex-situ depth-sensing indentation measurements of electrochemically produced Si-Li alloy films. *Electrochem. Commun*. 2011, 13, 818-821.

182. Evanoff, K.; Magasinski, A.; Yang, J.; G., Y., NanoSi-Coated Graphene Granules as Anodes for Li-ion Batteries. *Advanced Energy Materials* 2011.

183. Hertzberg, B.; Alexeev, A.; Yushin, G., Deformations in Si-Li Anodes Upon Electrochemical Alloying in Nano-Confined Space. *J. Am. Chem. Soc*. 2010, 132, 8548-8549.

184. Balandin, A. A., Thermal properties of graphene and nanostructured carbon materials. *Nat Mater* 2011, 10, 569-581.

185. Wang, C.; Li, D.; Too, C. O.; Wallace, G. G., Electrochemical Properties of Graphene Paper Electrodes Used in Lithium Batteries. *Chem. Mater*. 2009, 21, 2604-2606.

186. Spahr, M. E.; Palladino, T.; Wilhelm, H.; Wursig, A.; Goers, D.; Buqa, H.; Holzapfel, M.; Novak, P., Exfoliation of Graphite during Electrochemical Lithium Insertion in Ethylene Carbonate-Containing Electrolytes. *Journal of The Electrochemical Society* 2004, 151, A1383-A1395-A1383-A1395.

187. Yu, M. F.; Lourie, O.; Dyer, M. J.; Moloni, K.; Kelly, T. F.; Ruoff, R. S., Strength and breaking mechanism of multiwalled carbon nanotubes under tensile load. *Science* 2000, 287, 637-640.

188. Park, J. G.; Smithyman, J.; Lin, C.-Y.; Cooke, A.; Kismarahardja, A. W.; Li, S.; Liang, R.; Brooks, J. S.; Zhang, C.; Wang, B., Effects of surfactants and alignment on the physical properties of single-walled carbon nanotube buckypaper. *Journal of Applied Physics* 2009, 106, 104310-104310.

189. Pham, G. T.; Park, Y.-B.; Wang, S.; Liang, Z.; Wang, B.; Zhang, C.; Funchess, P.; Kramer, L., Mechanical and electrical properties of polycarbonate nanotube buckypaper composite sheets. *Nanotechnology* 2008, 19, 325705-325705.

190. Zhang, X.; Sreekumar, T. V.; Liu, T.; Kumar, S., Properties and Structure of Nitric Acid Oxidized Single Wall Carbon Nanotube Films. *The Journal of Physical Chemistry B* 2004, 108, 16435-16440.

191. Pushparaj, V. L.; Shaijumon, M. M.; Kumar, A.; Murugesan, S.; Ci, L.; Vajtai, R.; Linhardt, R. J.; Nalamasu, O.; Ajayan, P. M., Flexible energy storage devices based on nanocomposite paper. *Proceedings of the National Academy of Sciences* 2007, 104, 13574-13577.

192. Antunes, E. F.; Lobo, A. O.; Corat, E. J.; Trava-Airoldi, V. J.; Martin, A. A.; Verissimo, C., Comparative study of first- and second-order Raman spectra of MWCNT at visible and infrared laser excitation. *Carbon* 2006, 44, 2202-2211.

193. Tan, P.; Dimovski, S.; Gogotsi, Y., Raman Scattering of Non-Planar Graphite: Arched Edges, Polyhedral Crystals, Whiskers and Cones. *Phil. Trans. R. Soc. Lond. A* 2004, 362, 2289-2310.

194. Iqbal, Z.; Veprek, S., Raman scattering from hydrogenated microcrystalline and amorphous silicon. *Journal of Physics C: Solid State Physics* 1982, 15, 377-377.

195. Nguyen, J. J.; Evanoff, K.; Ready, W. J., Amorphous and nanocrystalline silicon growth on carbon nanotube substrates. *Thin Solid Films* 2011, 519, 4144-4147.

196. Mechanical Properties of Materials. In *CRC Materials Science and Engineering Handbook, Third Edition*, Shackelford, J.; Alexander, W., Eds. CRC Press: 2000.

197. Sun, Y.-P.; Fu, K.; Lin, Y.; Huang, W., Functionalized Carbon Nanotubes: Properties and Applications. *Acc. Chem. Res.* 2002, 35, 1096-1104.

198. Bandhauer, T. M.; Garimella, S.; Fuller, T. F., A Critical Review of Thermal Issues in Lithium-Ion Batteries. *Journal of The Electrochemical Society* 2011, 158, R1-R1.

199. Fleckenstein, M.; Bohlen, O.; Roscher, M. A.; Bäker, B., Current density and state of charge inhomogeneities in Li-ion battery cells with LiFePO4 as cathode material due to temperature gradients. *Journal of Power Sources* 2011, 196, 4769-4778.

200. Maleki, H.; Hallaj, S. A.; Selman, J. R.; Dinwiddie, R. B.; Wang, H., Thermal Properties of Lithium-Ion Battery and Components. *Journal of The Electrochemical Society* 1999, 146, 947-954.

201. Chen, S. C.; Wan, C. C.; Wang, Y. Y., Thermal analysis of lithium-ion batteries. *Journal of Power Sources* 2005, 140, 111-124.

202. Bonnefoi, L.; Simon, P.; Fauvarque, J. F.; Sarrazin, C.; Dugast, A., Electrode optimisation for carbon power supercapacitors. *Journal of Power Sources* 1999, 79, 37-42.

203. Jakubinek, M. B.; White, M. A.; Li, G.; Jayasinghe, C.; Cho, W.; Schulz, M. J.; Shanov, V., Thermal and electrical conductivity of tall, vertically aligned carbon nanotube arrays. *Carbon* 2010, 48, 3947-3952.

204. Matula, R. A., Electrical Resistivity of Copper, Gold, Palladium, and Silver. *J. Phys. Chem. Ref. Data* 1979, 8, 1147 - 1298.

205. Powell, R. W.; Ho, C. Y.; Liley, P. E., Thermal Conductivity of Selected Materials. Commerce, U. S. D. o., Ed. 1966.

206. Moshtev, R.; Johnson, B., State of the art of commercial Li ion batteries. *Journal of Power Sources* 2000, 91, 86-91.

207. Garcia, R. E.; Chiang, Y.-M., Spatially Resolved Modeling of Microstructurally Complex Battery Architectures. *Journal of The Electrochemical Society* 2007, 154, A856-A864-A856-A864.

208. Long, J. W.; Dunn, B.; Rolison, D. R.; White, H. S., Three-Dimensional Battery Architectures. *Chemical Reviews* 2004, 104, 4463-4492.

209. Ripenbein, T.; Golodnitsky, D.; Nathan, M.; Peled, E., Novel porous-silicon structures for 3D-interlaced microbatteries. *Electrochimica Acta* 2010, 56, 37-41.

210. Notten, P. H. L.; Roozeboom, F.; Niessen, R. A. H.; Baggetto, L., 3-D Integrated All-Solid-State Rechargeable Batteries. *Advanced Materials* 2007, 19, 4564-4567.

211. Shaijumon, M. M.; Perre, E.; Daffos, B.; Taberna, P.-L.; Tarascon, J.-M.; Simon, P., Nanoarchitectured 3D Cathodes for Li-Ion Microbatteries. *Advanced Materials* 2010, 22, 4978-4981.

212. Bazin, L.; Mitra, S.; Taberna, P. L.; Poizot, P.; Gressier, M.; Menu, M. J.; Barnabe, A.; Simon, P.; Tarascon, J. M., High rate capability pure Sn-based nano-architectured electrode assembly for rechargeable lithium batteries. *Journal of Power Sources* 2009, 188, 578-582.

213. Taberna, P. L.; Mitra, S.; Poizot, P.; Simon, P.; Tarascon, J. M., High rate capabilities Fe3O4-based Cu nano-architectured electrodes for lithium-ion battery applications. *Nat Mater* 2006, 5, 567-573.

214. Wang, C.; Taherabadi, L.; Jia, G.; Madou, M.; Yeh, Y.; Dunn, B., C-MEMS for the Manufacture of 3D Microbatteries. *Electrochemical and Solid-State Letters* 2004, 7, A435 - A438-A435 - A438.

215. Inoue, Y.; Kakihata, K.; Hirono, Y.; Horie, T.; Ishida, A.; Mimura, H., One-step grown aligned bulk carbon nanotubes by chloride mediated chemical vapor deposition. *Applied Physics Letters* 2008, 92, 213113-213113.

216. Liu, P.; Zhang, J.-G.; Turner, J. A.; Tracy, C. E.; Benson, D. K.; Bhattacharya, R. N., Fabrication of LiV2O5 thin-film electrodes for rechargeable lithium batteries. *Solid State Ionics* 1998, 111, 145-151.

217. Wang, W.; Epur, R.; Kumta, P. N., Vertically aligned silicon/carbon nanotube (VASCNT) arrays: Hierarchical anodes for lithium-ion battery. *Electrochemistry Communications* 2011, 13, 429-432.

218. Ghosh, S.; Teweldebrhan, D.; Morales, J. R.; Garay, J. E.; Balandin, A. A., Thermal properties of the optically transparent pore-free nanostructured yttria-stabilized zirconia. *Journal of Applied Physics* 2009, 106, 113507-113507.

219. Ikkawi, R.; Amos, N.; Lavrenov, A.; Krichevsky, A.; Teweldebrhan, D.; Ghosh, S.; Balandin, A. A.; Litvinov, D.; Khizroev, S., Near-Field Optical Transducer for Heat-Assisted Magnetic Recording for Beyond-10-Tbit/in2 Densities. *Journal of Nanoelectronics and Optoelectronics* 2008, 3, 44-54.

220. Shamsa, M.; Ghosh, S.; Calizo, I.; Ralchenko, V.; Popovich, A.; Balandin, A. A., Thermal conductivity of nitrogenated ultrananocrystalline diamond films on silicon. *Journal of Applied Physics* 2008, 103, 083538-083538.

221. Evanoff, K.; Magasinski, A.; Yang, J.; Yushin, G., Nanosilicon-Coated Graphene Granules as Anodes for Li-Ion Batteries. *Advanced Energy Materials* 2011, 1, 495-498.

222. DiLeo, R. A.; Landi, B. J.; Raffaelle, R. P., Purity assessment of multiwalled carbon nanotubes by Raman spectroscopy. *Journal of Applied Physics* 2007, 101, 064307-064307.

223. Ramadass, P.; Haran, B.; Gomadam, P. M.; White, R.; Popov, B. N., Development of First Principles Capacity Fade Model for Li-Ion Cells. *Journal of The Electrochemical Society* 2004, 151, A196-A203-A196-A203.

224. Vetter, J.; Novák, P.; Wagner, M. R.; Veit, C.; Möller, K. C.; Besenhard, J. O.; Winter, M.; Wohlfahrt-Mehrens, M.; Vogler, C.; Hammouche, A., Ageing mechanisms in lithium-ion batteries. *Journal of Power Sources* 2005, 147, 269-281.

225. Abraham, D. P.; Knuth, J. L.; Dees, D. W.; Bloom, I.; Christophersen, J. P., Performance degradation of high-power lithium-ion cells--Electrochemistry of harvested electrodes. *Journal of Power Sources* 2007, 170, 465-475.

226. Balandin, A. A.; Shamsa, M.; Liu, W. L.; Casiraghi, C.; Ferrari, A. C., Thermal conductivity of ultrathin tetrahedral amorphous carbon films. *Applied Physics Letters* 2008, 93, 043115-043115.

227. He, Y.; Yu, X.; Wang, Y.; Li, H.; Huang, X., Alumina-Coated Patterned Amorphous Silicon as the Anode for a Lithium-Ion Battery with High Coulombic Efficiency. *Advanced Materials* 2011, 23, 4938-4941.

228. Jung, H.; Park, M.; Han, S. H.; Lim, H.; Joo, S.-K., Amorphous silicon thin-film negative electrode prepared by low pressure chemical vapor deposition for lithium-ion batteries. *Solid State Communications* 2003, 125, 387-390.

229. Kim, H.; Lee, J. T.; Lee, D.-C.; Magasinski, A.; Cho, W.-i.; Yushin, G., Plasma-Enhanced Atomic Layer Deposition of Ultrathin Oxide Coatings for Stabilized Lithium–Sulfur Batteries. *Advanced Energy Materials* 2013, 3, 1308-1315.

230. Riley, L. A.; Cavanagh, A. S.; George, S. M.; Jung, Y. S.; Yan, Y.; Lee, S.-H.; Dillon, A. C., Conformal Surface Coatings to Enable High Volume Expansion Li-Ion Anode Materials. *ChemPhysChem* 2010, 11, 2124-2130.

231. Liu, Y.; Hudak, N. S.; Huber, D. L.; Limmer, S. J.; Sullivan, J. P.; Huang, J. Y., In Situ Transmission Electron Microscopy Observation of Pulverization of Aluminum Nanowires and Evolution of the Thin Surface Al_2O_3 Layers during Lithiation–Delithiation Cycles. *Nano Letters* 2011, 11, 4188-4194.

232. George, S. M., Atomic Layer Deposition: An Overview. *Chemical Reviews* 2009, 110, 111-131.

233. Liu, X. H.; Huang, S.; Picraux, S. T.; Li, J.; Zhu, T.; Huang, J. Y., Reversible Nanopore Formation in Ge Nanowires during Lithiation–Delithiation Cycling: An In Situ Transmission Electron Microscopy Study. *Nano Letters* 2011, 11, 3991-3997.

234. Hao, S.; Wolverton, C., Lithium Transport in Amorphous Al2O3 and AlF3 for Discovery of Battery Coatings. *The Journal of Physical Chemistry C* 2013, 117, 8009-8013.

235. Fuller, C. S.; Severiens, J. C., Mobility of Impurity Ions in Germanium and Silicon. *Physical Review* 1954, 96, 21-24.

236. Choi, J. W.; McDonough, J.; Jeong, S.; Yoo, J. S.; Chan, C. K.; Cui, Y., Stepwise Nanopore Evolution in One-Dimensional Nanostructures. *Nano Letters* 2010, 10, 1409-1413.

237. Jung, Y. S.; Lu, P.; Cavanagh, A. S.; Ban, C.; Kim, G.-H.; Lee, S.-H.; George, S. M.; Harris, S. J.; Dillon, A. C., Unexpected Improved Performance of ALD Coated $LiCoO_2$/Graphite Li-Ion Batteries. *Advanced Energy Materials* 2013, 3, 213-219.

238. Zhao, J.; Wang, Y., Atomic layer deposition of epitaxial ZrO_2 coating on $LiMn_2O_4$ nanoparticles for high-rate lithium ion batteries at elevated temperature. *Nano Energy* 2013, 2, 882-889.

239. Ryu, I.; Choi, J. W.; Cui, Y.; Nix, W. D., Size-dependent fracture of Si nanowire battery anodes. *Journal of the Mechanics and Physics of Solids* 2011, 59, 1717-1730.

240. McDowell, M. T.; Lee, S. W.; Harris, J. T.; Korgel, B. A.; Wang, C.; Nix, W. D.; Cui, Y., In Situ TEM of Two-Phase Lithiation of Amorphous Silicon Nanospheres. *Nano Letters* 2013, 13, 758-764.

241. Maranchi, J. P.; Hepp, A. F.; Evans, A. G.; Nuhfer, N. T.; Kumta, P. N., Interfacial Properties of the a-Si/Cu :Active–Inactive Thin-Film Anode System for Lithium-Ion Batteries. *Journal of The Electrochemical Society* 2006, 153, A1246-A1253.

242. Ignat, M., Stresses and Mechanical Stability of CVD Thin Films. In *Chemical Vapor Deposition*, ASM International: 2001; Vol. 2.

243. Frank, O.; Tsoukleri, G.; Parthenios, J.; Papagelis, K.; Riaz, I.; Jalil, R.; Novoselov, K. S.; Galiotis, C., Compression Behavior of Single-Layer Graphenes. *ACS Nano* 2010, 4, 3131-3138.

244. Zhu, C.; Guo, W.; Yu, T. X.; Woo, C. H., Radial compression of carbon nanotubes: deformation and damage, super-elasticity and super-hardness. *Nanotechnology* 2005, 16, 1035 - 1039.

245. Shen, H., The Effects of Radial Compression on Thermal Conductivity of Carbon and Boron Nitride Nanotubes. *Journal of Nanomaterials* 2012, 2012.

246. Thermal and Physical Properties of Pure Metals. In *CRC Handbook of Chemistry and Physics*, Haynes, W. M., Ed. CRC Press, Taylor & Francis Group: Boca Raton, FL, 2010.

247. Zhang, J.; Ji, L.; Zuo, J.-M., Large Negative Thermal Expansion of an Individual Carbon Nanotube. In *American Physical Society*, 2008; Vol. 53.

248. Yoon, D.; Son, Y.-W.; Cheong, H., Negative Thermal Expansion Coefficient of Graphene Measured by Raman Spectroscopy. *Nano Letters* 2011, 11, 3227-3231.

249. Takimoto, K.; Fukuta, A.; Yamamoto, Y.; Yoshida, N.; Itoh, T.; Nonomura, S., Linear thermal expansion coefficients of amorphous and microcrystalline silicon films. *Journal of Non-Crystalline Solids* 2002, 299–302, Part 1, 314-317.

250. Marques, F. C.; Lacerda, R. G.; Champi, A.; Stolojan, V.; Cox, D. C.; Silva, S. R. P., Thermal expansion coefficient of hydrogenated amorphous carbon. *Applied Physics Letters* 2003, 83, 3099-3101.

251. Wu, F. Y.; Cheng, H. M., Structure and thermal expansion of multi-walled carbon nanotubes before and after high temperature treatment. *Journal of Physics D: Applied Physics* 2005, 38, 4302.

252. Hu, L.; Wu, H.; Gao, Y.; Cao, A.; Li, H.; McDough, J.; Xie, X.; Zhou, M.; Cui, Y., Silicon–Carbon Nanotube Coaxial Sponge as Li-Ion Anodes with High Areal Capacity. *Advanced Energy Materials* 2011, 1, 523-527.

253. Cui, L.-F.; Yang, Y.; Hsu, C.-M.; Cui, Y., Carbon–Silicon Core–Shell Nanowires as High Capacity Electrode for Lithium Ion Batteries. *Nano Letters* 2009, 9, 3370-3374.

254. Osaka, T.; Nara, H.; Mukaibo, H., Nano-Electrochemical Approach For Improvement Of Lithium-Tin Alloy Anode. In *Nanomaterials for Lithium-Ion Batteries: Fundamentals and Applications*, Yazami, R., Ed. Pan Stanford Publishing: 2013.

255. Ole Valoen, L.; Reimers, J. N., Transport Properties of LiPF6-Based Li-Ion Battery Electrolytes. *J. Electrochem. Soc.* 2005, 152, A882 - A891.

256. Boukhalfa, S.; Evanoff, K.; Yushin, G., Atomic layer deposition of vanadium oxide on carbon nanotubes for high-power supercapacitor electrodes. *Energy & Environmental Science* 2012.

257. Benson, J.; Kovalenko, I.; Boukhalfa, S.; Lashmore, D.; Sanghadasa, M.; Yushin, G., Multifunctional CNT-Polymer Composites for Ultra-Tough Structural Supercapacitors and Desalination Devices. *Advanced Materials* 2013, 25, 6625 - 6632.

258. Kim, H.; Lee, J. T.; Yushin, G., High temperature stabilization of lithium–sulfur cells with carbon nanotube current collector. *Journal of Power Sources* 2013, 226, 256-265.